Hydrogenation and Dehydrogenation Kinetics and Catalysts for New Hydrogen Storage Liquids

by

Farnaz Sotoodeh

M.Sc. in Chemical Engineering, Iran University of Science and Technology, 2006

B.Sc. in Chemical Engineering, Iran University of Science and Technology, 2003

A THESIS SUBMITTED IN PARTIAL FULFILLMENT
OF THE REQUIREMENTS FOR THE DEGREE OF

Doctor of Philosophy

in

THE FACULTY OF GRADUATE STUDIES

(Chemical and Biological Engineering)

The University of British Columbia

(Vancouver)

June 2011

Abstract

Due to the very low density of H_2, practical storage and recovery of H_2 has been a challenge in utilizing H_2 as an alternative fuel. Organic heteroaromatics have attracted interest because of their thermal stability and high storage capacity. In this study, H_2 storage and recovery from these compounds were investigated. The kinetics of the hydrogenation/dehydrogenation reactions was studied and DFT calculations were used to understand the dehydrogenation product distribution.

The hydrogenation of N-ethylcarbazole and carbazole at 403-423 K on a supported Ru catalyst was well described by first-order kinetics. The hydrogenation of N-ethylcarbazole was significantly faster than the hydrogenation of carbazole, and $>$95 % selectivity to dodecahydro-N-ethylcarbazole and dodecahydrocarbazole was achieved, respectively.

The dehydrogenation kinetics of dodecahydro-N-ethylcarbazole was studied at 101 kPa and 423-443 K over a Pd catalyst prepared by wet impregnation and calcination in air. The reactions followed first-order kinetics with 100 % conversion but only 69 % recovery of H_2 was achieved at 443 K, due to minimal selectivity to N-ethylcarbazole. The complete recovery of H_2 from dodecahydro-N-ethylcarbazole was achieved at 443 K and 101 kPa using Pd/SiO_2 catalysts prepared by incipient wetness impregnation with calcination in He. The dehydrogenation TOF and selectivity to N-ethylcarbazole were dependent upon the Pd particle size.

The effect of the N heteroatom on the dehydrogenation of polyaromatics was studied by comparison of dodecahydro-N-ethylcarbazole, dodecahydrocarbazole

and dodecahydrofluorene dehydrogenation over Pd catalysts. The dehydrogenation of dodecahydro-N-ethylcarbazole and dodecahydrocarbazole were structure sensitive. The dehydrogenation rate of dodecahydrocarbazole was slower than dodecahydro-N-ethylcarbazole. Despite catalyst poisoning through the N atom in dodecahydrocarbazole, the N heteroatom was found to favor dehydrogenation, making heteroaromatics better candidates for H_2 storage than aromatics.

The structure sensitivity of the reactions and the observed product distribution are explained in view of DFT calculations that showed that the adsorption of dodecahydro-N-ethylcarbazole on Pd required multiple catalytic sites and the heat of adsorption was dependent upon the surface structure. The effect of the ethyl group and the N heteroatom on the dehydrogenation rate of dodecahydro-N-ethylcarbazole was also investigated by comparing the adsorption energies of dodecahydro-N-ethylcarbazole with dodecahydrocarbazole and dodecahydrofluorene.

Preface

This dissertation consists of six manuscripts five of which are included in Chapters 2 to 6, and one of which is included in Appendix H. This PhD work has been done by Farnaz Sotoodeh under the direct supervision of Professor Kevin J. Smith in the Department of Chemical and Biological Engineering at the University of British Columbia. Preparation of the dissertation, literature review, experimental design and set−up, data collection and analysis, reaction modeling and kinetic study, theoretical molecular modeling of the dehydrogenation reactions, as well as the analysis and interpretation of the results in this thesis have been performed by Farnaz Sotoodeh under the supervision of Professor Kevin J. Smith.

The manuscripts included in this dissertation are listed below. For the manuscripts with co-authors, the contributions of Farnaz Sotoodeh have been described in detail.

1. F. Sotoodeh and K.J. Smith (2010) Kinetics of hydrogen uptake and release from heteroaromatic compounds for hydrogen storage, Industrial and Engineering Chemistry Research, 49, 1018-1026. A version of this manuscript is included in Chapter 2.

   The catalyst preparation and characterization, hydrogenation reactor set−up and performing the hydrogenation reactions, as well as the dehydrogenation reactor set−up, carrying out the dehydrogenation reactions, hydrogenation and dehydrogenation reactions sample collection and analysis of data, hydrogenation and dehydrogenation network mathematical modeling and coding, as well as the kinetic analysis of the reactions, have been done by Farnaz So-

toodeh. The preparation and writing of the manuscript was done by Farnaz Sotoodeh under direct supervision and final approval of Professor Kevin J. Smith.

2. F. Sotoodeh, L. Zhao and K.J. Smith (2009) Kinetics of H_2 recovery from dodecahydro-N-ethylcarbazole over a supported Pd catalyst, Applied Catalysis A: General 362, 155-162. A version of this manuscript is included in Chapter 3.

   The catalyst preparation, characterization, design and experimental set−up for the dehydrogenation reactions, sample collection and data analysis, kinetic study of the reactions, mathematical modeling of the reaction network and coding have been done by Farnaz Sotoodeh under the direct supervision of Professor Kevin J. Smith. The manuscript was prepared and written by Farnaz Sotoodeh with final approval of Professor Kevin J. Smith. Some portions of the liquid sample analysis of the dehydrogenation reactions were done by Liang Zhao.

3. F. Sotoodeh and K.J. Smith (2011) Structure sensitivity of dodecahydro-N-ethylcarbazole dehydrogenation over Pd catalysts, Journal of Catalysis 279, 36-47. A version of this manuscript is included in Chapter 4.

   The catalyst preparation and characterization, catalyst testing including the experimental reaction design and set−up, performing the reactions and data collection by sampling, data analysis of the experiments and results interpretation, kinetic studies of the dehydrogenation reactions, theoretical work including molecular design of the dehydrogenation reaction, DFT calculations using the Material Studio software and the theoretical data analysis, as well as interpretation of the results, have been done by Farnaz Sotoodeh under the direct supervision of Professor Kevin J. Smith. This manuscript was prepared and written by Farnaz Sotoodeh with final approval of Professor Kevin J. Smith.

4. F. Sotoodeh, B.J.M. Huber and K.J. Smith, The effect of the N-heteroatom

on the dehydrogenation of polyaromatics used for hydrogen storage, to be submitted. A version of this manuscript is included in Chapter 5.

The catalyst preparation and characterization, the hydrogenation and dehydrogenation reaction experimental set−up and design, performing the hydrogenation reactions of carbazole and N−ethylcarbazole, performing the dehydrogenation reactions of dodecahydro-N-ethylcarbazole, the kinetic study of the dehydrogenation reactions and the data analysis of the dehydrogenation reactions of dodecahydro-N-ethylcarbazole as well as interpretation of the results have been done by Farnaz Sotoodeh under the direct supervision of Professor Kevin J. Smith. The preparation and writing of the manuscript were done by Farnaz Sotoodeh with final approval of Professor Kevin J. Smith. Some part of the dehydrogenation reactions of dodecahydrocarbazole and dodecahydrofluorene and liquid sample analysis were done by Benjamin J.M. Huber.

5. F. Sotoodeh and K.J. Smith, Density functional theory study of dodecahydro-N-ethylcarbazole dehydrogenation over a Pd catalyst, to be submitted. A version of this manuscript is included in Chapter 6.

   Molecular design of the dehydrogenation reaction including building the chemical structure of the reactants, products and catalyst surface, performing the geometry optimization of the designed systems using Material Studio software, performing potential energy surface calculations by doing transition state search through each catalytic step, theoretical analysis of the obtained results, as well as interpretation of the results through comparison with the experimental results, have been done by Farnaz Sotoodeh under direct supervision of Professor Kevin J. Smith. The preparation and writing of the manuscript was done by Farnaz Sotoodeh with final approval of Professor Kevin J. Smith.

The following manuscript is included in the “Additional publications” section, Appendix H.

L. Zhao, F. Sotoodeh and K.J. Smith (2010) Increased surface area of unsupported Mo_2C catalyst by alkali-treatment, Catalysis Communications 11, 391-395.

Preparation of the 12 h alkali-treated Mo_2C catalyst, catalyst characterizations including X-ray diffraction (XRD), BET surface area and pore size distributions measurements of the 6 h and 12 h alkali-treated Mo_2C catalysts, as well as dehydrogenation reactions of tetrahydrocarbazole over a 5 wt % Pd/SiO_2 were done by Farnaz Sotoodeh under direct supervision of Professor Kevin J. Smith. Writing the manuscript, some portions of the catalyst preparation and characterization, as well as CO hydrogenation reactions were done by Liang Zhao.

Table of Contents

List of Tables

List of Figures

Glossary

a	=	Lattice parameter (nm)
AB	=	Ammonia borane
amu	=	Atomic mass unit
AT-2	=	Alkali-treated for 2 h
AT-6	=	Alkali-treated for 6 h
AT-12	=	Alkali-treated for 12 h
a.u.	=	Atomic unit
AW_{Pd}	=	Atomic mass of Palladium (g/mol)
BET	=	Brunauer Emmett Teller surface area analysis
c	=	Lattice parameter (nm)
C_{A0}	=	Reactant initial concentration (mol/cm^3)
C-H	=	Carbon hydrogen bond
D_{AB}	=	Bulk or Knudsen diffusivity (m^2/sec)
$d_{cluster}$	=	Cluster diameter (nm)
D_e	=	Effective diffusivity (m^2/sec)
DFT	=	Density Functional Theory
$DMol^3$	=	A unique density functional theory (DFT) quantum mechanical code
D.O.E.	=	Department of Energy
D.O.L.	=	Dehydrogenated Organic Liquid
DOS	=	Density of state
d_p	=	Average pore size (nm)
DTG	=	Differential thermal analysis

E_i	=	Numerical value of the energy of state i
EDX	=	Energy Dispersive X-ray spectroscopy
E_{XC}	=	Exchange correlation energy
GC/MS	=	Gas Chromatograph/Mass Spectrometer
GGA	=	generalized gradient approximation
GHSV	=	Gas hourly space velocity (h^{-1})
$\hat{H}$	=	Hamiltonian operator of the total energy for the system
Ha	=	Atomic energy unit (1 Hartree= 627.5 kcal/mol)
HC	=	Hydrocarbon
HF	=	Hartree-Fock
HRTEM	=	High Resolution Transmission Electron Microscopy
ΔH_R°	=	Heat of hydrogenation (kJ/mol)
i.d.	=	Inner diameter (nm)
k_B	=	Boltzmann constant
LCAO	=	Linear Combination of Atomic Orbitals
LDA	=	Local density approximation
LYP	=	Gradient−corrected correlation functional of Lee, Yang, and Parr
μ	=	Solvent viscosity (kg/(sec.m))
MFC	=	Mass flow controller
$mMmin^{-1}g_{cat}{}^{-1}$	=	Millimolar per minute per gram of catalyst
M_{Pd}	=	Palladium loading (wt %)
MS	=	Mass spectrometer
nm	=	Nanometer (= 10^{-9} m)
o.d.	=	Outer diameter (nm)
P_1	=	Frequency of reaction step
P_2	=	Frequency of reaction step
PBE	=	Perdew−Burke−Ernzerhof functional
PES	=	Potential energy surface
PGMs	=	Platinum group metals
PW91	=	Perdew and Wang generalized gradient approximation

R_0	=	Solute radius (m)
rpm	=	Revolutions per minute
S_{BET}	=	BET surface area (m^2/g)
$S_{t-micro}$	=	t-plot micropore area (m^2/g)
S_{t-ext}	=	t-plot external surface area (m^2/g)
SCCM	=	Standard cubic centimeter per minute
SCF	=	Self-consistent-field
SEM	=	Scanning Electron Microscopy
STP	=	Standard temperature and pressure
T	=	Temperature (K)
T_b	=	Boiling point (K)
TCD	=	Thermal conductivity detector
TGA	=	Thermal gravimetric analysis
THCZ	=	1,2,3,4-Tetrahydrocarbazole
T_m	=	melting point (K)
TOF	=	Turn-over frequency (s^{-1})
TPD	=	Temperature Programmed Desorption
TPR	=	Temperature Programmed Reduction
UHP	=	Ultra high purity
V_m	=	Adsorbed volume at monolayer coverage (cm^3/g_{cat})
V_p	=	Volume of pores between 1.7 nm and 300 nm width (cm^3)
Z_α	=	Charge of the nuclei
∇^2	=	Laplacian operator
ρ(r)	=	Electronic density
Ψ	=	Wave function
ϕ	=	Weisz-Prater criterion for internal mass transfer
α	=	Polanyi parameter (Chapter 4), degree (Chapter 6)
γ	=	Surface free energy
σ	=	Sigma bond
π	=	Pi bond (or electrons)

ϕ_P = Pellet porosity
σ_C = Constriction factor
$\tilde{\tau}$ = Tortuosity
λ = Wave length of radiation
β = Peak width in radian
θ = Angle of diffraction

Acknowledgments

First and foremost, I wish to express my deepest and sincerest gratitude to my supervisor, Professor Kevin J. Smith whose great personality, wide knowledge, encouragement, patience, guidance and important support during my work enabled me to develop an understanding of the project. It is an honor to know Professor Smith. He is a great teacher and I have learnt a lot from him. I hope to utilize his advices in my future career and my life.

I would like to sincerely thank Professor Jim C. Lim, Professor Elod Gyenge and Professor Walter Merida for being part of my examination committee.

I am grateful to the Chemical and Biological Engineering Department at the University of British Columbia for giving me the opportunity to pursue this research and NSERC for providing financial support for my research.

I would like to thank all of those who supported me during the completion of my thesis, the friendly catalysis group members (Xuebin Liu, Liang Zhao, Benjamin J.M. Huber, Zaman Fakhruz Sharif, Shahin Goodarznia, Hooman Rezaei, Shahrzad Jooya Ardakani, Ross Kukard, Victoria Whiffen and Rui Wang), CHBE office secretaries Helsa Leong, Lori Tanaka and Amber Lee, CHBE store personnel Ricard Ryoo and Horace Lam, CHBE IT manager Richard Zhang, CHBE workshop technicians Doug Yuen, Alex Thng, Graham Liebelt, Gordon Cheng, David Roberts and Charles Cheung, the Bioimaging facility in the Department of Botany at the University of British Columbia for the high resolution transmission electron microscopy (HRTEM) measurements specially Bradford Ross and Derrick

Horne, Marry Fletcher in the department of Material Engineering at the University of British Columbia for helping me in the SEM, TEM and X-ray measurements, Dr. Philip Wong at the advanced materials and process engineering laboratory (AMPEL) at the University of British Columbia for helping me on the set-up of the mass spectrometer, and Professor Philip G. Jessop's group at the Chemistry department of Queen's University, Kingston, Canada.

And last but not the least, I wish to thank my beloved parents, Niloofar and Fazel, for their love and support.

Dedication

To my beloved parents

and

to the loving memory of my grandfather

Chapter 1

Introduction

1.1 Introduction

Hydrogen, an alternative fuel, can be produced from different sources such as fossil fuels and renewables such as water with the aid of solar or wind energy [1–7], and biomass [8–10]. Furthermore, hydrogen is non-toxic and does not have any contaminating impact on the environment, because the only products of burning hydrogen are water and energy [1].

Although using hydrogen has many advantages, there is a gap in the technology of hydrogen storage as well as in hydrogen transport infrastructure [1]. Because of the low density of hydrogen, storage and transport of hydrogen requires the use of large scale compressors [11]. Also, current gas piping systems can not be used for pure hydrogen transport due to the embrittlement effect of hydrogen on steel [1]. Although alternative methods, including compressed or liquified hydrogen [12], or using hydrogen carriers such as methanol and organic liquids, have been considered, the hydrogen storage capacity and safety of the storage system are key factors that will determine their efficacy [1]. Due to the above mentioned reasons, the storage and transportation of hydrogen is considered one of the toughest challenges in the hydrogen economy [11].

A fuel efficient automobile requires $\sim$ 4 to 8 kg of H_2 stored on-board the vehicle to match current fuel consumption needs [13]. Cryogenic tanks used for storage of liquid hydrogen or high pressure hydrogen tanks, are normally heavy and expensive and therefore often impractical [13]. Numerous other storage methods have been examined [13–17]. These methods can be summarized as: physical hydrogen storage, including cryogenic methods and high pressure tanks, chemical storage methods, including reversible absorption in metal or metal hydrides and reversible absorption on solids [13], and hydrogen storage on organic heteroaromatic compounds [15–17]. Among these alternatives, organic heteroaromatic compounds have received increasing attention. They have high volumetric and/or gravimetric hydrogen storage capacity, which minimizes the need for changing the existing transport infrastructure. Also, the stored hydrogen can be liberated from the storage medium through a chemical reaction without decomposition of the storage medium.

1.2 Objective of this thesis

The objective of this thesis was to study the kinetics of hydrogenation and dehydrogenation reactions used for hydrogen storage and recovery from organic heteroaromatic compounds. The focus was to improve the dehydrogenation catalytic reactions by synthesizing and/or modifying the catalysts in order to obtain high hydrogen recovery applicable for transportation applications. The objectives of the dehydrogenation reactions were to obtain 100 % selectivity to the completely dehydrogenated product and to avoid hydrogenolysis reactions so that the stored H_2 could be completely recovered.

1.3 Approach

The approach to reach the objective was to use both experimental techniques and theoretical methods. N-ethylcarbazole was chosen as a potential candidate for hydrogen storage and recovery. Hydrogenation reactions were carried out over a pre-reduced commercial catalyst to obtain dodecahydro-N-ethylcarbazole, the required feed for the dehydrogenation experiments. Various catalysts with different particle sizes and preparation methods were synthesized and used for the dehydrogenation reactions. Density functional theory (DFT) calculations were used to understand the mechanism of the dehydrogenation reaction of dodecahydro-N-ethylcarbazole over Pd and to investigate the role of the N heteroatom on the reaction, by comparing the adsorption energies of dodecahydro-N-ethylcarbazole and its dehydrogenated products with dodecahydrocarbazole and dodecahydrofluorene. The goal of the experimental work was to achieve a significant improvement in the selectivity to N-ethylcarbazole by modifying the catalyst properties.

In the experimental study, the Pd/SiO_2 catalysts were prepared by impregnation of a silica support with different loadings of Pd (0.5 to 10 wt %). Two different environments, air and He, were used for calcination of the catalysts. Temperature programmed reduction was used to reduce the oxide form of the precursor from PdO to Pd for the former, and $PdCl_2$ to Pd for the latter. The prepared catalysts were analyzed using different characterization techniques, including BET, TPR, CO pulse chemisorptions, TPD, SEM, EDX and HRTEM. A 300 cm^3 autoclave batch reactor with continuous monitoring and control of stirrer speed, temperature,

and pressure was used for the hydrogenation reactions. Hydrogenation reactions were carried out at different temperatures over a commercial pre-reduced Ru catalyst and liquid samples were withdrawn from the reactor at certain time intervals in order to study the kinetics of the reactions. For the dehydrogenation reactions, a 50 cm^3 glass flask reactor with flow of He as a carrier gas for continuous removal of the produced hydrogen, was used. The exit gas composition was continuously monitored using a quadrupole mass spectrometer. Liquid samples were also withdrawn from the reactor periodically. The analysis of the liquid samples from the dehydrogenation reactions was done by a GC/MS. Power law kinetic models were applied to the hydrogenation and dehydrogenation reactions for the produced intermediates and products.

A Pd(111) surface was used to study the dehydrogenation of dodecahydro-N-ethylcarbazole by DFT. The surface model was used to investigate the potential energy surface of the formation of N-ethylcarbazole from dodecahydro-N-ethylcarbazole. For this purpose, the dodecahydro-N-ethylcarbazole molecule was first adsorbed on the surface by considering different adsorption modes. Then, stepwise removal of a H atom was investigated. In order to determine the energy barrier corresponding to each step, a transition state search was performed between two stable surface intermediates. A Pd(110) surface was created to study the adsorption geometry of the dodecahydro-N-ethylcarbazole molecule and to study the structure sensitivity of the dehydrogenation reaction. To investigate the effect of the N heteroatom as well as the ethyl group in the dehydrogenation reaction of dodecahydro-N-ethylcarbazole, adsorption geometries and energies of similar compounds, dodecahydrocarbazole and dodecahydrofluorene on the Pd(111) surface were also studied.

1.4 Hydrogen storage

To achieve global introduction of hydrogen fuel cells, a safe and practical hydrogen storage system is needed [18]. In order to achieve a hydrogen economy, developing a reliable hydrogen storage system that meets the cost and safety requirements for both on-board (vehicular applications) and off-board (such as power generation stations) uses is crucial [19]. The challenge of the past decade has been to store

enough hydrogen on-board a vehicle for an average driving distance of 300 miles, within reasonable cost limitations and comparable to current gasoline vehicles [19].

For transportation applications, there are many criteria that are important for hydrogen storage. Among these, hydrogen storage density (gravimetric and volumetric densities), hydrogen release (recovery) rate as well as cost are very critical. The technical targets for hydrogen storage for the years 2010 and 2015 (see Table 1.1) have been determined by the U.S. Department of Energy (D.O.E.) [20, 21], by comparing to the current gasoline systems in terms of weight, volume, operating conditions at which hydrogen is released, system cost, etc.

Table 1.1: U.S. Department of energy (D.O.E.) revised targets for hydrogen storage systems [20, 21]

Storage parameter	**Target 2010**	**Target 2015**
Gravimetric capacity (kWh/kg) [21]	1.5	1.8
H_2 (wt%) [21]	4.5	5.5
Volumetric capacity (kWh/L) [21]	0.9	1.3
H_2 (g H_2/L system) [21]	28	40
Durability/Operability [20, 21]:		
• Operating ambient temperature	• -30/50 °C	• -40/60 °C
• Min/max delivery temperature	• -40/85 °C	• -40/85 °C
• Cycle life (1/4 tank to full)[a]	• 1000	1500
• Max delivery pressure from tank [21]	• 12 bar (abs)	12 bar (abs)
System fill time for 5 kg H_2 (min) [21]	4.2	3.3

[a]Equivalent to 200,000 and 300,000 miles, respectively, based on current gasoline tank specifications [21].

There are different approaches to on-board hydrogen storage that are currently under study. These approaches include compressed hydrogen, liquified hydrogen, hydrogen storage on metal hydrides, ammonia borane based compounds, boron based compounds like metal borohydrides, organic materials for example carbazole and its substituted forms, and adsorbents with high surface area such as activated carbon [22, 23]. Those materials that can be recharged with hydrogen gas on-board the vehicle are considered as "reversible" hydrogen storage systems, for example, high pressure or liquified hydrogen, and hydrogen adsorbents [23]. On the other hand, there are methods in which hydrogen needs to be stored and recovered from the storage material through a chemical reaction [24], so called "off-board regen-

erable" systems [23]. In these systems, the dehydrogenated medium is removed from the vehicle and transported to an off-board station for re-hydrogenation or in other words "re-generation" of the fuel [23].

There are certain advantages and drawbacks using each of the indicated methods for hydrogen storage. For instance, compressed or liquified hydrogen does not have satisfactory storage capacities [25, 26]. Furthermore, cost of the cryogenic and high pressure equipment is prohibitive [23]. A very important parameter for chemical storage of hydrogen is the heat of the dehydrogenation reaction (reverse reaction of hydrogenation used for hydrogen storage). The desirable value of heat of dehydrogenation is reported to be 40 kJ/mol [27]. It has been indicated by Cooper et al. [28] that heat of dehydrogenation of $\sim$ 42 to 54 kJ/mol H_2 will enable the catalytic dehydrogenation reaction at temperatures $<$473 K. The other important factor is the rate of hydrogen discharge (recovery) and the kinetics of the dehydrogenation reactions on-board the vehicle. For hydrogen storage on adsorbents such as carbon-based compounds, slow kinetics is reported [26] and normally cryogenic temperatures are required due to the weak bonding between the hydrogen and the adsorbent [23]. In this case, gravimetric capacities as well as cost of the cryogenic equipment need to be addressed.

Therefore, the big challenge in transportation applications has been to develop a hydrogen storage system with sufficient storage capacity to enable a vehicle to drive an average distance of 300 miles within the limitations imposed by safety and economic considerations. This will require a minimum storage of 5 kg hydrogen on-board the vehicle [14]. The following sections discuss different approaches to hydrogen storage.

1.5 Compressed hydrogen

It has been shown that the volumetric density of hydrogen does not have a linear relationship with pressure. In other words, increasing the pressure does not lead to a linear increase in the hydrogen density [25]. For example, the hydrogen density is 20 kg/m^3 at 300 bar [25]. This volumetric density can be increased to 40 kg/m^3 at 700 bar and 70 kg/m^3 at 2000 bar [25]. The latter is impractical [25] and can not be used on-board the vehicle. The volume of 5 kg hydrogen is 60 m^3, 0.25 m^3

and 0.125 m^3 at pressures of 1 bar, 300 bar and 700 bar, respectively [25]. The observed decrease in the hydrogen volume by increasing the pressure from 300 to 700 bar is not as significant as the volume decrease by increasing the pressure from 1 bar to 300 bar. The hydrogen pressure that is typically used is 350 bar and 700 bar [25, 29, 30]. However, the energy and the system requirements for compression of hydrogen is the main issue [12] that limits the use of compressed hydrogen and research is needed to improve the compressed hydrogen storage system [25].

1.6 Liquified hydrogen

Liquified hydrogen can be obtained by decreasing the hydrogen gas temperature at a constant pressure [25]. A liquid hydrogen container can be filled on-board the vehicle in 3 min [30]. Liquid hydrogen has a density of approximately 80 kg/m^3 at 22 K and a pressure of 4 bar [25]. Compared to compressed hydrogen, the volume required for storage of liquified hydrogen is lower [25]. However, due to the physical properties of hydrogen gas, there are many limitations and constraints to the use of liquified hydrogen as a storage system [25]. The boiling point of hydrogen at atmospheric pressure is 20 K, a temperature at which other gases are solid [25]. In order to keep hydrogen liquid, the weight and volume of the cooling equipment will need to be added to the storage system [31] and strong thermal insulators are required to keep hydrogen from being vaporized [25]. The 2015 targets of the department of energy (D.O.E.) of 40 g H_2/L system include the hydrogen storage material as well as the total storage system such as high pressure tanks for compressed hydrogen [14], which means that the theoretical density of the storage material needs to be higher in order to achieve the required storage capacity for the whole system.

1.7 Off-board regenerable storage

One category of materials that has the potential to meet the H_2 storage density requirements for transportation applications is off-board regenerable systems. Many of the compounds that have high volumetric/gravimetric hydrogen storage capacities have been studied as summarized in Table 1.2 [14], and are described in the following sections.

Table 1.2: Different categories of hydrogen storage materials [14]

Hydrogen storage category	**Example**
Ammonia Borane-based	Ammonia borane complexes (ammonia borane NH_3BH_3)
Boron-based	Metal borohydride such as $NaBH_4$
Metal hydrides	Metal hydride such as $NaAlH_4$
Nitrogen-Based	Metal amides and metal nitrides
Organic materials	Substituted carbazole such as N-ethylcarbazole (hydrogenated forms)

1.7.1 Ammonia borane-based H_2 storage materials

A chemical reaction with controlled temperature and pressure is needed in this group of materials for "charge" (or uptake) and "discharge" (or release) of hydrogen [31]. Ammonia borane (AB, NH_3BH_3) is one example. It is solid and stable at room temperature [31] and soluble in relatively polar solvents [32]. The melting point of NH_3BH_3 varies from 383 to 387 K [32]. The hydrogen content of ammonia borane is 190 g H_2/kg material, equal to 100-140 g H_2/L [31], or 19.6 wt % hydrogen [26, 33]. The high hydrogen storage capacity as well as its stability has made ammonia borane a potential candidate for hydrogen storage and recovery applications. Hydrogen can be released from ammonia borane on-board the vehicle. However, there are technical issues that need to be addressed before the commercial use of ammonia borane, one of which is the rate at which hydrogen is released. Also, since hydrogen is released from the compound, a cost effective pathway should be developed to regenerate ammonia borane [31]. Currently, no energy efficient approach is available for regenerating ammonia borane from the products [34]. In work by Stephens et al. [34], dehydropolymerization of NH_3BH_3 was reported to have practical reaction rates over an Ir catalyst and very high hydrogen recovery over a Ni catalyst. However, no catalyst was reported to have both high reaction rate and high hydrogen recovery [34]. Other options, such as adding water or ionic liquids in order to improve the catalytic hydrogen recovery from ammonia borane, also decrease the storage capacity of the system [34] and

hence, would not be practical. Therefore, the challenge is to discover and develop a system with high storage capacity, as well as fast and complete hydrogen recovery.

1.7.2 Chemical hydrides

Chemical hydrides are another group of materials which have the potential for hydrogen storage. Complex metal borohydrides with the general formula of $M(BH_4)_n$ have been of interest because of their high hydrogen storage capacity [27]. One example is sodium borohydride ($NaBH_4$) that has a theoretical hydrogen content of 10.6 wt%. The hydrolysis reaction of sodium borohydride, shown in reaction 1.1, is an exothermic reaction that produces hydrogen and energy in the presence of a catalyst [35, 36],

$$NaBH_4(aq) + 2H_2O \rightarrow 4H_2 + NaBO_2 + \sim 300kJ \tag{1.1}$$

$Pt-LiCoO_2$ catalyst was reported by Kojima et al. [37] to work very well for this reaction. The produced H_2 has high purity and does not poison the fuel cell catalyst [35]. A 30 wt % solution of $NaBH_4$ has the volumetric storage capacity of about 63 g H_2/L, which is comparable to the volumetric storage of 71 g H_2/L for cryogenic liquid H_2 and 23 g H_2/L for compressed hydrogen at 5000 psi [35]. Therefore, $NaBH_4$ is a potential candidate for hydrogen storage in terms of storage capacity [36]. However, hydrogen generation through reaction 1.1 is not reversible [37]. Hence new methodologies for recycling the hydrolysis byproduct, $NaBO_2$, into $NaBH_4$ are needed [37]. "Lack of reversibility" in the hydrogen generation reactions from metal borohydrides is also reported by Li et al. [38] to limit their use in transportation applications.

Metal hydrides exist in different forms and categories among which hydrides in the form of A, AB, A_2B, AB_2 and AB_5 have been investigated extensively [25]. In these categories, A stands for the element that makes a strong hydride and B the element that forms a weak hydride [25]. An example is MgH_2 with high theoretical hydrogen storage capacity of 7.5 wt % [25] which has been of interest for hydrogen storage applications [39]. However, the main obstacle in using MgH_2 for hydrogen storage and recovery is its high decomposition temperature [39] and thermodynamic stability [25, 40]. Methods such as doping Mg with transition metals

like Ni in order to decrease the dehydrogenation temperature of the metal hydride have been studied [39], however, these will result in reducing the storage capacity of the system [40]. Therefore, using light elements such as Li, B, Na and Al in the storage systems have been considered [25].

Other approaches, such as coating sodium hydride with plastic in the form of pellets that can be sliced open to react with water, as proposed by PowerBall Technologies reported by DiPietro [41] are also very costly and not practical.

1.7.3 Organic materials

Storage and release of hydrogen from organic molecules is done through hydrogenation and dehydrogenation reactions. Since the hydrogen is stored in the organic molecule covalently, system compression or liquifaction will not be needed [11]. A liquid organic compound on which hydrogen is stored through a hydrogenation reaction is used as a fuel on-board the vehicle. This fuel can be a hydrocarbon produced from crude oil or alcohols [11]. The advantage of using a liquid fuel is that the need for changing the fuel transport and storage infrastructure will be minimized [11]. The fuel undergoes a catalytic dehydrogenation reaction on-board the vehicle to release hydrogen. The liberated hydrogen is then directed to the fuel cell or the engine in the vehicle and the dehydrogenated fuel is stored in a tank for off-board regeneration through hydrogenation reactions [11, 42]. The following list describes some of the criteria for a liquid hydrogen carrier:

- Absolute value of heat of hydrogenation between 42 to 54 kJ/mole H_2 to enable the dehydrogenation reaction at temperatures below 473 K [43].
- High boiling point (T_b>573 K) to decrease the vapor exposure on-board the vehicle [43].
- Low melting point (T_m<233 K) for the system to stay liquid at low temperatures [44].
- Low contaminating effect on the environmental [43].
- Low cost of production.

- Selective hydrogenation and dehydrogenation reactions, with no decomposition of the organic compound [43].

1.8 Hydrogenation/dehydrogenation reactions and catalysts

Hydrogenation and dehydrogenation reactions are well studied in heterogeneous catalysis. A heterogeneous catalyst typically consists of an active phase which catalyzes the reaction, a support which is normally a high surface area material and a promoter that improves catalyst activity and/or selectivity [45]. Table 1.3 shows some examples of different catalyst components [45].

Table 1.3: Examples of different components of a heterogeneous catalyst [45]

Catalyst component	**Compound example**
Active catalytic phase	metals such as Pt, Pd, Ni metal oxides such as MoO_2, CuO metal sulfides such as MoS_2
Promoter	metal oxides such as K_2O, MgO
Support	activated carbon, metal oxides such as SiO_2

Transition metals and their carbides [45–48], sulfides [46] and nitrides [45, 47, 48] are well known to be very active in catalytic reactions. Pt-group (precious) metals such as Pd, Ru and Pt, as well as transition metals such as Ni and Cu have been shown to be active in hydrogenation reactions [45]. However, precious metals are much more expensive than transition metals and more active [45]. Dehydrogenation is the reverse of hydrogenation and therefore, the catalysts used for hydrogenation are typically used for dehydrogenation reactions as well [45]. Dehydrogenation is an endothermic reaction [45] as opposed to hydrogenation which is exothermic. Representative active catalytic phases for hydrogenation and dehydrogenation reactions are listed in Table 1.4.

1.9 Selection of organic materials for hydrogen storage

Extensive literature is available addressing a wide variety of hydrogenation/dehydrogenation reactions relevant in H_2 storage including alkenes/alkanes, benzenes/-

Table 1.4: Active catalytic phases for hydrogenation and/or dehydrogenation reactions

Active phase	Example	Reaction
Transition metals	Fe, Ni, Ru, Pd, Pt	hydrogenation, dehydrogenation [45]
Transition metal sulfides	sulfides of Mo, Ni	hydrogenation [45]
Transition metal carbides	carbides of Fe, Mo	hydrogenation [45], dehydrogenation [47]
Transition metal nitrides	nitrides of Mo	dehydrogenation [48]

cyclohexanes, aldehydes, ketones/alcohols and their appropriate catalysts as well as reaction conditions [49–52]. For example, hydrogenation of benzene has been reported over Ni at 323 K, hydrogen pressure of 80 kPa and benzene pressure of 9 kPa. The reaction was first-order in hydrogen pressure with activation energy of 38 kJ/mol [52]. However, many of these organics do not meet the hydrogen storage capacity and other criteria (such as high boiling point) required to be used for H_2 storage. Recent work on hydrogen storage [15, 16, 43] is available showing that organic aromatic compounds such as carbazole and its substituted forms have good potential for hydrogen storage. These compounds are mainly in the form of crystalline powders at ambient conditions with high melting and boiling points. Some of these materials are listed in Table 1.5.

However, there is little information on the hydrogenation/dehydrogenation reaction mechanism, thermodynamics, kinetics and catalysts for these compounds. In work by Cooper et al. [43], fused multi-ring aromatic systems with high boiling and melting points were also reported to have high hydrogen storage capacity as well as a low absolute value of the standard heat of hydrogenation, -ΔH_R°, which was also reported through the experimental and theoretical (density functional theory) work of Pez et al. [15, 16] (See Table 1.5 for hydrogen capacity and -ΔH_R° of some of these compounds). As mentioned before, substrates having a lower absolute value of -ΔH_R° are desired as they are thermodynamically more easily dehydrogenated. However, despite high hydrogen capacity of these heavy compounds and low volatility due to their high boiling points, they usually have high viscosity and are often in the form of a crystalline solid, and thus can not be used by themselves as a liquid fuel.

The dehydrogenation mechanism of 1,2,3,4-tetrahydrocarbazole (THCZ), a po-

Table 1.5: Examples of substituted carbazole structures with high hydrogen capacity and low heat of hydrogenation.

Compound	**Structure**	**wt % H_2**[a]	**-ΔH_R°, kJ/mol**[b]
carbazole [11, 16, 23]	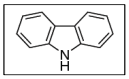	6.7	60.4 [16]
9-Ethylcarbazole [11, 15]	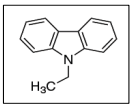	5.7	50.6 [15]
Hexaazatriphenylene [16]	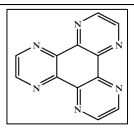	7.1	53.9 [16]
Pyrrole oligomer [15]	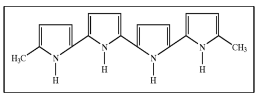	5.2	52.2 [15]
Dibenzofuran [16]	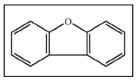	6.7	64.6 [16]
Borafluorene [15]	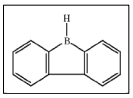	6.8	42.6 [15]

[a] Storage capacity of the hydrogenated compound.
[b] Due to negligible amount of entropy change[15], $\Delta H_R^\circ \sim \Delta G_R^\circ$.

tential compound for hydrogen storage, was studied by Crawford et al. [53] and Hindle et al. [54] both experimentally and theoretically using density functional theory (DFT) calculations. 1,2,3,4-tetrahydrocarbazole is in the form of a solid powder with high boiling point (598 K) and melting point (391 K). Therefore, the dehydrogenation reaction was carried out in the liquid phase by dissolving the 1,2,3,4-tetrahydrocarbazole in mesitylene. Two different catalysts were used in the reaction: 5 wt % Pd/Al_2O_3 with a Brunauer-Emmett-Teller (BET) surface area of 143 m^2/g and 22 % metal dispersion measured by CO pulse chemisorption [53, 54], and Pd/C with a BET surface area of 1358 m^2/g and 16.5 % metal dispersion [54]. The reaction was zero-order in the substrate (THCZ) concentration, and the cata-

lysts showed 100 % selectivity to the desired carbazole product. However, it was shown from the experiments that product inhibition slowed the rate of reaction significantly and 81 % conversion was obtained after about 27 h at 101 kPa and 413 K [53]. The product inhibition was confirmed by the DFT study, and was attributed to the higher adsorption energy of the product carbazole to the catalyst surface and its lower solubility in mesitylene, compared to that of 1,2,3,4-tetrahydrocarbazole [53, 54]. The DFT results in the work by Crawford et al. [53] showed that THCZ molecule in its most stable adsorption geometry adsorbs to the catalyst surface through the aromatic ring parallel to the surface and the aliphatic ring tilted away by a degree of approximately 30^o. In this adsorption geometry, a maximum number of C-Pd bonds can form [53].

In work by Pez et al. [15, 16] reversible catalytic hydrogenations of extended pi-conjugated substrates, including aromatic hydrocarbons with oxygen and nitrogen heteroatoms, comprising 5 or 6 membered rings, were studied using supported Pt-group metal catalysts such as Rh/C and Ru/Al_2O_3. Because the heat of hydrogenation ($-\Delta H_R^\circ$) data is only available for some small pi-conjugated molecules, this value was calculated using density functional theory (DFT) for the potential substrates for hydrogen storage [15, 16]. Based on these results, it was shown that nitrogen as a heteroatom in 5 or 6 membered rings, provided a lower $-\Delta H_R^\circ$ in this category of compounds and are therefore effective substrates for hydrogen storage.

Clot et al. [55] have also shown by DFT calculations that H_2 recovery is thermodynamically favored from five membered rings compared to six membered rings in the presence of a N heteroatom in the organic materials.

Wang et al. [56] reported iridium complexes to be active catalysts for the dehydrogenation of dodecahydro-N-ethyl carbazole at 473 K. However, the reaction did not proceed to the production of the completely dehydrogenated product, N-ethylcarbazole, and octahydro-N-ethylcarbazole and tetrahydro-N-ethylcarbazole were reported to be the only observed products. Also, much lower catalytic activity was observed at the lower temperature of 423 K during 48 h dehydrogenation reaction. Decalin as a hydrogen storage candidate was dehydrogenated over a Pt/C catalyst. Loutfy et al. [57] performed catalytic decalin dehydrogenation by use of a batch-type membrane reactor at high temperatures of 533 K, 553 K, 573 K and 593 K and obtained conversions below 85 % after 2.2 h. Decalin conversion of

higher than 95 % was attained within 1.5 h at temperature of 553 K in the work by Hodoshima et al. [58]. However, the reported reaction temperature was too high and impractical for hydrogen recovery for transport applications.

1.10 Summary

Research done on hydrogen storage options has led to the conclusion that the "off-board regenerable" systems are preferred to "reversible on-board"s due to several advantages including high volumetric and/or gravimetric hydrogen densities. Organic materials such as substituted carbazoles and some fused multi-ring aromatic compounds have been shown to have high storage capacity as well as low heat of hydrogenation. However, hydrogenation and dehydrogenation of these materials has been sparsely reported over platinum group metal catalysts. Furthermore, kinetics and selectivity of hydrogenation/dehydrogenation reactions with a view to maximize both hydrogenation and dehydrogenation rate and minimize the side reactions (i.e. maximize the selectivity) has not been well studied.

Therefore, substituted carbazoles with high hydrogen storage capacity were chosen for further study in the present work and the hydrogenation/dehydrogenation reaction rate, kinetics and selectivity were determined over platinum group metal catalysts. Density functional theory techniques were also used to better understand the reaction network and catalyst reactivity.

1.11 Molecular modeling of heterogeneous catalysis

Molecular modeling in heterogeneous catalytic systems has attracted growing attention due to the ability of first principle techniques to calculate the adsorption energies of the adsorbate to the catalyst surface, find binding energies of the substrates, and predict the potential energy surface of the chemical reactions. Catalysis is a process that occurs at the molecular level, and therefore simulating this process can provide the answer to questions regarding the catalyst behavior as well as the reaction mechanism [59].

Extensive theoretical studies are available in the literature for different heterogeneous catalytic systems including zeolites, metal or metal oxide catalysts. Quantum mechanical techniques are used to calculate the energetics of the system

as well as the interaction between the molecules and catalyst surface. The strength of the interaction forces between the molecules and catalyst surface determines the extent of the adsorption and desorption, compound decomposition on the catalyst surface, as well as the reaction kinetics [59].

1.11.1 Schrödinger equation

The objective of most quantum mechanical techniques is to find the approximate solution to the Schrödinger equation developed by E. Schrödinger in 1926 [60]. The time-independent form of the Schrödinger equation is defined as [61],

$$\hat{H}\Psi_i(\vec{x}_1,\vec{x}_2,...,\vec{x}_N,\vec{R}_1,\vec{R}_2,...,\vec{R}_M) = E_i\Psi(\vec{x}_1,\vec{x}_2,...,\vec{x}_N,\vec{R}_1,\vec{R}_2,...,\vec{R}_M) \qquad (1.2)$$

In this equation, $\hat{H}$ is the Hamiltonian operator, M is the number of nuclei in the system, and N the number of electrons where no magnetic or electric field is present [61]. $\hat{H}$ is an operator that represents the total energy of the system and is defined as follows [61],

$$\hat{H} = -\frac{1}{2}\sum_{i=1}^{N}\nabla_i^2 - \frac{1}{2}\sum_{A=1}^{M}\frac{1}{M_A}\nabla_A^2 - \sum_{i=1}^{N}\sum_{A=1}^{M}\frac{Z_A}{r_{iA}} + \sum_{i=1}^{N}\sum_{j>i}^{N}\frac{1}{r_{ij}} + \sum_{A=1}^{M}\sum_{B>A}^{M}\frac{Z_AZ_B}{R_{AB}} \qquad (1.3)$$

The first term takes into account the kinetic energy of the electrons, the second term describes the kinetic energy of the nuclei, and the last terms show the attractive electrostatic interaction between the electrons and nuclei and repulsive forces because of electron-electron and nucleus-nucleus interactions [61]. Wave function Ψ is the solution of Eq. 1.4 that describes the "state of a system" and contains all the information about the system under study [62]. "The Schrödinger equation describes the wave properties of an electron in terms of its position, mass, total energy, and potential energy" [63]. The numerical value, E_i, is the energy of state "i" which is defined by Ψ_i [61].

The probability for an electron to be found at a given coordinate is proportional

to Ψ^2 [63] which gives us a physical sense of the wave function Ψ, since it can not be observed [61]. According to "*Pauli's exclusion principle*", two electrons can not occupy the same state [61] and therefore, the probability of finding electrons somewhere in space equals 1 [61, 63]. This can be shown as follows [61],

$$\int ... \int |\Psi(\vec{x}_1, \vec{x}_2, ..., \vec{x}_N)|^2 d\vec{x}_1 d\vec{x}_2 ... d\vec{x}_N = 1 \tag{1.4}$$

Finding an analytical solution to the Schrödinger equation is too complex for systems consisting of many atoms and therefore, approximations need to be made [64]. One approximation was proposed by Born and Oppenheimer in 1927 [65] in which the nuclei were assumed to be at a fixed position because of their much slower movement due to their heavier mass, compared to the electrons [64]. The solution obtained by this approximation resulted in a system energy which was only dependent on the nuclei position, a so called "potential energy surface" (PES) [64, 66]. The point associated with the lowest energy on the potential energy surface is the ground state energy of the system [64].

In the Hartree−Fock (HF) approximation, the N-electron wave function, which is complicated to solve, is approximated by the product of N single-electron wave functions (or spin orbitals) [61, 64, 67]. Basis functions are the functions used to define these orbitals [64] and this method is called the Linear Combination of Atomic Orbitals (LCAO) [61, 64]. In the Hartree−Fock technique, a set of orbitals are guessed and the HF equations are solved in an iterative procedure referred to as the self-consistent-field (SCF) method [61].

Quantum mechanic methods used for solving the Schrödinger equation can be categorized into ab initio approaches, semi empirical methods or density functional theory techniques [68]. Ab initio methods are very time consuming and costly [64] because they solve the Schrödinger equation [68]. Hartree−Fock method as explained earlier is one example of these approaches [68]. In semi-empirical quantum approaches however, the calculations are simplified by applying some assumptions to the equations [64] and adjusting integrations for example, by eliminating most of the two electron integrals [68]. In some semi empirical approaches experimental data are used to simplify some parts of the calculations [64]. Compared to ab

initio methods, semi empirical ones also require intensive calculating resources although they are less expensive than ab initio approaches [64]. Another approach in quantum mechanic calculations is density functional theory (DFT) which introduces functionals of electron density by which many electronic properties can be generated [64, 69]. DFT methods have shown to produce reasonable results at low cost and therefore are widely used in molecular simulations [68].

1.11.2 Density functional theory (DFT)

Hohenberg and Kohn in 1964 proved that the ground-state energy and other electronic properties of a molecular system is a unique functional of the electron density [62, 70]. The Hohenberg and Kohn theory however did not specify exactly how to calculate the ground state electron density without solving the wave function [62]. This was developed later through a series of equations by Kohn and Sham in 1965 [62, 70, 71]. The idea of using the electron density, ρ(r), simplified the problem of solving the 3N variable Schrödinger equation to a function of only three spatial variables [70]. Consider the total energy functional as follows [70],

$$E[\Psi_i] = E_{known}[\Psi_i] + E_{XC}[\Psi_i] \tag{1.5}$$

where $E_{known}[\Psi_i]$ represents all the terms which can be described in an analytical form, and E_{XC} includes everything else [70]. For $E_{known}[\Psi_i]$ we have [70],

$$\begin{aligned} E_{known}[\Psi_i] &= \frac{h^2}{m}\sum_{i=1}\int \Psi_i^*\nabla^2\Psi_i d^3r + \int V(r)\rho(r)d^3r \\ &+ \frac{e^2}{2}\int\int \frac{\rho(r)\rho(r')}{|r\ r'|}d^3r d^3r' + E_{ion.} \end{aligned} \tag{1.6}$$

in which the terms on the right are "the electron kinetic energies, the Coulomb interactions between the electrons and the nuclei, the Coulomb interactions between pairs of electrons, and the Coulomb interactions between pairs of nuclei", respectively [70]. $E_{XC}[\Psi_i]$ is referred to as the exchange−correlation functional

which consists of all other effects that are not considered in the $E_{known}[\Psi_i]$ term [70] in Eq. 1.5. Since the exact functional for the exchange−correlation energy is not known, different models were introduced to make an approximation for this functional [70]. One of these approximations is called the local density approximation (LDA) assuming a "uniform electron gas" [61, 62, 72]. The exchange−correlation energy is obtained from [61],

$$E_{XC}^{LDA}[\rho] \cong \int \rho(\vec{r})\varepsilon_{XC}[\rho(\vec{r})]d\vec{r} \tag{1.7}$$

where in this equation $\varepsilon_{XC}[\rho(\vec{r})]$ is the exchange−correlation energy of an electron in a uniform electron gas [61].

Another approximation includes functionals that consider the "gradient" and "non-homogeneity" in the charge density [61, 62]. These methods are referred to as generalized gradient approximations (GGA) [61, 62] or gradient−corrected functional [62]. Although generalized gradient approximation methods contain more physical data about the charge density, they are not always more accurate than the local density approximation methods [70]. There are many GGA functionals available in the literature. Perdew and Wang (PW91) GGA for the correlation functional [73], the gradient−corrected exchange functional of Becke (B) [74], the Lee, Yang, and Parr (LYP) gradient−corrected correlation functional [75], and the Perdew−Burke−Ernzerhof functional (PBE) [76] are some examples in this category.

It was found that for chemisorption problems, reasonable results can be obtained by using the nonlocal corrections to the exchange−correlation potential as well as the adsorbate−surface geometry optimization [77].

1.12 Molecular modeling in heterogeneous catalysis

Techniques that are used in modeling of heterogeneous catalytic systems include cluster methods [77–79], embedded-cluster [79, 80] methods, and periodic models [79, 81]. A good and successful simulation not only benefits from an accurate method, but also the proximity of the used model to the real catalytic system [79]. These methods are briefly discussed in the following sections.

1.12.1 Cluster models

Cluster models are built by using a limited number of atoms [79]. Cluster models are used widely in simulating the catalytic surfaces because of the limitations in the availability of the computational resources [77]. The model clusters can have different sizes and number of atoms depending on the type of the system under study as well as the desired level of accuracy [79]. In small clusters, the size of the cluster can have a significant effect on the interaction energy which are well known experimentally [82, 83]. "An important advantage of the cluster approach is that the active site is explicitly described by the interactions between the local molecular orbitals of the adsorbate and the surface" [79]. However, a cluster model is generally limited by its small size which is not capable of representing the system completely [77, 79].

1.12.2 Embedded-cluster model

The embedded−cluster model tries to deal with the difficulties raised from the cluster termination [79]. In the embedded-cluster approach, the local area around the active site is modeled and the cluster is inserted in a large external environment [79]. Various systems such as metal oxides and zeolites have been modeled successfully using this methodology [79]. Although this approach simplifies the quantum mechanical calculations, accurate matching of the interface between the cluster and the external environment is one of the main difficulties of this approach [79].

1.12.3 Periodic quantum−mechanical calculations

Periodic quantum−mechanical methodology can be used to model the well-defined systems such as metals surfaces [79, 84]. A unit cell is created in this approach and is repeated in one to three directions representing a linear, surface or a bulk system [79]. Therefore, the cost of calculation increases accordingly by increasing the size of the unit cell [79]. This approach provides a more complete picture of the system structure [79]. However, compared to the industrial non-ideal systems, only systems with high periodicity can be modeled currently within feasible computational time and cost [79].

In this thesis, a periodic slab with four Pd layers and total number of 108 Pd atoms were used to represent the Pd(111) surface, and periodic quantum mechanical calculations were employed to investigate different reaction steps and energy barriers of dehydrogenation reactions. Material Studio and DMol^3 module was used for molecular simulation of the catalyst surface, optimizing the geometry of the adsorbate/surface system, defining the adsorption energies of surface intermediates and the potential energy surface (PES) by performing the transition state search.

1.13 Outline of the dissertation

This dissertation is arranged in the following order:

Chapter 1: Provides an introduction to the subject of hydrogen storage and different approaches that are used for this purpose. A brief introduction to molecular heterogeneous catalysis and its application in the modeling of dehydrogenation reactions for hydrogen recovery is also described.

Chapter 2: Reports the results of hydrogenation reactions of N-ethylcarbazole and carbazole, with details of a kinetic study as well as kinetic modeling of the reaction with the suggested reaction network.

Chapter 3: Dehydrogenation reaction of dodecahydro-N-ethylcarbazole over a 5 wt % Pd/SiO_2 catalyst is reported and compared to the data available in the literature. Kinetics of the reaction was studied and the modeling data are provided.

Chapter 4: The preparation method and characterization results of a series of Pd/SiO_2 catalysts with different Pd particle sizes and metal dispersions are reported. The dehydrogenation reaction of dodecahydro-N-ethylcarbazole over these catalysts is reported.

Chapter 5: The effect of the N heteroatom in the dehydrogenation reactions of organic polyaromartic compounds is studied and details are reported by comparing the dehydrogenation reaction rate of dodecahydro-N-ethylcarbazole, dodecahydrocarbazole and dodecahydrofluorene.

Chapter 6: Provides details of the molecular modeling and DFT calculations used to model the dehydrogenation reaction of dodecahydro-N-ethylcarbazole, as well as an investigation of the effect of N heteroatom in the dehydrogenation reaction of

the examined organic polyaromatic structures of dodecahydro-N-ethylcarbazole, dodecahydrocarbazole, and dodecahydrofluorene.

Chapter 7: Summarizes the conclusions of the previous chapters and offers recommendations for future work.

Chapter 2

Hydrogenation kinetics: N-ethylcarbazole and carbazole

A version of this chapter has been published:
F. Sotoodeh and K.J. Smith, Kinetics of Hydrogen Uptake and Release from Heteroaromatic Compounds for Hydrogen Storage, Ind. Eng. Chem. Res. 2010, 49, 1018-1026.

2.1 Introduction

One approach to hydrogen storage for fuel-cell vehicles is to use organic compounds that have a high capacity to bind hydrogen covalently. Storage and release of the hydrogen is achieved by hydrogenation and dehydrogenation of the organic compounds and these reactions are done in the presence of a catalyst. For transportation applications the H_2 storage (hydrogenation) would be done off-board the vehicle. Also, the candidate compounds must have high hydrogen release rates, more than 5.5 wt % H_2 storage capacity (calculated as the mass of H_2 liberated divided by the mass of hydrogenated compound), melting points below 313 K and boiling points above 473 K [20, 85]. Organic heteroaromatic compounds such as carbazole and its derivatives have attracted attention because they meet the storage capacity targets and the boiling point criteria.

Although some results have been reported for H_2 storage on heteroaromatic compounds, limited data are available on the kinetics of the reactions involved in H_2 uptake and release [14, 17, 55, 86]. Carbazole and N-ethylcarbazole, when hydrogenated to dodecahydrocarbazole and dodecahydro-N-ethylcarbazole, have hydrogen storage capacities of 6.70 and 5.79 wt % [14, 16, 87], respectively. They are, therefore, potential candidates for hydrogen storage applications. However, the hydrogenation-dehydrogenation kinetics of these compounds are not well established, especially at the low temperature (< 473 K) conditions required for on-board dehydrogenation reactions. In addition, although platinum group metals are widely used for hydrogenation and dehydrogenation reactions, the influence of the heteroatom present in these compounds on the reaction kinetics needs to be understood, given that strong heteroatom adsorption can lead to a loss in catalyst activity. The N heteroatom associated with N-ethylcarbazole and dodecahydro-N-ethylcarbazole is bound to an ethyl group, whereas in the corresponding carbazole compounds, the N heteroatom is free to interact with the catalyst surface through the lone pair of electrons associated with the N.

In the present chapter, the complete hydrogenation cycle needed for hydrogen storage has been investigated for both carbazole and N-ethylcarbazole. The kinetics of the hydrogenation reactions needed for hydrogen storage on N-ethylcarbazole and carbazole are reported. N-ethylcarbazole was hydrogenated over a supported

Ru catalyst in an autoclave batch reactor at 7 MPa and 403-423 K. Kinetic models of the hydrogenation reactions, as well as the activation energies of the reactions, are reported. For comparison, carbazole was hydrogenated at 7 MPa and 443 K, using the same catalyst and experimental set-up used for the hydrogenation of N-ethylcarbazole.

2.2 Experimental

2.2.1 Catalyst preparation and characterization

A commercial 5 wt % Ru on alumina catalyst (Aldrich, 5 wt % Ru, reduced), received in a reduced state, was used as the hydrogenation catalyst and was re-reduced prior to use. The catalyst was characterized to determine BET surface area, pore volume and pore size using a Micromeritics ASAP 2020 analyzer. A Micromeritics Autochem II 2920 was used for Temperature Programmed Reduction (TPR) analysis of the catalyst and to determine the metal dispersion by CO pulse chemisorption (see Appendices A and B for details).

2.2.2 Catalyst activity

The hydrogenation of N-ethylcarbazole was carried out at 403, 413 and 423 K and a H_2 pressure of 7 MPa, in a 300 cm^3 autoclave batch reactor with continuous monitoring and control of stirrer speed, temperature and pressure. The schematic of the hydrogenation reactor is shown in Figure 2.1.

Approximately 100 cm^3 of a 6 wt % solution of N-ethylcarbazole (Aldrich, 97 %) in decalin (Sigma-Aldrich, 98 %) and 1 g of the 5 wt % reduced Ru/alumina catalyst, with a particle size < 150 μm, were loaded into the reactor. The reactor was first purged in a 55 cm^3(STP) min^{-1} flow of N_2 for about 1 h and then heated to the desired temperature while purging with ultra high purity (UHP) hydrogen at a 55 cm^3(STP) min^{-1} flow and low pressure (< 35 kPa) to ensure no reaction occurred. After the desired temperature was reached, the reactor was pressurized in hydrogen to 7 MPa, corresponding to more than 2.5 times the amount needed for complete hydrogenation of the N-ethylcarbazole reactant, while stirring at a speed of 600 rpm. The H_2 pressure was monitored continuously during the experiment. Small

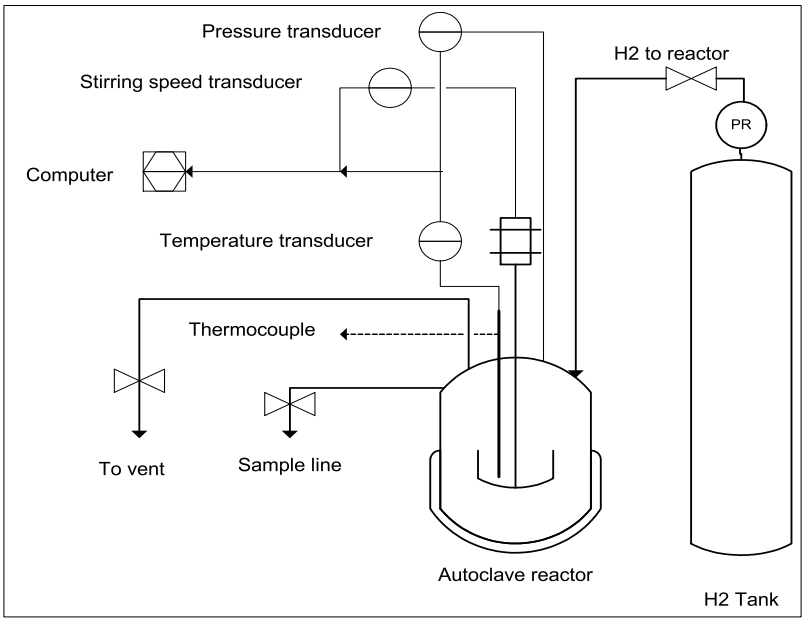

Figure 2.1: Schematic diagram for high pressure hydrogenation system

volumes (< 0.5 cm^3) of liquid sample were removed from the reactor periodically for analysis by gas chromatography. Hydrogenation of carbazole was carried out using the same autoclave reactor at 7 MPa and 423 K. In this case a 1 wt % solution of carbazole (Aldrich, 95 %) in decalin (Sigma-Aldrich, 98 %), and 1 g of the 5 wt % reduced Ru/alumina catalyst with a particle size < 150 μm were loaded into the reactor. The same start-up and sampling procedure used for the hydrogenation of N-ethylcarbazole was used for the hydrogenation of carbazole. However, due to the extremely low solubility of carbazole in decalin at room temperature, liquid samples were only taken at the end of the experiment and the identity of the final product was confirmed by GC/MS analysis with a Shimadzu QP-2010S GC/MS using a Restek RTX5 30M x 0.25 mm capillary column. Table 2.1 summarizes the physical properties of the reactants, solvent and the catalyst.

The absence of internal and external mass transfer effects on the measured reaction kinetics was confirmed experimentally and by theoretical analysis. For the

Table 2.1: Physical properties of hydrogenation reaction materials

Compound	N-ethylcarbazole	Carbazole	Decalin	Ru/Al_2O_3
Appearance	white solid	white solid	clear liquid	black powder
MW (g/mol)	195.26	167.21	138.25	—
Density (g/cm^3)	1.07	1.301	0.896	—
Boiling point (K)	621.3	628	460-469	—
melting point (K)	343	519.3	233	—
flash point (K)	437.4	493	330	—
Purity (%)	97	$\succeq$ 95	$\succeq$ 98	$\succeq$ 98.5
Metal (wt %)	—	—	—	5

hydrogenation reactions, the gas-to-liquid mass transfer rates, estimated according to Zievernek et al. [88], were at least two orders of magnitude higher than the observed reaction rate. Furthermore, repeating the reactions at stirrer speeds of 600 and 1000 rpm showed that in both cases, the measured reaction rates were within ± 10 % of the average values. Internal mass transfer effects were minimal because of the small catalyst particle size and confirmed by the calculated Weisz-Prater criterion of $\phi < 1.0$ at the highest reaction temperature. Details of calculations are given in Appendix F.

2.3 Results and discussion

2.3.1 Catalyst properties

Table 2.2 summarizes the characterization data for the Ru/alumina catalyst. BET surface area, pore volume and average pore size were also measured for the 5 wt % reduced Ru/alumina catalyst.

Table 2.2: Catalyst properties of the pre-reduced Ru/alumina

Catalyst	BET, $m^2\ g^{-1}$	Pore volume, $cm^3\ g^{-1}$	Average pore size, nm	Degree of reduction, %	Metal dispersion, %
Ru/Al_2O_3	76.5	0.2	8.4	3.3	6.2

Temperature Programmed Reduction (TPR) profile of the commercial Ru/alumina is shown in Figure 2.2. The TPR profile shows a peak with maximum at about 370 K. Another peak, smaller than the previous one, with maximum at 429 K is

also observed, which can be attributed to different ruthenium species. Mazzieri et al. [89] reported a sharp peak at 413 K for Ru on alumina catalyst with a smaller peak observed at about 468 K. In the present thesis, the Ru catalyst was received in a reduced state and the low degree of reduction for this catalyst reflects the stability of the reduced Ru in air. CO pulse chemisorption data were used to determine that the Ru dispersion was 6.2 % on the re-reduced Ru/alumina catalyst.

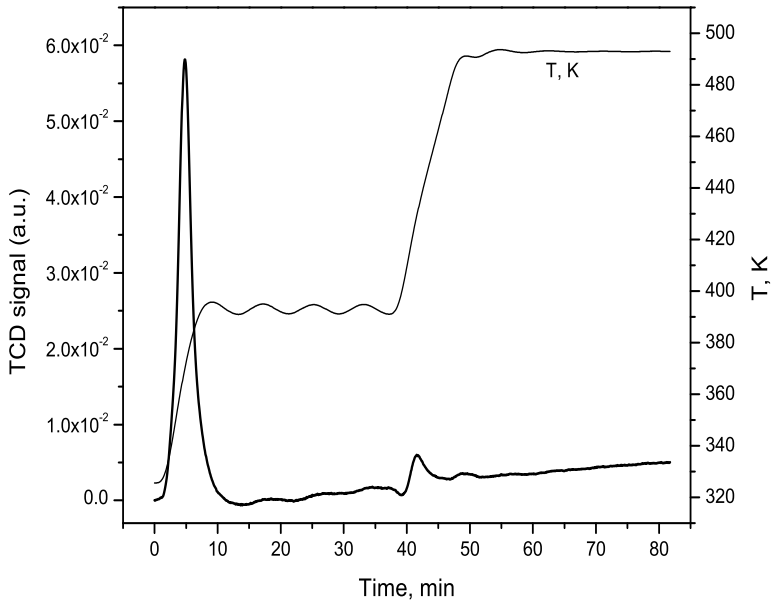

Figure 2.2: TPR results for the reduced Ru/Al_2O_3

2.3.2 Catalyst activity

When N-ethylcarbazole was hydrogenated at H_2 pressure of 7 MPa and temperature of 423 K, the conversion of N-ethylcarbazole proceeded to 98 % after 1 h, with an initial rate of H_2 consumption of 58.4 mM min^{-1} $g_{cat}{}^{-1}$. Analysis of the liquid samples by GC/MS confirmed the production of partially and completely hydrogenated compounds during the reaction, as represented in Figure 2.3.

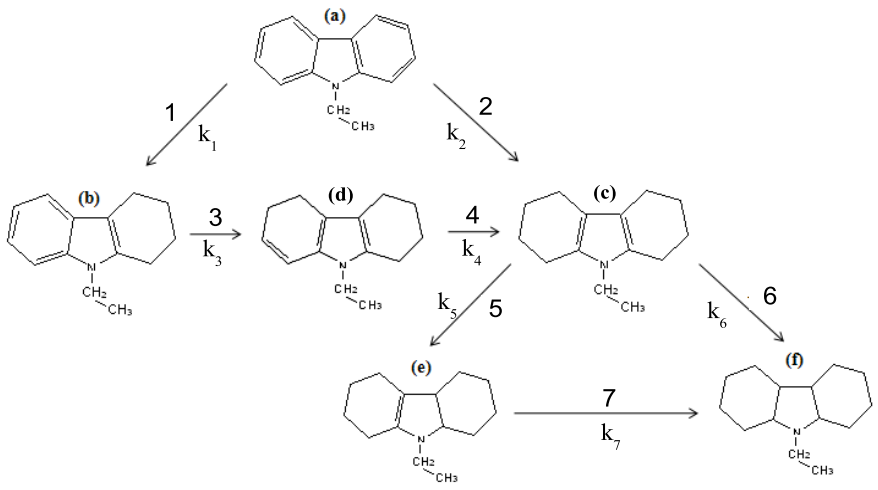

Figure 2.3: Hydrogenation reaction pathway of N-ethylcarbazole; (a) N-ethylcarbazole, (b) tetrahydro-N-ethylcarbazole, (c) octahydro-N-ethylcarbazole, (d) hexahydro-N-ethylcarbazole, (e) decahydro-N-ethylcarbazole, (f) dodecahydro-N-ethylcarbazole.

The reaction pathway in Figure 2.3 was suggested from the product distributions measured over time at three temperatures as shown in Figure 2.4-2.6. These data showed that N-ethylcarbazole hydrogenation proceeded through the stepwise saturation of double bonds, leading to the production of tetrahydro-N-ethylcarbazole and octahydro-Nethylcarbazole as the primary reaction products. Rapid consumption of tetrahydro-N-ethylcarbazole and subsequent production of hexahydro-N-ethylcarbazole suggested that the reaction proceeded to the production of hexahydro-N-ethylcarbazole from tetrahydro-N-ethylcarbazole. The product distribution showed slower consumption of hexahydro-N-ethylcarbazole compared to tetrahydro-N-ethylcarbazole. Octahydro-N-ethylcarbazole, one of the main intermediates, can undergo saturation of the double bonds through two parallel

paths to produce decahydro-N-ethylcarbazole, and dodecahydro-N-ethylcarbazole which is the major final product. The reaction completed with more than 95 % selectivity to the desired dodecahydro-Nethylcarbazole, and less than 5 % selectivity to the product octahydro-N-ethylcarbazole. The total amount of hydrogen consumed during hydrogenation corresponded to approximately 5.3 wt % of the reactant. This is very close to the storage criterion of Department of Energy (D.O.E.) and confirms that N-ethylcarbazole is a promising compound for hydrogen storage.

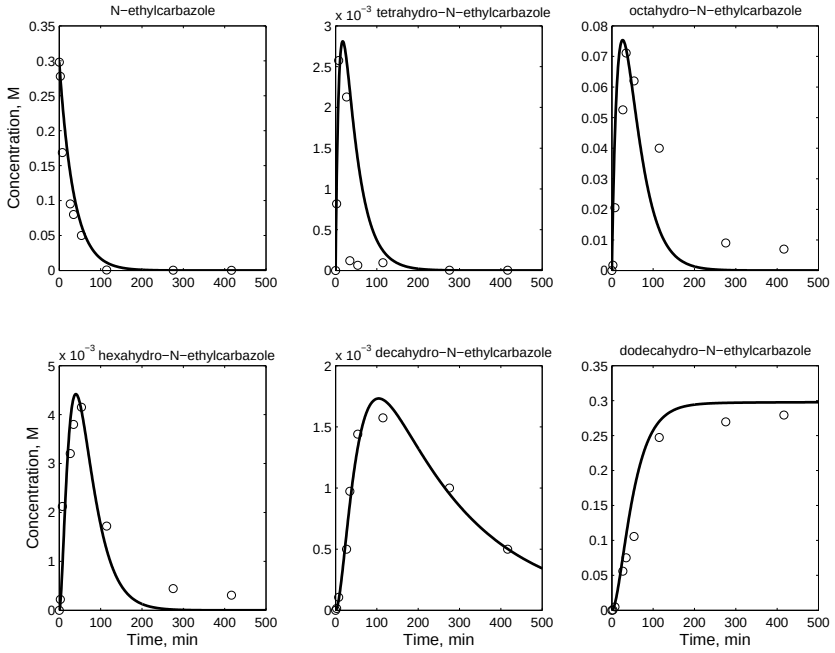

Figure 2.4: Product distribution over time for N-ethylcarbazole hydrogenation at 423 K. Note the different scale of each plot.

The experimental product distribution data measured over time at three reaction temperatures were used to model the reaction kinetics. The kinetic model based on the reaction network shown in Figure 2.3 assumed that reactions were 1^{st}-order in the concentration of the heteroaromatic organic compounds and zero-order in hydrogen. The parameters (rate constants) of the kinetic model were estimated by minimizing an objective function (see Appx. G), defined as the sum of squares of

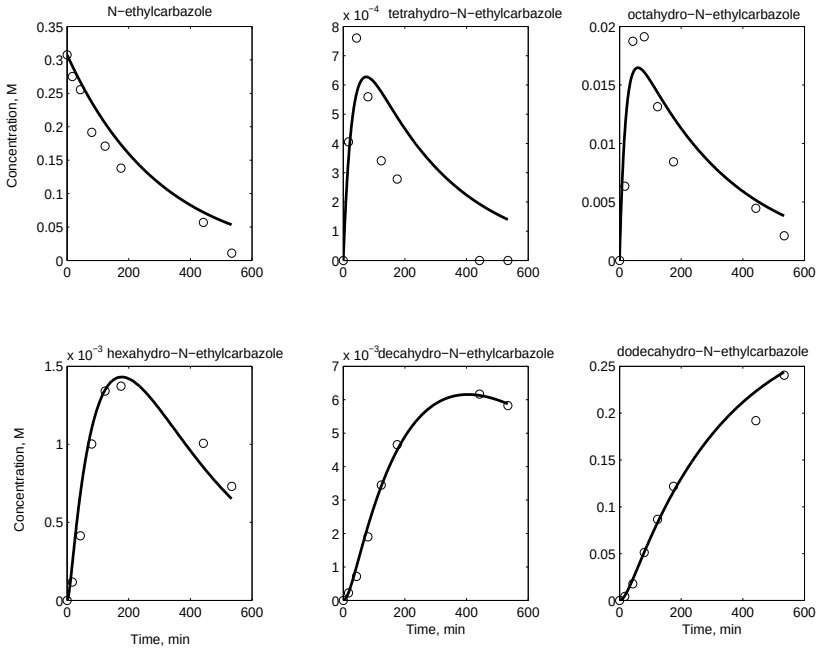

Figure 2.5: Product distribution over time for N-ethylcarbazole hydrogenation at 413 K. Note the different scale of each plot.

the difference between the experimental component concentrations and those calculated by the kinetic model, using a weighted least-squares method. The objective function was minimized using a Nelder-Mead simplex (direct search) method. At each iteration on the parameter values, the concentration of each compound as a function of time was calculated by numerical integration of the five ordinary differential equations that described the time rate-of-change of the hydrogenated product concentrations. In addition, the mole balance constraint was used to calculate the reactant concentration at each time step. Although reaction orders from 0 to 2 in increments of 0.5 were examined for all heteroaromatic organic compounds as well as hydrogen, the assumed 1^{st}-order kinetics for reactant and hydrogenated products and zero-order kinetics for hydrogen gave the best fit of the experimental data based on a minimum magnitude of the residual sum of squares. A zero-order reaction in hydrogen likely reflects the excess hydrogen at high pressure present during

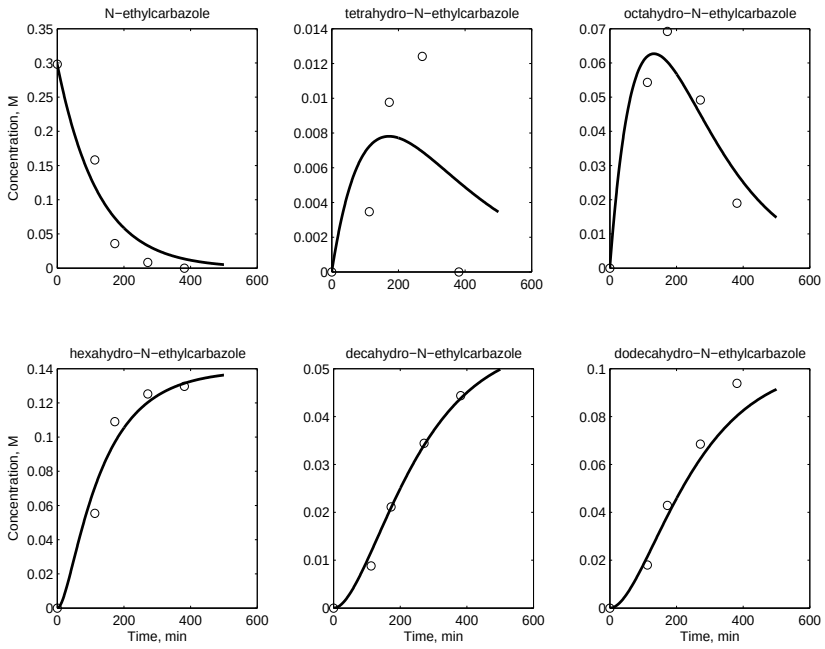

Figure 2.6: Product distribution over time for N-ethylcarbazole hydrogenation at 403 K. Note the different scale of each plot.

the hydrogenation reactions, and the relatively narrow range of H_2 pressures investigated herein, that results in an approximate constant concentration of H_2 in the liquid phase as the reaction proceeded. Therefore, although the reaction rate is influenced by a change in hydrogen pressure (i.e. atmospheric pressure will result in much lower hydrogenation reaction rate than the 7 MPa initial H_2 pressure used here), the zero-order kinetic model best describes the reaction rate at the reactions condition used in the present work. The activation energies for the reactions were determined by linear regression according to the Arrhenius equation. Individual 1^{st}-order rate constants estimated at 403, 413, and 423 K, as well as the activation energies are reported in Table 2.3.

The model results calculated using the obtained rate constants are plotted against the experimental product concentrations in Figure 2.4-2.6. The standard error of the parameter estimates are reported in Table 2.3 (the method used to calculate the

Table 2.3: 1^{st}-order rate constants and activation energies for the hydrogenation of N-ethylcarbazole over Ru/alumina catalyst

k h^{-1}	403 K	413 K	423 K	activation energy kJ/mol
k_1	0.021 ± 0.012	0.042 ± 0.018	0.096 ± 0.012	107.6 ± 7.0 (R^2 = 0.99)
k_2	0.444 ± 0.018	1.020 ± 0.018	1.764 ± 0.018	97.9 ± 10.3 (R^2 = 0.98)
k_3	0.840 ± 0.462	2.034 ± 0.600	5.646 ± 1.188	134.9 ± 7.5 (R^2 = 0.99)
k_4	0.000 ± 0.000	0.606 ± 0.672	2.538 ± 0.414	208.0 ± 0.0 (R^2 = 1)
k_5	0.006 ± 0.006	0.012 ± 0.012	0.024 ± 0.006	98.2 ± 1.4 (R^2 = 0.99)
k_6	1.140 ± 0.060	2.964 ± 0.528	3.300 ± 0.024	75.8 ± 33.6 (R^2 = 0.83)
k_7	0.000 ± 0.000	0.048 ± 0.024	0.252 ± 0.084	240.9 ± 0.0 (R^2 = 1)

standard errors of the estimated parameters is described in Appendix G). The optimum parameter values of the rate constants are given in Table 2.3. Although a global search method has been used in obtaining the optimum parameters, many parameter sets were found to fit the data. The only reported parameter values are the one with the least standard error values, which shows comparable magnitude to the literature reported standard errors [90] in non-linear optimization problems. It should be noted that a simple power law model with fixed exponents has been used to fit the kinetics of a complex reaction network over a relatively wide range of reaction temperatures. The model results confirmed that the production of intermediates and the final product were well described by the simplified 1^{st}-order kinetic model shown in Figure 2.3. The data for the concentration of tetrahydro-N-ethylcarbazole showed the largest difference between the measured and calculated concentrations, but the concentration of this compound was the lowest among all compounds by approximately 1 order of magnitude.

Table 2.3 summarizes the obtained rate constants for the individual reactions of the model (Figure 2.3), as well as the activation energies estimated from the rate constants. The rate constants for reaction 4 (k_4) and reaction 7 (k_7) of Figure 2.3, corresponding to the conversion of hexahydro-N-ethylcarbazole and decahydro- N-ethylcarbazole, were zero at 403 K, confirming the higher activation barrier for the consumption of these two intermediates compared to the other products. The estimated rate constants for the conversion of tetrahydro-N-ethylcarbazole (k_3) and hexahydro-N-ethylcarbazole (k_4) were consistent with the observed slower consumption of hexahydro-N-ethylcarbazole compared to the more rapid consumption

of tetrahydro-Nethylcarbazole in the first 10 min of the reaction. Comparing the apparent activation energies of Table 2.3, it is seen that the production of octahydro-N-ethylcarbazole from hexahydro-N-ethylcarbazole (reaction 4) and the production of dodecahydro-N-ethylcarbazole from decahydro-N-ethylcarbazole (reaction 7) have the highest activation energies, in agreement with the experimental observation of low consumption rates of hexahydro-N-ethylcarbazole and decahydro-N-ethylcarbazole.

A comparison of the N-ethylcarbazole conversion at the three reaction temperatures is shown in Fig. 2.7. The results confirmed that the reactions were 1^{st}-order in N-ethylcarbazole concentration with an apparent activation energy for N-ethylcarbazole consumption of 99.5 kJ/mol.

Hydrogenation of N-ethylcarbazole was also carried out using a range of initial reactant concentrations from 3.5 - 6 wt % at 413 K to determine the effect of initial concentration on reaction rate. The rate constants for each reactant concentration obtained from the experimental data are summarized in Table 2.4 and shown in Figure 2.8.

Table 2.4: Rate constants for N-ethylcarbazole hydrogenation with different initial concentrations at 413 K.

Initial concentration, wt %	k C_{A0}[a], mol. ml^{-1}. min^{-1}
3.5	$2.73\times10^{-6} \pm 6.00\times10^{-7}$
4.5	$3.24\times10^{-6} \pm 2.50\times10^{-7}$
6.0	$5.39\times10^{-6} \pm 1.35\times10^{-6}$

[a] See Appendix E for sample calculation

The data showed that the rate constants increased with increasing initial reactant concentration, confirming the 1^{st}-order concentration dependence of the reaction rate.

Carbazole was hydrogenated using the same autoclave reactor and catalyst to produce the reactant for the dehydrogenation reaction. At a H_2 pressure of 7 MPa and a temperature of 423 K, 100 % conversion of carbazole was achieved after about 13 h. Due to the extremely low solubility of carbazole in decalin, only a

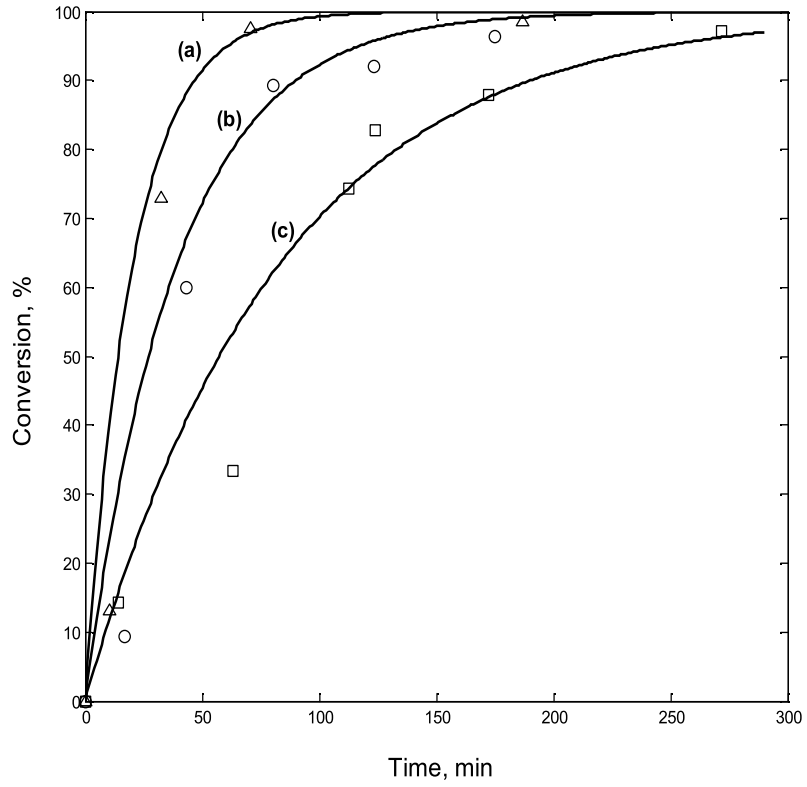

Figure 2.7: Comparison between 6 wt % N-ethylcarbazole conversions at different temperatures: (a) 423 K, (b) 413 K, (c) 403 K. Data points correspond to the experimental data and the solid lines are fitted first-order kinetic models.

few liquid samples were withdrawn after a reaction time of 10 h. Liquid sample analysis by GC/MS confirmed the production of dodecahydrocarbazole as the main product. The reaction proceeded with more than 97 % selectivity to the completely hydrogenated product, dodecahydrocarbazole, after about 13 h. The initial rate of H_2 consumption by carbazole was 18.44 $mMmin^{-1}g_{cat}{}^{-1}$ at 423 K. Since the intermediate products could not be monitored as a function of time in this case, the kinetics of carbazole consumption were described by a first-order rate equation in

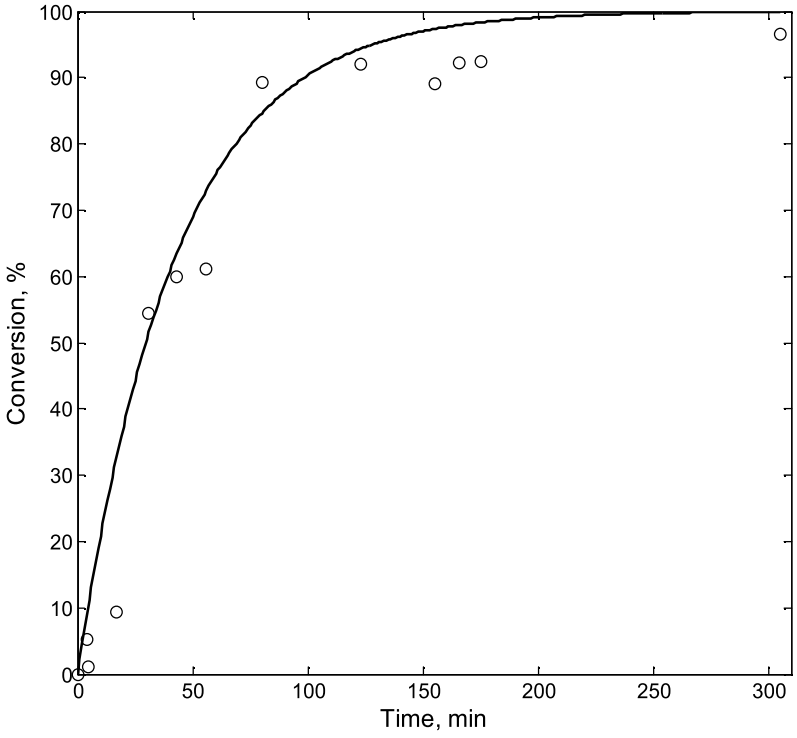

Figure 2.8: Comparison between measured and calculated conversion profile for N-ethylcarbazole hydrogenation at 413 K at three different initial concentrations of N-ethylcarbazole. First-order rate constants are reported in Table 2.4. (○) experimental data, (solid line) fitted first-order kinetic model.

carbazole concentration and zero-order in H_2 concentration. The same mathematical procedure used to model the kinetics of N-ethylcarbazole hydrogenation was used to model carbazole hydrogenation. Different reaction orders for the organic heteroaromatic compounds as well as hydrogen were examined in the model. The chosen orders are based on the best fit of experimental data. A comparison between the initial rates, the first-order rate constants, and turn-over frequencies (TOFs) for the consumption of carbazole and N-ethylcarbazole at 423 K is presented in Table 2.5.

Table 2.5: Initial Reaction Rates, rate constants, and TOFs for hydrogenation of N-ethylcarbazole and carbazole at 423 K over Ru/alumina catalyst

reactant	N-ethylcarbazole	carbazole
rate constant,[a] k, h^{-1}	2.952 ± 0.122	0.318 ± 0.034
catalyst/reactant, g g^{-1}	0.17	1.00
initial rate[b], mM min^{-1} $g_{cat}{}^{-1}$	58.36	18.44
TOF[c], s^{-1}	0.223	0.108
reaction time[d], h	1.16	13.33

[a] with respect to N-ethylcarbazole and carbazole consumption.
[b] Reaction rate with respect to H_2 consumption.
[c] molecule reactant s^{-1} Ru surface $atom^{-1}$.
[d] reaction time for 100 % conversion.

N-ethylcarbazole hydrogenation showed a higher initial reaction rate and proceeded to 100 % conversion in a significantly shorter reaction time with lower metal loading of the catalyst, compared to carbazole. The slower hydrogenation rate of carbazole compared to N-ethylcarbazole can be attributed to the strong adsorption of the carbazole molecule through the N heteroatom to the metal surface. The inhibiting effects of basic N in organic compounds on precious metal catalysts, due to the unshared pair of electrons on N, is well-known [91]. The steric hindrance associated with the ethyl group of N-ethylcarbazole prevents the adsorption of the molecule on the metal surface through the N, as has been previously reported for similar geometries [92]. Therefore, although carbazole has a higher theoretical H_2 storage capacity than N-ethylcarbazole, the inhibiting effect of the N atom slowed the hydrogenation reaction and complete H_2 saturation of carbazole was obtained in a much longer reaction time compared to N-ethylcarbazole, making carbazole a

less practical candidate for H_2 storage.

2.4 Conclusion

N-Ethylcarbazole hydrogenation was faster than the hydrogenation of carbazole over a supported Ru catalyst in the temperature range 403-423 K, whereas the selectivity to the completely hydrogenated products, dodecahydro-N-ethylcarbazole and dodecahydrocarbazole was 95 % and 97 %, respectively. Both N-ethylcarbazole and carbazole hydrogenation reactions followed first-order kinetics. The faster hydrogenation reaction rate of N-ethylcarbazole compared to carbazole is attributed to the strong interaction of N electron pair with the catalyst surface. In the case of N-ethylcarbazole, steric hindrance of the ethyl group likely prevents the N lone pair from interacting strongly with the surface, resulting in faster hydrogenation reaction rate.

Chapter 3

Kinetics of H_2 recovery from dodecahydro-N-ethylcarbazole over a supported Pd catalyst

A version of this chapter has been published:
F. Sotoodeh, L. Zhao and K.J. Smith. Kinetics of H_2 recovery from dodecahydro-N-ethylcarbazole over a supported Pd catalyst, Applied Catalysis A: General 362 (2009) 155-162.

3.1 Introduction

Storing and releasing H_2 from organic molecules is done through catalytic hydrogenation and dehydrogenation reactions. Platinum-group metal catalysts (PGMs) are widely used in heterogeneous catalysis for hydrogenation and dehydrogenation reactions [93, 94]. These catalysts are very active, but low selectivity as well as catalyst deactivation due to hydrogenolysis and coke formation, respectively, are issues that require careful control of process conditions and catalyst properties [95]. Key to success is a high surface area and stability of the catalyst to ensure rapid uptake and release of hydrogen. N-Carbazole and N-ethylcarbazole are organic heteroaromatic compounds with hydrogen storage capacity $>$ 5.5 wt % and boiling point $>$ 473 K when completely hydrogenated, making them possible candidates for hydrogen storage. Some studies have been reported on hydrogen storage by N-ethylcarbazole [16, 96]. However, there is little information on the hydrogenation and dehydrogenation reaction rates and kinetics of N-ethylcarbazole. Kinetics of hydrogen uptake by N-ethylcarbazole was studied in Chapter 2. In the present work, the kinetics of hydrogen recovery from dodecahydro-N-ethylcarbazole has been studied over a 5 wt % Pd/SiO_2 catalyst. To compare the dehydrogenation rate and storage capacity, two important criteria for vehicular applications, dehydrogenation of 1,2,3,4-tetrahydrocarbazole has also been measured over the supported 5 wt % Pd catalyst.

3.2 Experimental

3.2.1 Catalyst preparation

The supported Pd catalyst, with a Pd loading of 5 wt %, was prepared by the wet impregnation method reported by Song et al. [97]. Silica gel (Sigma-Aldrich) with a surface area of 300 m^2/g and pore volume of 1.15 ml/g was used as the support. The silica gel (9.5 g) was impregnated with 20 mL of a 0.2 M aqueous solution of Pd^{2+} prepared from $PdCl_2$ (Sigma-Aldrich, 99.9 +%), and left to age for 24 h. The sample was then dried at 393 K for 24 h and calcined at 748 K for 3 h. The obtained sample was reduced in 30 ml (STP)/min of H_2 at 723 K and cooled to room temperature in He at 30 ml (STP)/min. A commercial 5 wt % Ru on alumina

(Aldrich, 5 wt % Ru, reduced) was used as the hydrogenation catalyst and was re-reduced prior to use.

3.2.2 Catalyst characterization

Temperature Programmed Reduction (TPR) of the calcined Pd on silica was performed using a Micromeritics Autochem II 2920. About 0.12 g of calcined Pd/silica was loaded in the reactor and heated to 673 K at a rate of 5 K/min in 30 ml (STP)/min flow of 10 % H_2 in Ar. The final temperature was held for 30 min.

The CO uptake of Pd/SiO_2 was determined by pulsed chemisorption using a Micromeritics Autochem II 2920. Approximately 1 g of the catalyst was loaded in the reactor and pre-reduced in 50 ml (STP)/min of 10 % H_2 in Ar while heating from 313 K to 673 K at a rate of 5 K/min, and holding the final temperature for 30 min. The reactor was then cooled to 313 K in a He flow of 50 ml (STP)/min before repeated injection of pulses of CO into the reactor from a 20 ml (STP)/min flow of 10 % CO in He. The injection was continued until the TCD detector response showed no more CO uptake by the sample. The metal dispersion was calculated using an assumed Pd:CO of 1:1 [98].

A Micromeritics ASAP 2020 Accelerated Surface Area and Porosimetry analyzer was used for measuring the total BET surface area, pore volume and average pore width of the Pd/SiO_2 catalyst before and after reduction. Approximately 0.2 g of the catalyst was loaded in the sample tube for initial degassing. The sample tube was evacuated at a rate of 1.33 kPa/s and temperature rate of 10 K/min until the vacuum reached 0.04 kPa. The temperature was then held at 473 K for 240 min. After degassing, the sample was transferred to the analysis section for BET surface area analysis using N_2.

3.2.3 Catalyst activity

The hydrogenation of N-ethylcarbazole was carried out at temperature range of 403 - 423 K and 7 MPa as in a 300 cm^3 autoclave batch reactor with continuous monitoring and control of stirrer speed (600 rpm), temperature and pressure. Details of the hydrogenation experiments have been discussed in Chapter 2. The recovered product from hydrogenation of N-ethylcarbazole was filtered and used as reactant

for dehydrogenation. The dehydrogenation was carried out in a 50 ml glass flask reactor using 0.3 g of the reduced 5 wt % Pd/SiO_2 (dehydrogenation catalyst) at a temperature range of 423 - 443 K and 101 kPa as shown in Figure 3.1.

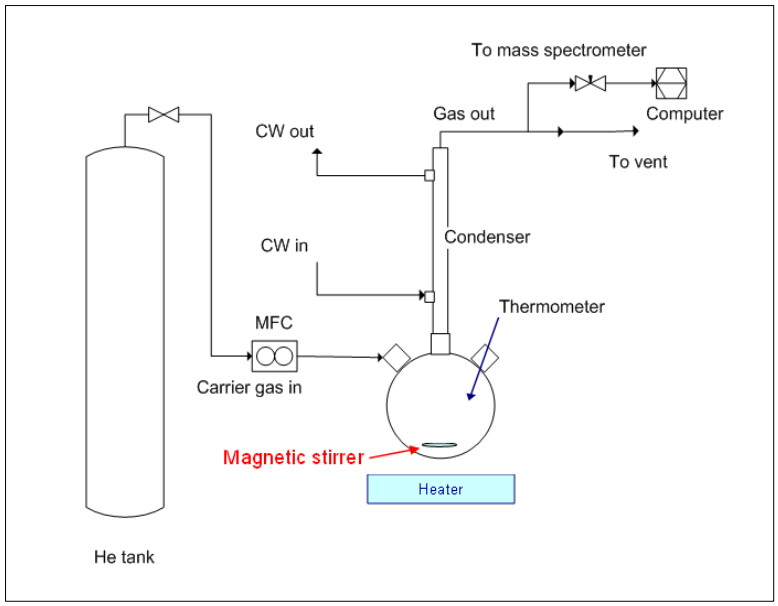

Figure 3.1: Schematic diagram for atmospheric dehydrogenation system

The reactor was stirred and heated to the desired temperature while purging in He flow at 170 cm^3 (STP) /min. After reaching a stable temperature, the catalyst was injected into the reactor. Helium was used as a carrier gas for continuous removal of the produced hydrogen, and the exit gas composition was continuously monitored using a quadrupole mass spectrometer (Residual Gas Analyzer 200 amu). Liquid samples of < 0.1 ml were also withdrawn from the reactor, periodically. The analysis of the liquid samples form the dehydrogenation reactions was done using a 14-A Shimadzu gas chromatograph equipped with a flame ionization detector (FID) and an AT^{TM}-5 25M x 0.53 mm capillary column. Product identities were also confirmed by a Shimadzu QP-2010S GC/MS using a Restek RTX5 30M x 0.25 mm capillary column.

Dehydrogenation reactions of 1,2,3,4-tetrahydrocarbazole (Aldrich, 99 %) were carried out for comparison of hydrogen production rates with dodecahydro-N-ethylcarbazole, using the same experimental set-up and procedure. 3 wt % of 1,2,3,4-tetrahydrocarbazole in mesitylene (Aldrich, 98 %) and 0.2 g of the reduced 5 wt % Pd/SiO_2 was loaded into the reactor with the constant flow of He as carrier gas for continuous removal of hydrogen, and the reaction was performed at a temperature range of 413 - 423 °C and 101 kPa in a 50 ml glass flask reactor.

3.3 Results and discussions

3.3.1 Catalyst properties

Temperature programmed reduction (TPR) profile for the calcined Pd/SiO_2 is shown in Figure 3.2. A peak at 337 K was observed. The H_2 profile is consistent with the release of H_2 from the decomposition of a β-palladium hydride phase which is reported to form at room temperature over large Pd particles ($>$ 2 nm) [99, 100].

CO pulse chemisorption data were used to determine that 4.2 % of the total Pd atoms were available at the catalyst surface. BET surface area, pore volume and average pore size were measured for the 5 wt % Pd/SiO_2 after calcination and reduction and the results are summarized in Table 3.1.

Table 3.1: Pd/SiO_2 catalyst properties

Catalyst status	BET, m^2/g	Pore volume, cm^3/g	Average pore size, nm	Metal dispersion, %
Calcined	311.5	0.9	9.6	—
Reduced	325.6	1.1	9.5	4.2

3.3.2 Catalyst activity

Dehydrogenation of dodecahydro-N-ethylcarbazole

The products from N-ethylcarbazole hydrogenation in decalin at 423 K, containing 5.8 wt % dodecahydro-N-ethylcarbazole1 wt % and $<$ 0.2 wt % octahydro-N-ethylcarbazole, were transferred to a 50 ml stirred reactor for the dehydrogena-

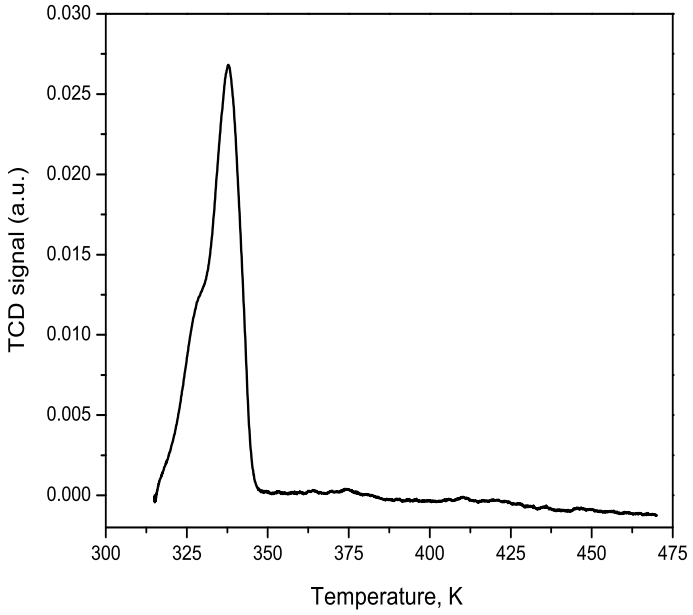

Figure 3.2: TPR profile for the calcined Pd/SiO_2

tion test. Previous studies showed that decalin dehydrogenation occurs at T $>$ 473 K [57, 58, 101, 102], and our own tests confirmed no decalin dehydrogenation at T $<$ 453 K, which made it possible to use decalin as a solvent for the dehydrogenation experiments. The reduced 5 wt % Pd/SiO_2 (0.3 g) was used as the dehydrogenation catalyst and the hydrogen generated was monitored continuously using a quadropole mass spectrometer attached to the gas outlet from the reactor. The reactions were carried out at temperatures of 423, 433 and 443 K. The product distribution over time suggested that tetrahydro-N-ethylcarbazole and octahydro-N-ethylcarbazole were the primary intermediates at all three temperatures, and no significant amounts of N-ethylcarbazole was produced, as confirmed by the GC/MS analysis of liquid samples.

First order kinetics were fitted to the obtained experimental data in order to calculate the rate constant for the production of tetrahydro-N-ethylcarbazole and

octahydro-N-ethylcarbazole. Fig. 3.3 illustrates the experimental product distribution over time at three temperatures and the fitted first order model. The apparent activation energy for dodecahydro-N-ethylcarbazole consumption was found to be 126.7 kJ/mol. The initial reaction rates, rate constants, as well as the percent hydrogen recovered at each temperature are summarized in Table 3.2. The initial reaction rates were obtained from the first 15 min of the experiment.

Table 3.2: Initial reaction rates, rate constants and hydrogen recovery for dehydrogenation of dodecahydro-N-ethylcarbazole

T, K	Initial reaction rate, mM min^{-1} $g_{cat}{}^{-1}$	Rate constant[a], k, min^{-1}	k_1, min^{-1}	k_2, min^{-1}	H_2 recovery after 17 h, wt %
423	3	0.0016	0.0012	0.0006	2.1
433	8.5	0.0044	0.0013	0.0027	3.3
443	12	0.0075	0.0027	0.0035	4.0

[a]For dodecahydro-N-ethylcarbazole consumption.

One hundred percent of the reactant, dodecahydro-N-ethylcarbazole, was converted at the three temperatures, resulting in 2 wt % H_2 recovery after 2 h and 4 wt % H_2 recovery after 17 h at 443 K. However, although 100 % conversion was achieved in the present study, only 66 % of the total stored H_2 was recovered at 443 K because of the dehydrogenation to tetrahydro-N-ethylcarbazole and octahydro-N-ethylcarbazole, and not N-ethylcarbazole.

Dehydrogenation of 1,2,3,4-tetrahydrocarbazole

To compare the hydrogen release rate and storage capacity on N-ethylcarbazole, the dehydrogenation of 1,2,3,4-tetrahydrocarbazole was carried out at temperatures of 413 and 423 K using a solution of 3 wt % reactant in mesitylene. Reduced 5 wt % Pd/SiO_2 (0.2 g) was used as dehydrogenation catalyst with constant flow of He as a carrier gas for continuous removal of the produced H_2. Gas and liquid phase analysis confirmed that no byproducts were generated, and that the reaction proceeded selectively to carbazole, as also previously reported [53]. The initial rates of 1,2,3,4,-tetrahydrocarbazole dehydrogenation on 5 wt % Pd/SiO_2 catalyst at 413

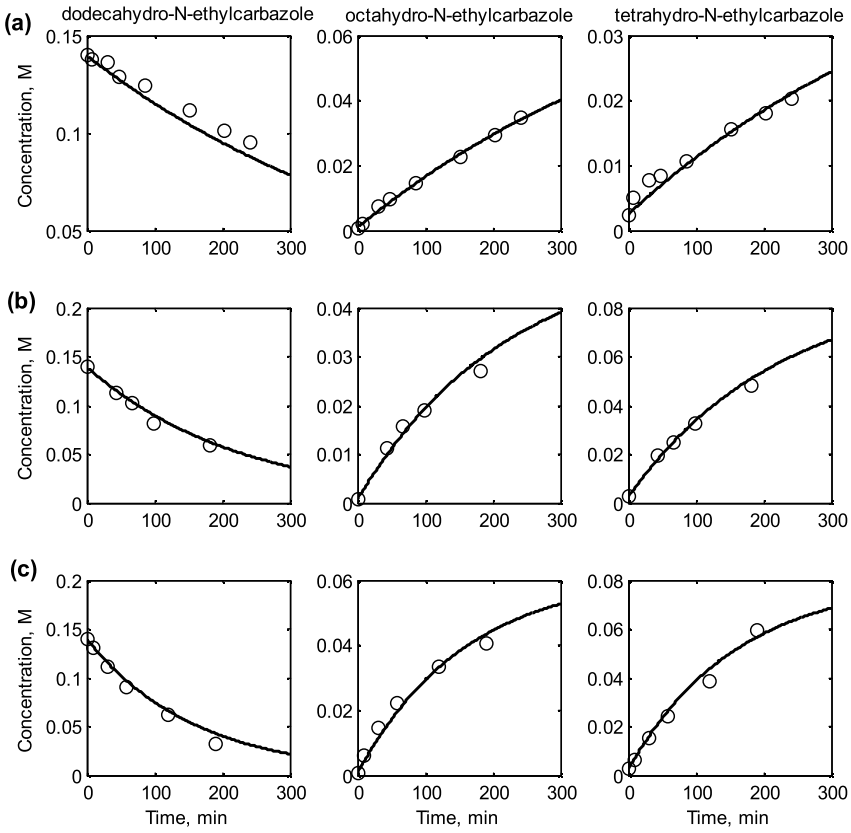

Figure 3.3: Product distribution for dehydrogenation of dodecahydro-N-ethylcarbazole obtained by GC/MS: (a) 423 K, (b) 433 K, (c) 443 K. (○) experimental data, (solid line) fitted model. The rate constants are reported in Table 3.2.

and 423 K and 101 kPa, were 17 and 18.5 mM min^{-1} $g_{cat}{}^{-1}$, respectively. These values are comparable to the average rate of 10 mM min^{-1} $g_{cat}{}^{-1}$ reported by Crawford et al. [53] for Pd/alumina at 413 K. The activation energy was estimated as 67.7 kJ/mol, in good agreement with the calculated value of 64.4 kJ/mol from DFT study done by Crawford et al. [53] and 67 kJ/mol obtained by the experimental work of Hindle et al. [54]. The reaction proceeded to 25 % conversion at 423 K after 400 min and 17 % conversion at 413 K after 350 min. The obtained results confirmed that the reaction followed zero order kinetics with respect to 1,2,3,4,-tetrahydrocarbazole consumption, which is consistent with the reaction kinetics for the production of carbazole. The carbazole concentration increased approximately linearly as seen in Fig. 3.4 up to about 15 % 1,2,3,4,-tetrahydrocarbazole conversion at 423 K and about 12 % at 413 K. Then, a positive order relationship was observed because of product inhibition as also reported previously [54]. Only 0.6 wt % of the hydrogen (equal to 25 % of the theoretical reactant hydrogen capacity) was recovered during the experiment.

Table 3.3 compares the dehydrogenation reaction of 1,2,3,4,-tetrahydrocarbazole and dodecahydro-N-ethylcarbazole. Comparing the two compounds, it can be seen that the theoretical H_2 capacity is higher for dodecahydro-N-ethylcarbazole. At the same temperature of 423 K, the same recovery was obtained. However, because the dehydrogenation reaction of dodecahydro-N-ethylcarbazole has a higher activation energy (127 kJ/mol) compared to 1,2,3,4-tetrahydrocarbazole (67 kJ/mol), increasing the temperature from 423 K to 443 K, increased the amount of evolved H_2 from dodecahydro-N-ethylcarbazole significantly from 25 % to 60 % after about 6 h.

3.4 Conclusion

Dehydrogenation of the hydrogenation product, dodecahydro-N-ethylcarbazole, showed that the reaction proceeded to 100 % conversion, but only 66 % of the stored hydrogen was recovered during dehydrogenation at 443 K after 17 h, because of the production of the two intermediates octahydro-N-ethylcarbazole and tetrahydro-N-ethylcarbazole, with minimal production of N-ethylcarbazole. However, this amount is comparable with the dehydrogenation reaction of 1,2,3,4-tetrahydrocarbazole where only 25 % of the hydrogen was recovered at 423 K,

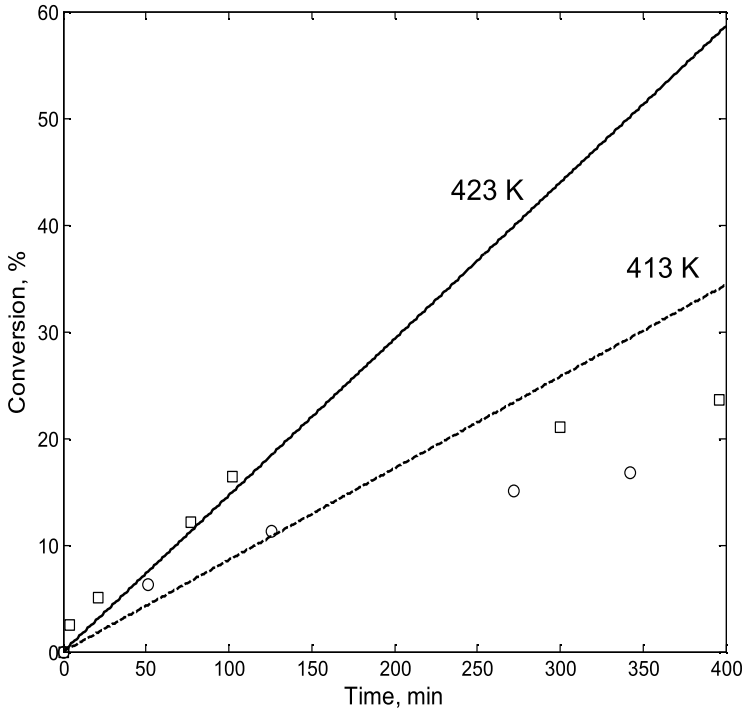

Figure 3.4: Comparison of 1,2,3,4-tetrahydrocarbazole conversion at different temperatures obtained from liquid samples analysis

Table 3.3: Comparison between dehydrogenation of 1,2,3,4-tetrahydrocarbazole and dodecahydro-N-ethylcarbazole over a 5 wt % Pd/SiO_2 catalyst

Compound	Theoretical H_2 release[a], (wt %)	H_2 recovery[b], (%)	Catalyst to reactant ratio, ($g.g^{-1}$)	Duration, (min)	T, (K)
1,2,3,4-tetra-hydrocarbazole	2.3	25	0.2	370	423
Dodecahydro-N-ethylcarbazole	5.8	25	0.3	370	423
	5.8	60	0.3	370	443

[b] Amount of H_2 released in the experiment divided by theoretical amount of released H_2.

[a] Theoretical amount of released H_2 in grams divided by the weight of hydrogenated compound in grams

leading to the conclusion that N-ethylcarbazole is a more applicable compound for hydrogen storage.

Chapter 4

Structure sensitivity of dodecahydro-N-ethylcarbazole dehydrogenation over Pd catalysts

A version of this chapter has been published:
F. Sotoodeh and K.J. Smith (2011) Structure sensitivity of dodecahydro-N-ethylcarbazole dehydrogenation over Pd catalysts. Journal of Catalysis, 279, 36-47.

4.1 Introduction

As discussed in the previous chapters, hydrogen is an alternative, non-toxic, environmentally benign energy carrier with H_2O the only product when H_2 is converted into thermal energy (by combustion) or electrical energy (using fuel cells). However, hydrogen has a very low density at ambient conditions making it difficult to store and transport. On-board vehicular hydrogen storage, including compressed or liquid (cryogenic) hydrogen, suffer from high energy inputs and low gravimetric storage capacities. On the other hand, organic aromatic compounds that bind hydrogen covalently, have the potential to meet the 6 wt % H_2 storage density demands of automotive applications [20]. The catalytic dehydrogenation reaction must be fast, selective and have low enthalpy so that the reaction is thermodynamically favored at low temperature ($<$ 473 K) [44]. However, a review of literature data shows very slow dehydrogenation reaction rates and low selectivity to the completely dehydrogenated product for some organic compounds. For example, the high enthalpy of dehydrogenation of cyclohexane (205.5 kJ/mol with H_2 capacity 7.1 wt %) and methylcyclohexane (202.5 kJ/mol with H_2 capacity 6.1 wt %) means that high temperatures ($>$ 573 K) are required for on-board H_2 recovery by dehydrogenation [87, 103, 104]. Pez et al. [16] have shown that incorporation of a heteroatom in the aromatic ring can lower the dehydrogenation enthalpy of the candidate compounds. Complete conversion of indoline, with a hydrogen capacity of 1.7 wt %, was reported over Pd/C and Rh/C catalysts after 24 h in refluxing toluene ($\sim$383 K) [105]. However, the low hydrogen content of indoline means that this is not a practical choice for transport applications. Dehydrogenation of 4-aminopiperidine (hydrogen capacity 5.9 wt %) over a 10 wt % Pd/SiO_2 catalyst resulted in 66 % conversion at 443 K after 4 h [44]. Complete conversion of dodecahydro-N-ethylcarbazole (hydrogen capacity 5.8 wt %) was obtained over a 5 wt % Pd/SiO_2 at 443 K and 101 kPa after 17 h with only 4.0 wt % H_2 recovery, due to a low selectivity toward the completely dehydrogenated N-ethylcarbazole product [106, 107]. Dehydrogenation of dodecahydrocarbazole (hydrogen capacity 6.7 wt %) was reported to be even slower than dodecahydro-N-ethylcarbazole, most likely due to product inhibition by carbazole, where only 53 % conversion was achieved after 17 h at 443 K and 101 kPa [106, 107]. In a similar dehydrogenation

study of dodecahydro-N-ethylcarbazole over homogeneous Ir-complex catalysts, no selectivity toward N-ethylcarbazole was reported at 473 K, and octahydro-N-ethylcarbazole and tetrahydro-N-ethylcarbazole were the only products [56].

Limited data are available on the relationship between catalytic activity and catalyst dispersion for the hydrogenation and dehydrogenation reactions of organic aromatics, and contradictory interpretations have been reported. For example, Benedetti et al. [99] reported that the hydrogenation of 2,4-dinitrotoluene over Pd/SiO_2 was favored by an increase in Pd particle size. However, Suh et al. [108] noted that hydrogenation of 2,4-dinitrotoluene over Pd/C catalysts was structure insensitive and that increases in specific activity on larger Pd particles was attributed to diffusion limitations within the pores of the microporous carbon support. In other work on the hydrogenation of 2,4-dinitrotoluene over a Pd/C catalyst, it was found that in the range of dispersions investigated (Pd particle size 3 - 10 nm) the specific activities increased as the Pd dispersion decreased [100]. In a study of pyrrole hydrogenation over Pt catalysts, with particle size from $<$ 1 nm to 5 nm, reported by Kuhn et al. [109], it was demonstrated that ring hydrogenation was structure insensitive, while ring opening to n-butylamine was structure sensitive and found to be more facile over larger Pt nanoparticles.

Adsorption geometries of aromatic organic compounds relevant to hydrogen storage over metal surfaces have been shown to involve several surface metal atoms, suggesting that the dehydrogenation reactions may be structure sensitive. Crawford et al. [53] investigated the mechanism of 1,2,3,4-tetrahydrocarbazole dehydrogenation over a Pd catalyst, and showed by experiment and density-functional theory (DFT) calculations that the reaction proceeded through a flat adsorption geometry of 1,2,3,4-tetrahydrocarbazole involving several Pd surface sites. Lu et al. [110], using periodic DFT calculations, also reported a flat adsorption of tetracene over several Ru surface atoms, with the long axis of tetracene parallel to the surface. The optimized structure showed that adsorption of tetracene required multiple Ru atoms. Tilted and parallel adsorption of quinoline on a Pt cluster investigated by Vargas et al. [92] also indicated that several surface Pt atoms were involved in the adsorption.

In this chapter, the structure sensitivity of the dehydrogenation of dodecahydro-N-ethylcarbazole was investigated over a series of Pd/SiO_2 catalysts, prepared with

Pd loadings of 0.5 to 10 wt %, such that the Pd dispersion (particle size) varied from 6.5 % (15 nm) to 52 % (1.9 nm). The activity and selectivity of each catalyst for the dehydrogenation of dodecahydro-N-ethylcarbazole is reported.

4.2 Experimental

4.2.1 Catalyst preparation

The SiO_2-supported Pd catalysts (0.5 wt % to 10 wt %) were prepared by incipient wetness of the support [111]. Silica gel (Sigma-Aldrich, BET surface area 400 m^2/g, pore volume 1.15 cm^3/g, particle size < 90 μm) was used as the support. Approximately 10 grams of the silica gel was drop-wise impregnated with an aqueous solution of Pd^{2+}, prepared from 0.5 N HCl and the $PdCl_2$ (Sigma-Aldrich, 99.9+ %), at a concentration sufficient to yield the required Pd loading from one impregnation. The impregnated support was left to age for 48 h before being dried at 393 K for 8 h and calcined at 773 K for 6 h in a He flow of 30 cm^3 (STP)/min. The calcined catalyst precursor was subsequently reduced in a H_2 flow of 30 cm^3 (STP)/min while heating at a rate of 10 K/min to 673 K. The final temperature was held for 1 h before cooling the reduced catalyst to room temperature in a 30 cm^3 (STP)/min flow of He.

The Pd catalysts were compared to a previously reported 5 wt % Pd/SiO_2 catalyst that was prepared by wet impregnation but dried at 393 K for 24 h and calcined at 748 K for 3 h in air rather than inert He [106]. Using the same procedure, a 10 wt % Pd/SiO_2 catalyst calcined in air was also prepared in the present study.

4.2.2 Catalyst characterization

Temperature-programmed reduction (TPR) of the calcined Pd/SiO_2 catalyst precursors was performed using a Micromeritics Autochem II 2920 analyser fitted with a thermal conductivity detector (TCD). About 0.2 g of each sample was loaded into a u-tube reactor and flushed for 30 min in a 50 cm^3 (STP)/min flow of 10 % H_2 in Ar at room temperature, before heating to 673 K at a rate of 10 K/min with the final temperature held for 1 h.

In order to clarify the TPR profiles, additional TPR studies were done using a

quartz u-tube reactor placed in a temperature programmable muffle furnace with a quadrupole mass spectrometer (SRC Residual Gas Analyzer, 200 amu) connected to the reactor effluent in order to continuously monitor the products generated during the temperature-programmed calcination and reduction. The calcination and reduction steps, using 0.4 grams of sample, followed the same procedure as that used in the Micromeritics Autochem II 2920 analyser. To investigate the reducibility of the catalyst at room temperature, the catalysts were flushed in a 50 cm^3 (STP)/min flow of 10 % H_2 in He for 3 h at room temperature after the calcination and prior to the TPR.

Temperature-programmed desorption (TPD) of CO from the Pd catalysts was also performed using the Micromeritics Autochem II 2920 analyser. About 0.2 g of the dried catalyst was loaded into the reactor and calcined at 773 K for 6 h in a flow of Ar at 30 cm^3 (STP)/min, followed by TPR at 10 K/min to a final temperature of 673 K in a 30 cm^3 (STP)/min flow of 10 % H_2 in Ar, holding the final temperature for 1 h. The catalyst was then flushed in a 30 cm^3 (STP)/min flow of Ar for 1 h and cooled to room temperature, before being exposed to a 50 cm^3 (STP)/min flow of 10 % CO in He at 313 K for 1 h. The catalyst was subsequently flushed in 50 cm^3 (STP)/min He for 2 h. The temperature-programmed desorption was then started in the same He flow by heating the sample to 773 K at a rate of 10 K/min and holding the final temperature for 1 h.

The catalysts were also characterized by high-resolution transmission electron microscopy (HRTEM), scanning electron microscopy (SEM) and energy dispersive X-ray analysis (EDX). SEM, EDX and EDX-mapping were done using a variable pressure 120 keV Hitachi S-3000N equipped with a light element EDX detector. A FEI Tecnai G2 200 keV with a LaB6 filament capable of 1.4 $\AA$ point-to-point resolution was used for high resolution transmission electron microscopy (HRTEM). Pd/SiO_2 samples with variable Pd loadings were ground to a fine powder using an agate mortar and pestle and dispersed in ethanol ultrasonically. A droplet of the suspension was then put on a 200 mesh copper grid with formvar carbon coating. The sample was left to dry before analysis.

4.2.3 Catalyst activity

The dodecahydro-N-ethylcarbazole reactant was prepared by hydrogenation of N-ethylcarbazole at 423 K and a H_2 pressure of 7 MPa using a 300 cm^3 autoclave batch reactor, as previously discussed in Chapter 2.

The dehydrogenation reactions were carried out in a 50 cm^3 glass flask reactor at stirring speed of 550 rpm, operated in batch mode at 443 K and 101 kPa using the reduced Pd/SiO_2 catalysts. For each experiment, 10 cm^3 of the product recovered from N-ethylcarbazole hydrogenation was diluted in 20 cm^3 of decalin (Sigma-Aldrich, 98 %), and added to the reactor as reactant of the dehydrogenation reaction. The reactor was stirred and heated to the desired temperature while purging in He flow at 171 cm^3 (STP)/min. Once the reaction temperature was reached, the catalyst was injected into the reactor using a syringe. The He flow was maintained and acted as a carrier gas for continuous removal of the produced hydrogen. The reactor exit gas composition was continuously monitored using a quadrupole mass spectrometer (SRC Residual Gas Analyzer, 200 amu). Liquid samples of $\sim$0.1 cm^3 were withdrawn from the reactor periodically and analysed using a Shimadzu QP-2010S GC/MS and a Restek RTX5 30 m 0.25 mm capillary column. Internal mass transfer effects were minimal because of the small catalyst particle size and confirmed by the calculated Weisz-Prater criterion of $\Phi < 1.0$ at the reaction temperature.

4.3 Results

4.3.1 Catalyst properties

H_2 TPR profiles of the 0.5 wt %, 10 wt % He-calcined, and 10 wt % air-calcined Pd/SiO_2 catalysts are presented in Figure 4.1.

A negative peak in all the TPR profiles, indicative of a net H_2 evolution from the sample rather than H_2 consumption, was observed at temperatures between 333 - 360 K. Babu et al. [112] reported very similar H_2 TPR profiles for 5 wt % and 3 wt % Pd/alumina catalysts, where H_2 evolution from the Pd in the region 348 - 373 K, was observed. In work by Amairia et al. [113], H_2 TPR profiles from Pd/Al_2O_3-ZrO_2 also showed H_2 evolution at 358 K. The H_2 profile is consistent

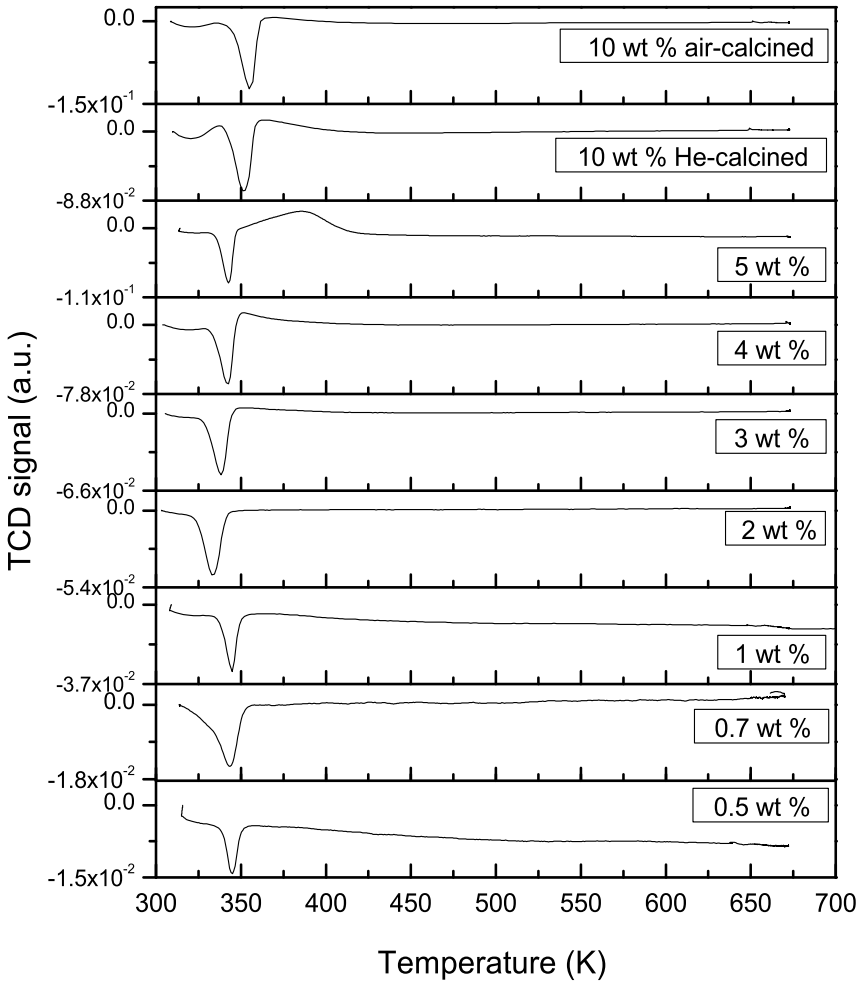

Figure 4.1: TPR patterns of SiO_2 supported Pd catalysts.

with the release of H_2 from the decomposition of a β-palladium hydride phase which is reported to form at room temperature over large Pd particles ($>$ 2 nm) [99, 100, 112–115] and in the present work, was likely generated during the low temperature flush in 10 % H_2 in He for 30 min that followed catalyst calcination.

Figure 4.2 and Figure 4.3 compare the effluent gas profiles as measured by mass spectrometer during the thermal treatment of the silica gel support and the catalyst precursors.

The silica gel and the 10 wt % Pd/SiO_2 precursor, were calcined at 773 K in He (Figure 4.2-a and 4.2-b, respectively) or air (Figure 4.3-a and 4.3-b, respectively). The He-calcined and the air-calcined 10 wt % Pd/SiO_2 catalyst precursors were then flushed in 10 % H_2 in He at room temperature (Figure 4.2-c and Figure 4.3-c), and reduced in the same flow of gas by temperature programming to 673 K at 10 K/min (Figure 4.2-d and Figure 4.3-d). Calcination of the silica gel in He (Figure 4.2-a) resulted in the production of two water peaks at about 425 K and 773 K. The two water peaks were also observed during the calcination of the silica gel in air at approximately 500 K and 773 K (Figure 4.3-a). Comparing the calcination of the Pd/SiO_2 in He or air (Figure 4.2-b and Figure 4.3-b, respectively), shows that a sharp peak between 423 - 500 K and a second broader peak at 773 K for water evolution were observed for both samples. HCl evolution was also detected for the catalyst calcined in He with a peak temperature at 773 K (Figure 4.2-b), whereas no HCl was observed for the sample calcined in air (Figure 4.3-b). Subsequent flushing of the catalysts in a flow of 10 % H_2 in He at room temperature resulted in the production of water and HCl from both catalysts, with more HCl observed for the catalyst calcined in He (Figure 4.2-c) compared to the one calcined in air (Figure 4.3-c). The catalyst flush steps were followed by TPR in a flow of 10 % H_2 in He at 20 K/min to 673 K which revealed a significant production of HCl (especially for the catalyst calcined in He) as well as water. For the Pd/SiO_2 calcined in He, the peak in water evolution occurred at 488 K and the peak in HCl evolution occurred at 578 K (Figure 4.2-d). For the air calcined sample, the corresponding peak temperatures were 520 K and 620 K, respectively (Figure 4.3-d).

Table 4.1 summarizes the properties of the catalysts prepared in the present study (i.e. 0.5 wt % - 10 wt % Pd/SiO_2 prepared by calcination in He and the 10 wt % Pd/SiO_2 catalyst prepared by calcination in air), and the 5 wt % Pd/SiO_2

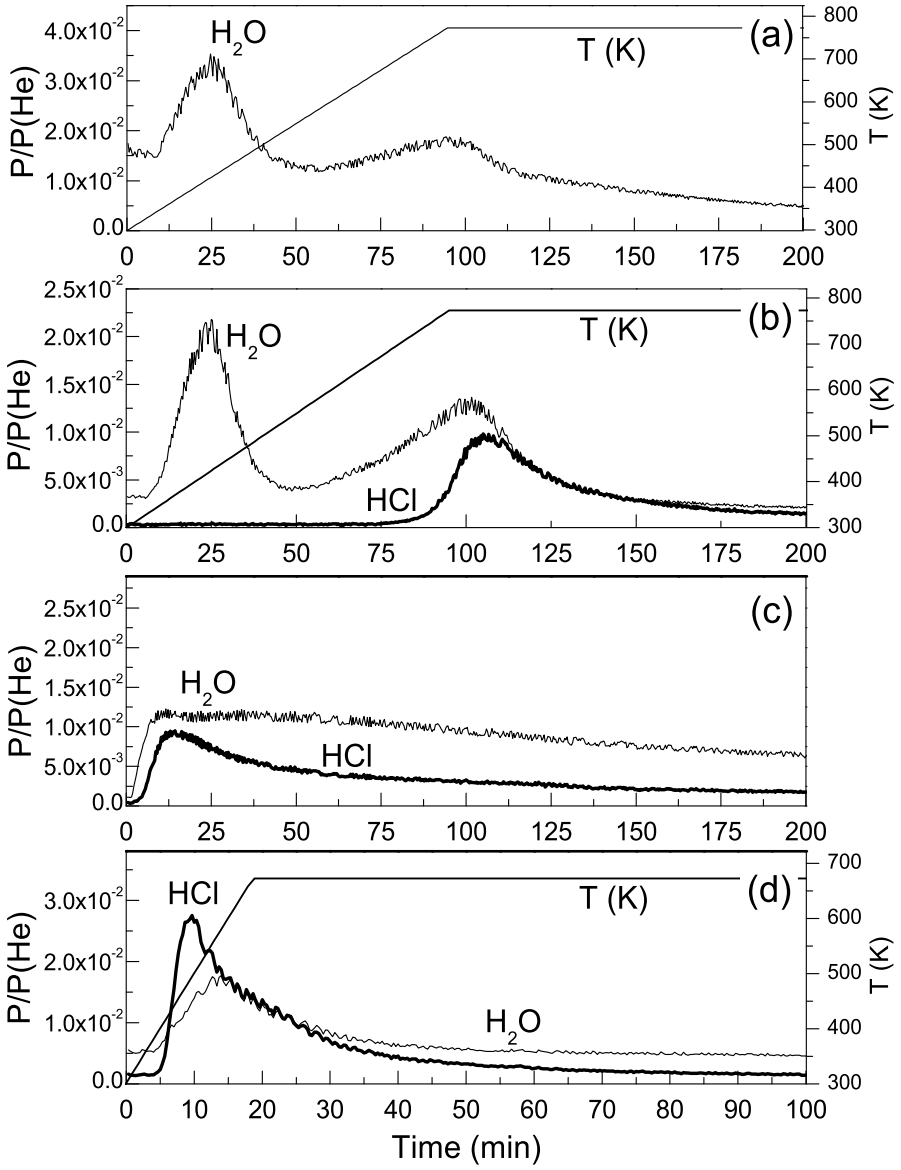

Figure 4.2: Profile of effluent gases during thermal treatment of catalyst samples in He as measured by mass spectrometer using 0.4 g of sample. (a) SiO_2 gel calcination in He at 773 K, (b) 10 wt % Pd/SiO_2 calcination in He at 773 K, (c) 10 wt % Pd/SiO_2 flush in 10 % H_2 in He at room temperature, (d) 10 wt % Pd/SiO_2 reduction in 10 % H_2 in He at 673 K.

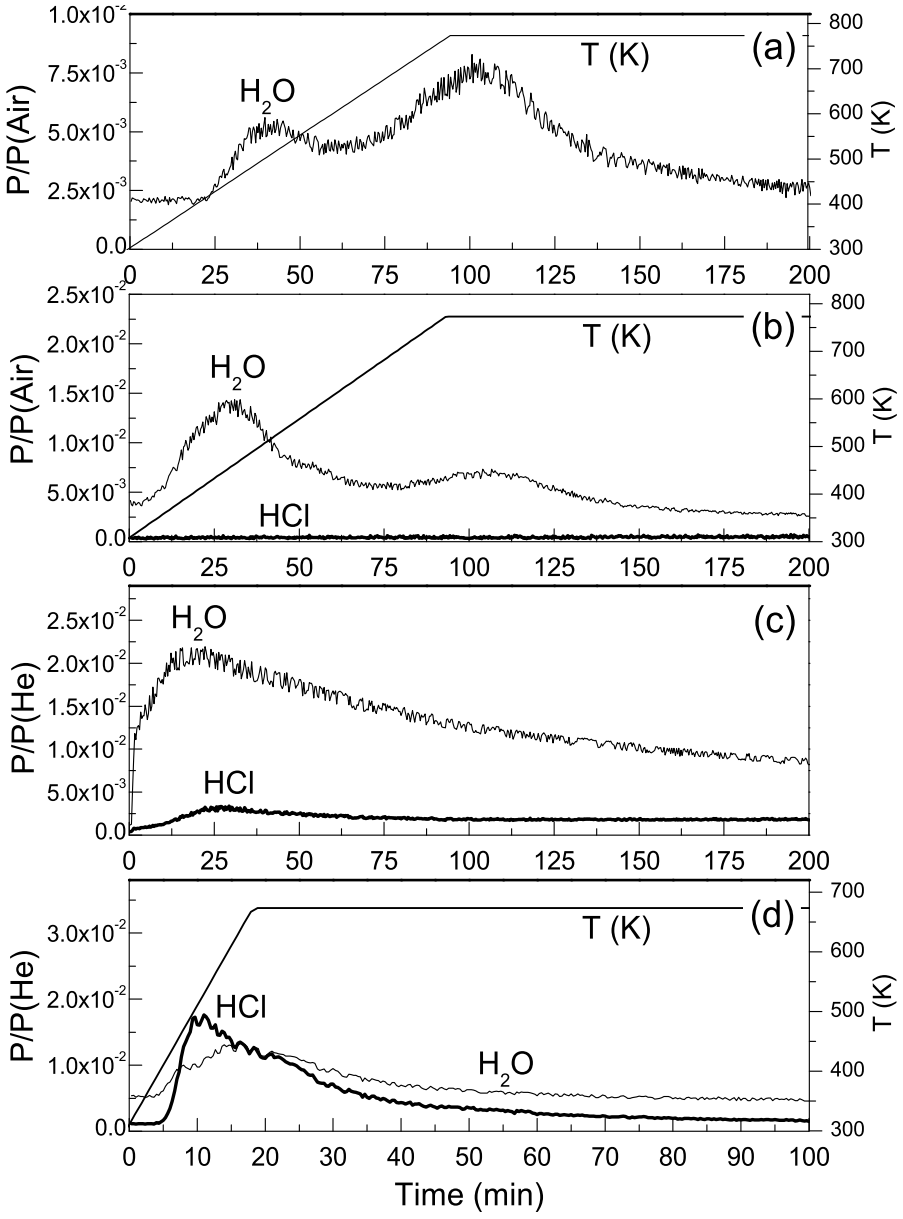

Figure 4.3: Profile of effluent gases during thermal treatment of catalyst samples in air as measured by mass spectrometer using 0.4 g of sample. (a) SiO_2 gel calcination in air at 773 K, (b) 10 wt % Pd/SiO_2 calcination in air at 773 K, (c) 10 wt % Pd/SiO_2 flush in 10 % H_2 in He at room temperature, (d) 10 wt % Pd/SiO_2 reduction in 10 % H_2 in He at 673 K.

catalyst prepared by wet impregnation and calcination in air, reported by Sotoodeh et al. [106].

Table 4.1: Pd/SiO_2 catalyst properties

Pd (wt %)	CO desorbed (μmol.g^{-1})	Dispersion (%)	Pd particle size[a] (nm)	Average Pd particle diameter (nm)
0.5	20.9	51.9	1.9	3.6[b] $\pm$ 0.1[c]
0.7	25.3	44.7	2.2	4.0 $\pm$ 0.2
1	22.5	28.3	3.6	4.6 $\pm$ 0.2
2	25.7	16.0	6.3	6.1 $\pm$ 0.1
3	31.0	12.9	7.7	7.0 $\pm$ 0.1
4	34.4	11.0	9.1	7.3 $\pm$ 0.4
5	30.3	7.9	12.5	13.2 $\pm$ 0.9
10	53.1	6.5	15.4	15.5 $\pm$ 0.7
10[d]	—	3.6[e]	27.9[e]	23.7 $\pm$ 2.7
5[d]	—	4.2[e]	23.8 [e]	—

[a] obtained from CO TPD analysis.
[b] Average Pd particle size obtained by fitting HRTEM data to a log-normal distribution.
[c] Standard deviation of average particle size obtained from the log-normal fit.
[d] reduced after calcination in air.
[e] obtained by CO pulse chemisorption.

Figure 4.4 shows the results obtained from the temperature programmed desorption (TPD) of CO from the Pd/SiO_2 catalysts. The major desorption peak occurred at 343 - 362 K, in good agreement with the desorption peak temperature of 320 - 350 K reported by Myyrylainen et al. [116] for the TPD of CO from a Pd(100) surface.

The CO uptake determined from the TPD experiments was used to estimate the catalyst dispersion at each Pd loading, as well as the Pd particle diameter, assuming a CO:Pd adsorption stoichiometry of 1:1 [98]. The results, summarized in Table 4.1, show that the Pd particle size of the Pd/SiO_2 catalysts varied from 2 - 15 nm as the Pd loading increased from 0.5 wt % to 10 wt %. By comparing these results to the 10 wt % and the 5 wt % Pd/SiO_2 [106, 107] catalysts calcined in air and shown in Table 4.1, it is clear that a significant increase in the dispersion of the Pd catalysts was obtained by calcination in He rather than air. The particle size decreased from 27.9 nm to 15.4 nm for the 10 wt % Pd/SiO_2 by calcining the catalyst in He rather

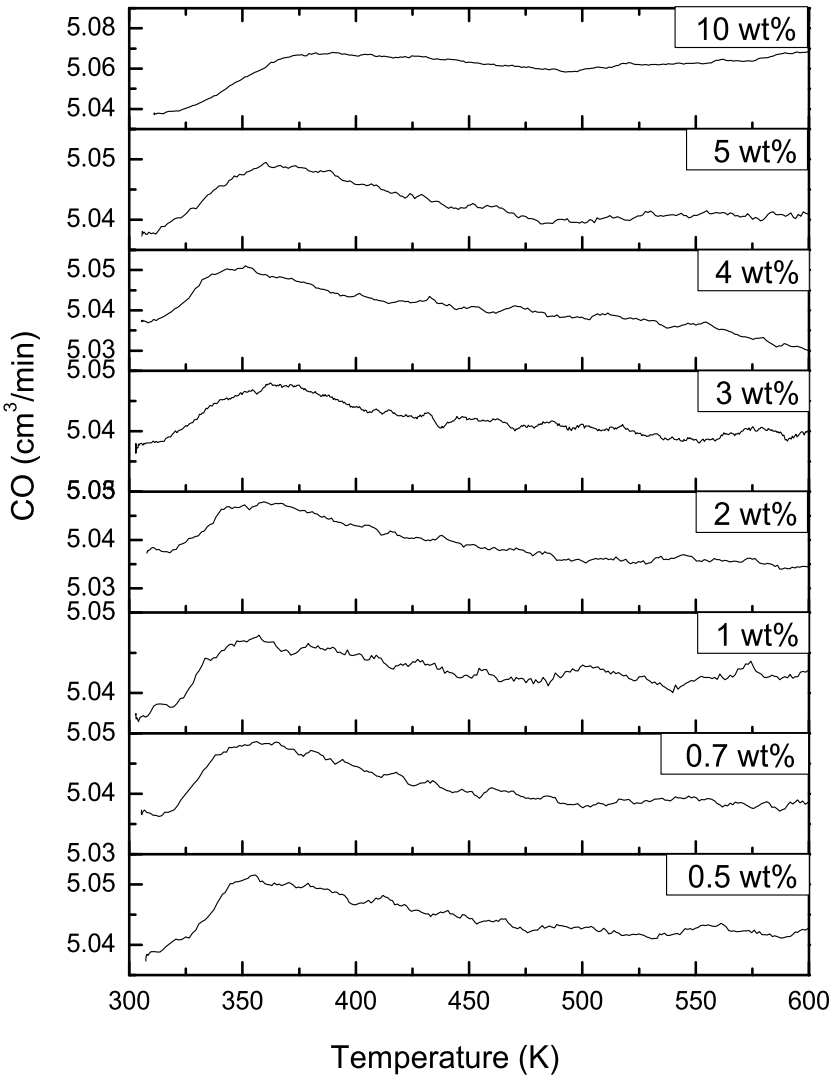

Figure 4.4: Temperature programmed desorption (TPD) of CO from Pd/SiO_2 catalysts with different Pd loadings at a heating rate 10 K/min.

than air. The 5 wt % Pd/SiO_2 calcined in He had a Pd metal dispersion of 7.9 %, almost twice the value of 4.2 % obtained for the 5 wt % Pd/SiO_2 catalyst prepared by calcination in air [106, 107].

The reduced and calcined Pd/SiO_2 samples were analyzed by SEM and EDX to investigate the catalyst morphology, as well as the elemental composition. Table 4.2 summarizes the EDX elemental analysis of the 5 wt % Pd/SiO_2 catalysts, reported as the average of at least 10 point analyses, after various thermal treatments.

Table 4.2: EDX elemental analysis of the 5 wt % Pd/SiO_2 catalysts

Status	Reduced after He calcination	Reduced after air calcination	Calcined in He	Calcined in air
Element	Concentration (wt %)			
Oxygen	56.3 ± 3.1	57.8 ± 0.2	52.4 ± 0.4	57.6 ± 0.3
Silicon	38.6 ± 1.9	35.9 ± 0.2	37.9 ± 1.3	37.7 ± 0.1
Chlorine	0.00 ± 0.00	0.03 ± 0.01	0.8 ± 0.1	1.0 ± 0.1
Palladium	5.1 ± 1.9	6.2 ± 0.1	8.8 ± 1.2	3.7 ± 0.2

Calcination in He or air at 773 K for 6 h did not remove all the Cl present in the precursor and Cl was identified after calcination in He or air. However, as shown in Table 4.2, no Cl was present after TPR of the sample calcined in He, whereas a small amount of Cl was detected after the TPR of the sample calcined in air.

Further insight into the size distribution of the Pd/SiO_2 catalysts was obtained by high resolution transmission electron microscopy (HRTEM) of the reduced Pd/SiO_2 catalysts as summarized in Table 4.1. Figure 4.5-a,b,c shows selected HRTEM images of the reduced 10 wt %, 4 wt % and 0.5 wt % Pd/SiO_2 catalysts, respectively.

The Pd size distribution obtained from several HRTEM images were fitted to a log-normal distribution to obtain an estimate of the average Pd particle diameter and standard deviation with Pd loading. The results, reported in Table 4.1, showed good agreement with the values calculated from the CO TPD data.

4.3.2 Catalyst activities

Dehydrogenation of the dodecahydro-N-ethylcarbzole was carried out over each of the reduced Pd/SiO_2 catalysts. The reactor was operated at 443 K and 101 kPa. Decalin was used as the solvent in the dehydrogenation reaction. The stability of

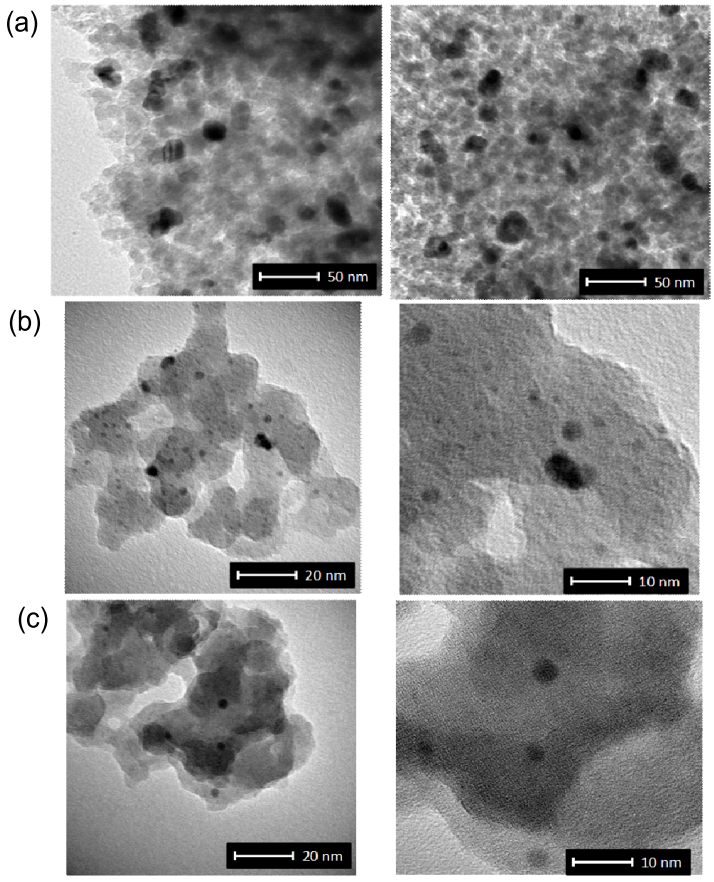

Figure 4.5: Selected HRTEM images of reduced Pd/SiO_2 samples: (a) 10 wt % Pd, (b) 4 wt % Pd, (c) 0.5 wt % Pd. Samples were calcined in He flow at 773 K for 6 h prior to reduction in H_2 at 673 K for 1 h.

decalin at reaction temperatures below 473 K over Pd/SiO_2 catalysts were confirmed in previous studies [57, 58, 106]. Figures 4.6, 4.7 and 4.8 show the product distribution as a function of reaction time obtained from the GC/MS liquid sample analysis of the dehydrogenation products.

The data show that octahydro-N-ethylcarbazole and tetrahydro-N-ethylcarbazole were the primary products of the reaction, and the reactions proceeded with further conversion of these two intermediates and the production of the completely dehydrogenated product, N-ethylcarbazole, which can be shown by the following,

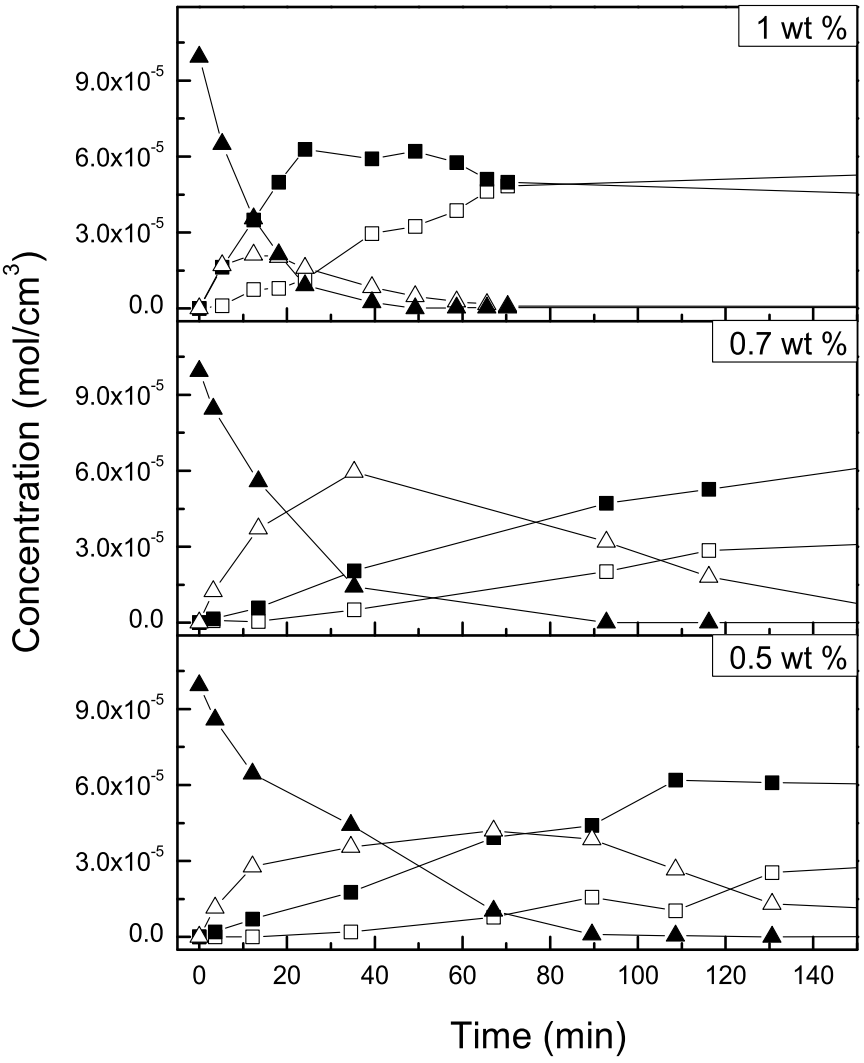

Figure 4.6: Product distribution from dodecahydro-N-ethylcarbazole dehydrogenation at 443 K and 101 kPa over Pd/SiO_2 with Pd loading of 0.5, 0.7 and 1 wt %; (▲) dodecahydro-N-ethylcarbazole, (△) octahydro-N-ethylcarbazole, (■) tetrahydro- N-ethylcarbazole, (□) N-ethylcarbazole.

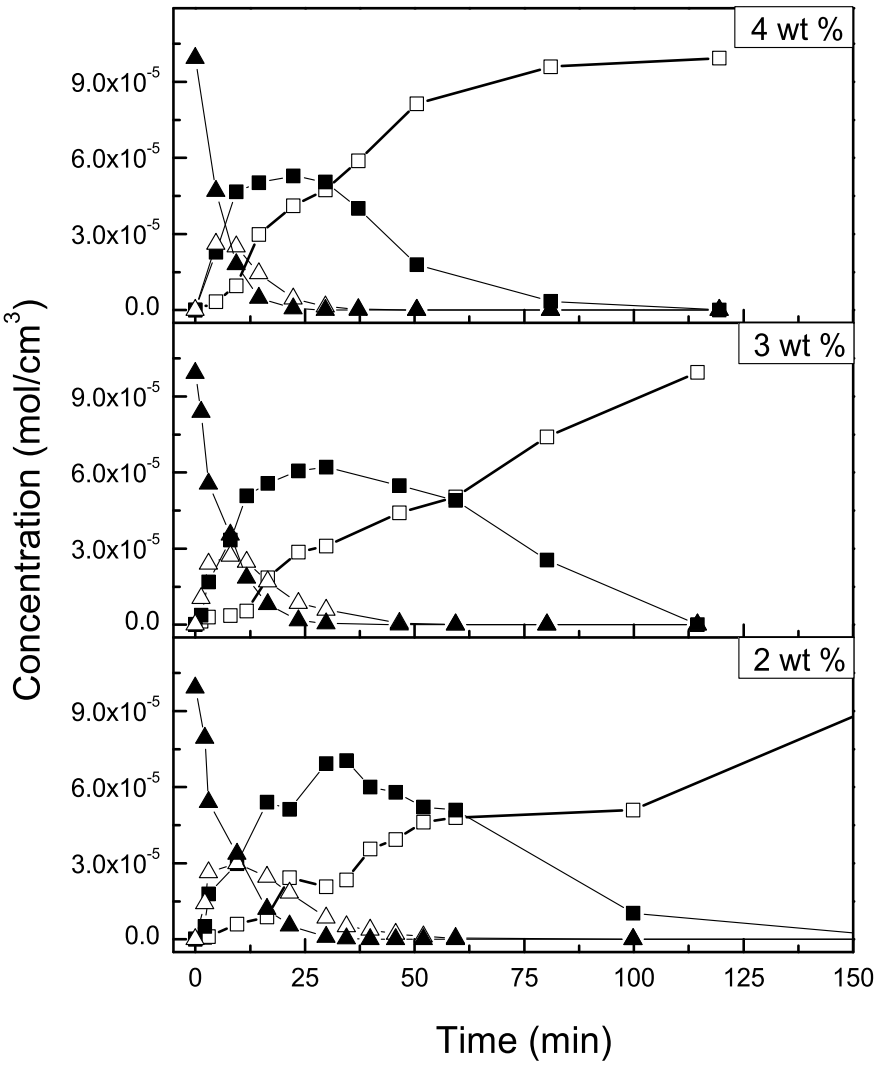

Figure 4.7: Product distribution from dodecahydro-N-ethylcarbazole dehydrogenation at 443 K and 101 kPa over Pd/SiO_2 with Pd loading of 2, 3 and 4 wt %; (▲) dodecahydro-N-ethylcarbazole, (△) octahydro-N-ethylcarbazole, (■) tetrahydro- N-ethylcarbazole, (□) N-ethylcarbazole.

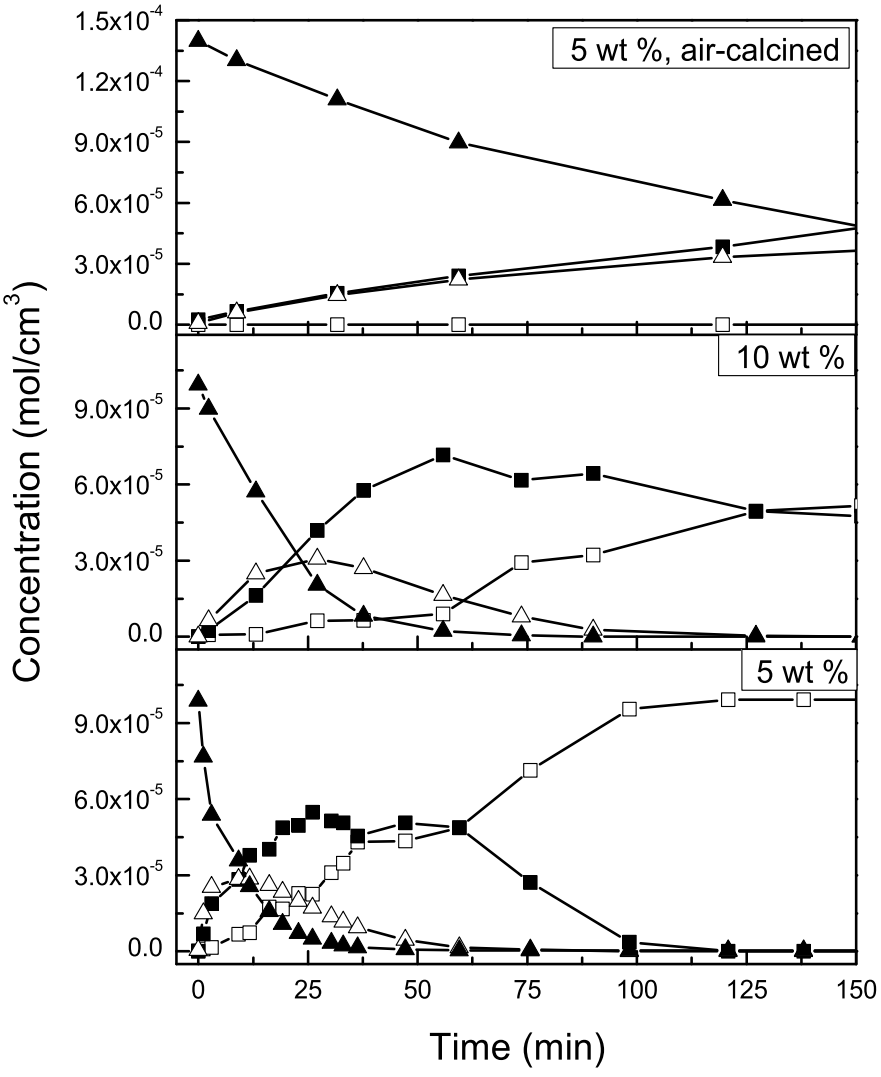

Figure 4.8: Product distribution from dodecahydro-N-ethylcarbazole dehydrogenation at 443 K and 101 kPa over Pd/SiO_2 with Pd loading of 5, 10 and 5 wt % (air calcined) [106]; (▲) dodecahydro-N-ethylcarbazole, (△) octahydro-N-ethylcarbazole, (■) tetrahydro- N-ethylcarbazole, (□) N-ethylcarbazole.

$$C_{14}H_{25}N \rightarrow C_{14}H_{21}N + 2H_2 \rightarrow C_{14}H_{17}N + 2H_2 \rightarrow C_{14}H_{13}N + 2H_2 \qquad (4.1)$$

Comparing the product distributions in Figures 4.6, 4.7 and 4.8 as a function of the catalyst Pd loading, it is clear that the same intermediates and products were identified for each catalyst. However, the product selectivity was dependent upon the Pd loading and hence the Pd particle size, and in no case was hexahydro-N-ethylcarbazole nor decahydro-N-ethylcarbazole (two other possible hydrogenation reaction intermediates) observed. More importantly, the catalysts prepared by calcination in He were remarkably selective to the completely dehydrogenated compound, N-ethylcarbazole. As shown by the data of Figures 4.6 and 4.7, increased Pd loading from 0.5 - 4 wt %, corresponding to an increase in Pd particle size from 2 - 9 nm, resulted in a significant increase in the catalyst selectivity to the N-ethylcarbazole product. The consumption of octahydro-N-ethylcarbazole and tetrahydro-N-ethylcarbazole was much slower for the 0.5 wt % and 0.7 wt % catalysts. As seen in Figure 4.6, no consumption of tetrahydro-N-ethylcarbazole was observed in the first 120 min of the reaction. However, complete conversion of the two intermediates, octahydro-N-ethylcarbazole and tetrahydro-N-ethylcarbazole, to N-ethylcarbazole was obtained within about 95 min over the 4 wt % Pd/SiO_2 (Figure 4.6). The selectivity to N-ethylcarbazole decreased with a further increase in the Pd loading to 5 wt % and 10 wt %, corresponding to Pd particle diameters of 13 - 15 nm (Figure 4.8). These results are compared to the low selectivity observed over the Pd/SiO_2 prepared by calcination in air with a Pd particle size of 25 nm (Figure 4.8), reported previously [106].

The measured consumption of the reactant dodecahydro-N-ethylcarbazole as a function of time was fitted to a 1^{st}-order kinetic model and the estimated rate constants are reported in Table E.5. Initial turn-over frequencies (TOFs) with respect to the consumption of dodecahydro-N-ethylcarbazole were calculated using the estimated 1^{st}-order rate constants and the initial concentration of reactant used in the experiments, as follows:

$$TOF = (k.AW_{Pd}.C_{A0})/(M_{Pd}.D) \qquad (4.2)$$

where k is the 1^{st}-order rate constant for dodecahydro-N-ethylcarbazole consumption (L.min^{-1}.g$_{cat}$$^{-1}$), AW$_{Pd}$ is the atomic mass of Pd (g.mol^{-1}), C$_{A0}$ is the reactant initial concentration (mol.cm^{3} $^{-1}$), M$_{Pd}$ is the Pd loading (wt %) and D is the Pd dispersion (%).

Table 4.3: First order rate constants and turn-over frequencies (TOFs) for dehydrogenation of dodecahydro-N-ethylcarbazole at 443 K and 101 kPa over Pd/SiO_2 catalysts with different Pd loadings.

Pd (wt %)	Rate constant[a] (min^{-1})	Rate constant[a,b] (L.min^{-1}.g$_{cat}$$^{-1}$)	Initial concentration (mol.cm^{3} $^{-1}$)	TOF[c] (min^{-1})
0.5	0.0457 ± 0.0033	0.0036	9.9350×10^{-5}	14.67
0.7	0.0535 ± 0.0023	0.0049	9.9350×10^{-5}	16.32
1	0.0935 ± 0.0022	0.0134	9.9350×10^{-5}	50.43
2	0.1496 ± 0.0048	0.0374	9.9272×10^{-5}	123.45
3	0.1668 ± 0.0047	0.0626	9.9260×10^{-5}	169.39
4	0.2148 ± 0.0082	0.0921	9.9350×10^{-5}	221.16
5	0.1139 ± 0.0015	0.0683	9.8764×10^{-5}	179.54
10	0.0618 ± 0.0034	0.0618	9.9350×10^{-5}	100.50
5[d]	0.0075 ± 0.0002	0.0045	1.3969×10^{-4}	31.85

[a] with respect to dodecahydro-N-ethylcarbazole consumption.
[b] for sample calculation, see Appx. E.
[c] molecule dodecahydro-N-ethylcarbazole.min^{-1}.Pd surface atom^{-1}.
[d] Reported previously by Sotoodeh et al. [106].

It is seen from Table E.5 that the reaction rate constant based on catalyst concentration increased significantly from 0.0036 L.min^{-1}.g$_{cat}$$^{-1}$ for the 0.5 wt % catalyst to 0.0921 L.min^{-1}.g$_{cat}$$^{-1}$ for the 4 wt % catalyst, and decreased to 0.0618 L.min^{-1}.g$_{cat}$$^{-1}$ with a further increase in Pd loading to 10 wt %. The same trends were observed for the TOF of the reaction, where the 4 wt % catalyst resulted in the highest TOF of 221.2 min^{-1} for the consumption of dodecahydro-N-ethylcarbazole. The catalysts with 0.5 wt % and 0.7 wt % Pd loading resulted in the lowest values of the reaction rate constants and TOFs. Figure 4.9 plots the dodecahydro-N-ethylcarbazole dehydrogenation TOFs versus the Pd particle size for all the Pd/SiO_2 catalysts of the present study. From Figure 4.9 it follows that the catalyst with a Pd particle size of about 9 nm, corresponding to the 4 wt % Pd/SiO_2 catalyst, had the highest TOF. On the other hand, decreasing the particle size to about 2 nm with the 0.5 wt % Pd catalyst resulted in a significant reduction

in the TOF. Furthermore, an increase in the Pd particle size to about 12.5 nm with the 5 wt % and 15 nm with the 10 wt % catalysts, as well as the previously reported 24 nm with the 5 wt % catalyst prepared by calcination in air [106, 107], showed a decrease in the reactant consumption TOF.

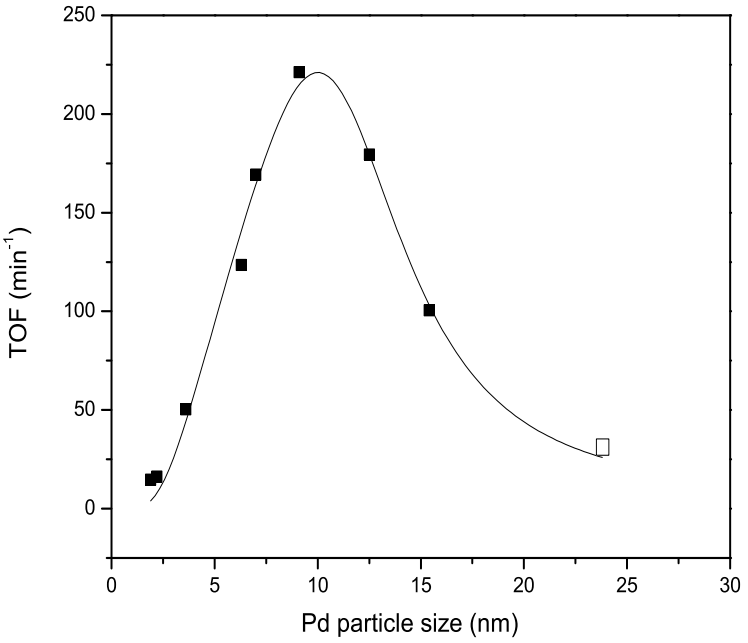

Figure 4.9: TOFs for dodecahydro-N-ethylcarbazole dehydrogenation at 443 K and 101 kPa over Pd/SiO_2 catalyst with different Pd metal particle size. The open data point represents the TOF over the 5 wt % Pd/SiO_2 reported by Sotoodeh et al. [106, 107]. The solid line represents the data fit using Murzin's model [117]. The fitted parameter values were: P_1 = 1.394±1.189, P_2 = 0.0020±0.0016, γ = 81.60±12.01 and α = 0.124±0.030, with R^2 = 97.7 %.

Catalyst selectivity to N-ethylcarbazole at 50 % reactant conversion, as well as the selectivity after 1 h reaction at 443 K and 101 kPa over the different Pd/SiO_2 catalysts, is summarized in Table 4.4. At 50 % conversion, a maximum selectivity of 15.3 % to N-ethylcarbazole was obtained in 4 min over the 4 wt % Pd/SiO_2.

Table 4.4: Comparison of the selectivity to N-ethylcarbazole and the conversion of dodecahydro-N-ethylcarbazole at 443 K and 101 kPa over Pd/SiO_2 catalysts calcined in He.

Pd (wt %)	Selectivity to N-ethylcarbazole at 50 % reactant conversion (%)	Reaction time to obtain 50 % conversion (min)	Selectivity to N-ethylcarbazole at 1 h (%)
0.5	3.1	27.9	8.8
0.7	3.0	17.0	14.2
1	4.7	9.5	39.0
2	9.0	5.0	48.3
3	9.5	4.7	50.8
4	15.3	3.8	94.8
5	11.1	5.5	49.6
10	5.5	16.1	17.9

The selectivities at 50 % reactant conversion, shown in Table 4.4, demonstrate that increasing the Pd loading from 0.5 wt % to 4 wt % and accordingly increasing the Pd metal particle diameter from 2 nm to 9 nm, increased the observed selectivity to the completely dehydrogenated product, N-ethylcarbazole. With a further increase in Pd particle size a decrease in the selectivity to N-ethylcarbazole was observed. The selectivity to N-ethylcarbazole decreased to 11.1 % and 5.5 % for the 5 wt % and the 10 wt % catalysts, respectively (Table 4.4). Complete conversion of the reactant was achieved in 22 min over the 4 wt % catalyst, with 95 % selectivity to N-ethylcarbazole during the first hour of reaction.

The H_2 recovery profile of the dehydrogenation of dodecahydro-N-ethylcarbazole at 443 K and 101 kPa over the 4 wt % Pd/SiO_2 is compared to the 5 wt % Pd/SiO_2 reported previously [106] in Figure 4.10. The dramatic increase in the evolved H_2, observed using the 4 wt % Pd/SiO_2 catalyst, is clear with the H_2 recovery completed within 96 min. Complete conversion of the reactant was obtained in only 22 min.

Table 4.5 summarizes the H_2 recovery results obtained for all of the Pd catalysts.

Complete H_2 recovery, equal to the theoretical amount of 5.8 wt %, was obtained in 1.6 h using the 4 wt % Pd/SiO_2 catalyst. These results are excellent compared to the 17 h required for complete conversion reported previously over

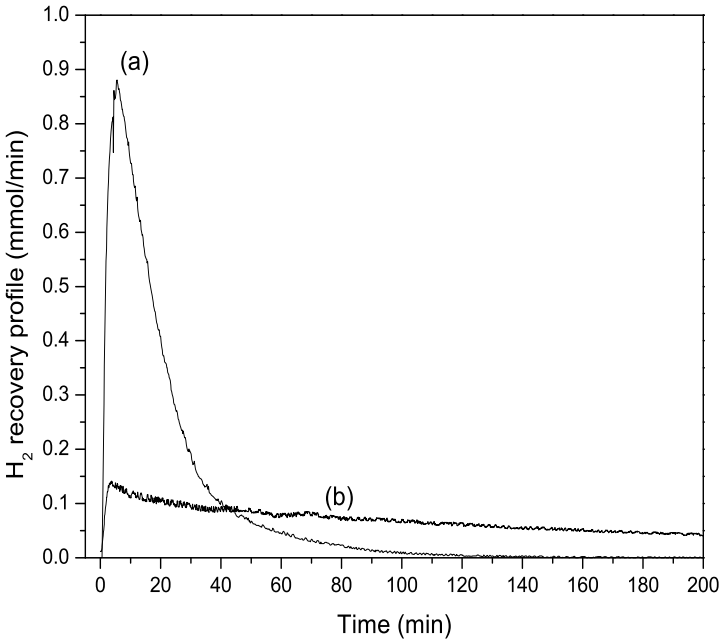

Figure 4.10: H_2 recovery comparison for dodecahydro-N-ethylcarbazole dehydrogenation at 443 K and 101 kPa (a) over 4 wt % Pd/SiO_2 prepared by calcination in He (b) over 5 wt % Pd/SiO_2 calcined in air and reported previously [106].

the 5 wt % Pd/SiO_2 with 4.2 % metal dispersion [106]. The results demonstrate that the 4 wt % Pd/SiO_2 catalyst with average particle diameter of 9 nm and 11 % Pd metal dispersion was the most active catalyst among those examined for the dehydrogenation of dodecahydro-N-ethylcarbazole.

4.4 Discussion

4.4.1 Catalyst properties

The water peaks observed during temperature-programmed calcination of silica gel in He or air at 373 - 473 K (Figure 4.2 and 4.3) are ascribed to the removal

Table 4.5: H_2 recovery for the dehydrogenation of dodecahydro-N-ethylcarbazole at 443 K and 101 kPa over Pd/SiO_2 with different Pd loadings.

Pd (wt %)	H_2 recovery[a,b] in 1 h, (wt %)	Final H_2 recovery (wt %)
0.5	2.5	3.8 (6 h)[c]
0.7	3.1	4.4 (6 h)
1	3.3	5.2 (6 h)
2	4.7	5.8 (2.7 h)
3	4.8	5.8 (1.9 h)
4	5.4	5.8 (1.6 h)
5	4.7	5.8 (3 h)
10	4.0	5.8 (6 h)
5[d]	1.1	4.0 (17 h)

[a]Mass of H_2 released divided by the initial mass of dodecahydro-N-ethylcarbazole
[b]Theoretical H_2 recovery of dodecahydro-N-ethylcarbazole is 5.8 wt %.
[c]Experimental time to achieve the H_2 recovery reported.
[d]Reported by Sotoodeh et al. [106, 107]

of surface and micropore-absorbed water [118, 119], whereas the water loss at higher temperature (773 K) is ascribed to water loss from hydrogen-bonded silanol groups. The latter assignment follows work by Li et al. [119] who reported an infrared (IR) analysis of silica gel as temperature was increased to 773 K. The intensity of a band at 3650 cm^{-1}, related to hydrogen-bonded silanol groups, decreased with increased temperature, whereas a band at 3720 cm^{-1}, related to free silanol groups, increased slightly due to the conversion of some of the hydrogen-bonded silanol groups absorbing at 3650 cm^{-1} into free silanol groups absorbing at 3720 cm^{-1} plus water.

The preparation of Pd catalysts supported on Al_2O_3 [120] and SiO_2 [121] using $PdCl_2$ as the precursor has been well studied. $PdCl_4{}^{2-}$ results when $PdCl_2$ is dissolved in acidic solutions [122] and Contescu et al. [120] have shown that the $PdCl_4{}^{2-}$ is partially hydrolysed in solution to yield $PdCl_2(H_2O)^-$ and $PdCl_2(H_2O)_2$ species. These species adsorb electrostatically onto acidified alumina. In the present work, the impregnation was conducted at low pH (< 2), below the isoelectric point of silica, so that a similar electrostatic adsorption on $SiOH_2{}^+$ can be expected. When the impregnated alumina was dried in air at 385 K for 3 h, Contescu et al. [120] demonstrated that $PdCl_4$ (70 - 75 %) and $PdCl_xO_y$ (25 - 30

%) were generated as a consequence of dehydration of the hydrolysed $PdCl_4^{2-}$ and reaction with atmospheric oxygen. Calcination at higher temperature (up to 925 K) in air resulted in further oxidation of the precursor, yielding PdO_x (35 - 45 %) and an increased amount of $PdCl_xO_y$ (55 - 65 %). The presence of $Pd_xO_yCl_z$ species on Pd/Al_2O_3 catalysts has been identified in other studies [112]. Vilarrasa-García et al. [123] detected the formation of metallic Pd and palladium oxychloride by XPS of activated carbons impregnated with $PdCl_2$ and dried in He at 393 K for 6 h. Palladium oxychloride species were also identified by XPS of air-calcined Pd catalysts before reduction in H_2 by Normand et al. [124]. The TPR data of Figure 4.3 are consistent with these same transformations of the precursor impregnated on silica. Accordingly, H_2O was released at ∼460 K and a second peak was observed at 773 K (Figure 4.3). The two H_2O peaks likely correspond to the water removal from the silica support as discussed earlier, as well as dehydration of two different hydrolysed Pd-species, as identified by Contescu et al. [120]. Of most significance, however, is the fact that no HCl (nor any other chlorinated products), were observed during the air drying and calcination of the catalyst precursors. This implies that the Pd precursors did not lose Cl during drying and calcination in air, and the catalyst precursor, following drying, must be mostly PdO_xCl_y species, such as the $PdClO_4$ and $PdCl_2O_3$ identified on Pd/alumina precursors following similar drying and calcination steps [120]. Furthermore, there was no colour change observed following calcination of the Pd/SiO_2 catalyst precursor in air, indicative of PdO_xCl_y species rather than PdO_x.

In contrast, Figure 4.2 shows that when the impregnated silica was dried and calcined in inert He, a significant amount of HCl was detected, suggesting that reactions of the type $PdCl_2 + H_2O \rightarrow PdO + 2\ HCl$ occurred, rather than the oxidations that occurred in air to yield PdO_xCl_y. In this instance the samples recovered after calcination were black, indicative of PdO_x species. The TPR profile also shows that only one peak was observed for the HCl evolution, and this occurred at a temperature very similar to the second peak temperature for water evolution (∼773 K). The profile is consistent with the dehydration of the hydrolysed Pd-precursors as already mentioned, and indicates that the removal of the Cl likely only occurs from $PdCl_2$ or $PdCl_4^{2-}$ species, rather than hydrolysed Pd species.

Following calcination, the precursors were flushed in H_2 at room temperature

before being reduced according to the TPR protocol already described. HCl and H_2O were both evolved from the catalysts during the hydrogen flush and the TPR, confirming the reduction of the precursors to Pd^0 during both processes. The reduction of $PdCl_2$ at room temperature has been previously reported [125, 126]. Although the reduction profiles for the He and air calcined samples were very similar, for both the flush and the TPR, the sample calcined in He evolved more HCl, indicative of the easier reduction of $PdCl_2$ and PdO_x species on the He calcined sample than the reduction of PdO_xCl_y species present on the air calcined sample [120].

Different stoichiometry for CO adsorption on supported Pd has been reported in the literature [98]. The difference observed in Table 4.1 between the CO TPD and the HTREM results can be explained by the possible change in the stoichiometry for CO adsorption on Pd sites as the metal particle size increases. As reported in Table 4.1, catalyst dispersion was significantly increased for the catalysts prepared by calcination in He, compared to the catalyst prepared by wet impregnation and calcination in air [106, 107]. The effect of pre-treatment on Pd catalyst dispersion has been reported previously by Zou et al. [121] where an increase in Pd dispersion was observed by calcination in a noble gas instead of O_2. The lower dispersion in the latter case was attributed to the competitive interaction between Pd and the oxygen in the support versus Pd and the gas phase oxygen, that resulted in a partial weakening of the metal-support interaction and agglomeration of the Pd. In the present work, the improved dispersion is more likely a consequence of the different precursors that result from calcination in air (PdO_xCl_y) versus He (PdO_x). The Pd oxychloride is known to be more difficult to reduce than the PdO_x [120] and the data of Figure 4.2 and Figure 4.3 show that the peak reduction temperature was about ~ 40 K higher for the air calcined sample than the He calcined sample. During the calcination process in He, both Cl and H_2O are lost from the Pd precursor, and this likely results in a strong interaction between the Pd and the O of the SiO_2 support that anchors the Pd to the support. Consequently, during TPR the Pd remains well dispersed. In the case of the air dried sample however, because of the formation of PdO_xCl_y species that will reduce the interaction of Pd with the SiO_2, agglomeration of the PdO_xCl_y can occur, resulting in significantly lower dispersion of the air calcined sample compared to the He calcined sample.

Furthermore, the PdO_xCl_y has been identified as providing nucleation sites for Pd crystallite growth [120], and the presence of PdO_xCl_y species in the air calcined samples likely contributes to a reduced dispersion as well.

4.4.2 Catalyst activity and selectivity

From Figure 4.9 and Table 4.4 it is seen that the 4 wt % Pd/SiO_2 catalyst, with a Pd particle diameter of about 9 nm, resulted in a maximum in the dodecahydro-N-ethylcarbazole dehydrogenation TOF and a maximum in selectivity to the completely dehydrogenated product N-ethylcarbazole. The N-ethylcarbazole selectivity over the 4 wt % Pd/SiO_2 catalyst was 15.3 % at 50 % reactant conversion and 95 % after 1 h of reaction, significantly higher than that obtained for the other catalysts of Table 4.4. Complete conversion of the reactant was obtained in 22 min over the 4 wt % Pd/SiO_2 catalyst, which is significantly shorter than the 17 h reaction time reported for dodecahydro-N-ethylcarbazole dehydrogenation at 443 K and 101 kPa over the 5 wt % Pd/SiO_2 catalyst calcined in air [106]. In the present work, the complete H_2 recovery from dodecahydro-N-ethyl carbazole obtained over the 4 wt % Pd/SiO_2 catalyst after 1.6 h at 443 K, shows the significantly superior activity of the Pd/SiO_2 catalysts prepared by calcination in He rather than air.

The results reported herein are significant for hydrogen recovery applications, since the dehydrogenation reactions had previously been reported to be very slow with no selectivity to the completely dehydrogenated product, N-ethylcarbazole. Wang et al. [56] reported Ir complexes to be active for the dehydrogenation of dodecahydro-N-ethylcarbazole. Complete conversion occurred after 48 h at 473 K but dehydrogenation to the fully unsaturated product N-ethylcarbazole did not occur and octahydro-N-ethylcarbazole and tetrahydro-N-ethylcarbazole were reported to be the only observed products. Crawford et al. [53] and Hindle et al. [54] reported that the dehydrogenation of tetrahydrocarbazole at 413 K and 101 kPa proceeded to 81 % conversion over a 5 wt % Pd/Al_2O_3 catalyst in 27 h, with an initial reaction rate of 10 mM. $min_{-1}.g_{cat}{}^{-1}$, in reasonable agreement with the initial rate of 17 $mM.min_{-1}.g_{cat}{}^{-1}$ reported by the authors [106] over the 5 wt % Pd/SiO_2 at 413 K and 101 kPa. Although 100 % selectivity to the completely dehydrogenated product carbazole was obtained, product inhibition was shown to slow

the reaction rate significantly. Decalin, another hydrogen storage candidate, was dehydrogenated over a Pt/C catalyst by Loutfy et al. [57] in a batch-type membrane reactor at temperatures of 533 - 593 K. Conversions below 85 % were reported after 2.2 h. Conversions $>$ 95 % were obtained within 1.5 h at 553 K by Hodoshima et al. [58]. However, these reported reaction temperatures ($>$ 535 K) are too high and impractical for hydrogen recovery for transport applications.

The dependence of the dodecahydro-N-ethylcarbazole dehydrogenation TOF and selectivity to N-ethylcarbazole on Pd particle size, clearly demonstrated in the present work, suggests that the dehydrogenation reaction is structure sensitive. Pd particle size likely plays an important role in providing an adequate ensemble of catalytic sites for adsorption of the large dodecahydro-N-ethylcarbazole molecule and the other dehydrogenation intermediates. The maximum in TOF with particle size observed in the present work has also been observed in other reaction systems. For example, Binder et al. [127] reported a maximum in the ethene hydrogenation TOF over Pd/TiO_2 catalysts at atmospheric pressure and 293 K, with the maximum occurring for a catalyst with a Pd particle size of 3 nm. Bezemer et al. [128] also reported a maximum in CO hydrogenation TOF over a series of Co catalysts, with the maximum occurring for a Co particle size of about 3 nm. Murzin [117, 129] has shown that the maximum in TOF can be accounted for by an analysis of the kinetic consequences of the different reactivities of edges and terraces present on the metal catalyst and the dependence of the fraction of edges on the cluster or particle size. Accordingly, for both two-step reaction mechanisms and Langmuir-Hinshelwood kinetics, the TOF can be written as [117, 129],

$$TOF = \frac{P_1 e^{(1-\alpha)\gamma/d_{cluster}}}{1 + P_2 e^{\gamma/d_{cluster}}} \tag{4.3}$$

Where P_1 and P_2 are combinations of individual reaction frequencies, α is the Polanyi parameter, γ is the parameter accounting for the differences in Gibbs free energy of adsorption on terraces and edges and $d_{cluster}$ is the cluster diameter. The same equation will apply to the dehydrogenation TOF of dodecahydro-N-ethylcarbazole, and Figure 4.9 shows the standard non-linear least-squares fit of

the data from the present study applied to equation 4.3. The estimated parameter values are reported in Figure 4.9 and the maximum in TOF at a particle size of about 9 nm is well explained by Murzin's model. The Polanyi parameter obtained from the data fit was somewhat lower than the 0.5 often observed in heterogeneous catalytic reaction [117, 129]. Furthermore, the difference in the Gibbs free energy of adsorption on terraces versus edges is suggested to be significantly larger (300 kJ/mol) than that reported for ethene hydrogenation [117]. The present study has considered the effect of the preparation method on the Pd particle size, which is believed to be the major contributor to the significant change observed in catalyst selectivity. However, the change in the calcination environment may also generate surface defects due to chlorine and water removal from the precursors formed on the support, which can affect the activity of the catalyst. Density functional theory calculations were also used to confirm the structure sensitivity of the dehydrogenation reaction of dodecahydro-N-ethylcarbazole. The details are discussed in Chapter 6.

4.5 Conclusion

The complete recovery of the H_2 stored on dodecahydro-N-ethylcarbazole was achieved at 443 K and 101 kPa using Pd/SiO_2 catalysts, prepared by incipient wetness impregnation with calcination in He rather than air. The dehydrogenation turn-over frequency (TOF) and selectivity to the completely dehydrogenated product, N-ethylcarbazole, were dependent upon Pd particle size, with a maximum in both occurring with a 4 wt % Pd/SiO_2 catalyst that had an average Pd particle size of 9 nm. Over this catalyst the dehydrogenation reaction proceeded to complete conversion within 22 min and complete H_2 recovery (5.8 wt %) within 1.6 h at 443 K and 101 kPa.

Chapter 5

The effect of the N-heteroatom on the dehydrogenation of polyaromatics used for hydrogen storage

A version of this chapter is to be submitted:
F. Sotoodeh, B.J.M. Huber and K.J. Smith. The effect of the N-heteroatom on the dehydrogenation of polyaromatics used for hydrogen storage, to be submitted.

5.1 Introduction

As indicated in the previous chapters, incorporation of a heteroatom in the aromatic ring can lower the dehydrogenation enthalpy of the candidate compounds [16]. In the present chapter, the effect of N heteroatom on the dehydrogenation reaction rate was studied by comparing the rates of hydrogen recovery from dodecahydro-N-ethylcarbazole, dodecahydrocarbazole and dodecahydrofluorene over Pd catalysts. The N heteroatom of dodecahydro-N-ethylcarbazole is bound to an ethyl group that should decrease the N - catalyst interaction compared to dodecahydrocarbazole, whereas there is no N heteroatom in dodecahydrofluorene.

5.2 Experimental

5.2.1 Catalyst preparation

A commercial pre-reduced 5 wt % Pd on activated carbon catalyst (Aldrich, 5 wt % Pd, reduced) was used for the dehydrogenation reactions. A 2 wt % Pd/SiO_2 catalyst was prepared by incipient wetness of the support [97, 111], described previously in Chapter 4. The prepared 2 wt % Pd/SiO_2 catalyst was used for a comparative activity study with a 5 wt % Pd/SiO_2 prepared previously by wet impregnation, as well as the 5 wt % Pd/C with the same particle size. The reported 5 wt % Pd/SiO_2 catalyst was dried at 393 K for 24 h and calcined at 748 K for 3 h in air instead of He. Details of the catalyst preparation procedure have been presented elsewhere [106] and aslo discussed in Chapter 3.

5.2.2 Catalyst characterization

N_2 adsorption-desorption isotherms measured at 77 K using a Micromeritics ASAP 2020 Accelerated Surface Area and Porosimetry analyzer, were used to determine the total BET surface area, pore volume and average pore diameter of the catalysts. Approximately 0.12 g of the catalyst was weighed and loaded into a quartz sample tube for initial degassing. The sample was first evacuated at a rate of 1.33 kPa/s until the vacuum reached 0.04 kPa. Simultaneously, the temperature was increased at a ramp rate of 10 K/min until it reached 363 K. The evacuation phase was followed

by a heating phase where the temperature was further increased at the same rate and then held at 473 K for 60 min. After initial degassing the catalyst was weighed again and transferred to the analysis section for the N2 adsorption-desorption measurement.

Temperature-programmed reduction (TPR) analysis and carbon monoxide (CO) pulse chemisorption were carried out on the 5 wt % Pd/C catalyst using a Micromeritics Autochem II 2920 analyzer. Approximately 0.12 g of the catalyst was loaded into the quartz sample tube. Prior to the TPR the sample was degassed in a He flow of 30 cm^3/min (STP) while heating to 423 K at a rate of 15 K/min. After subsequent cooling to ambient temperature, the sample was flushed in a flow of 10 % H_2 in He for 30 min prior to the start of the TPR. The catalyst was then reduced by heating to 673 K at a rate of 10 K/min in a 30 cm^3/min (STP) flow of 10 % H_2 in Ar. The final temperature was held for 30 min. After cooling the sample to ambient temperature, the CO pulse chemisorption analysis was initiated. The sample was flushed in a 30 cm_3/min (STP) flow of He carrier gas for 1 h. This was followed by repeated injections of pulses of CO into the reactor from a 20 cm^3/min (STP) flow of 10 % CO in He. The injection was continued until the TCD showed no further CO uptake by the sample. The metal dispersion was calculated using an assumed Pd:CO stoichiometry of 1:1 [98].

Temperature-programmed desorption (TPD) of CO from the 2 wt % Pd/SiO_2 catalyst was performed using a Micromeritics Autochem II 2920 analyser. About 0.2 g of the dried catalyst was loaded into the reactor and calcined at 773 K for 6 h in a 30 cm^3 (STP)/min flow of Ar, followed by TPR at 10 K/min to a final temperature of 673 K in a 30 cm^3 (STP)/min flow of 10 % H_2 in Ar, holding the final temperature for 1 h. The catalyst was then flushed in 30 cm^3 (STP)/min flow of Ar for 1 h and cooled to room temperature, before being exposed to a 50 cm^3 (STP)/min flow of 10 % CO in He at 313 K for 1 h. The catalyst was subsequently flushed in 50 cm^3 (STP)/min He for 2 h. The temperature-programmed desorption was then started by heating the sample to 773 K at a rate of 10 K/min and holding the final temperature for 1 h.

5.2.3 Catalyst activity

The hydrogenation of N-ethylcarbazole (Aldrich, 97 %) and carbazole (Sigma, Approx. 95 %) was carried out at 423 K and a H_2 pressure of 7 MPa to produce the reactant for the dehydrogenation reactions. A 300 cm^3 autoclave batch reactor with continuous monitoring and control of stirrer speed, temperature, and pressure was used for the hydrogenation reactions. Details of the experimental procedure and reactor set-up for hydrogenation reactions have been reported in Chapter 2.

The dehydrogenation of dodecahydrocarbazole as well as dodecahydrofluorene (Aldrich, 97 %) were carried out in a 50 cm^3 glass flask reactor at temperature in the range 423 - 443 K and 101 kPa, over the Pd/C catalyst, using the same reactor set-up and procedure discussed in Chapter 3. Liquid samples of volume of < 0.1 cm^3 were withdrawn from the reactor periodically. The analysis of the liquid samples obtained from the dehydrogenation reactions was done by a Shimadzu QP-2010S GC/MS using a Restek RTX5 30 m 0.25 mm capillary column.

A comparative study on dehydrogenation of dodecahydro-N-ethylcarbazole was performed over the 2 wt % Pd/SiO_2 and the 5 wt % Pd/C catalyst at 443 K and 101 kPa using the same dehydrogenation experiment set-up and procedure as that of used for dehydrogenation of dodecahydrocarbazole and dodecahydrofluorene.

5.3 Results

5.3.1 Catalyst properties

The BET surface area, pore volume and average pore size of the catalysts are summarized in Table 5.1. As expected, the Pd/C catalyst had a significantly larger BET surface area (1055.1 $m^2.g^{-1}$) compared to the 325.6 $m^2.g^{-1}$ of the 5 wt % Pd/SiO_2, due to the highly porous nature of the activated carbon compared to the support silica. Hindle et al. [54] also reported a BET surface area of 1358 $m^2.g^{-1}$ for a 10 wt % Pd/C. The average pore size obtained for the Pd/C catalyst was 2.0 nm, about 5 times smaller than the average pore size of 9.5 nm of the Pd/SiO_2.

H_2 TPR profiles of the 2 wt % Pd/SiO_2 and the 5 wt % Pd/C catalysts are presented in Figure 5.1-a,b, respectively. A negative peak in the TPR profiles was

Table 5.1: Catalyst properties

Catalyst	BET surface area ($m^2.g^{-1}$)	Pore volume ($cm^3.g^{-1}$)	Average pore size (nm)	Active particle size (nm)	Pd metal dispersion (%)
5 wt % Pd/C	1055.1	0.55	2.0	6	19[a]
5 wt % Pd/SiO_2[b]	325.6	1.1	9.5	24	4[a]
2 wt % Pd/SiO_2	346.63	1.1	10.1	6	16[c]

[a] Obtained from CO pulse chemisorption.
[b] Reported by Sotoodeh et al. [106]
[c] Obtained from TPD of CO.

observed at temperatures between 333 - 337 K. In the work of Babu et al. [112] very similar H_2 TPR profiles were observed for 3 and 5 wt % alumina-supported Pd catalysts and a negative peak in the region of 348-373 K was detected. Amairia et al. [113] also reported a negative H_2 peak at 358 K for the H_2 TPR profiles of Pd/Al_2O_3-ZrO_2 samples. The observed negative peaks in the H_2 profiles from the TPR experiments are likely due to the release of H_2 from the decomposition of a Pd-hydride phase formed on large Pd particles (> 2 nm) [100, 112, 113].

As shown in Table 5.1, CO pulse chemisorption of the commercial 5 wt % pre-reduced Pd/C catalyst resulted in about 19 % metal dispersion and an active particle diameter of 6 nm. The CO TPD results show a 16 % Pd metal dispersion as well as an active particle size of about 6 nm for the 2 wt % Pd/SiO_2 catalyst prepared by calcination in He. The results are comparable with the metal dispersion of 4 % and the particle size of 24 nm reported previously for a 5 wt % Pd/SiO_2 catalyst prepared by calcination in air [106].

5.3.2 Catalyst activities

Dehydrogenation of dodecahydrocarbazole

The hydrogenation of carbazole at 423 K and 7 MPa using the 300 cm^3 autoclave batch reactor proceeded with more than 97 % selectivity to the completely hydrogenated product, dodecahydrocarbazole, after about 13 h. Details of the kinetics of carbazole hydrogenation have been discussed previously [107]. The hydrogenated product, containing 1 wt % dodecahydrocarbazole dissolved in decalin, was trans-

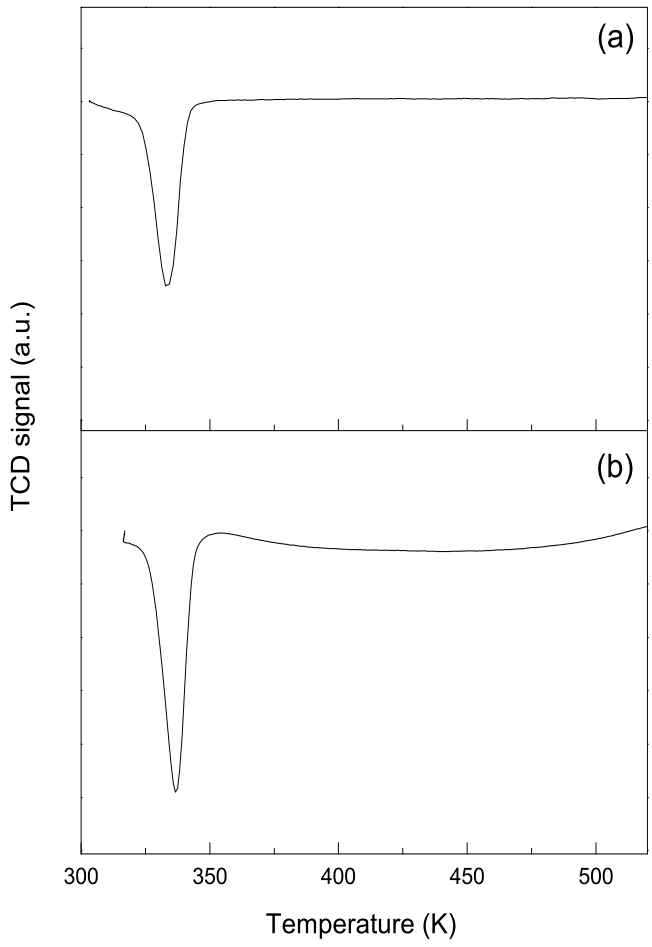

Figure 5.1: TPR patterns of (a) 2 wt % reduced Pd/SiO_2 catalyst prepared by calcination in He; (b) 5 wt % commercial pre-reduced Pd/C catalyst.

ferred to the 50 cm^3 dehydrogenation glass flask reactor for the dehydrogenation reaction at three different temperatures (423 K, 433 K and 443 K) using the reduced 5 wt % Pd/C catalyst. For all three experiments the catalyst to reactant mass ratio was kept at 0.28 to make it possible to compare this work with the previously reported dehydrogenation of dodecahydrocarbazole reported using a 5 wt % Pd/SiO_2 with 4 % dispersion and a Pd particle diameter of 24 nm [106, 107]. From the product distribution of the dehydrogenation reaction shown in Figure 5.2 it follows that the same intermediates and products were present in each case and the reaction rate increased by increasing the temperature.

Complete conversion of the dodecahydrocarbazole was achieved after 30 min at 443 K, after 2 h at 433 K and after $>$ 6.5 h at 423 K. Previous works reported 53 % reactant conversion for the dehydrogenation of dodecahydrocarbazole after 17 h over a 5 wt % Pd/SiO_2 with Pd particle diameter of 24 nm at 443 K and 101 kPa [106], and 81 % of 1,2,3,4-tetrahydrocarbazole conversion after 27 h over a 5 wt % Pd/Al_2O_3 at 413 K and 101 kPa [53]. As shown in Figure 5.2, octahydrocarbazole was produced in a significant amount as a primary product that was subsequently consumed. Tetrahydrocarbazole appeared as a secondary product in an even higher concentration and reacted more slowly. Hexahydrocarbazole was only produced in very small amounts observed shortly after octahydrocarbazole and was consumed very quickly suggesting a sequential dehydrogenation reaction pathway. Table 5.2 compares the kinetic data obtained for the dehydrogenation reactions at three different temperatures.

Table 5.2: Kinetic data obtained from liquid phase analysis for dodecahydrocarbazole dehydrogenation in decalin using a 5 wt % Pd/C catalyst at various temperatures and 101 kPa.

T (K)	Rate constant, k (h^{-1})	Initial rate ($mM.min^{-1}.g_{cat}{}^{-1}$)	Initial concentration ($mol.ml^{-1}$)	TOF (min^{-1})	Time for 100 % reactant conversion (h)
443	7.96	65.1	4.63×10^{-5}	21.2	0.5
433	2.14	20.3	2.84×10^{-5}	8.1	2.0
423	0.55	5.2	2.83×10^{-5}	2.1	$>$ 6.5

The 1^{st}-order rate constants (k) were calculated by fitting 1^{st}-oder kinetics to the dodecahydrocarbazole conversion data. The initial reaction rates and turn-over

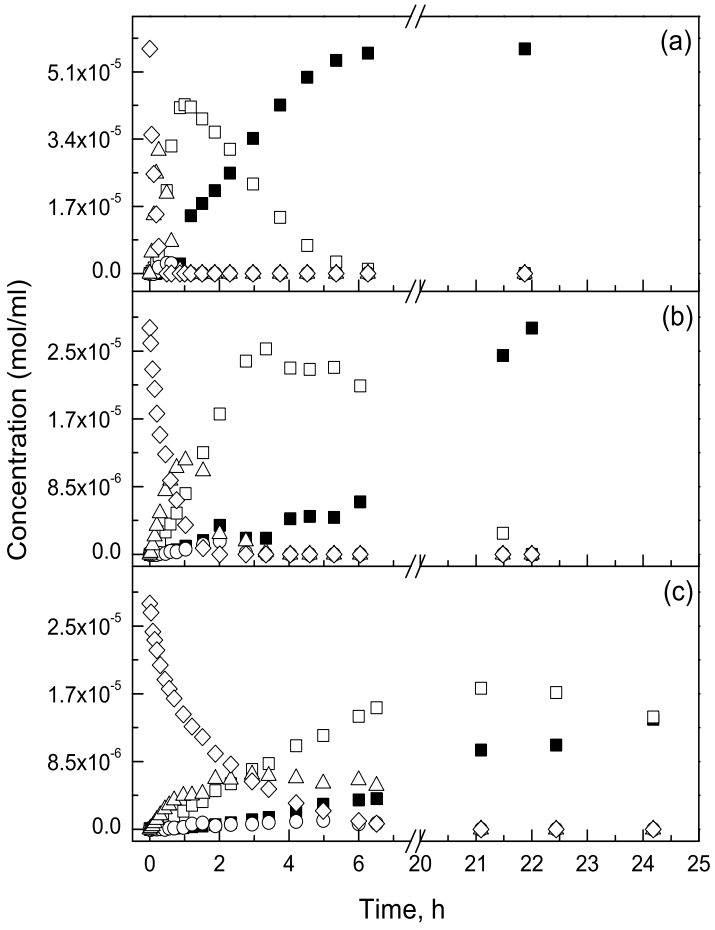

Figure 5.2: Product distributions over time for dehydrogenation of dodecahydrocarbazole in decalin at 101 kPa and (a) 443 K, (b) 433 K, (c) 423 K over the 5 wt % Pd/C catalyst. (■) carbazole, (□) tetrahydrocarbazole, (○) hexahydrocarbazole, (△) octahydrocarbazole, (◇) dodecahydrocarbazole.

frequencies (TOFs) were calculated from the 1^{st}-order rate constants and the initial reactant concentrations. From Table 5.2 it is seen that increasing the temperature from 423 - 443 K increased the dodecahydrocarbazole consumption TOF from 2.1 min^{-1} to 21.2 min^{-1}, respectively. Accordingly, the 1^{st}-order rate constant for dodecahydrocarbazole consumption also increased from 0.55 h^{-1} at 423 K to 7.96 h^{-1} at 443 K. In previous work on the dodecahydrocarbazole dehydrogenation at 443 K over a 5 wt % Pd/SiO_2 catalyst, the 1^{st}-order rate constant was determined as 0.45 h^{-1} [107]. An apparent activation energy of 208.9 $\pm$ 0.2 kJ/mol for dehydrogenation of dodecahydrocarbazole was obtained by linear regression of the Arrhenius equation for the calculated 1^{st}-order reaction rate constants as shown in Figure 5.3.

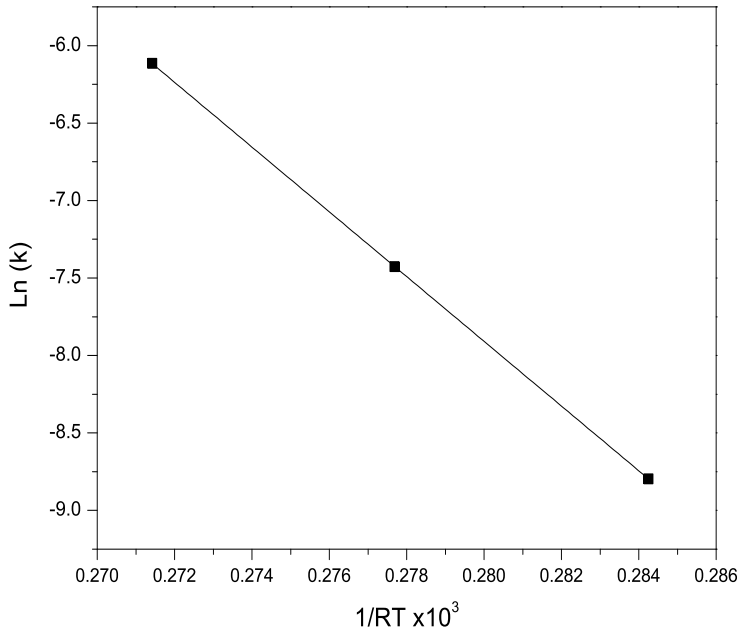

Figure 5.3: Arrhenius plot for dehydrogenation of dodecahydrocarbazole at 423 - 443 K and 101 kPa over a 5 wt % Pd/C.

Table 5.3 summarizes the H_2 recovery data for the dehydrogenation of dodec-

ahydrocarbazole at three different temperatures.

Table 5.3: H_2 recovery for the dehydrogenation of dodecahydrocarbazole at various temperatures and 101 kPa over a 5 wt % Pd/C catalyst.

Temperature (K)	Reaction time (h)	H_2 recovery[a] (wt %)
443	6.3	6.6
433	21.5	6.6
423	21.1	4.3

[a]amount of released H_2 in grams divided by the weight of hydrogenated compound in grams (theoretical H_2 recovery of doecahydrocarbazole is 6.7 wt %).

The H_2 recovery increased by increasing the temperature. A 6.6 wt % H_2 recovery (very close to the theoretical value of 6.7 wt % H_2 release capacity) was obtained after 6.3 h for the dehydrogenation reaction at 443 K, while the same recovery was obtained after 21.5 h for the reaction at 433 K. For the experiment at 423 K, only 4.3 wt % of the stored H_2 was recovered after 21.1 h.

Dehydrogenation of dodecahydrofluorene in decalin

Dehydrogenation of dodecahydrofluorene was conducted at 443 K and 101 kPa using 0.2 g of the 5 wt % Pd/C catalyst and a 2.3 wt % solution of commercially available dodecahydrofluorene in decalin. The product distribution obtained by analyzing the liquid samples is shown in Figure 5.4.

It was found that decahydrofluorene and hexahydrofluorene were two reaction intermediates produced in very small amounts, and the reaction proceeded with production of the completely dehydrogenated compound fluorene as the major product. Conversion of the reactant, dodecahydrofluorene, was found to be very slow. By fitting 1^{st}-order kinetics to the data obtained for the consumption of dodecahydrofluorene, a rate constant of 0.012 h^{-1}, an initial reaction rate of 0.127 $mM.min^{-1}.g_{cat}{}^{-1}$ and a TOF of 0.043 min^{-1} were obtained. After 19 h of reaction, a dodecahydrofluorene conversion of only 10.1 % and a yield of 9.6 % for the completely dehydrogenated product fluorine were achieved. Although the reaction kinetics were slow, the catalyst selectivity to the final product fluorene was found 95.6 %. The product distribution in Figure 5.4 suggested that the decahydrofluorene and hexahydrofluorene were the primary intermediates and fluorene was a

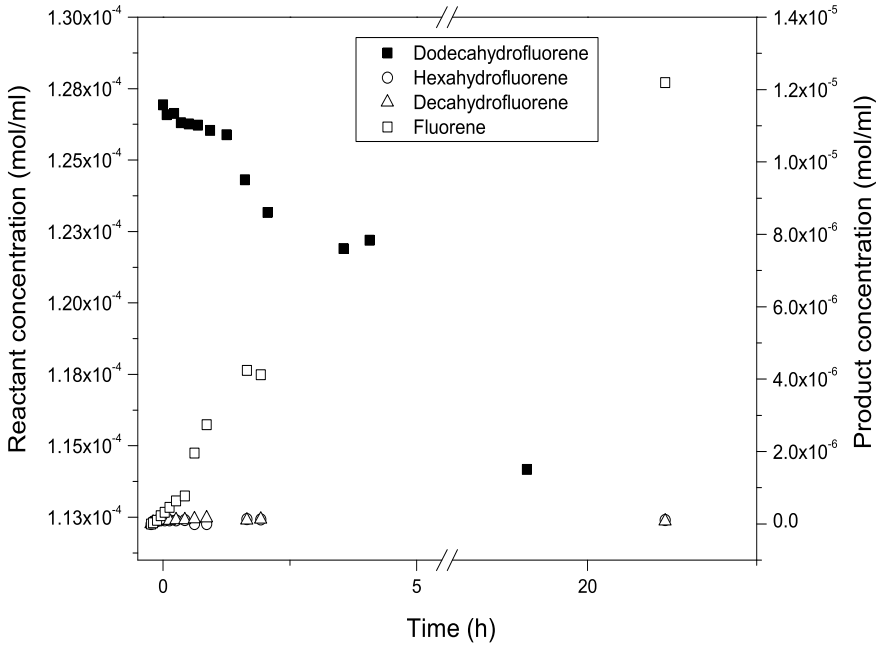

Figure 5.4: Product distribution over time for dodecahydrofluorene dehydrogenation in decalin at 443 K and 101 kPa over the 5 wt % Pd/C catalyst. Reactant concentrations (closed data points) are shown on the left Y-axis and products concentrations (open data points) on the right Y-axis.

secondary product. In the work by Cooper et al. [130] dehydrogenation of pure perhydrofluorene (dodecahydrofluorene) under 101 kPa H_2 pressure at 503 K using a Pt/Al_2O_3 catalyst resulted in 99 % conversion to fluorene with $>$ 99 % selectivity. However, the reported temperature is too high for on-board hydrogen recovery and therefore impractical for transport applications.

Solvent effect in the dehydrogenation of dodecahydrofluorene

In order to investigate whether the solvent decalin had an inhibitory effect on the dehydrogenation reaction rate of the dodecahydrofluorene, the dehydrogenation reaction was carried out without a solvent at 443 K and 101 kPa using 15 cm^3 pure

dodecahydrofluorene loaded into the dehydrogenation reactor with 0.5 g of the 5 wt % Pd/C catalyst. The product distribution obtained from pure dodecahydrofluorene dehydrogenation, as shown in Figure 5.5, illustrates the presence of the same products as in the experiment carried out in the solvent decalin.

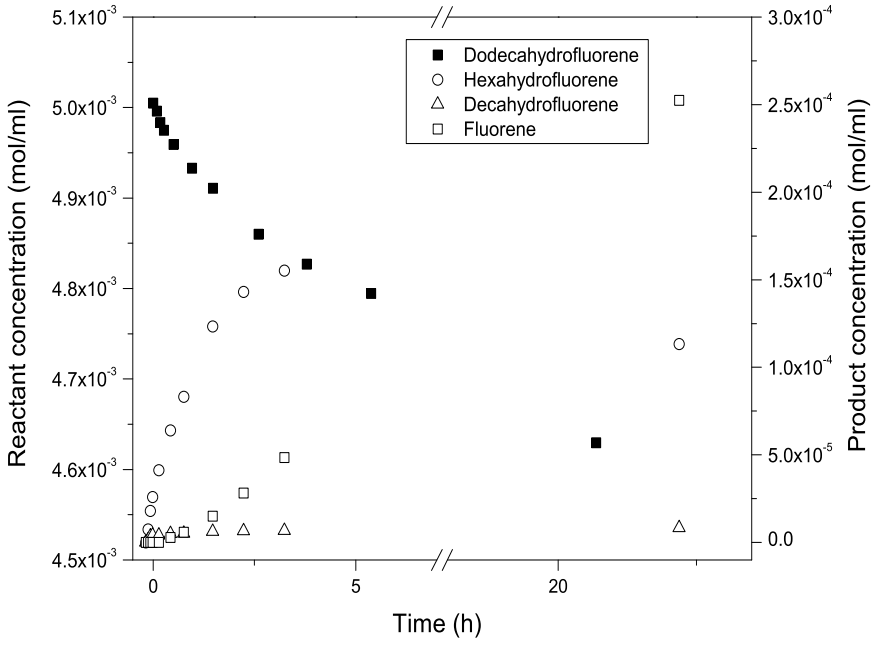

Figure 5.5: Product distribution over time for dehydrogenation of pure dodecahydrofluorene at 443 K and 101 kPa over the 5 wt % Pd/C catalyst. Reactant concentrations (closed data points) are shown on the left Y-axis and products concentrations (open data points) on the right Y-axis.

Again, fluorene exhibited the progression of a secondary product and first appeared in the sample taken after 30 min. The primary product hexahydrofluorene exhibited the behaviour of an intermediate that was initially formed and then consumed. Table 5.4 summarizes the obtained kinetic results for the dehydrogenation of dodecahydrofluorene with and without the presence of solvent.

A rate constant of 0.0122 h^{-1} was found by fitting 1^{st}-order kinetics to the ex-

Table 5.4: Comparison of kinetic data obtained from liquid phase analysis for dodecahydrofluorene dehydrogenation with and without a solvent at 443 K and 101 kPa over 5 wt % Pd/C catalyst.

Status	Rate constant, k (h^{-1})	Initial rate ($mM.min^{-1}.g_{cat}{}^{-1}$)	TOF (min^{-1})
Using solvent (decalin)	0.0120	0.127	0.043
Pure reactant	0.0122	2.040	0.349

perimental data obtained for the consumption of dodecahydrofluorene. The initial reaction rate and the catalyst TOF with respect to the reactant consumption were found to be 2.04 mM. $min^{-1}.g_{cat}{}^{-1}$ and 0.349 min^{-1}, respectively. Also, dodecahydrofluorene conversion of 12.4 % with a yield of 12.0 % and a selectivity of 96.5 % for the production of the completely dehydrogenated product fluorene was achieved. The obtained results for the 1^{st}-order rate constant of the dehydrogenation of the pure dodecahydrofluorene compared to the reaction in decalin solvent confirms that there is no solvent effect in the reaction. In both cases, only about 1 wt % of the hydrogen was recovered from the hydrogenated compound, which is far from the theoretical capacity of 6.74 wt %. Although the previous work on the dodecahydrofluorene by Cooper et al. [130] resulted in full hydrogen recovery at 503 K, the department of energy (D.O.E.) temperature criterion of 473 K for on-board dehydrogenation reactions limits the use of dodecahydrofluorene as a candidate for hydrogen recovery.

5.3.3 Dehydrogenation reaction comparison of dodecahydro-N-ethylcarbazole, dodecahydrocarbazole, dodecahydrofluorene

Table 5.5 summarizes the kinetic results as well as the H_2 recovery for the dehydrogenation reactions of dodecahydro-N-ethylcarbazole, dodecahydrocarbazole and dodecahydrofluorene. Comparing the dehydrogenation of dodecahydro-N-ethylcarbazole with dodecahydrocarbazole over the Pd catalyst with an active Pd particle diameter of 24 nm, it is seen that the reaction TOF of 31.8 min^{-1} obtained for dodecahydro-N-ethylcarbazole is significantly higher than the 0.79 min^{-1} for dodecahydrocarbazole.

Decreasing the Pd particle size from 24 nm to 6 nm resulted in a dramatic

Table 5.5: Dehydrogenation reaction comparison of dodecahydro-N-ethylcarbazole, dodecahydrocarbazole and dodecahydrofluorene at 443 K and 101 kPa.

Reactant	H_2 capacity[a] (wt %)	Particle size (nm)	Initial concentration (mol.ml^{-1})	TOF[b] (min^{-1})	Conversion (%)	H_2 recovery[c] (wt %)
Dodecahydro-N-ethylcarbazole	5.79	24[d]	1.40×10^{-4}	31.8	100(17 h)[e]	4.00(17 h)[f]
		6 [g]	9.92×10^{-5}	97.8	100(40 min)	5.79(2.7 h)
		6[h]	9.92×10^{-5}	59.6	100(94 min)	5.79(12 h)
Dodecahydro-carbazole	6.70	24[d]	1.14×10^{-4}	0.8	53(17 h)	1.90(17 h)
		6[h]	4.63×10^{-5}	21.2	100(30 min)	6.57(6.3 h)
Dodecahydro-fluorene (in decalin)	6.74	6[h]	2.84×10^{-5}	0.04	10.1(19 h)	1.06(19 h)
Dodecahydro-fluorene (pure)	6.74	6[h]	5.00×10^{-3}	0.35	12.4($>$ 70 h)	0.75(70 h)

[b] Molecule of reactant.min^{-1}.Pd surface atom^{-1}.
[a] Theoretical H_2 released (grams) divided by the weight of hydrogenated compound (grams).
[c] H_2 released in experiment (grams) divided by the weight of hydrogenated compound (grams).
[d] Using 5 wt % Pd/SiO_2.
[e] Experimental time for the obtained conversion.
[f] Experimental time for the obtained H_2 recovery.
[g] Using 2 wt % Pd/SiO_2.
[h] Using 5 wt % Pd/C.

increase in the reaction TOF for dodecahydro-N-ethylcarbazole consistent with the structure sensitivity of this reaction reported previously over a series of Pd catalysts [131].

The data for dodecahydro-N-ethylcarbazole dehydrogenation over the 2 wt % Pd/SiO_2 and the 5 wt % Pd/C, both of which have an average Pd particle size of 6 nm, also show some impact of the SiO_2 and C supports, with the dehydrogenation TOF higher on the SiO_2 supported Pd than the C supported Pd. The reason for the difference in TOF is not clearly understood, but it is likely a consequence of different thermal treatments during preparation between the Pd/SiO_2 catalyst and the commercial Pd/C catalyst. As shown recently, the atmosphere

present during thermal treatment of the Pd catalyst precursor can have a profound effect on the catalyst activity [131]. Nonetheless, the data of Table 5.5 show that both dodecahydro-N-ethylcarbazole and dodecahydrocarbazole dehydrogenation are structure sensitive reactions. For both reactants, the TOF increased as the Pd particle size decreased. Note, however, that the shorter time for complete H_2 recovery reported in Table 5.5 for dodecahydrocarbazole dehydrogenation compared to dodecahydro-N-ethylcarbazole dehydrogenation, is a consequence of differences in reactant molar concentration and catalyst concentration in each case.

5.4 Discussion

5.4.1 Catalyst properties

As reported in Table 5.1, catalyst dispersion was significantly increased for the 2 wt % Pd/SiO_2 catalyst prepared by the modified preparation method and calcination in He, compared to the catalyst prepared by wet impregnation and calcination in air [106, 107]. Zou et al. [121] also reported the effect of pre-treatment on the Pd catalyst dispersion where an increase in the catalyst dispersion was observed by calcination in noble gas instead of O_2. The lower dispersion in the latter was attributed to the competitive interaction of oxygen in the support with gas phase oxygen that caused partial weakening of surface metal bond and metal agglomeration and therefore resulting in a lower metal dispersion. More recently, the improved dispersion that follows calcination in He rather than air has been shown to be a consequence of the different precursors that result from calcinations in air (PdO_xCl_y) versus He (PdO_x).

In the TPR profiles, the observed negative peak for the pre-reduced 5 wt % Pd/C and the reduced 2 wt % Pd/SiO_2 catalysts is attributed to the decomposition of the β-palladium hydride phase which is reported to form at room temperature over large Pd particles (> 2 nm) [100, 114, 115] during the flushing step that was done in a flow of 10 % H_2 in He for 30 min prior to the start of the TPR.

5.4.2 Catalyst activities

The sudden increase in the H_2 recovery rate from dodecahydrocarbazole by increasing the temperature from 423 K to 443 K is expected as very high activation energy of 208.9 $\pm$ 0.2 kJ/mol was found for the dehydrogenation reaction of dodecahydrocarbazole. The obtained activation energy for dodecahydrocarbazole dehydrogenation is relatively high compared to the reported 126.8 kJ/mol value for the dehydrogenation of dodecahydro-N-ethylcarbazole over a 5 wt % Pd/SiO_2 catalyst [107], and the 67.7 kJ/mol value for the dehydrogenation of tetrahydrocarbazole over the same 5 wt % Pd/SiO_2 [106]. The latter was found in good agreement with the 64.4 kJ/mol value obtained by the DFT study of Crawford et al. [53] and confirmed by the experimental work with the value of about 67 kJ/mol reported by Hindle et al. [54]. The high activation energy for dehydrogenation of dodecahydrocarbazole can be attributed to the strong interaction of the N heteroatom with the Pd surface atoms, resulting in strong adsorption of the molecule to the surface. In dodecahydro-N-ethylcarbazole, the ethyl group hindrance prevents the N heteroatom to interact strongly with the surface and hence results in a lower dehydrogenation activation energy.

The present study has compared kinetic results as well as the H_2 recovery for the dehydrogenation reactions of dodecahydro-N-ethylcarbazole, dodecahydrocarbazole and dodecahydrofluorene. The data show that the dehydrogenation reactions of dodecahydro-N-ehylcarbazole and dodecahydrocarbazole are structure sensitive. The lower reaction TOF obtained for dodecahydrocarbazole dehydrogenation is attributed to the effect of the N-heteroatom lone electron pair which interacts strongly with the catalyst surface and poisons the active catalytic sites and therefore, decreases the reaction rate. Catalyst poisoning by the product carbazole was also reported by the work of Hindle et al. [54] for dehydrogenation reaction of tetrahydrocarbazole. Interaction of the N heteroatom with the catalyst surface however, is decreased for dodecahydro-N-ethylcarbazole and its dehydrogenated product most likely due to the steric hindrance of the ethyl group. The effect of the N heteroatom in catalyst poisoning was also reported for H_2 storage through hydrogenation reaction of carbazole compared to N-ethylcarbazole [107]. 100 % conversion of the reactant N-ethylcarbazole was obtained in about 1 h at 423 K over

a Ru/Al_2O_3 catalyst, whereas the complete conversion of carbazole was obtained after about 13 h at the same reaction temperature and a catalyst/reactant ratio of 6 times higher than that used for N-ethylcarbazole hydrogenation.

Comparing the kinetics of the dehydrogenation reaction of dodecahydrofluorene with dodecahydrocarbazole in Table 5.5, it is seen that a much lower TOF for dodecahydrofluorene was obtained compared to dodecahydrocarbazole. Furthermore, the very small amount of H_2 recovery at the reaction temperature of 443 K after a very long experimental time, suggests that the N-heteroatom favors the dehydrogenation reactions of organic heteroaromatic compounds significantly. The effect of introducing the N heteroatom to replace a carbon in polycyclic aromatic hydrocarbons was also reported to result in a lower absolute value of the standard enthalpy of hydrogenation, and therefore decrease the reversible dehydrogenation barrier [16]. As discussed earlier, complete H_2 recovery from dodecahydrofluorene obtained in a work by Cooper et al. [130] at 503 K suggests a high reaction barrier for the dehydrogenation of dodecahydrofluorene at 101 kPa. However, this temperature is not within the limits of on-board H_2 recovery determined by the department of energy. Noticeably, although dodecahydrocarbazole and its dehydrogenated products have been shown to poison the catalytic active sites significantly due to the strong interaction of the N-heteroatom lone electron pair with the surface, the presence of the N-heteroatom in the polycyclic aromatic structures still has a positive effect in increasing the H_2 recovery rate.

5.5 Conclusion

Dodecahydro-N-ethylcarbazole dehydrogenation was compared to dodecahydrocarbazole and dodecahydrofluorene. Complete H_2 recovery from both dodecahydro-N-ethylcarbazole and dodecahydrocarbazole was achieved over a Pd catalyst with an active particle diameter of about 6 nm. However, the dehydrogenation reaction TOF of dodecahydro-N-ethylcarbazole was found to be about 5 times faster than that of dodecahydrocarbazole. The faster reaction rate for dodecahydro-N-ethylcarbazole was attributed to the effect of the ethyl group which prevented the N lone electron pair to interact strongly with the catalyst surface. It was found that the dehydrogenation reactions of the both reactants were structure sensitive, where

the active particle size had a significant effect on the selectivity of the dehydrogenation reactions to the completely dehydrogenated products, N-ethylcarbazole and carbazole. It is concluded that N-ethylcarbazole is a more practical candidate for both H_2 storage and release than carbazole, although its storage capacity is about 13 % lower (5.8 wt % for N-ethylcarbazole compared to 6.7 wt % capacity for carbazole).

Dodecahydrofluorene dehydrogenation reaction was shown to be the slowest among those examined. Only about 12 % of the reactant was converted and a H_2 recovery of less than 1 wt % was achieved in more than 20 h which is impractical for on-board H_2 recovery applications. The results supported the assertion that the presence of a N-heteroatom in the polycyclic structure favors the dehydrogenation reactions significantly. It was found from the present work that despite catalyst deactivation by strong adsorption through the N-heteroatom of dodecahydrocarbazole and the other dehydrogenated intermediates, the TOF of the dodecahydrocarbazole dehydrogenation reaction was still about 80 times higher than the corresponding value for dodecahydrofluorene dehydrogenation.

Chapter 6

Density functional theory study of dodecahydro-N-ethylcarbazole dehydrogenation over a Pd catalyst

A version of this chapter is to be submitted:
F. Sotoodeh and K.J. Smith. Density Functional Theory Study of Dodecahydro-N-ethylcarbazole Dehydrogenation over a Pd Catalyst, to be submitted.

6.1 Introduction

Organic heteroaromatic compounds such as carbazole and N-ethylcarbazole have high gravimetric storage capacity as discussed earlier, and their hydrogenated forms can release hydrogen at low temperatures of less than 473 K and therefore are potential candidates for hydrogen storage and recovery. As indicated in Chapter 4, dehydrogenation of dodecahydro-N-ethylcarbazole was found to be structure sensitive. In a DFT study by Crawford et al. [53] on the mechanism of 1,2,3,4-tetrahydrocarbazole dehydrogenation over a Pd catalyst, it was shown that the reaction proceeded through a flat 1,2,3,4-tetrahydrocarbazole adsorption geometry involving several Pd surface sites, indicative of a structure sensitive reaction. Adsorption of tetracene over a Ru surface was also reported to be flat requiring multiple Ru surface atoms [110]. Investigation of the adsorptions of quinoline on a Pt cluster reported by Vargas et al. [92], also indicated that several Pt atoms on the surface were involved in the adsorption. From the experimental and theoretical studies on benzene adsorption on Pd(111) it was revealed that depending on the surface coverage, benzene is adsorbed parallel with the surface (through the interaction of π electrons) or in a tilted geometry [132–137] with multiple Pd atoms involved in the adsorption.

As discussed in Chapter 4, it was found that the dehydrogenation reaction of dodecahydro-N-ethylcarbazole was structure sensitive and a modified Pd catalyst resulted in 100 % selectivity to the product N-ethylcarbazole in a significantly shorter reaction time. In the present chapter, density functional theory (DFT) calculations are used to study the dehydrogenation reaction network of dodecahydro-N-ethylcarbazole over a Pd(111) surface and to better understand the observed dehydrogenation reaction pathway, the product distribution and the structure sensitivity of the reaction. Furthermore, the obtained results for the adsorption geometry of dodecahydro-N-ethylcarbazole are compared to those of dodecahydrocarbazole and dodecahydrofluorene, two other candidates for H_2 recovery for transport applications, in order to understand the slow H_2 recovery reaction rate observed experimentally for the two latter compounds.

6.2 Computational methods

The DFT calculations were performed using DMol^3 [138, 139] program and the graphical molecular displays were generated with Materials Studio 4.4.0.0. (Accelrys Software Inc.). The geometry of the reactant and the products were optimized using the double-numeric quality basis set (DNP) with the gradient-corrected GGA functional of Becke [74] and PBE description of exchange and correlation effects [140, 141]. For the numerical integration, a Fermi smearing of 2×10^{-3} Ha (1 Ha = 27.21 eV), a real-space cut-off of 4.0 $\AA$ and the MEDIUM quality mesh size of the program (using about 1000 grid points for each atom in the calculation) were used.

Different possible geometries of the reactant and product molecules were optimized in order to identify the most probable isomers. Adsorption geometries of the most probable isomers of the reactant and products on Pd(111) surface were examined to determine the first adsorption sites. For this purpose, the Pd(111) surface was modeled by periodic slabs of four Pd layers with a 30 $\AA$ vacuum region between the slabs, and a (3×3) supercell was created to provide adequate surface. For each adsorption case, the molecule and the top layer of the Pd(111) surface were allowed to relax. Density functional semi-core pseudopotentials (DSPP) were used for the Pd substrate. The tolerances of energy, gradient, and displacement convergence were 2×10^{-5} Ha, 4×10^{-3} Ha/$\AA$, and 5×10^{-3} $\AA$, respectively. Adsorption energies were determined by subtracting the energies of the molecule in vacuum and the Pd(111) surface from the energy of the adsorption system, as follows,

$$E_{adsorption} = E_{adsorbed\ molecule/surface} - E_{molecule\ in\ vacuum} - E_{surface} \qquad (6.1)$$

Where in this equation $E_{adsorbed\ molecule/surface}$ is the energy of the adsorption system, $E_{molecule\ in\ vacuum}$ is the energy of the adsorbed molecule in vacuum, and $E_{surface}$ is the energy of the surface.

6.3 Results and discussion

6.3.1 Molecular structures

Dodecahydro-N-ethylcarbazole

Figure 6.1 and 6.2 shows the chemical structure of dodecahydro-N-ethylcarbazole molecule with a label assigned to H and C atoms, respectively.

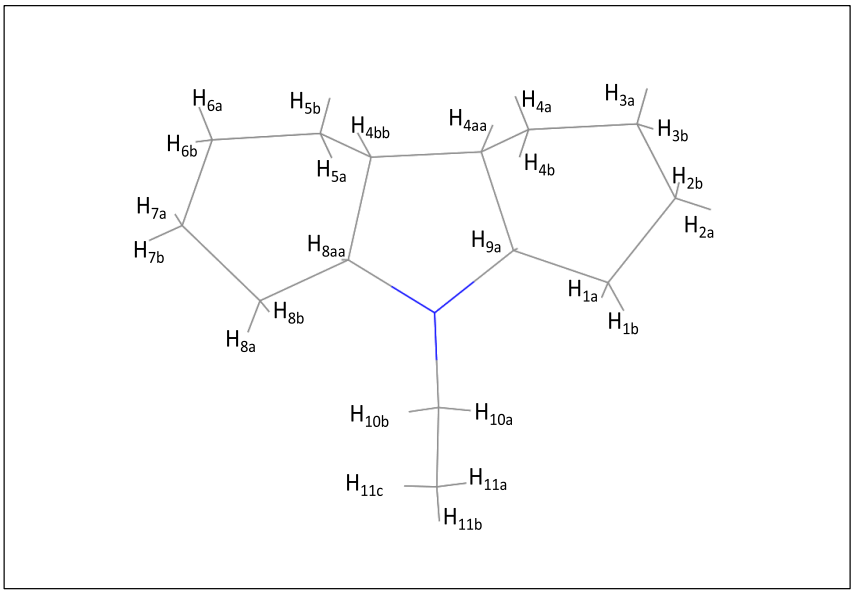

Figure 6.1: Chemical structure of dodecahydro-N-ethylcarbazole with labeled H atoms

The geometries of different isomers of the dodecahydro-N-ethylcarbazole molecule, the dehydrogenation reactant, were optimized to find the most probable isomers. Dodecahydro-N-ethylcarbazole molecule has a non-flat, distorted chemical structure. Table 6.1 compares the optimized structure and the total and binding energies

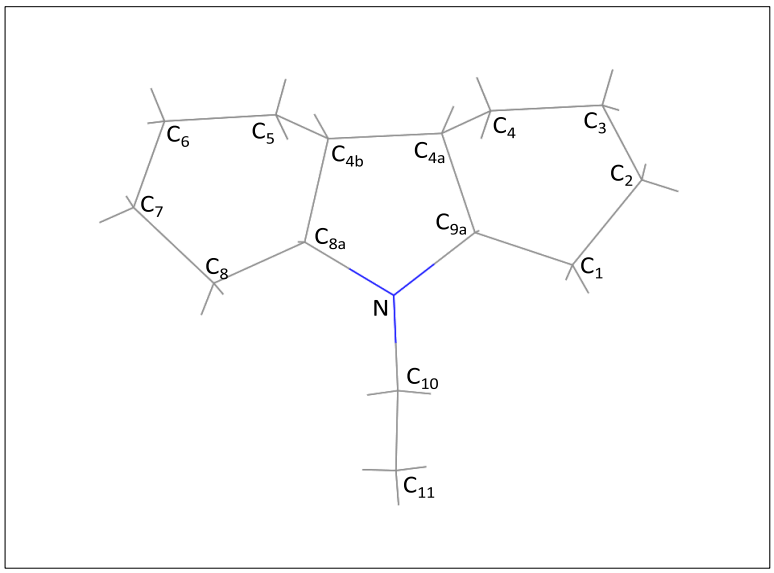

Figure 6.2: Chemical structure of dodecahydro-N-ethylcarbazole with labeled C and N atoms. For dodecahydrofluorene, N is replaced by C_9.

of the most probable isomers of dodecahydro-N-ethylcarbazole in vacuum.

The optimized geometries of the isomers were obtained by changing the position of the H atom in the 5-membered ring. As in Table 6.1, isomer No. 1 was found to have total and binding energies of -602.6875 Ha and -6.5514 Ha, respectively. The two 6-membered rings of isomer No. 1 are symmetric with respect to the yz plane and all four H atoms in the 5-membered ring face down. With this configuration, the ethyl group and the two 6-membered rings tilt away upwards. In isomer No. 2, with total and binding energies of -602.6886 Ha and -6.5524 Ha, H_{4aa} (refer to Figures 6.1 and 6.2 for atoms labeling) faces up whereas the other three H atoms in the 5-membered ring face down. The absolute value of the binding energy of this isomer was found to be 3 kJ/mol higher than isomer No. 1 (1 Ha = 2625.5 kJ/mol). The higher binding energy of isomer No. 1 implies more stability of this isomer in vacuum. In isomer No. 3 however two of H atoms in the 5-membered ring are in the opposite direction with the other two. The calculated total and binding energies for this isomer are -602.6848 Ha and -6.5487 Ha, respectively. The

Table 6.1: Optimized geometries and energies of the most probable isomers of dodecahydro-N-ethylcarbazole in vacuum

Isomer No.	Top view	Front view	Energy (a.u.[a]): Total (Binding)
1	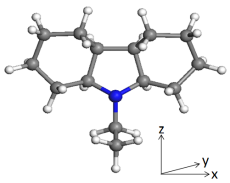	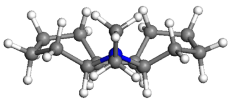	-602.6875 (-6.5514)
2	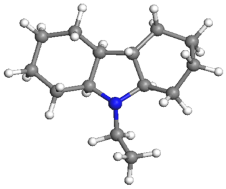	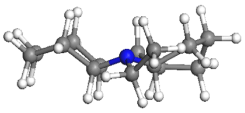	-602.6886 (-6.5524)
3	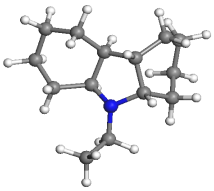	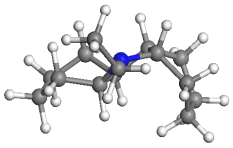	-602.6848 (-6.5487)

[a] Atomic unit or Hartree (Ha), 1 a.u. = 27.211 eV = 2625.5 kJ/mol.

existence of three stable isomers for dodecahydro-N-ethylcarbazole was confirmed experimentally by observing three separate peaks from GC/MS liquid sample analysis of hydrogenation experiments of N-ethylcarbazole reported previously by the authors [107], with one dominant and two small peaks. Eblagon et al. [96] also reported three peaks for dodecahydro-N-ethylcarbazole in the hydrogenation reaction of N-ethylcarbazole.

Decahydro-N-ethylcarbazole

The optimized geometries of different possible isomers of decahydro-N-ethylcarbazole are shown in Table 6.2.

Table 6.2: Chemical structures and energies of decahydro-N-ethylcarbazole isomers in vacuum; the structures with symmetric double bond on the left 6-membered rings are not shown due to having the same energy.

No.	Double bond position	Chemical structure	Energy (a.u.): Total (Binding)
1	C_{4a}-C_{9a}	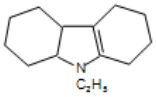	-601.49 (-6.35)
2	C_{9a}-C_1	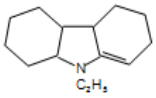	-601.48 (-6.34)
3	C_1-C_2	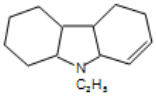	-601.47 (-6.33)
4	C_2-C_3	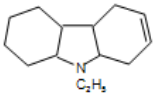	-601.47 (-6.33)
5	C_3-C_4	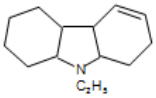	-601.47 (-6.33)
6	C_4-C_{4a}	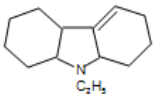	-601.48 (-6.34)
7	C_{4a}-C_{4b}	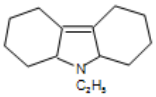	-601.47 (-6.34)

It was found that isomer No. 1 wherein one of the bonds in the 5-membered ring is dehydrogenated had the most stable structure with total and binding energy of -601.49 Ha and -6.35 Ha, respectively. The smallest energy difference between this isomer and the other examined ones is 26 kJ/mol, indicating that isomer No. 1 is likely the most stable isomer of decahydro-N-ethylcarbazole. As opposed to the hydrogenation reaction of N-ethylcarbazole where decahydro-N-

ethylcarbazole was reported as one of the intermediates produced in small quantities [107], this compound was not observed during the dehydrogenation reactions [106].

Octahydro-N-ethylcarbazole

Table 6.3 illustrates the optimized geometries and chemical structures of different isomers of octahydro-N-ethylcarbazole.

Table 6.3: Chemical structures and energies of octahydro-N-ethylcarbazole isomers in vacuum.

No.	Double bond position	Chemical structure	Energy (a.u.): Total (Binding)
1	C_{4a}-C_{9a} C_{4b}-C_{8a}	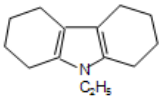	-600.32 (-6.18)
2	C_{4b}-C_{8a} C_5-C_6	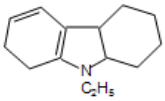	-600.27 (-6.13)
3	C_5-C_6 C_7-C_8	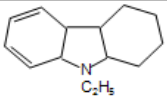	-600.25 (-6.12)
4	C_{4b}-C_{8a} C_7-C_8	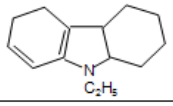	-600.27 (-6.13)
5	C_{4b}-C_{8a} C_1-C_2	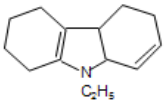	-600.27 (-6.13)
6	C_{4b}-C_{8a} C_6-C_7	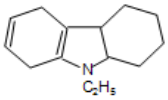	-600.27 (-6.13)
7	C_{4b}-C_{8a} C_3-C_4	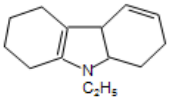	-600.27 (-6.13)

It is seen that isomer No. 1 in which the 5-membered ring is unsaturated had the highest absolute value of the total and binding energies (-600.3 Ha and -6.2 Ha, respectively). The energy difference of at least 131 kJ/mol between this isomer and the other isomers indicates that the suggested structure for isomer No. 1 most likely represents the structure of the produced octahydro-N-ethylcarbazole observed in the hydrogenation/dehydrogenation reactions [106].

Unlike dodecahydro-N-ethylcarbazole for which three different isomers were identified, only one peak in the GC/MS analysis of the liquid samples was detected for octahydro-N-ethylcarbazole implying that only one of the isomers of octahydro-N-ethylcarbazole is produced in the hydrogenation/dehydrogenation reactions. The same structure for octahydro-N-ethylcarbazole was reported in the work reported by Eblagon et al. [96] on the hydrogenation of N-ethylcarbazole by comparing the energy difference between the octahydro-N-ethylcarbazole isomers and N-ethylcarbazole molecule.

Hexahydro-N-ethylcarbazole

Table 6.4 shows the isomers of hexahydro-N-ethylcarbazole.

This molecule was reported as one of the intermediates of the hydrogenation reaction of N-ethylcarbazole which was produced in small amounts [107]. However, this intermediate was not observed in the dehydrogenation reactions. Among the three isomers shown in Table 6.4, isomer No. 1 and 2 have very similar total and binding energies. In these two isomers, the 5-membered ring and one of the bonds in the sextets are dehydrogenated. However, the most stable structure for hexahydro-N-ethylcarbazole molecule was found to be isomer No. 3 with 53 kJ/mol energy difference, in which one of the 6-membered rings is completely dehydrogenated. The higher stability of this isomer of hexahydro-N-ethylcarbazole, compared to the other two, is expected as partial dehydrogenation of one of the 6-membered rings results in the loss of resonance of the sextet and hence increasing instability of the molecule [106, 142]. Isomer No.3 was also found to be the stable structure of hexahydro-N-ethylcarbazole in other work on the hydrogenation of N-ethylcarbazole [96].

Table 6.4: Chemical structures and energies of hexahydro-N-ethylcarbazole isomers in vacuum.

No.	Double bond position	Chemical structure	Energy (a.u.): Total (Binding)
1	C_{4a}-C_{9a} C_{4b}-C_{8a} C_1-C_2	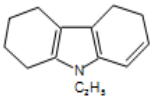	-599.09 (-5.95)
2	C_{4a}-C_{9a} C_{4b}-C_{8a} C_3-C_4	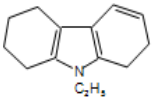	-599.09 (-5.96)
3	C_{4a}-C_{9a} C_1-C_2 C_3-C_4	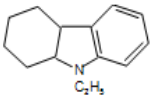	-599.11 (-5.97)

Tetrahydro-N-ethylcarbazole

Geometries of different isomers of tetrahydro-N-ethylcarbazole were optimized as summarized in Table 6.5.

It was found that isomer No. 2 in which the 5-membered ring and one of the 6-membered rings are unsaturated had the most stable structure in vacuum with at least 79 kJ/mol energy diference with the other isomers. The calculated total and binding energies were -597.9 Ha and -5.8 Ha, respectively. The same structure was reported by Crawford et al. [53] in the study of the adsorption of 1,2,3,4-tetrahydrocarbazole molecule on Pd(111) surface through the 5-membered and the aromatic rings for which the dehydrogenation reaction was initiated by removing the hydrogen atoms from the aliphatic rings. In work on N-ethylcarbazole hydrogenation, the same structure was reported for tetrahydro-N-ethylcarbazole in the suggested hydrogenation reaction network [96].

Table 6.5: Chemical structures and energies of tetrahydro-N-ethylcarbazole isomers in vacuum.

No.	Double bond position	Chemical structure	Energy (a.u.): Total (Binding)
1	C_1-C_2 C_3-C_4 C_5-C_6 C_7-C_8	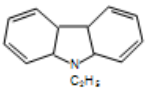	-597.78 (-5.69)
2	C_{4a}-C_{9a} C_{4b}-C_{8a} C_5-C_6 C_7-C_8	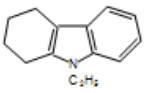	-597.93 (-5.79)
3	C_{4a}-C_{9a} C_{4b}-C_{8a} C_5-C_6 C_3-C_4	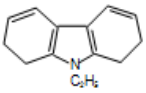	-597.88 (-5.74)
4	C_{4a}-C_{9a} C_{4b}-C_{8a} C_5-C_6 C_1-C_2	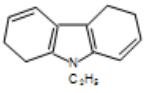	-597.88 (-5.75)
5	C_{4b}-C_{8a} C_5-C_6 C_7-C_8 C_3-C_4	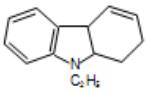	-597.89 (-5.75)
6	C_5-C_6 C_7-C_8 C_{4a}-C_{9a} C_3-C_4	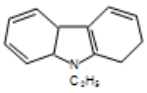	-597.84 (-5.69)
7	C_5-C_6 C_7-C_8 C_{4a}-C_{9a} C_1-C_2	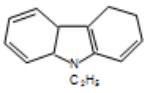	-597.83 (-5.69)
8	C_5-C_6 C_7-C_8 C_{4b}-C_{8a} C_{9a}-C_1	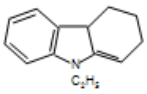	-597.90 (-5.76)
9	C_5-C_6 C_7-C_8 C_{4b}-C_{8a} C_4-C_{4a}	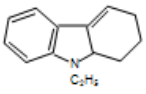	-597.90 (-5.76)

6.3.2 Dodecahydro-N-ethylcarbazole adsorption on the Pd(111) surface

Benzene adsorption structure is often used as a model system for the adsorption of aromatic compounds on transition metal surfaces [143]. Ab initio studies of the ad-

sorption of other aromatic molecules on transition metals have been limited, however, because of the large size of the aromatic molecules and thus the large number of transition metal atoms required to create an appropriate model of the metal surface. Larger molecules such as dodecahydro-N-ethylcarbazole also increase the number of possible adsorption orientations. The fcc(111) surface is an ideal substrate in that it is highly symmetric. In addition, it is also the closest-packed facet and the thermodynamically most stable [144]. Therefore, in the present work, the Pd(111) surface was chosen to study the adsorption and the dehydrogenation mechanism of dodecahydro-N-ethylcarbazole and to explain the observed dehydrogenation reaction network.

Eight adsorption modes with respect to each axial C-H bond positioned above a Pd atom (referred to as atop adsorption) were considered for the adsorption of dodecahydro-N-ethylcarbazole isomer No. 1 to the Pd(111) surface. As seen in Figure 6.3, the hollow/atop adsorption mode with respect to the 5-membered ring and the axial C-H bonds were distinguished, respectively.

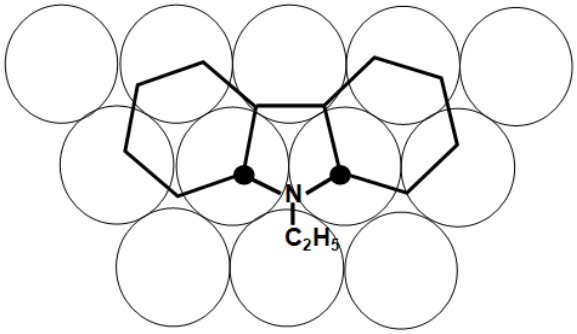

Figure 6.3: Hollow/atop adsorption of dodecahydro-N-ethylcarbazole isomer No. 1 on Pd(111); hollow with respect to the 5-membered ring; atop with respect to the axial C-H bonds. The dots indicate the position of the two stretched axial C-H bonds.

Among the four axial C-H bonds in the 5-membered ring and the two axial C-H bonds (perpendicular to the Pd(111) surface) in each of the 6-membered rings, atop adsorptions of dodecahydro-N-ethylcarbazole through H_{9a} and H_{8aa} atoms were found to be favorable and had very similar adsorption energies of -95.0 kJ/mol and -94.6 kJ/mol, respectively. As seen in Figure 6.3, the 5-membered ring is adsorbed on the hollow site of the Pd(111) surface and the two axial C-H bonds next to the N heteroatom are at atop position. The detailed structural properties of the adsorbed dodecahydro-N-ethylcarbazole molecule are summarized in Table 6.6. The weakening of the C-H bonds are characterized by a significant increase in the axial C_{9a}-H_{9a} and C_{8a}-H_{8aa} bond distance from 1.11 $\AA$ to about 1.16 $\AA$ as shown in Table 6.6.

Table 6.6: Bond lengths change for dodecahydro-N-ethylcarbazole's isomers atop adsorption on Pd(111).

No.	Adsorbing hydrogen	Adsorption energy (kJ/mol)	C-H distance, gas phase ($\AA$)	C-H distance, adsorbed ($\AA$)	H-Pd distance, adsorbed ($\AA$)
1	H_{9a}	-95.0	C_{9a}-H_{9a}: 1.11	1.16	1.99
			C_{8a}-H_{8aa}: 1.11	1.15	2.05
	H_{4aa}	-88.8	1.10	1.10	2.66
	H_{4bb}	-86.7	1.10	1.11	2.60
	H_{8aa}	-94.6	C_{8a}-H_{8aa}: 1.11	1.16	2.01
			C_{9a}-H_{9a}: 1.11	1.15	2.08
	H_{2b}	-93.1	1.10	1.11	2.49
	H_{3a}	-44.7	1.10	1.11	2.49
	H_{6a}	-36.8	1.10	1.12	2.26
	H_{7a}	-94.2	C_7-H_{7a}: 1.10	1.11	2.73
			C_{8a}-H_{8aa}:1.11	1.16	2.00
			C_{9a}-H_{9a}: 1.11	1.15	2.16
2	H_{9a}	-93.0	C_{9a}-H_{9a}: 1.12	1.15	2.22
			C_{8a}-H_{8aa}: 1.11	1.15	2.16
3	H_{3a}	-42.4	C_3-H_{3a}: 1.10	1.11	2.35
			C_6-H_{6a}: 1.10	1.12	2.19

This bond increase is larger than the increase from 1.11 $\AA$ to about 1.13 $\AA$ for the axial C-H bonds in cyclohexane [143] and likely explains the higher adsorption energy of -95 kJ/mol for dodecahydro-N-ethylcarbazole compared to -26.8 kJ/-mol for cyclohexane adsorption on Pt(111) surface. Comparing to the 1.6 $\AA$ bond

length of atop adsorbed H on Pt [145], this C-H bond increase is significant taking into account the obtained long H-Pt bond length of 2.0 *Å*. Figure 6.4-a shows the optimized geometry of dodecahydro-N-ethylcarbazole hollow/atop adsorption on Pd(111) surface with the stretched axial C_{9a}-H_{9a} and C_{8a}-H_{8aa} bonds.

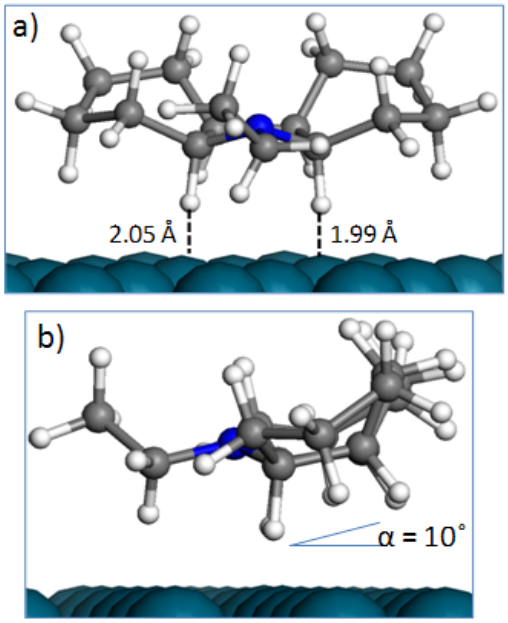

Figure 6.4: Optimized geometry of dodecahydro-N-ethylcarbazole isomer No. 1 hollow/atop adsorption on Pd(111) surface; (a) front view, (b) side view with N-Pd distance of 3.84 *Å* and the 5-membered ring at an angle of 10° to the surface.

The stretch in the two axial C-H bonds made the molecule tilt from the surface as seen in Figure 6.4-b, where the plane of 5-membered ring is tilted away at about 10° away from the Pd(111) surface. Adsorption through H_{7a} and H_{2b} where in each case the H atom was positioned approximately above a Pd atom, led to a similar adsorption geometry to that of H_{9a} and H_{8aa} with adsorption energies of -94.2 kJ/mol and -93.1 kJ/mol, respectively. The geometry optimization of both systems led to H_{7a} and H_{2b} atoms to tilt away from the surface with a small C-H bond length increase from 1.10 *Å* to 1.11 *Å*, and H_{9a} and H_{8aa} relocate at atop

position again with the corresponding C-H bond length increase from 1.11 $\AA$ to about 1.16 $\AA$. This confirmed the stability of the adsorption mode through the axial H_{9a} and H_{8aa}. Positioning H_{4aa} and H_{4bb} on top of a Pd atom however, led to weaker adsorption energies of -88.8 kJ/mol and -86.7 kJ/mol, respectively, with little increase in C_{4b}-H_{4bb} bond length from 1.10 $\AA$ to 1.11 $\AA$ and no change in the C_{4a}-H_{4aa} bond distance. Adsorption through H_{3a} and H_{6a} resulted in the least favorable adsorption mode with the adsorption energies of -44.7 kJ/mol and -36.8 kJ/mol, respectively, and the C_3-H_{3a} bond length increase from 1.10 $\AA$ to 1.11 $\AA$ and C_6-H_{6a} bond length increase from 1.10 $\AA$ to 1.12 $\AA$. An adsorption energy of -93.0 kJ/mol and similar adsorbed geometry was obtained for dodecahydro-N-ethylcarbazole isomer No. 2 compared to that of isomer No. 1 through H_{9a}. The C_{9a}-H_{9a} and C_{8a}-H_{8aa} bond distances increased from their corresponding values in the gas phase to 1.15 $\AA$, confirming the 5-membered ring as the favorable site for the first C-H bond weakening in the molecule. Isomer No. 3 adsorbed weakly to the surface with adsorption energy of -42.4 kJ/mol, with C_3-H_{3a} bond distance change from 1.10 $\AA$ to 1.11 $\AA$ and C_6-H_{6a} bond distance change from 1.10 $\AA$ to 1.12 $\AA$. As mentioned before, isomers No. 1, 2 and 3 were found to be the most stable isomers of dodecahydro-N-ethylcarbazole in the present work.

Hirshfield charges were obtained to have a better understanding of the reason for the observed stretch and weakening in the axial C-H bonds in the adsorption of dodecahydro-N-ethylcarbazole isomer No. 1 (shown in Table 6.7). Density of states of the adsorbed dodecahydro-N-ethylcarbazole were also calculated as illustrated in Figure 6.5.

From Table 6.7 it is seen that electron density of the two axial hydrogen atoms nearest to the surface increases significantly when adsorbed. The increase for H_{9a} and H_{8aa} is about 0.06 a.u., larger than the 0.04 a.u. increase for the axial hydrogen atoms reported for cyclohexane upon adsorption on Pt(111) and the 0.03 a.u. increase for the carbon atoms of adsorbed benzene on Pt(111) [144]. The charge increase for the other two hydrogen atoms in the 5-membered ring, H_{4aa} and H_{4bb}, is about 0.03 a.u. upon adsorption. The charge increase at the four axial hydrogen atoms in the 5-membered ring is compensated by a decrease in charge of about 0.06 a.u. for the corresponding surface Pd atoms. The charge on the N heteroatom however, decreases by about 0.06 a.u., indicating some interaction of

Table 6.7: Hirshfield charges on dodecahydro-N-ethylcarbazole.

Atom	Gas phase (a.u.)	Pd(111)	Hollow/atop (a.u.)	Charge change (a.u.)
H_{9a}	0.0110		-0.0470	-0.0580
H_{8aa}	0.0109		-0.0447	-0.0556
H_{4aa}	0.0275		-0.0026	-0.0301
H_{4bb}	0.0273		-0.0086	-0.0359
N	-0.0910		-0.0338	0.0572
$Pd_{9a}{}^{a}$		-0.0156	0.0479	0.0635
$Pd_{8aa}{}^{a}$		-0.0156	0.0441	0.0597
Pd_{4aa}-$_{4bb}{}^{a}$		-0.0156	0.0364	0.0520
C_{9a}	0.0138		0.0235	0.0097
C_{8a}	0.0136		0.0240	0.0104
C_{4a}	-0.0205		-0.0273	-0.0068
C_{4b}	-0.0201		-0.0259	-0.0058

[a]Refers to Pd atoms under the corresponding H atom.

the N heteroatom to the closest Pd atom on the surface. Overall, the total charge on the dodecahydro-N-ethylcarbazole molecule increases by 0.22 a.u. upon adsorption corresponding to a net electron density flow from the Pd surface to the dodecahydro-N-ethylcarbazole molecule. This electron density flow is mostly located at the two axial H_{9a} and H8aa atoms.

The projected density of states (PDOS) shown in Figure 6.5 indicates stabilization energies for the dodecahydro-N-ethylcarbazole molecule adsorbed atop on Pd(111) through H_{9a} and H_{8aa} by comparing the characteristic peaks for dodecahydro-N-ethylcarbazole molecule in vacuum (Figure 6.5-a) with that in the adsorbed state (Figure 6.5-b). The peaks corresponding to the energy value between 0.2-0.3 Ha for dodecahydro-N-ethylcarbazole in vacuum shown in Figure 6.5-a) are broadened and shifted to the negative values. The electronic states belonging to the adsorbed configuration of dodecahydro-N-ethylcarbazole in Figure 6.5-b, show the contributions from s and p-orbitals. The states above -0.35 Ha mainly have p characteristics, while the features below -0.45 Ha mainly come from s-orbitals. By comparing the density of states (DOS) of dodecahydro-N-ethylcarbazole in vacuum (Figure 6.5-a) with the adsorbed one in Figure 6.5-b, it is clear that the density of states of s and p-orbitals close the Fermi level, have changed when the molecule is adsorbed. Figure 6.5-c shows the change in the DOS of the Pd d-states (Figure

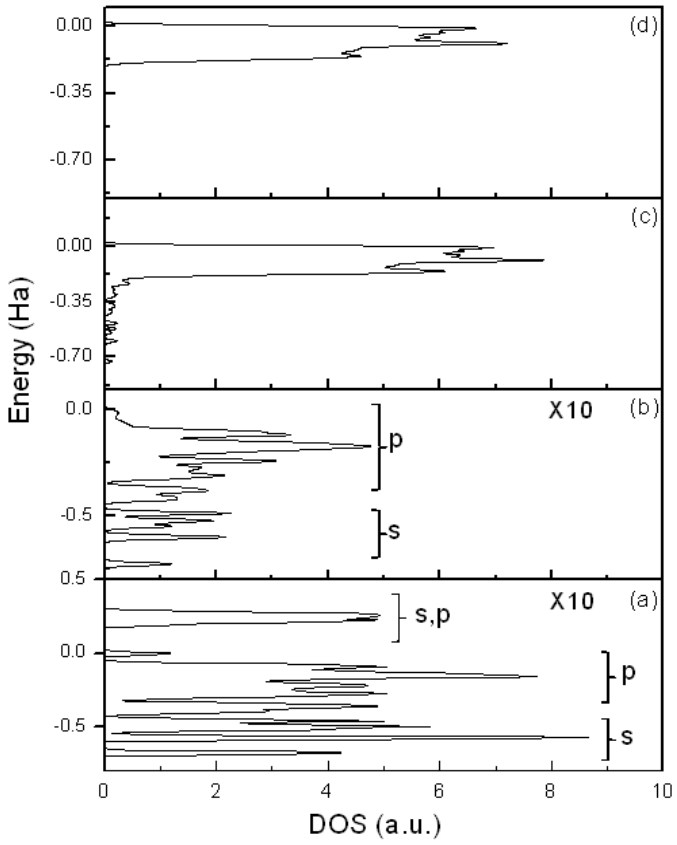

Figure 6.5: Densities of states for; (a) dodecahydro-N-ethylcarbazole in vacuum; (b) adsorbed dodecahydro-N-ethylcarbazole molecule; (c) dodecahydro-N-ethylcarbazole on Pd(111); (d) Pd(111) d-states.

6.5-d) upon adsorption of dodechydro-N-ethylcarbazole molecule.

6.3.3 Dodecahydro-N-ethylcarbazole dehydrogenation steps

For the dodecahydro-N-ethylcarbazole adsorption mode shown in Figure 6.4, H_{9a} and H_{8aa} are in close proximity to the Pd surface atoms and can react with the surface. The H_{9a} and H_{8aa} atoms are 1.99 $\AA$ and 2.05 $\AA$ from the nearest Pd surface atoms, respectively. As discussed earlier, from the C-H bond changes shown in

Table 6.6, it is clear that the routes involving an initial cleavage of either H_{9a} or H_{8aa} are the most likely. In order to gain some insight into the relative reactivity of the four sequential hydrogen removal steps, two reaction pathways shown in Figure 6.6 were considered in the present work for dehydrogenation of dodecahydro-N-ethylcarbazole to octahydro-N-ethylcarbazole over Pd(111).

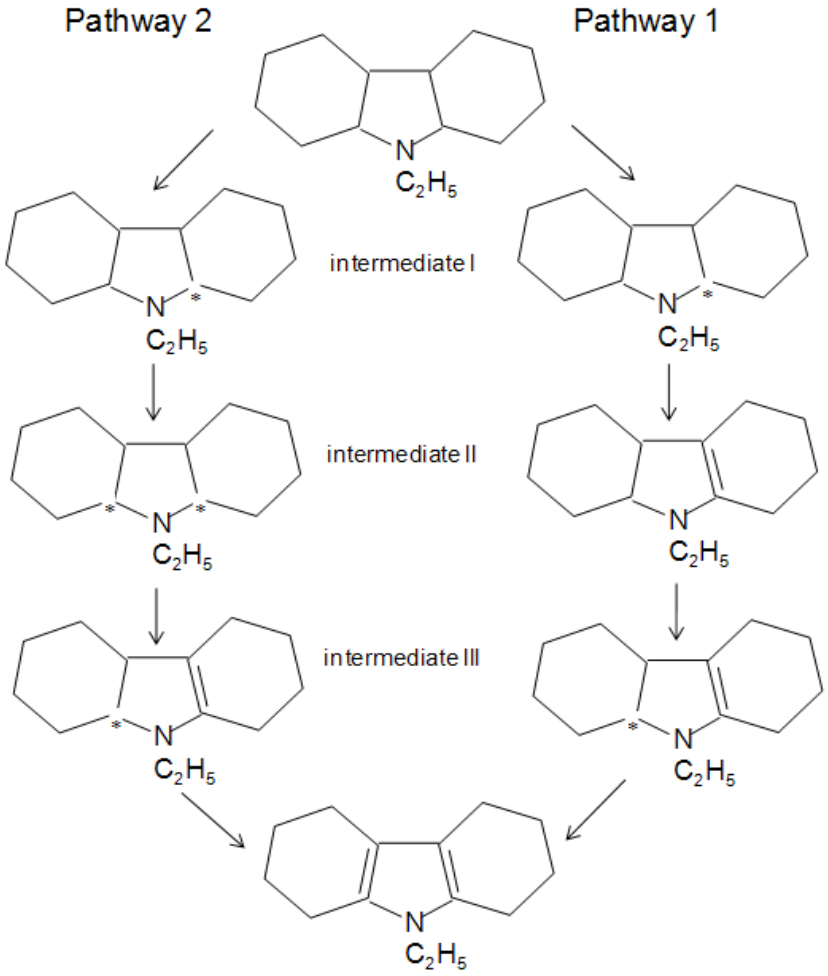

Figure 6.6: Two possible dehydrogenation pathways for dodecahydro-N-ethylcarbazole conversion to octahydro-N-ethylcarbazole; for both pathways dehydrogenation begins with dissociation of H_{9a}.

Both pathways start with dissociation of H_{9a} (intermediate I) as C_{9a}-H_{9a} showed the largest bond distance change upon adsorption of dodecahydro-N-ethylcarbazole (Table 6.6). In the reaction pathways illustrated in Figure 6.6, it is clear that the dissociation of H_{4aa} in pathway 1 and H_{8aa} in pathway 2 lead to the production of two unique intermediates denoted as intermediate II, resulting in the formation of a C=C double bond in pathway 1. This produced intermediate has the stable structure obtained for decahydro-N-ethylcarbazole (Table 6.2). Intermediate III for each pathway is produced by the third dehydrogenation step; and both species subsequently lose a further H atom to complete the dehydrogenation process. Reaction pathways 1 and 2 have been modeled over Pd(111) to determine their respective transition state energies and the reaction barriers for each of the dehydrogenation steps. As seen in Figure 6.7, removing the first hydrogen atom, H_{9a}, resulted in C_{4a}-H_{4aa} and C_{8a}-H_{8aa} bonds to stretch from an equilibrium bond length of 1.10 $\AA$ to 1.13 $\AA$ and 1.12 $\AA$, respectively.

The reaction barriers to all the dehydrogenation steps for removal of the first four hydrogen atoms are summarized in Table 6.8 and compared in Figure 6.8.

Table 6.8: Reaction barriers corresponding to the transition states (TSs) for each dehydrogenation step along the two dehydrogenation reaction pathways of dodecahydro-N-ethylcarbazole shown in Figure 6.6.

Pathway 1		Pathway 2	
Transition state (TS)	Barrier ($kJ.mol^{-1}$)	Transition state (TS)	Barrier ($kJ.mol^{-1}$)
TS1	14.1	TS1	14.1
TS2	126.3	TS2	159.5
TS3	106.5	TS3	69.1
TS4	41.6	TS4	129.6

The calculated reaction barrier for the dissociation of the C_{9a}-H_{9a} bond was 14.1 kJ/mol. For both pathways, the reactivity trend showed an increase in the energy barrier from the dehydrogenation step 1 to 2. The energy barrier decreased in both pathways from the dehydrogenation step 2 to 3. However, for the dehydrogenation step 4, the reaction barrier along pathway 1 decreased significantly, whereas a large increase in the reaction barriers from step 3 to 4 was obtained in pathway 2. From Table 6.8 it follows that the dehydrogenation pathway 1 is more

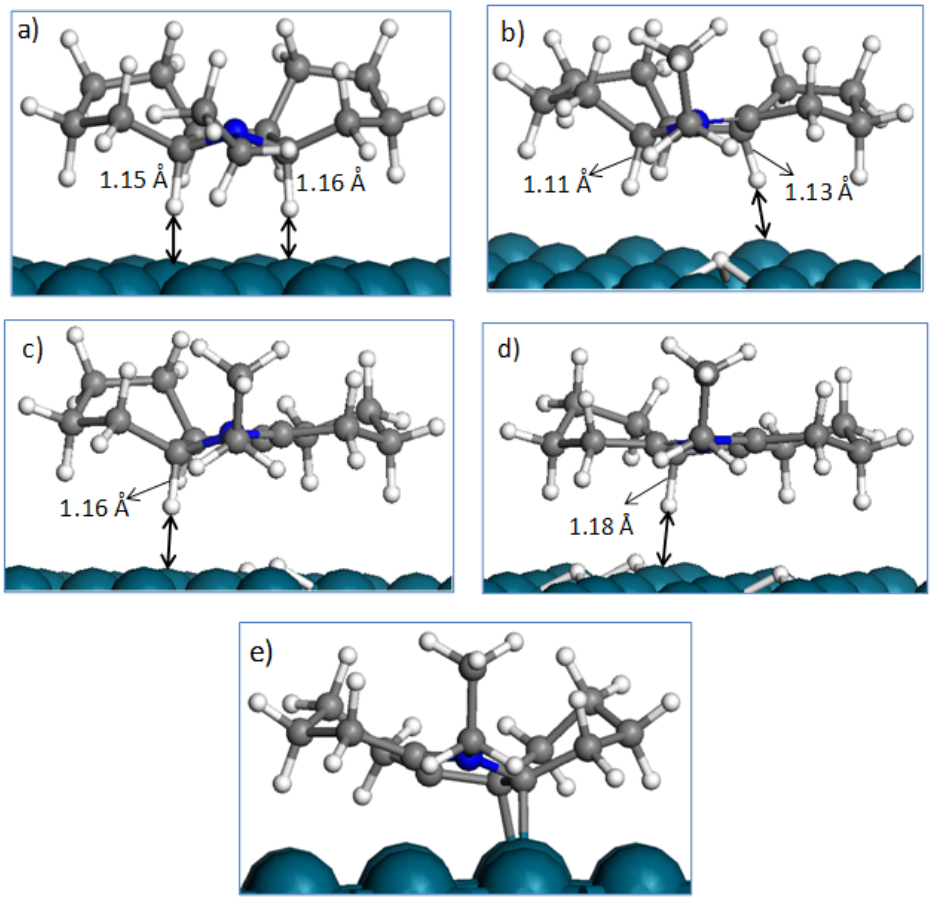

Figure 6.7: Schematic of pathway 1 for dehydrogenation of dodecahydro-N-ethylcarbazole; (a) adsorption geometry for dodecahydro-N-ethylcarbazole on Pd(111) showing the interaction between H_{9a} and H_{8aa} and the nearest Pd atoms at 1.99 and 2.05 *Å*, respectively, (b) the optimized geometry corresponding to the dissociation of C_{9a}-H_{9a} bond. The bond distance of C_{4a}-H_{4aa} and C_{8a}-H_{8aa} increased to 1.13 and 1.12 *Å*, respectively, (c) removal step of H_{4aa} with C_{8a}-H_{8aa} bond distance increased to 1.16 *Å*, (d) removal step of H8aa with C_{4b}-H_{4bb} bond distance increased to 1.18 *Å*, and (e) production of octahydro-N-ethylcarbazole.

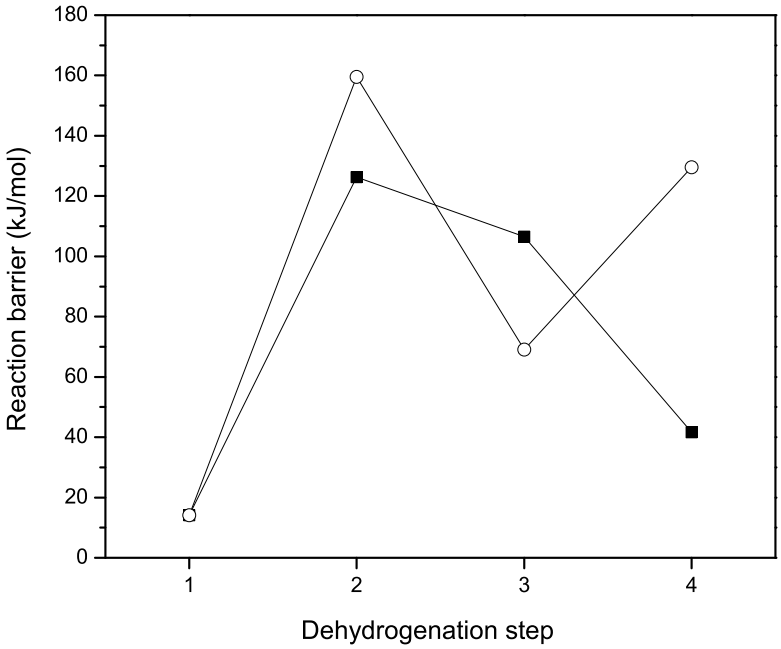

Figure 6.8: Comparison of the calculated reaction barriers for the progressive dehydrogenation of dodecahydro-N-ethylcarbazole over Pd(111) surface following the reaction pathways 1 (■) and 2 (○) illustrated in Figure 6.6.

likely, as a larger bond distance increase was observed for C_{4a}-H_{4aa} compared to C_{8a}-H_{8aa} after the 1^{st} dehydrogenation step (Figure 6.7) and the activation barrier for removal of H_{4aa} in pathway 1 was about 33 kJ/mol smaller than that of H_{8aa} in pathway 2. Also, the cleavage barrier of the 4^{th} hydrogen, H_{4bb}, leading to the formation of the 2^{nd} C=C double bond and production of octahydro-N-ethylcarbazole was 88 kJ/mol smaller in pathway 1 compared to pathway 2. As seen in both Table 6.8 and Figure 6.8, for pathway 1, the removal of the 2^{nd} hydrogen resulting in the production of decahydro-N-ethylcarbazole had the highest energy barrier, after which the hydrogen removal barriers decreased significantly. Furthermore, removal of the 2^{nd} hydrogen (H_{4aa}) resulted in a significant stretch in the C_{8a}-H_{8aa}

bond length from 1.11 $\AA$ (in vacuum) to 1.16 $\AA$ (Figure 6.7-c) indicating that the 3^{rd} H removal step is favored. This implies that decahydro-N-ethylcarbazole is, in fact, produced and consumed very quickly and confirms the experimental observations where no decahydro-N-ethylcarbazole was measured in the dehydrogenation of dodecahydro-N-ethylcarbazole.

It was found that octahydro-N-ethylcarbazole adsorbs to the surface in a di-σ mode through C_{9a} and C_{4a} atoms in the 5-membered ring with σ_{C-Pd} bond distances of 2.25 $\AA$ and 2.29 $\AA$, respectively (Figure 6.9), and an adsorption energy of -56.0 kJ/mol.

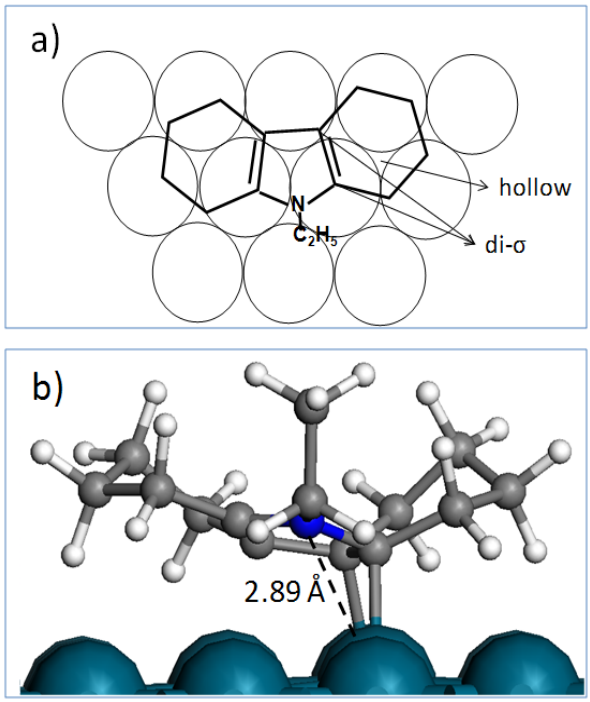

Figure 6.9: Octahydro-N-ethylcarbazole (a) aromatic hollow di-σ adsorption on Pd(111); (b) front view of the optimized geometry with N-Pd distance of 2.89 $\AA$ and the 5-membered ring at an angle of 5° to the surface.

The C-Pd bond distances are larger than the σ_{C-Pt} distances of 2.19 $\AA$ and 2.16 $\AA$ obtained for di-σ adsorption of 1,3-cyclohexadiene on Pt(111) [143] and σ_{C-Pt}

distances of 2.16 $\AA$ for adsorbed benzene [144].

Table 6.9 summarizes the structural properties of the adsorption of octahydro-N-ethylcarbazole. The C_{9a}=C_{4a} bond distance increased from 1.39 $\AA$ for the gas phase octahydro-N-ethylcarbazole molecule to 1.49 $\AA$ upon adsorption to the Pd(111) surface. This increase in the C_{9a}=C_{4a} bond distance supports the di-σ adsorption of the molecule through C_{9a} and C_{4a}. Saeys et al. [143] reported a bond distance of 1.51 $\AA$ for the C=C bond in the di-σ adsorption of 1,3-cyclohexadiene on Pt(111) surface.

Table 6.9: Selected parameters for the gas phase and adsorbed structure of octahydro-N-ethylcarbazole. C-Pd distances refer to corresponding Pd atom shown in Figure 6.9.

Variable	Gas phase ($\AA$)	Adsorbed ($\AA$)
C_{9a}-Pd	—	2.25
C_{4a}-Pd	—	2.29
C_{9a}-C_{4a}	1.39	1.49

In the optimized conformation shown in Figure 6.9, the two aliphatic rings as well as the other two C atoms in the 5-membered ring tilt away from the Pd(111) surface. Figure 6.10 compares the density of states for C_{9a} and C_{4a} in vacuum and upon adsorption to the surface obtained from periodic calculations. A significant shift and broadening of the energy levels of carbon p-orbitals are observed for both C_{9a} and C_{4a}, which likely point to the σ interaction of carbon atoms with the Pd surface.

Table 6.10 summarizes the energy barriers to the dehydrogenation steps from octahydro-N-ethylcarbazole to tetrahydro-N-ethylcarbazole.

Table 6.10: Reaction barriers corresponding to the transition states (TSs) for conversion of octahydro-N-ethylcarbazole to tetrahydro-N-ethylcarbazole.

Transition state (TS)	Removed H	Barrier (kJ.mol^{-1})
TS1	H_{1b}	137.7
TS2	H_{2b}	81.2
TS3	H_{4a}	83.9
TS4	H_{3a}	198.9

The adsorbed geometry of octahydro-N-ethylcarbazole dehydrogenation steps is also shown in Figure 6.11. Figure 6.11-a illustrates the optimized adsorbed

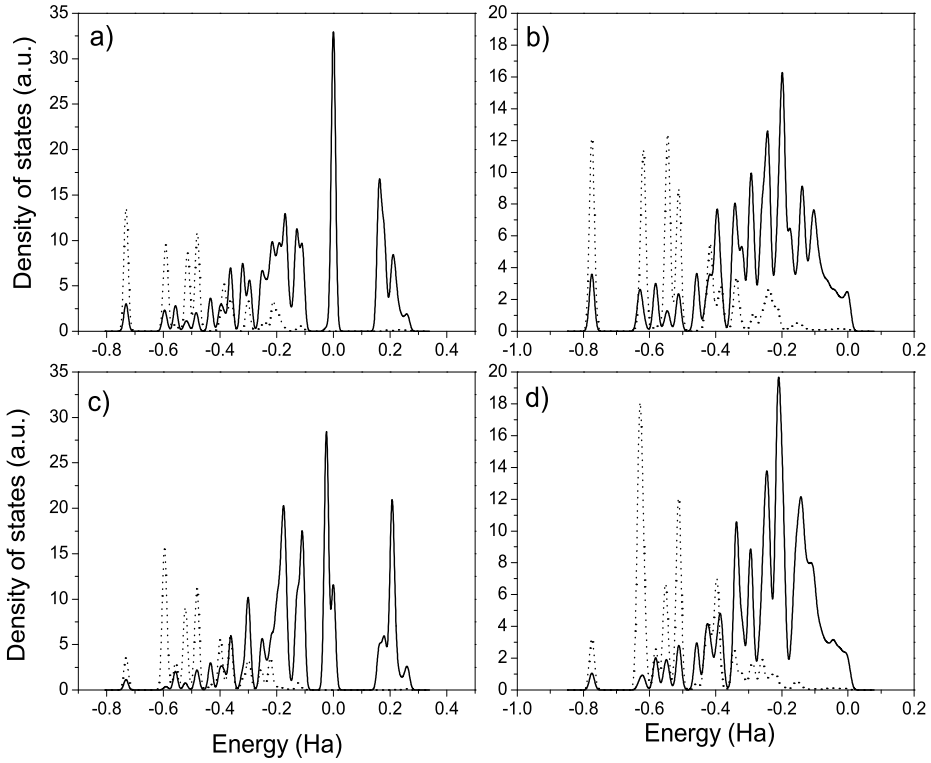

Figure 6.10: Densities of states (DOS) of octahydro-N-ethylcarbazole for; (a) C_{9a} in vacuum; (b) C_{9a} in the adsorbed molecule; (c) C_{4a} in vacuum; (d) C_{4a} in the adsorbed molecule. Dash lines represent the s-orbital and (solid line) represents the p-orbitals.

geometry of octahydro-N-ethylcarbazole with the interaction of H_{1b} atom with the surface. Both C_1-H_{1b} and C_2-H_{2b} bond distances increased to 1.11 $\AA$ upon the molecule adsorption, and therefore were likely to be the first bonds to dissociate. The energy barrier for C_2-H_{2b} cleavage was found to be 259.7 kJ/mol (not shown here), while this value was about 137.7 kJ/mol for cleavage of C_1-H_{1b} bond (Table 6.10), leading to the conclusion that dehydrogenation pathway for octahydro-N-ethylcarbazole starting from C_1-H_{1b} bond cleavage is likely more favored.

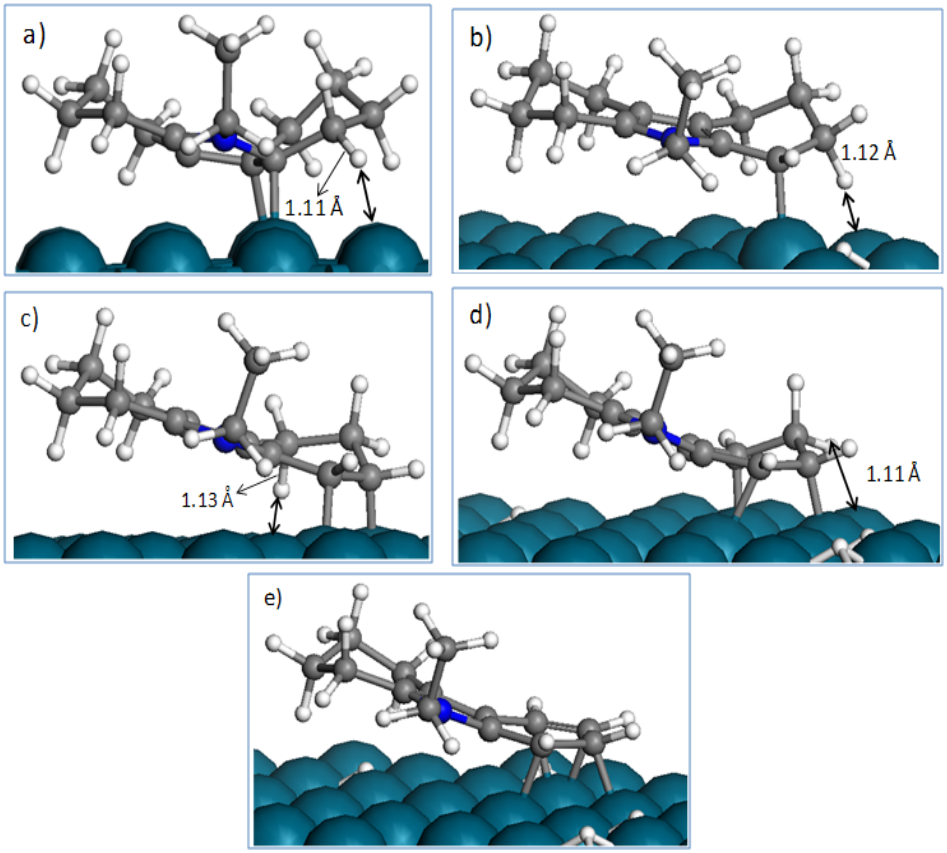

Figure 6.11: Dehydrogenation steps for octahydro-N-ethylcarbazole; (a) adsorbed geometry octahydro-N-ethylcarbazole showing the interaction between H_{1b} and the nearest Pd atom at 2.53 *Å*, (b) the optimized geometry corresponding to the dissociation of C_{9a}-H_{9a} bond and removal of H_{1b}. Interaction between H_{2b} and the nearest Pd atom at 2.24 *Å* increases, (c) increasing the interaction of H_{4a} with the nearest Pd atom at 2.16 *Å*, (d) optimized geometry corresponding to the dissociation of H_{4a} and increasing the interaction of H_{3a} with the nearest Pd atom at 2.5 *Å*, (e) production of tetrahydro-N-ethylcarbazole.

Comparing the obtained first step reaction barriers for production of octahydro-N-ethylcarbazole (14.1 kJ/mol, Table 6.8) with that of tetrahydro-N-ethylcarbazole (137.7 kJ/mol, Table 6.10), it is concluded that hydrogen removal from the 5-membered ring with a N-heteroatom is more favored than the 6-membered ring. This is in good agreement with the obtained experimental apparent activation energy of 144.3 kJ/mol for production of tetrahydro-N-ethylcarbazole [106], compared to the 67.1 kJ/mol obtained for production of octahydro-N-ethylcarbazole [106]. Figure 6.11-b illustrates the optimized geometry after removal of H_{1b}, showing the increased interaction of H_{2b} to the nearest Pd atom by an increase in C_2-H_{2b} bond distance to 1.12 $\AA$. It was noticeable that upon cleavage of C_1-H_{1b} bond, C_{9a} and C_{4a} detached from the surface and C_1 made a σ_{C-Pd} bond with the nearest Pd atom. The 2^{nd} dehydrogenation step resulted in removal of H_{2b} (Figure 6.11-c) and formation of a σ-bond between C_2 and the nearest Pd on the surface with an energy barrier of 81.2 kJ/mol. The removal of H_{2b} results in the formation of one of the hexahydro-N-ethylcarbazole isomers (Table 6.4). However, the considered dehydrogenation pathway for octahydro-N-ethylcarbazole (which is very likely to occur), does not lead to the formation of the most probable isomer of hexahydro-N-ethylcarbazole (isomer No. 3 in Table 6.4). This is in agreement with the product distribution observed in dehydrogenation reactions where no hexahydro-N-ethylcarbazole was produced. Further removal of H atoms resulted in cleavage of C_{4a}-H_{4a} and C_3-H_{3a}.

The adsorption energy of tetrahydro-N-ethylcarbazole to the Pd(111) surface was calculated as -117.5 kJ/mol, significantly smaller than the -143.8 kJ/mol value reported for the adsorption of tetrahydrocarbazole on Pd(111) [53]. The tetrahydro-N-ethylcarbazole stable adsorption geometry and structural properties are shown in Figure 6.12 and Table 6.11.

From Figure 6.12-a it is seen that the bridge adsorption of the aromatic ring of tetrahydro-N-ethylcarbazole is the favored geometry. Tetrahydro-N-ethylcarbazole adsorbs to the surface through C_{1-4} and the 5-membered ring tilts away from the surface at an angle of 25° (Figure 6.12-b) and a N-Pd distance of 3.28 $\AA$. The C_1-Pd and C_2-Pd distances are 2.24 $\AA$ and 2.25 $\AA$, respectively. These values are comparable to σ_{C-Pt} distance of 2.16 $\AA$ for adsorbed benzene and 2.17 $\AA$ for di-σ adsorbed ethane [143]. The C_3-Pd and C_4-Pd distances are longer at 2.28 $\AA$

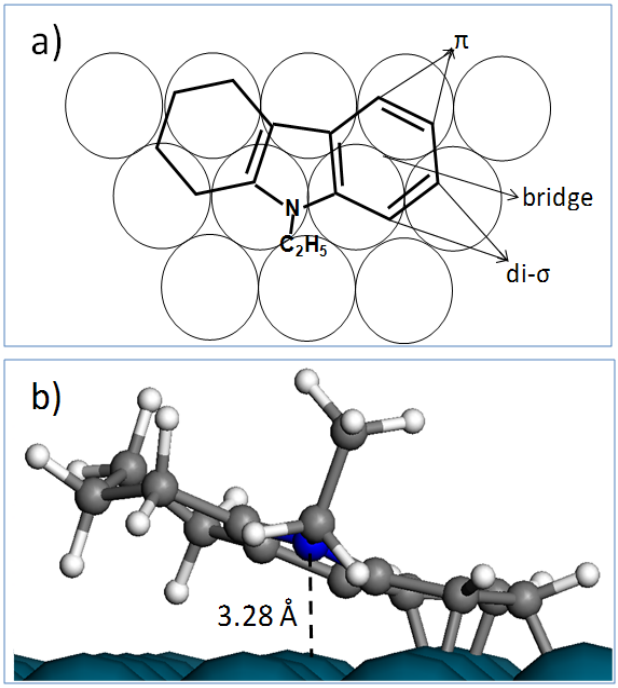

Figure 6.12: Tetrahydro-N-ethylcarbazole (a) aromatic bridge 1,2-di-σ/3,4-π adsorption on Pd(111); (b) front view of the optimized geometry with N-Pd distance of 3.28 *Å* and the 5-membered ring at an angle of 25° to the surface.

and 2.29 *Å*, respectively, more typical for π-adsorbed molecules, supported also by the larger increase observed in the C_1-C_2 bond distance of 1.46 *Å* for their σ-bonds to Pd atoms compared to 1.43 *Å* for the C_3-C_4 bond for their less strong π-adsorbed mode (Table 6.11). The obtained adsorbed geometry of tetrahydro-N-ethylcarbazole supports the dehydrogenation pathway considered for octahydro-N-ethylcarbazole, in which dehydrogenation starts by removal of hydrogen atoms from one of the sextets.

Table 6.11: Selected parameters for the gas phase and adsorbed structure of tetrahydro-N-ethylcarbazole. C-Pd distances refer to corresponding Pd atom shown in Figure 6.12.

Variable	Gas phase ($\AA$)	Adsorbed ($\AA$)
C_1-Pd	—	2.24
C_2-Pd	—	2.25
C_3-Pd	—	2.28
C_4-Pd	—	2.29
C_1-C_2	1.39	1.46
C_3-C_4	1.39	1.43

6.3.4 Dodecahydro-N-ethylcarbazole adsorption on Pd(110) surface

The structure sensitivity of the dodecahydro-N-ethylcarbazole dehydrogenation reaction was also investigated by comparing the adsorption geometry of dodecahydro-N-ethylcarbazole over a Pd(110) surface with that of Pd(111). Figure 6.13 illustrates the optimized geometry of the dodecahydro-N-ethylcarbazole adsorbed on top of the Pd(110) surface.

The molecule locates on the surface so that the interaction of the two H atoms adjacent to N, increases (Figure 6.13-a). The calculated adsorption energy on the Pd(110) surface was -83.2 kJ/mol. The C-H bond distance increase from 1.11 $\AA$ to about 1.16 $\AA$ was observed for the adsorption of the molecule over the Pd(110) surface (Figure 6.13-b) which was the same as that obtained on the Pd(111) surface. No other C-H bond distance change was identified. Figure 6.13-c shows the top view of the adsorption geometry of dodecahydro-N-ethylcarbazole. The two H atoms adjacent to the N heteroatom are in atop positions, but note that the remaining H atoms of the 5-membered ring are located above Pd atoms in the second layer of the Pd(110) surface, making H removal on this surface less likely than on the Pd(111) surface. Because of the less packed structure of the Pd(110) surface compared to the Pd(111) surface, the interaction between Pd and the remaining H atoms in the 5-membered ring is not possible. These H atoms are located above Pd atoms of the second layer of the Pd(110) surface (shown in Figure 6.13-a in black) and the distance between the H and Pd atoms is such that there is no interaction. Hence to form octahydro-N-ethylcarbazole on the Pd (110) surface would require additional desorption and re-adsorption steps that are not required on the

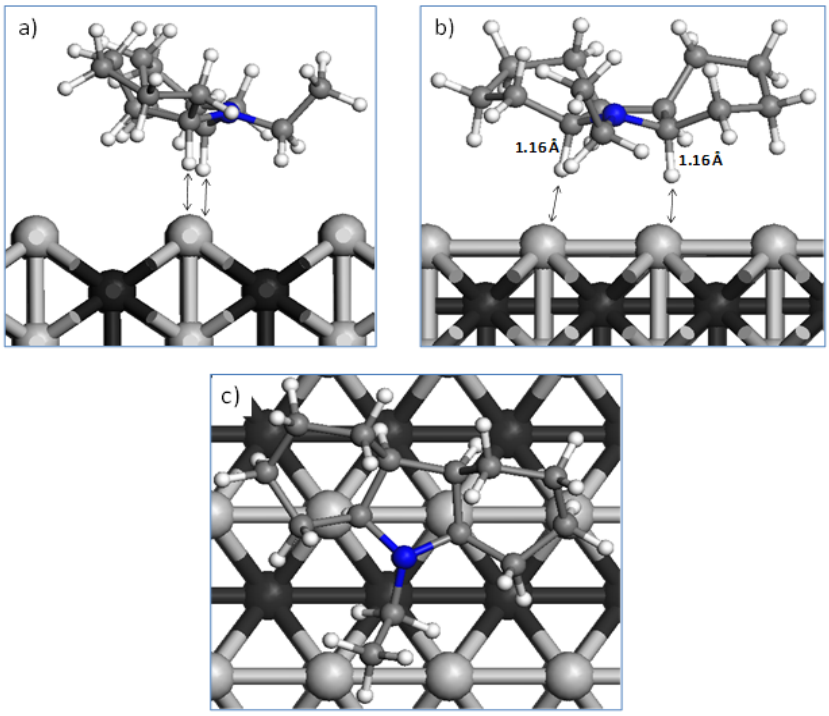

Figure 6.13: Optimized geometry of dodecahydro-N-ethylcarbazole adsorbed over Pd(110) surface; (a) side view showing the interaction of the two H atoms with the first layer Pd surface, (b) front view showing the C-H bond distances increase from 1.10 $\AA$ in vacuum to 1.16 $\AA$ upon approaching the surface , (c) top view. The molecule moves so that the two C-H bonds adjacent to N heteroatom are at atop positions over the nearest Pd atoms. Blue: N, white: H, gray: C, light gray: first layer Pd atoms, black: second layer Pd atoms.

Pd(111) surface. These observations also point to the fact that the dehydrogenation of dodecahydro-N-ethylcarbazole is structure dependent.

6.3.5 Heteroatom effect on the catalyst reactivity

The effect of the N heteroatom on the dehydrogenation reaction was studied by comparing the adsorption energies and surface/adsorbate charge transfer of dodecahydro-N-ethylcarbazole, dodecahydro-carbazole and dodecahydrofluorene molecules. Fig-

ure 6.14 compares the adsorption geometries of the three different molecules.

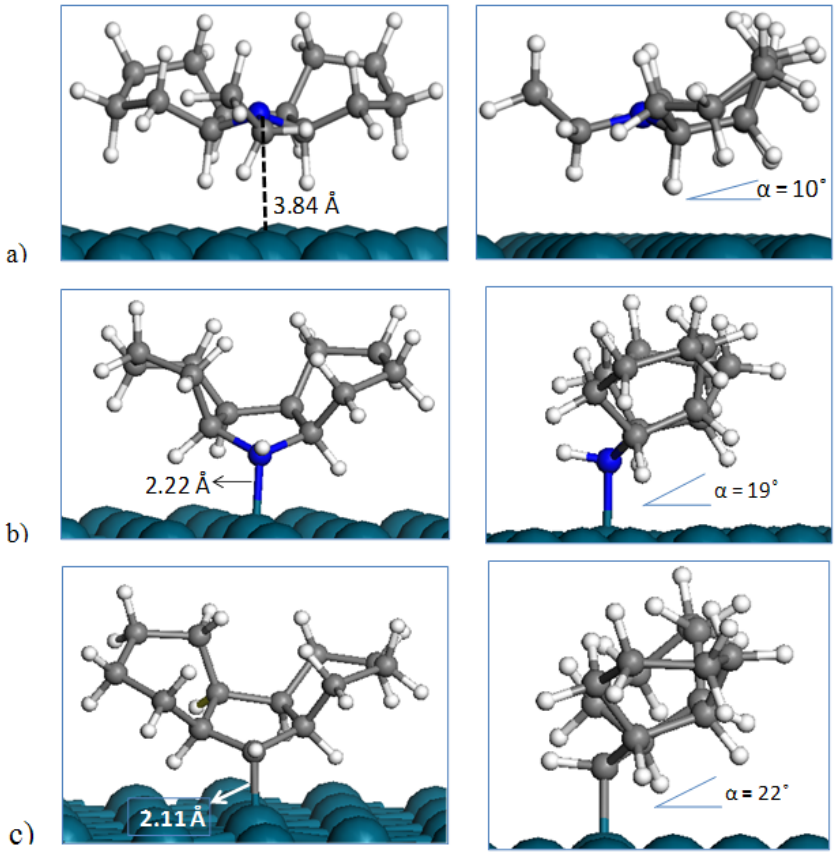

Figure 6.14: Comparison between the adsorbed structures of (a) dodecahydro-N-ethylcarbazole, (b) dodecahydrocarbazole, and (c) dodecahydrofluorene over Pd(111). (left) front view, (right) side view.

As discussed earlier, dodecahydro-N-ethylcarbazole adsorption to the Pd(111) surface was characterized by a significant stretch of C_{9a}-H_{9a} and C_{8a}-H_{8aa} bonds (Figure 6.14-a) with adsorption energy of -95.0 kJ/mol. These stretches in the C-H bonds resulted in an approximate 10° rotation of the 5-membered ring plane with respect to the axis parallel with the surface. The N heteroatom in dodecahydro-N-ethylcarbazole had a distance of 3.84 *Å* to the nearest Pd atom on the sur-

face, whereas this distance for dodecahydrocarbazole was found to be 2.22 $\AA$ (Figure 6.14-b). The shorter N-Pd distance obtained for dodecahydrocarbazole compared to dodecahydro-N-ethylcarbazole is indicative of a stronger interaction of the docecahydrocarbazole N heteroatom with the Pd(111) surface, whereas for dodecahydro-N-ethylcarbazole the ethyl group prevents the N heteroatom from interacting as strongly as that in dodecahydrocarbazole. This is also seen by the approximately 19° rotation of the plane of the 5-membered ring from the axis parallel to the Pd(111) surface (Figure 6.14-b), assisting the interaction of N atom with the surface compared to dodecahydro-N-ethylcarbazole. The adsorption energy of dodecahydrocarbazole on the Pd(111) was -109.4 kJ/mol, with an absolute value of 14 kJ/mol higher than that of dodecahydro-N-ethylcarbazole (Table 6.12).

Table 6.12: Comparison of adsorption energies.

Compound name	Adsorption energy ($kJ.mol^{-1}$)	Compound name	Adsorption energy ($kJ.mol^{-1}$)
Dodecahydro-N-ethylcarbazole	-95.0	Tetrahydro-N-ethylcarbazole	-117.5
Dodecahydrocarbazole	-109.4	Tetrahydrocarbazole	-143.8[a]
Dodecahydrofluorene	-180.8	Tetrahydrofluorene	-218.6

[a]Reported by Crawford et al. [53].

No significant change in the C-H bond distances of the 5-membered ring was observed for dodecahydrocarbazole upon adsorption (Table 6.13). The stronger interaction of N heteroatom in dodecahydrocarbazole is likely responsible for the much slower dehydrogenation reaction rate observed compared to dodecahydro-N-ethylcarbazole. Dodecahydrofluorene however, showed a much stronger adsorption than dodecahydrocarbazole and dodecahydro-N-ethylcarbazole. The N heteroatom in the dodecahydrocarbazole molecule is replaced by a C atom through which the adsorption of dodecahydrofluorene occurred (Figure 6.14-c) with a short C-Pd distance of 2.11 $\AA$. The adsorption energy of dodecahydrofluorene was found to be -180.8 kJ/mol, which points to a significantly stronger surface adsorption of the molecule compared to dodecahydrocarbazole or dodecahydro-N-ethylcarbazole. The 5-memebred ring plane had a rotation of about 22° in this case shown in Figure 6.14-c, as expected by the observed short C-Pd distance of 2.11 $\AA$.

Compared to the large increases in the C-H bond lengths of the 5-membered ring in the adsorbed dodecahydro-N-ethylcarbazole (Table 6.6), no significant increase was observed for doecahydrofluorene, as summarized in Table 6.13.

Table 6.13: Bond lengths change for dodecahydrofluorene and dodecahydrocarbazole upon adsorption to Pd(111) surface.

Dodecahydro-fluorene	Vacuum	Adsorbed	Dodecahydro-carbazole	Vacuum	Adsorbed
Adsorbing atom	C-H (Å)	C-H (Å)	Adsorbing atom	C-H (Å)	C-H (Å)
C_9-Pd (2.11 Å)	C_9-H_9: 1.09	1.10	N-Pd (2.22 Å)	N-H_9: 1.02	1.02
	C_{9a}-H_{9a}: 1.11	1.12		C_{9a}-H_{9a}: 1.11	1.11
	C_{8a}-H_{8aa}: 1.11	1.13		C_{8a}-H_{8aa}: 1.11	1.11
	C_{4a}-H_{4aa}: 1.10	1.11		C_{4a}-H_{4aa}: 1.10	1.10
	C_{4b}-H_{4bb}: 1.10	1.10		C_{4b}-H_{4bb}: 1.10	1.11

Hirshfield charges for dodecahydrocarbazole and dodecahydrofluorene upon adsorption to the surface were obtained from the periodic calculations in order to make a comparison with dodecahydro-N-ethylcarbazole. The charge decrease of about 0.08 a.u. on the N heteroatom in dodecahydrocarbazole upon adsorption due to the N lone pair charge donation (Table 6.14), together with the large charge decrease of 0.13 a.u. on the attaching Pd atom is responsible for the formed σ_{N-Pd} bond.

The total charge on the dodecahydrocarbazole molecule increased by 0.095 a.u., which is almost two times smaller than the 0.22 a.u. charge increase on dodecahydro-N-ethylcarbazole molecule upon adsorption. This can be explained by the larger amount of electron donation through N in dodecahydrocarbazole that is closer to the surface in this case, which compensates the net charge transfer through the Pd surface to the molecule. The smaller overall charge increase on the molecule is likely the reason for the small change in the C-H bond distances of the 5-membered ring for the adsorbed dodecahydrocarbazole and therefore, a slower dehydrogenation rate observed for dodecahydrocarbazole compared to dodecahydro-N-ethylcarbazole. For dodecahydrofluorene on the other hand, the charge on the replaced C atom increased by about 0.05 a.u.(Table 6.15) with a significant charge decrease of about 0.16 a.u. on the attaching Pd atom. The overall charge on the dodecahydrofluorene molecule was increased by about 0.31 a.u., in-

Table 6.14: Hirshfield charges for dodecahydrocarbazole in vacuum and adsorbed structure.

Atom	Gas phase (a.u.)	Pd(111) (a.u.)	Adsorbed (a.u.)	Charge change (a.u.)
H_{9a}	0.0200		-0.0382	-0.0582
H_{8aa}	0.0236		-0.0216	-0.0452
H_{4aa}	0.0283		0.0011	-0.0272
H_{4bb}	0.0297		-0.0243	-0.054
$Pd_9{}^a$		-0.0156	0.1134	0.129
$Pd_{9a}{}^a$		-0.0156	0.0426	0.0582
$Pd_{8aa}{}^a$		-0.0156	0.0225	0.0381
$Pd_{4aa-4bb}{}^a$		-0.0156	0.0359	0.0515
N	-0.1701		-0.0918	0.0783
C_{9a}	-0.0148		0.0042	0.019
C_{8a}	-0.0112		0.0037	0.0149
C_{4a}	-0.0185		-0.0277	-0.0092
C_{4b}	-0.0185		-0.0278	-0.0093

[a]Refers to Pd atoms under the corresponding H atom.

dicative of a net flow of charge transfer from the surface to the molecule which is mostly concentrated on the σ bond formed between the C and the Pd and is responsible for the strong adsorption of the molecule to the surface. The very small change in the C-H bond distances of the molecule can explain the very slow H_2 recovery from this molecule as observed experimentally (see Chapter 5).

The adsorption geometries of tetrahydro-N-ethylcarbazole, tetrahydrocarbazole and tetrahydrofluorene molecules on Pd (111) are shown in Figure 6.15. Tetrahydro-N-ethylcarbazole adsorption occurred through four carbon atoms in the aromatic 6-membered ring, with the 5-membered ring and the aliphatic 6-membered ring tilted away from the surface. The N atom distance from the nearest Pd atom was 3.28 $\AA$ (Figure 6.15-a). The adsorption energies are summarized in Table 6.12. Lower adsorption energy of tetrahydro-N-ethylcarbazole compared to tetrahydrocarbazole, can be attributed to the effect of the ethyl group. The steric hindrance of the ethyl group does not allow the molecule to interact strongly with the catalyst through the N atom. As can be seen in Figure 6.15-b, tetrahydrocarbazole adsorbs through six carbon atoms in the aromatic ring, with a shorter distance (3.05 $\AA$) from the N atom to the nearest surface atom. The stronger adsorption of tetrahydrocarbazole

Table 6.15: Hirshfield charges for dodecahydrofluorene in vacuum and adsorbed structure.

Atom	Gas phase (a.u.)	Pd(111) (a.u.)	Adsorbed (a.u.)	Charge change (a.u.)
H_{9a}	0.0273		-0.0326	-0.0599
H_{8aa}	0.0281		-0.0415	-0.0696
H_{4aa}	0.0255		-0.0203	-0.0458
H_{4bb}	0.0263		0.0125	-0.0138
$Pd_9{}^a$		-0.0156	0.1395	0.1551
$Pd_{9a}{}^a$		-0.0156	0.0500	0.0656
$Pd_{8aa}{}^a$		-0.0156	0.0563	0.0719
$Pd_{4aa-4bb}{}^a$		-0.0156	0.0382	0.0538
$C_9{}^b$	-0.0332		-0.0823	-0.0491
C_{9a}	-0.0266		-0.0402	-0.0136
C_{8a}	-0.0294		-0.0333	-0.0039
C_{4a}	-0.0187		-0.0276	-0.0089
C_{4b}	-0.0184		-0.0236	-0.0052

[a] Refers to Pd atoms under the corresponding H atom.
[b] Replaced for N.

compared to tetrahydro-N-ethylcarbazole is also clear from the higher adsorption energy of tetrahydrocarbazole (Table 6.12).

A similar adsorption geometry for tetrahydrocarbazole was obtained by the DFT work of Crawford et al. [53], who reported an adsorption energy of -143.8 kJ/mol. The optimized geometry of the adsorbed tetrahydrofluorene on the other hand, suggested that the molecule adsorbs to the surface through the 6 carbon atoms in the aromatic ring, as well as the N replaced carbon atom with an even shorter distance of 2.89 $\AA$ than tetrahydrocarbazole to the attaching Pd atom. The adsorption energy of tetrahydrofluorene was found to be -218.6 kJ/mol, significantly higher than that of tetrahydro-N-ethylcarbazole and tetrahydrocarbazole, implying a much stronger adsorption of tetrahydrofluorene to the Pd(111) surface. The very slow dehydrogenation reaction rate observed for dodecahydrofluorene (as discussed in Chapter 5) is very well supported by the strong adsorption of dodecahydrofluorene and tetrahydrofluorene to the catalyst surface.

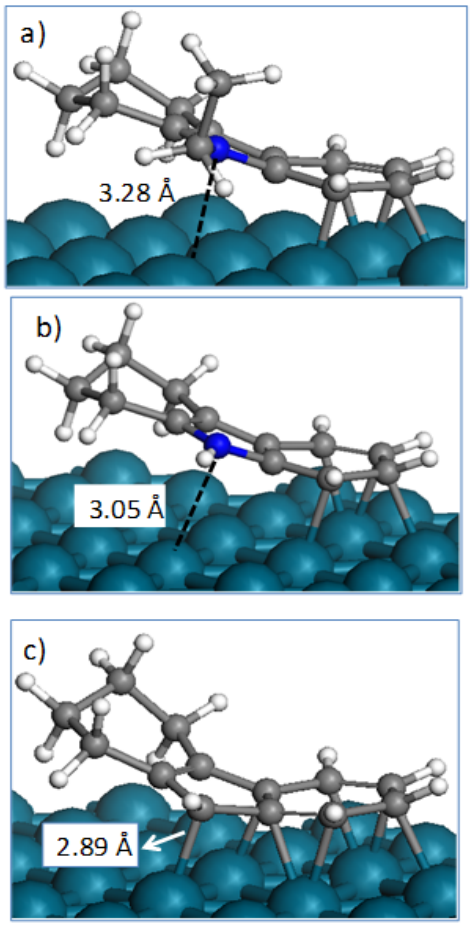

Figure 6.15: Comparison between the adsorbed structures of; (a) tetrahydro-N-ethylcarbazole, (b) tetrahydrocarbazole, and (c) tetrahydrofluorene, over Pd(111).

6.4 Conclusion

The structure sensitivity of the dodecahydro-N-ethylcarbazole dehydrogenation reaction was confirmed by the DFT results indicating that dodecahydro-N-ethylcarbazole interacts with the Pd(111) surface involving several Pd atoms. The dehydrogenation reaction was found to start by removing of the H atoms from the 5-membered ring to produce octahydro-N-ethylcarbazole, followed by stepwise H removal of one of the aliphatic rings to produce tetrahydro-N-ethylcarbazole. The obtained results supported the observed experimental product distribution for dodecahydro-N-ethylcarbazole dehydrogenation, with no production of hexahydro-N-ethylcarbazole and decahydro-Nethylcarbazole. The strong interaction of the N heteroatom in dodecahydrocarbazole was found to be responsible for the slower dehydrogenation reaction rate of doecahydrocarbazole compared to that of dodecahydro-N-ethylcarbazole. Dodecahydrofluorene was found to dehydrogenate much slower than dodecahydrocarbazole, due to its very strong adsorption to the catalyst surface. It can be concluded that the N heteroatom favors the dehydrogenation reaction of dodecahydrocarbazole compared to dodecahydrofluorene, although it was shown that dodecahydrocarbazole dehydrogenation product inhibition decreased the reaction rate due to the strong interaction of the N with the surface.

Chapter 7

Conclusions and recommendations

7.1 Conclusion

Organic heteroaromatic compounds were chosen for the hydrogen storage study of this work, due to their thermal stability and high H_2 storage capacity. H_2 storage was carried out through hydrogenation reactions over a commercial Ru catalyst and the kinetics of the reactions were quantified. The hydrogenated compounds were tested for H_2 recovery through a series of dehydrogenation reactions at different temperatures over Pd/SiO_2 catalysts prepared over a range of Pd loadings with different particle sizes and metal dispersions. The kinetics of the dehydrogenation reactions were studied and the obtained experimental results were confirmed by theoretical DFT calculations.

In the hydrogenation of N-ethylcarbazole and carbazole, two H_2 storage candidates, it was found that N-ethylcarbazole hydrogenates much faster than carbazole. The slower hydrogenation reaction rate obtained for carbazole compared to N-ethylcarbazole was attributed to the strong interaction of the N heteroatom electron pair with the catalyst surface, which poisons the catalyst. In the case of N-ethylcarbazole and its hydrogenated products, the steric hindrance by the ethyl group prevents the N from interacting strongly with the surface and hence, increase the hydrogenation rate. From the obtained results, it is concluded that N-ethylcarbazole is a better candidate for H_2 storage applications than carbazole.

The measured TOFs of the dehydrogenation of dodecahydro-N-ethylcarbazole over Pd catalysts with a range of Pd loadings and particle sizes, suggested that the dehydrogenation reaction of dodecahydro-N-ethylcarbazole is structure sensitive. The results were well described by the model proposed by Murzin [117] supporting the structure sensitivity of the reactions. It was found that modifying the catalyst preparation method by calcining the catalyst in He rather than air had a significant effect on the catalyst activity and selectivity. Complete conversion and 100 % selectivity to the completely dehydrogenated product, N-ethylcarbazole, was achieved over a 4 wt% Pd/SiO_2 catalyst with a Pd particle diameter of $\sim$9 nm. The results were a significant improvement compared to previously reported dehydrogenation results for organic (hetero)aromatic compounds [53, 54, 56, 106].

The effect of the N heteroatom on the dehydrogenation reaction rates of the organic (hetero)aromatics was studied by comparing the dehydrogenation reaction rate of dodecahydro-N-ethylcarbazole, dodecahydrocarbazole and dodecahydrofluorene. Dodecahydro-N-ethylcarbazole had the highest reaction TOF compared to the other two compounds. Dodecahydrocarbazole showed a smaller TOF compared to dodecahydro-N-ethylcarbazole most likely due to catalyst poisoning through the N atom. The dehydrogenation TOF for dodecahydrofluorene was found to be even lower than dodecahydrocarbazole. From the measured TOFs of the dehydrogenation reactions it was concluded that the presence of a N heteroatom favors the dehydrogenation of organic polyaromatic compounds, although catalyst poisoning occurs due to the interaction of the N electron pair with the catalyst surface. Therefore, compounds with N heteroatoms are more favored for H_2 recovery applications. Furthermore, comparing the dehydrogenation of dodecahydro-N-ethylcarbazole and dodecahydrocarbazole, it is concluded that dodecahydro-N-ethylcarbazole is a better H_2 recovery candidate than dodecahydrocarbazole.

Density functional theory calculations were used to model the dehydrogenation reaction of dodecahydro-N-ethylcarbazole, to study the obtained product distribustion observed experimentally, and to investigate the effect of the N heteroatom in the dehydrogenation reactions of organic (hetero)aromatics. The obtained results confirmed the structure sensitivity of the dehydrogenation reactions of dodecahydro-N-ethylcarbazole and dodecahydrocarbazole. The DFT results supported the dehydrogenation product distribution observed experimentally for dodecahydro-N-ethylcarbazle dehydrogenation. Also, the small dehydrogenation reaction TOFs obtained for dodecahydrocarbazole and dodecahydrofluorene was attributed to the strong adsorption of these two compounds and their dehydrogenated intermediates to the catalyst surface.

7.2 Recommendations

1. Heteroatom effect:
   In the present work, it was shown that the presence of a N heteroatom de-

creases the dehydrogenation barrier and improves the dehydrogenation reaction rate significantly. The effect of other heteroatoms (such as S, P and O) in the chemical structure of the organic polyaromatic compounds on the dehydrogenation reaction rates, should also be studied. Both a theoretical approach by comparing the electronic structure of the heteroatom and its effect on the adsorption structure and energies of the organic compound, and an experimental approach through dehydrogenation reactions, should be used.

Furthermore, the effect of having more than one heteroatom in the chemical structure of the organic heteroaromatics on the adsorption energies and dehydrogenation reaction barrier should be investigated.

2. Effect of the chemical structure of the organic heteroaromatics:
   DFT calculations could be used to study the applicability of organic compounds having more fused rings or a larger branch attached to the heteroatom in their chemical structure for on-board H_2 recovery by comparing their adsorption energies to the catalyst surface with the currently studied ones.

3. Use of catalyst promoters:
   Catalyst promoters such as Ni or K can be used in the Pd catalysts to study their effect on the dehydrogenation reaction TOF and selectivity.

4. Recyclability, cost and system modification:
   The catalysts used in the present work need to be tested for recyclability in order to be used for transport applications. This can be done by recovering the catalyst after dehydrogenation reaction through filtration and drying of the catalyst. The recovered catalyst can then be tested in a fresh reactant solution in decalin for recyclability. Also, Pd is known to form a Pd−hydride phase by adsorbing the hydrogen present in the system and this might lead to some deactivation of the catalyst after many recycling attempts. The possible deactivation of Pd catalyst can be further studied and other alternatives such as Pt can be investigated. Furthermore, the dehydrogenation system studied in this thesis is a batch reactor in which the solid catalyst is dispersed by continuous mixing. For an on-board dehydrogenation application, a fixed

catalytic bed may be required in order to be able to use the catalyst for many cycles.

Material cost also needs to be addressed. As was indicated earlier, about 5 kg of H_2 is required for a fuel cell vehicle to be able to travel approximately 300 miles. This will mean that $\sim$1.5 kg catalyst and $\sim$85 kg of the pure reactant will be required on board the vehicle. Considering the cost of approximately $ 1/kg [146] for the reactant, and $ 10/kg for the catalyst [146] precursor, the total cost of reactant and the catalyst will be approximately $ 100/5 kg H_2 ($ 20/kg H_2). Having the D.O.E. criterion of total system cost of $ 133/kg H_2 for year 2010 [21], the presented result in this work are promising in terms of cost of H_2 recovery.

Bibliography

[1] V. Balema. *Material Matters, Hydrogen Storage Materials*, volume 2, chapter Introduction, page 2. Aldrich, 2007. → pages 2

[2] J.Y. Lee, M. Yoo, K. Cha, T.W. Lim, and T. Hur. Life cycle cost analysis to examine the economical feasibility of hydrogen as an alternative fuel. *International Journal of Hydrogen Energy*, 34:4243–4255, 2009. → pages

[3] T. Pregger, D. Graf, W. Krewitt, C. Sattler, M. Roeb, and S. Moller. Prospects of solar thermal hydrogen production processes. *International Journal of Hydrogen Energy*, 34:4256–4267, 2009. → pages

[4] A.S. Joshi, I. Dincer, and B.V. Reddy. Solar hydrogen production: A comparative performance assessment . *International Journal of Hydrogen Energy*, (doi:10.1016/j.ijhydene.2010.11.122), 2010. → pages

[5] A. Steinfeld. Solar thermochemical production of hydrogen, a review. *Solar Energy*, 78(5):60315, 2005. → pages

[6] R.J. Mantz and H. De Battista. Hydrogen production from idle generation capacity of wind turbines. *International Journal of Hydrogen Energy*, 33:4291–4300, 2008. → pages

[7] M. Santarelli, M. Cali, and S. Macagno. Design and analysis of stand-alone hydrogen energy systems with different renewable sources. *International Journal of Hydrogen Energy*, 29(15):157186, 2004. → pages 2

[8] J. Chen, Y. Lu, L. Guo, X. Zhang, and P. Xiao. Hydrogen production by biomass gasification in supercritical water using concentrated solar energy: System development and proof of concept. *International Journal of Hydrogen Energy*, 35:7134–7141, 2010. → pages 2

[9] Y.J. Lu, H. Jin, L.J. Guo, X.M. Zhang, C.Q. Cao, and X. Guo. Hydrogen productionnext term by previous termbiomassnext term gasification in

supercritical water with a fluidized bed reactor. *International Journal of Hydrogen Energy*, 33:6066–6075, 2008. → pages

[10] P.C. Hulteberg and H.T. Karlsson. A study of combined biomass gasification and electrolysis for hydrogen production. *International Journal of Hydrogen Energy*, 34:772–782, 2009. → pages 2

[11] E.D. Naeemi, D. Graham, and B.F. Norton. *Material Matters, Hydrogen Storage Materials*, volume 2, chapter Introducing HYDRNOL: Organic Liquid Storage for Hydrogen, page 23. Aldrich, 2007. → pages 2, 10, 13

[12] L.M. DAS. On-board hydrogen storage systems for automotive application . *International Journal of Hydrogen Energy*, 21(9):789–800, 1996. → pages 2, 7

[13] R.H. Crabtree. Hydrogen storage in liquid organic heterocycles. *Energy and Environmental Science*, 1:134–138, 2008. → pages 2

[14] *Material Matters, Hydrogen Storage Materials*, volume 2. Aldrich, 2007. → pages 6, 7, 8, 24

[15] G. Pez, A. Scott, A.C. Cooper, and H. Cheng H. Hydrogen Storage by Reversible Hydrogenation of Pi-conjugated Substrates. *US patents*, (Pub. No. 2857A1), 2005. → pages 2, 12, 13, 14

[16] G. Pez, A. Scott, A.C. Cooper, and H. Cheng H. Hydrogen Storage by Reversible Hydrogenation of Pi-conjugated Substrates. *US patents*, (7101530B2), 2006. → pages 12, 13, 14, 24, 40, 51, 79, 94

[17] G. Pez, A. Scott, A.C. Cooper, and H. Cheng H. Hydrogen Storage by Reversible Hydrogenation of Pi-conjugated Substrates. *US patents*, (7429372), 2008. → pages 2, 24

[18] A.C. Cooper, K.M. Campbell, and G.P. Pez. An Integrated Hydrogen Storage and Delivery Approach Using Organic Liquid Phase Carriers. Technical Report 16, Lyon France, 13 - 16 June 2006. → pages 4

[19] Global Greenhouse Warming.com. → pages 4, 5

[20] S. Satyapal, J. Petrovic, C. Read, G. Thomas, and G. Ordaz. The U.S. Department of Energy's National Hydrogen Storage Project: Progress Towards Meeting Hydrogen-Powered‘ Vehicle Requirements. *Catalysis Today*, 120:246–256, 2007. → pages 5, 24, 51

[21] Targets for Onboard Hydrogen Storage Systems for Light-Duty Vehicles. *US Department of Energy, Office of Energy Efficiency and Renewable Energy and The FreedomCAR and Fuel Partnership*, September 2009. → pages 5, 136

[22] T. Zhang, L.T. Fan, W.P. Walawender, M. Fan, A.E. Bland, T. Zuo, and D.W. Collins. Hydrogen storage on carbon adsorbents: a review. *Environanotechnology*, pages 137–163, 2010. → pages 5

[23] C. Read, G. Thomas, G. Ordaz, and S. Satyapal. *Material Matters, Hydrogen Storage Materials*, volume 2, chapter U.S. department of energys system targets for on-board vehicular hydrogen storage, page 3. Aldrich, 2007. → pages 5, 6, 13

[24] C.L. Aardahl and S.D. Rassat. Overview of systems considerations for on-board chemical hydrogen storage. *International Journal of Hydrogen Energy*, 34:6676–6683, 2009. → pages 5

[25] A. Leon (Ed.). *Hydrogen Technology, Mobile and Portable Applications*. Green Energy and Technology. Springer, 2008. → pages 6, 7, 9, 10

[26] M. Diwan, D. Hanna, and A. Varma. Method to release hydrogen from ammonia borane for portable fuel cell applications. *International Journal of Hydrogen Energy*, 35:577–584, 2010. → pages 6, 8

[27] G.L. Soloveichik. *Material Matters, Hydrogen Storage Materials*, volume 2, chapter Metal Borohydrides as Hydrogen Storage Materials, page 11. Aldrich, 2007. → pages 6, 9

[28] A.C. Cooper, H. Cheng, and G.P. Pez. Hydrogen Storage by Reversible Hydrogenation of Liquid-phase Hydrogen Carriers. *Air Products and Chemicals Inc.*, 2006. → pages 6

[29] T.Q. Hua, R.K. Ahluwalia, J.K. Peng, M. Kromer, S. Lasher, K. McKenney, K. Law, and J. Sinha. Technical assessment of compressed hydrogen storage tank systems for automotive applications. *International Journal of Hydrogen Energy*, 36:3037–3049, 2011. → pages 7

[30] R.K. Ahluwalia and J.K. Peng. Dynamics of cryogenic hydrogen storage in insulated pressure vessels for automotive applications. *International Journal of Hydrogen Energy*, 33:4622–4633, 2008. → pages 7

[31] A. Karkamkar, C. Aardahl, and T. Autrey. *Material Matters, Hydrogen Storage Materials*, volume 2, chapter Recent Developments on Hydrogen Release from Ammonia Borane, page 6. Aldrich, 2007. → pages 7, 8

[32] J. Yang, A. Sudik, D.J. Siegel, Sh. Hirano, A.R. Drews, and C.M. Wolverton. Hydrogen Storage Materials Containing Ammonia Borane. *United States Patent Application Publication*, (US 2011 0008693A1), January 2011. → pages 8

[33] H.L. Jiang and Q. Xu. Catalytic hydrolysis of ammonia borane for chemical hydrogen storage. *Catalysis Today*, (doi:10.1016/j.cattod.2010.09.019), 2010. → pages 8

[34] F.H. Stephens, V. Pons, and R.T .Baker. Ammoniaborane: the Hydrogen Source par Excellence? *The Royal Society of Chemistry, Dalton Transactions*, page 26132626, 2007. → pages 8

[35] Y. Wu and R. M. Mohring. Sodium Borohydride for Hydrogen Storage. *Prepr. Pap.-Am. Chem. Soc., Div. Fuel Chem.*, 48(2):940, 2003. → pages 9

[36] I.E. Ture, F.O. Tabakoglu, and G. Kurtulus. Economical Aspects of Sodium Borohydride for Hydrogen Storage. In *16th World Hydrogen Energy Conference (WHEC)*, Lyon France, 13-16 June 2006. → pages 9

[37] Y. Kojima and T. Haga. Recycling Process of Sodium Metaborate to Sodium Borohydride. *International Journal of Hydrogen Energy*, 28:989 993, 2003. → pages 9

[38] S. Li, M. Willis, and P. Jena. Reaction intermediates during the dehydrogenation of metal borohydrides: A cluster perspective. *The Journal of Physical Chemistry C*, 114(39):1684916854, 2010. → pages 9

[39] J. Lu, Y.J. Choi, Z.Z. Fang, H.Y. Sohn, and E. Ronnebro. Hydrogen Storage Properties of Nanosized MgH2 0.1TiH2 Prepared by Ultrahigh Energy High Pressure Milling. *Journal of American Chemical Society*, 131:1584315852, 2009. → pages 9, 10

[40] G. Liang. Synthesis and Hydrogen Storage Properties of Mg-Based Alloys. *Journal of Alloys and Compounds*, 370(123), 2004. → pages 9, 10

[41] J.P. DiPietro and E.G. Skolnik. Analysis of Sodium Hydride-based Hydrogen Storage system. *Prepared for US Department of Energy Office of Power Technologies Hydrogen Program*, 1999. → pages 10

[42] T. Tsuji, Y. Shinya, T. Hiaki, and N. Itoh. Hydrogen solubility in a chemical hydrogen storage medium, aromatic hydrocarbon, cyclic hydrocarbon, and their mixture for fuel cell systems. *Fluid Phase Equilibria*, 228-229:499–503, 2005. → pages 10

[43] A.C. Cooper, D.E. Fowler, A.R. Scott, A.H. Abdourazak, H. Cheng, F.C. Wilhelm, B.A. Toseland, K.M. Campbell, and G.P. Pez. Hydrogen Storage and Delivery by Reversible Hydrogenation of Liquid-phase Hydrogen Carriers. *Air Products and Chemicals Inc.*, 2005. → pages 10, 11, 12

[44] Y. Cui, S. Kwok, A. Bucholtz, B. Davis, R. Whitney, and P. Jessop. The Effect of Substitution on the Utility of Piperidines and Octahydroindoles for Reversible Hydrogen Storage. *New Journal of Chemistry*, 32:1027–1037, 2008. → pages 10, 51

[45] C.H. Bartholomew and R.J. Farrauto. *Fundamentals of Industrial Catalytic Processes*. Wiley, 2 edition, 2006. → pages 11, 12, 155

[46] G.A. Somorjai. *Introduction to Surface Chemistry and Catalysis*. Wiley, New York, 1994. Ch. 7. → pages 11

[47] Sh.K. Bej, Ch. A. Bennett, and l.T. Thompson. Acid and Base Characteristics of Molybdenum Carbide Catalysts. *Applied*. → pages 11, 12

[48] J.G. Chen. Carbide and Nitride Overlayers on Early Transition Metal Surfaces: Preparation, Characterization, and Reactivities. *Chemical Reviews*, 96:1477–1498, 1996. → pages 11, 12

[49] P.N. Rylander. *Catalytic Hydrogenation over Platinum Metals*. Academic Press NY, 1967. → pages 12

[50] P.N. Rylander. *Catalytic Hydrogenation in Organic Synthesis*. Academic Press NY, 1979. → pages

[51] P.N. Rylander. *Catalytic Processes in organic conversions, in Catalysis, Science and Technology*. Springer Verlag Berlin, 1983. → pages

[52] R. Mezaki and H. Inoue. *Rate Equations of Solid-Catalyzed Reactions*. University of Tokyo Press, 1991. → pages 12

[53] P. Crawford, R. Burch, C. Hardacre, K.T. Hindle, P. Hu, B. Kalirai, and D.W. Rooney. Understanding the Dehydrogenation Mechanism of Tetrahydrocarbazole over Palladium Using a Combined Experimental and

Density Functional Theory Approach. *J. Phys. Chem.*, 111:6434–6439, 2007. → pages 13, 14, 45, 47, 52, 75, 84, 93, 97, 105, 121, 126, 129, 133, 182, 188

[54] K.T. Hindle, R. Burch, P. Crawford, C. Hardacre, P. Hu, B. Kalirai, and D.W. Rooney. Dramatic Liquid-phase Dehydrogenation Rate Enhancements Using Gas-phase Hydrogen Acceptors. *Journal of Catalysis*, 251:338–344, 2007. → pages 13, 14, 47, 75, 81, 93, 133, 182

[55] E. Clot, O. Eisenstein, and R.H. Crabtree. Computational structure-activity Relationships in H2 Storage: How Placement of N Atoms Affects Release Temperatures in Organic Liquid Storage Materials. *Chemical Communications, Cambridge, United Kingdom*, 22:2231–2233, 2007. → pages 14, 24

[56] Zh. Wang, I. Tonks, J. Belli, and C.M. Jensen. Dehydrogenation of N-ethylperhydrocarbazole Catalyzed by PCP Pincer Iridium Complexes: Evaluation of a Homogenous Hydrogen Storage System. *Organomet. Chem.*, (doi: 10.1016/ j.jorganchem 2009.03.052), 2009. → pages 14, 52, 75, 133

[57] R.O. Loutfy and E.M. Veksler. Investigation of Hydrogen Storage in Liquid Organichydrides. In *International Hydrogen Energy Forum*, pages 335–340, Munich, Germany, September 11-15 2000. → pages 14, 44, 63, 76

[58] Sh. Hodoshima, H. Arai, Sh. Takaiwa, and Y. Saito. Catalytic Decalin Dehydrogenation/Naphthalene Hydrogenation Pair as a Hydrogen Source for Fuel-Cell Vehicle. *Intl. J. Hydrogen Energy*, 28(1255-1262), 2003. → pages 15, 44, 63, 76

[59] R.A. van Santen and M. Neurock. *Molecular Heterogeneous Catalysis A Conceptual and Computational Approach*. Wiley-VCH, 2006. → pages 15, 16

[60] E. Schrodinger. *Ann. Phys.*, page 79, 1926. → pages 16

[61] W. Koch and M.C. Holthausen. *A Chemist's Guide to Density Functional Theory*. Wiley-VCH, 2 edition, 2001. → pages 16, 17, 19

[62] I.N. Levine. *Quantum Chemistry*. Prentice Hall, New Jersey, 5 edition. → pages 16, 18, 19

[63] G.L. Miessler and D.A. Tarr. *Inorganic Chemistry*. Pearson Prentice Hall, third edition, 2004. → pages 16, 17

[64] A.B. Richon. An Introduction to Molecular Modeling. *Mathematec*, 83(1), 1994. → pages 17, 18

[65] M. Born and J.R. Oppenheimer. *Annals of Physics*, 84:457, 1927. → pages 17

[66] Accelrys Software inc., San Diego: Accelrys Software Inc. *Materials Studio Manual*, release 4.4 edition, 2008. → pages 17

[67] A. Szabo and N.S. Ostlund. *Modern Quantum Chemistry: Introduction to Advanced Electronic Structure Theory*. MacMillan Publishing Co., New York, 1982. → pages 17

[68] P.R. Westmoreland, P.A. Kollman, A.M. Chaka, P.T. Cummings, K. Morokuma, M. Neurock, E.B. Stechel, and P. Vashishta. Applications of Molecular and Materials Modeling. WTEC panel report Ch. 2: Electronic Structure, Thermochemistry and Kinetics, In Application of Molecular and Material Model, International Technology Research Institute, Baltimore, Maryland, January 2002. → pages 17, 18

[69] M. Springborg, editor. *Density-Functional Methods in Chemistry and Materials Science*. Research in Theoretical Chemistry. Wiley, 1997. → pages 18

[70] D.S. Sholl and J.A. Steckel. *Density Functional Theory , A Practical Introduction*. Wiley, 2009. → pages 18, 19

[71] W. Kohn and L.J. Sham. Self-Consistent Equations Including Exchange and Correlation Effects. *Physical Review: A*, 140:1133–8, 1965. → pages 18

[72] L. Hedin and B.I. Lundqvist. Explicit Local Exchange Correlation Potentials. *J. Phys. C*, 4:2064–2083, 1971. → pages 19

[73] J.P. Perdew and Y. Wang. Accurate and Simple Analytic Representation of the Electron-Gas Correlation Energy. *Phys. Rev.*, B45:13244–13249, 1992. → pages 19

[74] A.D. Becke. A Multicenter Numerical Integration Scheme for Polyatomic Molecules. *J. Chem. Phys.*, 88:2547–2553, 1988. → pages 19, 98

[75] C.T. Lee, W. Yang, and R.G. Parr. Development of the Colle-Salvetti Correlation-Energy Formula into a Functional of the Electron Density. *Phys. Rev. B*, 37:785–789, 1988. → pages 19, 181, 182

[76] J.P. Perdew, K. Burke, and M. Ernzerhof. *M. Phys. Rev. Lett.*, 77:3865, 1996. → pages 19

[77] R.A. Van Santen and M. Neurock. Concepts in Theoretical Heterogeneous Catalytic Reactivity. *Catal. Rev.-Sci. Eng.*, 37(4):557–698, 1995. → pages 19, 20

[78] R.A. van Santen and M. Neeurock. *Theory of Surface Chemical Reactivity*. VCH-Wiley, Berlin, 1998. → pages

[79] M. Neurock. *Catalysis In Application of Molecular and Material Modeling; Applications of Molecular and Materials Modeling*, chapter 8, pages 77–105. International Technology Research Institute, January 2002. → pages 19, 20

[80] J.L. Whitten and H. Yang. *Surf. Sci. Rep.*, 24:59–112, 1996. → pages 19

[81] B. Hammer and J.K. Norskov. *Adv. in Catal.*, 45:71–129, 2000. → pages 19

[82] A. Kaldor and D.M. Cox. *High Temp. Sci.*, 27:1, 1990. → pages 20

[83] D.M. Cox, M.R. Zakin, and A. Kaldor. *NATO ASI Ser., in Physical Chemistry of Small Clusters*, (158):741, 1987. → pages 20

[84] M.C. Payne, M.P. Teter, D.C Allan, T.A. Arias, and J.D. Joannopoulos. *Reviews of Modern Physics*, 64:1045– 1097, 1992. → pages 20

[85] W. Oelerch, T. Klassen, and R. Bormann. Mg-based Hydrogen Storage Materials with Improved Hydrogen Sorption. *Material Transactions*, 42(8), 2001. → pages 24

[86] H.Y. Zhao, S.T. Oyama, and E.D. Naeemi. Hydrogen Storage Using Heterocyclic Compounds: The Hydrogenation of 2-methylthiophene. *Catalysis Today*, 149(1-2):172–184, 2010. → pages 24

[87] U. Eberle, M. Felderhoff, and F. Schuth. Chemical and Physical Solutions for Hydrogen Storage. *Angew. Chem. Int. Ed.*, 48:66086630, 2009. → pages 24, 51

[88] M.M.P. Zieverink, M.T. Kreutzer, F. Kapteijn, and J.A. Moulijn. Gas-Liquid Mass Transfer in Benchscale Stirred Tanks: Fluid Properties and Critical Impeller Speed for Gas Induction. *Ind. Eng. Chem. Res.*, 45:45744581, 2006. → pages 27

[89] V. Mazzieri, F. Coloma-Pascual, A. Arcoya, P.C. LArgentiere, and N.S. Fygoli. XPS, FTIR and TPR characterization of Ru/Al2O3 catalysts. *Applied Surface Science*, 210:222230, 2003. → pages 28

[90] R. Grover. Estimation and use of standard errors of latent class model parameters. *Journal of Marketing Research*, 24(3):298–304, 1987. → pages 33

[91] L. Hegedus and T. Mathe. Hydrogenation of Pyrrole Derivatives Part V. Poisoning Effect of Nitrogen on Precious Metal on Carbon Catalysts. *Applied Catalysis A: General*, 226:319322, 2002. → pages 37

[92] A. Vargas, Th. Brgi, and A. Baiker. Adsorption of cinchonidine on platinum: a DFT insight in the mechanism of enantioselective hydrogenation of activated ketones. *Journal of Catalysis*, 226:6982, 2004. → pages 37, 52, 97

[93] P. Klusona and L. Cerveny. Selective Hydrogenation over Ruthenium Catalysts. *Applied Catalysis A: General*, 128(1):13–31, 1995. → pages 40

[94] P. Chou and M.A. Vannice. Benzene Hydrogenation over Supported and Unsupported Palladium : II. Reaction Model. *Journal of Catalysis*, 107:140–153, 1987. → pages 40

[95] A. Arnold, F. Dobert, and J. Gaube. *Handbook of Heterogeneous Catalysis*, volume 5 - p. 2165. VCH, Germany, 1997. → pages 40

[96] K. M. Eblagon, D. Rentsch, O. Friedrichs, A. Remhof, A. Zuettel, A. J. Ramirez-Cuesta, and Sh. C. Tsang. Hydrogenation of 9-Ethylcarbazole as a Prototype of a Liquid Hydrogen Carrier. *Internayional Journal of Hydrogen Energy*, 35:11609–11621, 2010. → pages 40, 101, 104, 105

[97] J.R. Song, L.X. Wen, L. Shao, and J.F. Chen. *Appl. Surf. Sci.*, (253):26782684, 2006. → pages 40, 79

[98] R. F. HICKS, Q. J. YEN, and A. T. BELL. Effects of Metal-Support Interactions on the Chemisorption of H2 and CO on Pd/SiO2 and Pd/La203. *Journal of Catalysis*, 89:498–510, 1984. → pages 41, 60, 74, 80

[99] A. Benedetti, G. Fagherazzi, F. Pinna, G. Rampazzo, M. Selva, and G. Strukul. The Influence of a Second Metal Component (Cu, Sn, Fe) on Pd/SiO2 Activity in the Hydrogenation of 2,4-Dinitrotoluene. *Catalysis Letters*, 10:215–224, 1991. → pages 43, 52, 57

[100] G. Neri, M. Musolino, C. Milone, D. Pietropaolo, and S. Galvagno. Particle Size Effect in the Catalytic Hydrogenation of 2,4-Dinitrotoluene over Pd/C Catalysts. *Applied Catalysis A: General*, 208:307–316, 2001. → pages 43, 52, 57, 82, 92

[101] OR. Stull, Jr. EF. Westrum, and GC. Sinke. pages 15–20, 1969. → pages 44

[102] E. Newson, TB. Truong, P. Hottinger, FV. Roth, and THH. Schucan. In *Proc. of the 12th World Hydrog. Eng. Conf., Buenos Aires, Argentina*, pages 935–42, 1998. → pages 44

[103] G. Cacciola, N. Giordano, and G. Restuccia. Cyclohexane as a Liquid Phase Carrier in Hydrogen Storage and Transport. *International Journal of Hydrogen Energy*, 9:411–419, 1984. → pages 51

[104] D. Klvana, A. Touzani, J. Chaouki, and G. Belanger. 1991. *International Journal of Hydrogen Energy*, 16:55–60, 1991. → pages 51

[105] A. Moores, M. Poyatos, Y. Luo, and R. Crabtree. Catalysed Low Temperature H2 Release from Nitrogen Heterocycles. *New Journal of Chemistry*, 30:1675–1678, 2006. → pages 51

[106] F. Sotoodeh, L. Zhao, and K.J. Smith. Kinetics of H2 Recovery from Dodecahydro-N-Ethylcarbazole over a Supported Pd Catalyst. *Applied Catalysis A: General*, 362:155–162, 2009. → pages 51, 53, 60, 62, 63, 66, 67, 68, 69, 70, 71, 72, 74, 75, 79, 82, 84, 92, 93, 103, 104, 121, 133, 182

[107] F. Sotoodeh and K.J. Smith. Kinetics of Hydrogen Uptake and Release from Heteroaromatic Compounds for Hydrogen Storage. *Industrial and Engineering Chemistry Research*, 49(1018-1026), 2010. → pages 51, 60, 62, 69, 72, 74, 82, 84, 86, 92, 93, 101, 103, 104, 184

[108] D. Suh, T. Park, and S. Ihm. Characteristics of Carbon-Supported Palladium Catalysts for Liquid-Phase Hydrogenation of Nitroaromatics. *Industrial and Engineering Chemistry Research*, 31:1849, 1992. → pages 52

[109] J.N. Kuhn and W. Huang and Ch.K. Tsung and Y. Zhang and G.A. Somorjai. Structure Sensitivity of Carbon-Nitrogen Ring Opening: Impact of Platinum Particle Size from below 1 to 5 nm upon Pyrrole Hydrogenation Product Selectivity over Monodisperse Platinum Nanoparticles Loaded onto Mesoporous Silica. *Journal of American Chemical Society*, 130:14026–14027, 2008. → pages 52

[110] Y. Lu, H. Zhang, Y. Xu, B. Song, H. Li, S.N Bao, and P. He. Adsorption Structures of Tetracene on the Ru(1 0 1 0) Surface. *Applied Surface Science*, 253:2025–2030, 2006. → pages 52, 97

[111] J.R. Regalbuto. *Catalyst Preparation: Science and Engineering*. Taylor and Francis group, LLC, 2007. → pages 53, 79

[112] N. Babu, N. Lingaiah, R. Gopinath, P. Reddy, and P. Prasad. Characterization and Reactivity of Alumina-Supported Pd Catalysts for the Room-Temperature Hydrodechlorination of Chlorobenzene. *Journal of Physicaal Chemistry C*, 111:6447–6453, 2007. → pages 55, 57, 73, 82

[113] C. Amairia, S. Fessi, A. Ghorbel, and A. Rives. Methane Oxidation Behaviour over SolGel Derived Pd/Al2O3-ZrO2 Materials: Influence of the Zirconium Precursor, journal = Journal of Molecular Catalysis A Chemical, year = 2010, volume = 332, pages = 25-31,. → pages 55, 82

[114] M. Gurrath, T. Kuretzky, H. Boehm, L. Okhlopkova, A. Lisitsyn, and V. Likholobov. Palladium Catalysts on Activated Carbon Supports: Influence of Reduction Temperature, Origin of the Support and Pretreatments of the Carbon Surface. *Carbon*, 38:1241–1255, 2000. → pages 92

[115] J. Bakker, A. Geert van der Neut, M. Kreutzer, J. Moulijn, and F. Kapteijn. Catalyst Performance Changes Induced by Palladium Phase Transformation in the Hydrogenation of Benzonitrile. *Journal of Catalysis*, 274:176–191, 2010. → pages 57, 92

[116] M. Myyrylainen and T.T. Rantala. Kinetic Monte Carlo Modeling of CO Desorption and Adsorption on Pd(1 1 0) Surface. *Catal.sis Today*, 100:413417, 2005. → pages 60

[117] D.Y. Murzin. Kinetic Analysis of Cluster Size Dependent Activity and Selectivity. *Journal of Catalysis*, 276:85–91, 2010. → pages 69, 76, 77, 133

[118] R. Iler. *The Chemistry of Silica*. John Wiley and Sons, New York, 1979. → pages 72

[119] Z. Li, Q. Zhao, C. Liu, and Y. Wang. → pages 72

[120] C. Contescu, D. Macovei, C. Craiu, C. Teodorescu, and J.A. Schwarz. Thermal Induced Evolution of Chlorine-Containing Precursors in Impregnated Pd/Al203 Catalysts. *Langmuir*, 11:2031, 1995. → pages 72, 73, 74, 75

[121] W. Zou and R. Gonzalez. The preparation of silica supported Pd catalysts: the effect of pretreatment variables on particle size. *Catalysis Letters*, 12:73–86, 1992. → pages 72, 74, 92

[122] T. Mang, H. Knozinger, J. Hightower, W. Delgass, E. Iglesia, and A. Bell. → pages 72

[123] E. Vilarrasa-Garcia, A. Infantes-Molina, R. Moreno-Tost, E. Rodriguez-Castellon, A. Jimenez-Lopez, Jr. C.L Cavalcante, and D.C.S. Azevedo. Thiophene Adsorption on Microporous Activated Carbons Impregnated with PdCl2. *Energy Fuels*, 24:3436–3442, 2010. → pages 73

[124] F.L. Normand, J. Barrault, R. Breault, L. Hilaire, and A. Kiennemann. Catalysis with Palladium Deposited on Rare Earth Oxides: Influence of the Support on Reforming and Syngas Activity and Selectivity. *The Journal of Physical Chemistry*, 95:257, 1991. → pages 73

[125] J. Murthy, S.Ch. Shekar, A. Padmasri, A. Venugopal, V. Kumar, B.M. Nagaraja, V. Shashikala, B.D. Raju, P. Kanta Rao, and K.S. Rama Rao. Promotional Effect of Magnesia Addition to Active Carbon Supported Pd Catalyst on the Characteristics and Hydrodechlorination Activity of CCl2F2. *Catalysis Communications*, 5:161–167, 2004. → pages 74

[126] W. Jozwiak and T. Maniecki. Influence of Atmosphere Kind on Temperature Programmed Decomposition of Noble Metal Chlorides. *Thermochimica Acta*, 435:151–161, 2005. → pages 74

[127] A. Binder, M. Seipenbusch, M. Muhler, and G. Kasper. Kinetics and Particle Size Effects in Ethene Hydrogenation over Supported Palladium Catalysts at Atmospheric Pressure. *Journal of Catalysis*, 268:150–155, 2009. → pages 76

[128] G.L. Bezemer, J.H. Bitter, H.P.C.E. Kuipers, H. Oosterbeek, J.E. Holewijn, X.Xu, F. Kapteijn, A.J. van Dillen, and K.P. de Jong. Cobalt Particle Size Effects in the Fischer-Tropsch Reaction Studied with Carbon Nanofiber Supported Catalysts. *Journal of American Chemical Society*, 128:3956, 2006. → pages 76

[129] D.Y. Murzin. Size-Dependent Heterogeneous Catalytic Kinetics. *Journal of Molecular Catalysis A Chemical*, 315:226–230, 2010. → pages 76, 77

[130] A. Cooper, A. Scott, D. Fowler, J. Cunningham, M.Ford, F. Wilhelm, V. Monk, H. Cheng, and G. Pez. Hydrogen Storage by Reversible Hydrogenation of Liquid-Phase Hydrogen Carriers. FY 2008 Annual Progress Report, DOE Hydrogen Program. *Air Products and Chemicals, Inc.*, pages 602–606, 2008. → pages 88, 90, 94

[131] F. Sotoodeh and K.J. Smith. Structure sensitivity of dodecahydro-n-ethylcarbazole dehydrogenation over pd catalysts. *Journal of Catalysis*, Accepted on Dec. 30th 2010. → pages 91, 92

[132] H. Ohtani, M.A. Van Hove, and G.A. Somorjai. Molecular Structure of Benzene Coadsorbed with CO on Pd(ll1): A Dynamical Low-Energy Electron Diffraction Analysis. *Journal of Physical Chemistry*, 92:3974, 1988. → pages 97

[133] A. Barbieri, M.A. Van Hove, and G.A. Somorjai. Benzene coadsorbed with CO on Pd(111) and Rh(111): detailed molecular distortions and induced substrate relaxations. *Surface Science*, 306:261–268, 1994. → pages

[134] H. Hoffmann, F. Zaera, R.M. Ormerod, R.M Lambert, L.P. Wang, and W.T. Tysoe. Discovery of a Tilted Form of Benzene Chemisorbed on Pd(111): As NEXAFS and Photoemission Investigation. *Surface Science*, 232:259–265, 1990. → pages

[135] A.F. Lee, K. Wilson, R.M. Lambert, A. Goldoni, A. Baraldi, and G. Paolucci. On the Coverage-Dependent Adsorption Geometry of Benzene Adsorbed on Pd111: A Study by Fast XPS Photoemission and NEXAFS. *Journal of Physical Chemistry B*, 104:11729, 2000. → pages

[136] W.T. Tysoe, R.M. Ormerod, R.M. Lambert, G.Zgrablich, and A. Ramirez Cuesta. Overlayer Structure and Kinetic Behavior of Benzene on Paladium. *Journal of Physical Chemistry B*, 97:3365, 1993. → pages

[137] H. Orita and N. Itoh. Simulation of Phenol Formation from Benzene with a Pd Membrane Reactor: Ab Initio Periodic Density Functional Study. *Applied Catalysis A: General*, 258(1):17–23, 2004. → pages 97

[138] M. Ohara, Y. Kim, S. Yanagisawa, Y. Morikawa, and M. Kawai. Role of Molecular Orbitals Near the Fermi Level in the Excitation of Vibrational Modes of a Single Molecule at a Scanning Tunneling Microscope Junction. *Physical Review Letters*, 100:136104, 2008. → pages 98

[139] W. Dou, D. Guan, F. Song, N. Li, H. Zhang, H. Li, P. He, H. Chen, S. Bao, and P. Hofmann. Valence Electronic Properties of n-Channel Organic Materials Based on Fluorinated Derivatives of Perylene Diimides. *Journal of Chemical Physics*, 244711:128, 2008. → pages 98

[140] B. Hammer, L.B. Hansen, and J.K. Norskov. Improved Adsorption Energetics within Density-Functional Theory Using Revised Perdew-Burke-Ernzerhof Functionals. *Physical Review B*, 59:74137421, 1999. → pages 98

[141] J.P. Perdew, K. Burke, and M. Ernzerhof. Generalized Gradient Approximation Made Simple. *Physical Review Letters*, 77:38653868, 1996. → pages 98

[142] J.L. Garnett and W.A. Sollich-Baumgartner. Pi Complex Adsorption in Hydrogen Exchange on Group VIII Transition Metal Catalysts. *Advances in Catalysis*, 16:95–121, 1996. → pages 104

[143] M. Saeys, M. Reyniers, M. Neurock, and G. Marin. Adsorption of Cyclohexadiene, Cyclohexene and Cyclohexane on Pt(111). *Surface Science*, 600:3121–3134, 2006. → pages 106, 108, 117, 118, 121

[144] M. Saeys, S.G. Marie-Francoise, M. Reynier, M. Neurock, and G.B. Marin. Density Functional Study of Benzene Adsorption on Pt(111), Density Functional Study of Benzene Adsorption on Pt(111). *Journal of Physical Chemistry B*, 106:7489–7498, 2002. → pages 107, 110, 118

[145] M. Saeys, M. Neurock, and G.B. Marin. Density Functional Theory Analysis of Benzene (De)hydrogenation on Pt(111): Addition and Removal of the First Two H-atoms. *Journal Physical Chemistry*, 107:3844–3855, 2003. → pages 109

[146] Alibaba.com, 1999. Founded in Hangzhou, China. → pages 136

[147] S. Brunauer, P.H. Emmett, and E. Teller. *Am. Chem. Soc.*, 1938. → pages 155

[148] Micromeritics Instrument Corporation. *AutoChem II 2920 Automated Catalyst Characterization System Operators Manual V3.05*, 2006. → pages 156

[149] H.S. Fogler. *Elements of Chemical Reaction Engineering*. Printice Hall PTR, 4 edition, 2006. → pages 173, 174

[150] F. Weiyang and H.J. Bart. Prediction of Diffusivities in Liquids. *Chem. Eng. Technol*, 8(21):659, 1998. → pages 173

[151] P. Englezos and N. Kalogerakis. *Applied Parameter Estimation for Chemical Engineers*, chapter 8. Marcel-Dekker, New York, 2001. → pages 175

[152] S.T. Oyama. Preparation and Catalytic Properties of Transition Metal Carbides and Nitrides. *Catalysis Today*, 15:179–200, 1992. → pages 181, 182

[153] M. Espinnoza, J. Cruz-Reyes, M. Del Valle-Granados, E. Flores-Aquino, M. Avalos-Borja, and S. Fuentes-Moyado. *Catalysis Letters*, 120:137–142, 2008. → pages 181

[154] S.B. Derouane-Abd Hamid, J.R. Anderson, I. Schmidt, C. Bouchy, C.J.H. Jacobsen, and E. G. Derouane. *Catalysis Today*, 63:461–469, 2000. → pages 181

[155] C. Bouhy, S.B. Derouane-Abd Hamid, and E.G. Derouane. *Chemical Communications*, 2:125–126, 2000. → pages

[156] S.Z. Li, J.S. Lee, T. Hyeon, and K.S. Suslick. *Applied Catalysis A: general*, 184:1–9, 1999. → pages

[157] M. Nagai, T. Miyao, and T. Tuboi. *Catalysis Letters*, 18:9–14, 1993. → pages 181

[158] G. Djega-Mariadassou, M. Boudart, G. Bugli, and C. Sayag. *Catalysis Letters*, 31:411–420, 1995. → pages 181

[159] M. Xiang, D. Li, H. Qi, W. Li, B. Zhong, and Y. Sun. *Fuel*, 86(9):1128–1303, 2007. → pages 181, 182, 191

[160] V. Keller, P. Weher, F. Garin, R. Ducros, and G. Maire. *Journal of Catalysis*, 153(1):9–16, 1995. → pages 181

[161] M. Nagai, A.M. Zahidul, and K. Matsuda. *Applied Catalysis A: general*, 3113(2):137–145, 2006. → pages 181, 191

[162] A. Szechenyi and F. Solymosi. *Journal of Physical Chemistry C.*, 111(26):9509–9515, 2007. → pages 181

[163] T.C. Xiao, A.P.E. York, V.C. Williams, H. Al-Megren, A. Hanif, Z-Y Zhou, and M.L.H. Green. *Chemical Materials*, 12(12):3896–3905, 2000. → pages 181, 182

[164] X. Li, D. Ma, L. Chen, and X. Bao. *Catalysis Letters*, 116(1-2):63–69, 2007. → pages 181

[165] J.M. Giraudon, L. Leclercq, G. Leclercq, A. Lofberg, and A. Frennet. *Journal of Material Sciences*, 28:2449–2454, 1993. → pages 181

[166] D. Zeng and M. Hampden-Smith. *Journal of Chemical Materials*, 5:681–689, 1993. → pages 181

[167] L.G. Rosa, J.C. Fernandes, and P.M. Amaral. *International Journal of Refractory Metals and Hard Materials*, 17:351–356, 1999. → pages 182

[168] P.M. Patterson, T.K. Das, and B.H. Davis. *Applied Catalysis A: general*, 251:449–455, 2003. → pages 182

[169] M.K. Neylon, S. Choi, H. Kwon, K.E. Curry, and L.T. Thompson. *Applied Catalysis A: general*, 183:253–263, 1999. → pages

[170] J.B. Claridge, A.P.E. York, A.J. Brungs, and M.L.H. Green. *Chemical Materials*, 12:132–142, 2000. → pages 182

[171] M. Ogura, S. Shinomiya, J. Tateno, Y. Nara, M. Nomura, E. Kikuchi, and M. Matsukata. *Applied Catalysis A: general*, 219:33–43, 2001. → pages 182, 185

[172] T. Suzuki and T. Okuhara. *Microporous Mesoporous Materials*, 43:83–89, 2001. → pages 182, 185

[173] S.F. Zaman and K.J. Smith. Synthesis gas conversion over MoP catalysts. *Catalysis Communications*, 10:468–471, 2009. → pages 185

Appendices

Appendix A

Catalyst preparation: calculations of required chemicals

Preparation of Pd/silica: Sample calculations for the required chemicals for preparing 5 wt% Pd on silica are as follows:

1. Required amount of Pd/silica catalyst =10 g

2. Amount of Pd in Pd/silica catalyst

$$= \frac{5\ g\ Pd}{100\ g\ Pd/silica}(10\ g\ Pd/silica) = 0.5\ g \tag{A.1}$$

3. Required amount of $PdCl_2$

$$= \frac{177.33\ g/mol\ PdCl_2}{106.4\ g\ Pd}(0.5\ g\ Pd) = 0.83\ g \tag{A.2}$$

4. Required amount of silica

$$= (10\ g\ Pd/silica) - (0.5\ g\ Pd) = 9.5\ g \tag{A.3}$$

5. Required amount of water solution

$$= (1.15\frac{ml}{g\ silica})(9.5\ g\ silica) = 10.925\ ml \tag{A.4}$$

Appendix B

Catalyst characterization techniques

B.1 Total BET surface area

Brunauer, Emmett and Teller in 1938 proposed a model that described the multilayer physisorption and calculated the monolayer coverage of the adsorbate [45, 147]. The BET equation is as follow:

$$\frac{P/P_0}{V(1-\frac{P}{P_0})} = \frac{C-1}{V_m C}(\frac{P}{P_0}) + \frac{1}{V_m C} \tag{B.1}$$

where C is a constant, V is the total volume adsorbed (STP) at pressure P, V_m is the volume adsorbed (STP) at monolayer coverage, and P_o is the saturation vapor pressure of the adsorbate gas (or vapor). A plot of the left-hand side in Equation B.1 vs. P/P_o should give a linear plot with a slope of $(C-1)/V_mC$ and an intercept of $1/V_mC$, from which V_m and C can be determined and surface area is then calculated. The preferred range of P/P_o for best results is 0.05 to 0.4.

B.2 Temperature-programmed reduction (TPR)

Temperature-programmed reduction (TPR) of the calcined Pd/SiO_2 catalyst precursors was performed using a Micromeritics Autochem II 2920 analyser fitted

with a thermal conductivity detector (TCD). About 0.2 g of each sample was loaded into a u-tube reactor and flushed for 30 min in a 50 cm^3 (STP)/min flow of 10 % H_2 in Ar at room temperature. The sample was then heated to 673 K at a rate of 10 K/min with the final temperature held for 1 h.

B.3 Temperature-programmed desorption (TPD)

Temperature-programmed desorption (TPD) of CO from the Pd catalysts was also performed using the Micromeritics Autochem II 2920 analyser. About 0.2 g of the dried catalyst was loaded into the reactor and calcined at 773 K for 6 h in a flow of Ar at 30 cm^3 (STP)/min, followed by TPR at 10 K/min to a final temperature of 673 K in a 30 cm^3 (STP)/min flow of 10 % H_2 in Ar, holding the final temperature for 1 h. The catalyst was then flushed in a 30 cm^3 (STP)/min flow of Ar for 1 h and cooled to room temperature, before being exposed to a 50 cm^3 (STP)/min flow of 10 % CO in He at 313 K for 1 h. The catalyst was subsequently flushed in 50 cm^3 (STP)/min He for 2 h. The temperature-programmed desorption was then started in the same He flow by heating the sample to 773 K at a rate of 10 K/min and holding the final temperature for 1 h.

B.3.1 Injection loop calibration

Injection loop must be calibrated before its first use to determine its precise volume under local conditions [148]. Calibration consists of:

- Determining the average area of a the peaks generated by injections of a known volume of gas through the analyzer septum using a glass syringe.
- Determining the average area of the peaks generated by injections of the same gas using the analyzers internal loop.
- Calculating the volume of the loop by comparing the average peak area generated by the loop injections with that generated by the syringe injections

Volume at STP

Volume at standard reduction of gas data to Standard Temperature Pressure (STP) conditions (273.13 K and 760 mmHg) is calculated as follows,

$$V_{STP} = V_a(\frac{273.15}{273.15 + T_a}) \times (\frac{P_a}{760\ mmHg}) \tag{B.2}$$

where
V_{STP}=Volume at STP, cm^3
V_a=Volume at ambient temperature and pressure, cm^3
T_a=Ambient temperature, °C
P_a=Ambient pressure, mmHg

Injection loop calibration

These equations are used during calibration of a dose loop,

$$V_{S_{STP}} = V_S(\frac{273.15}{273.15 + T_a}) \times (\frac{P_a}{760\ mmHg}) \tag{B.3}$$

and

$$V_l = (\frac{A_l \times V_{S_{STP}}}{A_S}) \tag{B.4}$$

where
$V_{S_{STP}}$=Volume of syringe at STP, cm^3
V_S=Physical volume of syringe, cm^3
T_a=Ambient temperature, °C
P_a=Ambient pressure, mmHg
V_l=Effective loop volume (at loop temperature), cm^3
A_l=Average peak area of loop injections
A_S=Average peak area of syringe injections

B.4 High resolution transmission electron microscopy (HRTEM)

A FEI Tecnai G2 200 keV with a LaB6 filament capable of 1.4 $\AA$ point-to-point resolution was used for high resolution transmission electron microscopy (HRTEM). Pd/SiO_2 catalyst samples with variable Pd loadings were ground for 20 min to a fine powder using an agate mortar and pestle. 1 mg of the sample was then dispersed in 10 ml ethanol ultrasonically for 5 min. A droplet of the suspension was then placed on a 200 mesh copper grid coated with formvar carbon and left to dry for 10 min before analysis.

Appendix C

Mass spectrometery

C.1 Mass flow controllers (MFCs) calibration

Mass spectrometer (MS) was used to continuously monitor the dehydrogenation reactor effluent. The MS was calibrated using a constant flow of He as a carrier gas, and stepwise increasing of known amount of H_2 gas introduced into the He flow. He and H_2 flow were controlled using a He 200 SCCM and a H_2 20 SCCM mass flow controller (MFC), respectively, which were calibrated using a bubble flow meter prior to the MS calibration. Table C.1 and C.2 summarize the He and H_2 MFC calibration results.

Table C.1: He 200 SCCM MFC calibration using a bubble flow meter and stop-watch for 79.9 % of the total flow.

Volume (ml)	Time (min)	flow (ml/min)
25	0.1485	168.3502
25	0.1463	170.8428
25	0.1463	170.8428
25	0.1475	169.4915
25	0.1452	172.2158
25	0.1473	169.6833
25	0.1442	173.4104
25	0.1433	174.4186
25	0.1458	171.4286
	Average flow (ml/min)	171.1871

Table C.2: H_2 20 SCCM MFC calibration using a bubble flow meter and stopwatch.

Controller knob (%)	volume (ml)	Time (min)	flow (ml/min)
10	5	1.87	2.67
15	10	2.51	3.98
20	10	1.90	5.25
25	15	2.30	6.52
30	15	1.91	7.84
35	25	2.72	9.18
40	25	2.40	10.41
50	25	1.93	12.95

Figure C.1 shows the calibration curve obtained by linear fit of the obtained calibration data summarized in Table C.2.

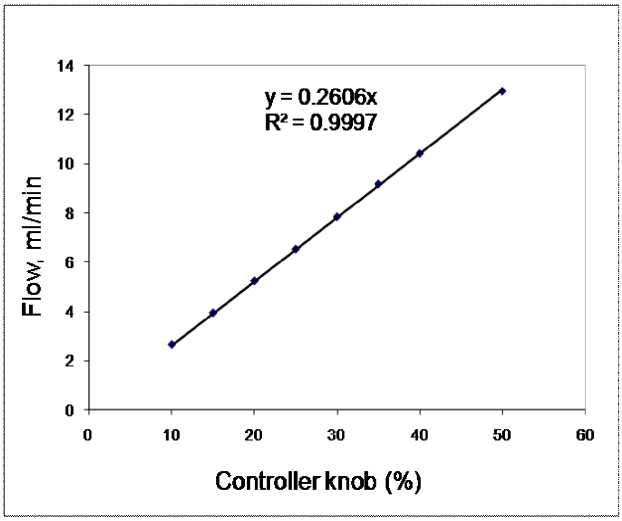

Figure C.1: H_2 20 SCCM MFC calibration curve obtained from the data shown in Table C.2.

C.2 Mass spectrometer (MS) calibration for H_2

The He flow was kept constant at 171.19 ml/min as a carrier gas during the MS calibration for H_2. H_2 flow was increased stepwise and the pressure of He and H_2

was continuously monitored. Table C.3 summarizes the measured partial pressures as well as the H_2 to He partial pressure ratio used to find the H_2 gas calibration factor.

Table C.3: MS calibration data for H_2 using a constant He flow of 171.19 ml/min as the carrier gas.

time (min)	He (torr)	H_2 (torr)	P(H_2)/P(He)	Y(H_2)/Y(He)[a]
0.00	6.109×10^{-5}	1.112×10^{-6}	0.01820	0.00000
5.00	6.111×10^{-5}	1.872×10^{-6}	0.03063	0.00152
41.00	6.061×10^{-5}	2.882×10^{-6}	0.04756	0.00304
93.00	6.112×10^{-5}	3.965×10^{-6}	0.06487	0.00457
140.00	6.178×10^{-5}	6.212×10^{-6}	0.10055	0.00761
168.00	6.195×10^{-5}	8.285×10^{-6}	0.13373	0.01066
198.00	6.255×10^{-5}	1.143×10^{-6}	0.18269	0.01522
232.00	6.283×10^{-5}	1.344×10^{-6}	0.21390	0.01827
267.00	6.310×10^{-5}	1.659×10^{-6}	0.26291	0.02283
303.00	6.375×10^{-5}	1.891×10^{-6}	0.29667	0.02588
332.00	6.411×10^{-5}	2.199×10^{-6}	0.34299	0.03045
365.02	6.401×10^{-5}	2.668×10^{-6}	0.41684	0.03806
407.02	6.460×10^{-5}	3.183×10^{-6}	0.49273	0.04567
436.02	6.483×10^{-5}	3.692×10^{-6}	0.56943	0.05328
467.02	6.544×10^{-5}	5.080×10^{-6}	0.77637	0.07612

[a] ratio of the moles of H_2 to the moles of He.

The calibration factor, M, is obtained from the slope of the linear fit plot of P(H_2)/P(He) vs. Y(H_2)/Y(He),

$$M.\frac{Y(H_2)}{Y(He)} = \frac{F(H_2)}{F(He)} = \frac{P(H_2)}{P(He)} \tag{C.1}$$

where F(H_2) and F(He) are the molar flow of H_2 and He, respectively. The obtained result is shown in Figure C.2.

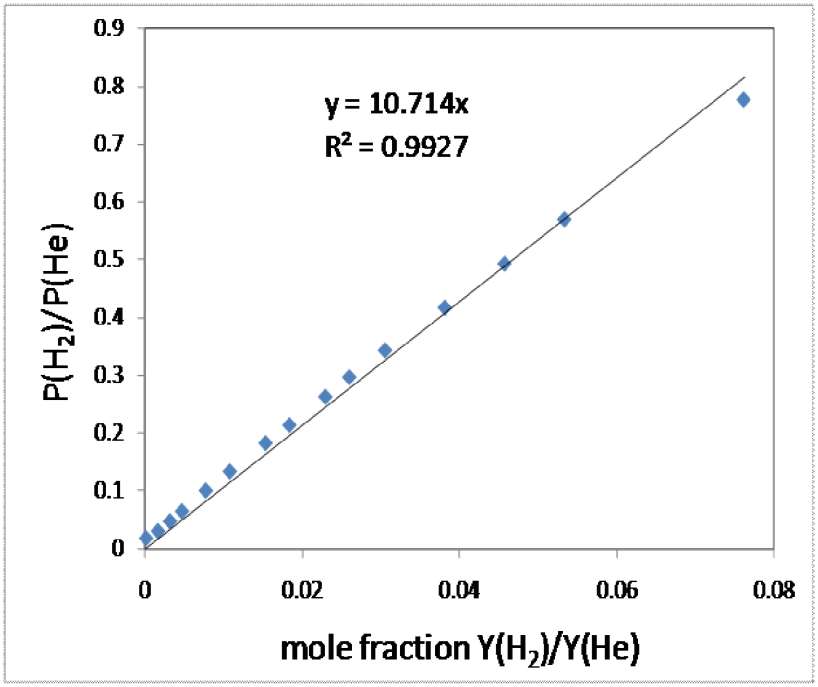

Figure C.2: MS calibration curve for H_2.

Appendix D

Gas chromatography

A Shimadzu QP-2010S gas chromatograph with a mass spectrometer detector (GC/MS) was used to analyze the obtained liquid samples from hydrogenation and dehydrogenation reactions using a Restek RTX5 30M x 0.25 mm capillary column.

D.1 Temperature program

The temperature program used for the sample analysis is summarized in Table D.1.

Table D.1: Tenperature program used in the Shimadzu QP-2010S GC/MS.

Parameter	Unit	Value
Initial column temperature	K	393
Initial column temperature hold time	min	5
Temperature ramp	K/min	10
Final column temperature	K	543
Final column temperature hold time	min	2
Total analysis time	min	22
Injection volume	μl	1

D.2 Calibration

If the hydrogenation reactant concentration in feed is C_{A0}, and the obtained area from GC/MS analysis is A_0, then a response factor (R.F.) is defined as:

$$R.F. = \frac{A_0}{C_{A0}} \tag{D.1}$$

Using the obtained response factor, the unknown concentration of the hydrogenation/dehydrogenation products can be calculated by dividing the obtained area for each compound by the response factor, as follows:

$$C_{compound} = \frac{A_{compound}}{R.F.} \tag{D.2}$$

where $C_{compound}$ is the concentration of compound of interest and $A_{compound}$ the obtained area from GC/MS.

Appendix E

Sample calculations

E.1 N-ethylcarbazole hydrogenation reaction at 413 K

The following section shows sample calculations for hydrogenation of a 6 wt% solution of N-thylcarbazole in decalin at 413 K and 6 MPa over a 5 wt% Ru/alumina catalyst. The commercial Ru/alumina catalyst was received in a pre-reduced state and was pre-treated before the hydrogenation reaction.

E.1.1 Experiment procedure

A solution of 6 g N-ethylcarbazole in 100 ml decalin was prepared and loaded to the reactor. 1 g of commercially reduced catalyst was added to the solution. The reactor was sealed properly and purged with N_2 for 30 min followed by hydrogen for another 30 min, then heated up to 413 K while purging with hydrogen with very small flow rate. After the temperature reached 413 K and remained constant, the reactor outlet was closed and reactor was pressurized with H_2. The reaction started immediately. The hydrogen pressure was monitored and liquid samples were taken for rate analysis.

Table E.1 shows the reactant and material information used for the hydrogenation reaction, as well as the reaction conditions.

Tables E.2 and E.3 show the obtained results for H_2 consumption and the liquid sample analysis. The final pressure took into account the pressure loos occurred in each sampling step. The total pressure loss was added to the obtained final pressure

Table E.1: Experiment information

Reactant loaded, g	6
Solvent loaded, ml	100
Catalyst loaded, g	1
Reactant loaded, mol	0.0298
Molarity in solvent, mol/ml	0.0003
Reaction pressure, MPa	6
Reaction Temperature, K	413
Stirrer speed, rpm	600
Reaction time, h	24

of the reactor.

Table E.2: Hydrogen consumption

Initial pressure (at 413 K), psi	856
Final pressure (at 413 K), psi	373+33 (pressure loss due to sampling) = 406
Initial conc.[a], mol/ml	0.000298
Initial conc., mol	0.0298
Final conc.[a], mol/ml	0.000005254
Final conc., mol	0.0005254
Stoichiometric consumption of H_2 for complete hydrogenation, mole	6×0.0298 = 0.1788
Initial H_2, mol	846/145.0377×200/8.314/413 = 0.34
Final H_2, mol	406/145.0377×212/8.314413 = 0.1728
Total H_2 consumed, mol	0.34-0.1728 = 0.1672
Expected reactor pressure after complete hydrogenation, psi	(0.34-0.1788)×8.314×413/212 ×145.0377 = 378.67

[a]Initial and final concentrations are based on liquid samples analysis.

The obtained rate constant is based on a linear fit to the experimental concentration data of the reactant measured during the experiment and analyzed by the GC, according to the following rate equation:

$$\begin{aligned} -r_A &= dC_A/dt = k\,C_A \\ &\Rightarrow Ln(C_A/C_{A0}) = -k\,t \end{aligned} \tag{E.1}$$

where C_{A0} and C_A are the initial reactant concentration and concentration at time

Table E.3: N-ethylcarbazole conversion obtained by GC analysis of the samples

Time (min)	N-ethylcarbazole (mol/ml)	X (%)	$Ln(C_A/C_{A0})$
0.00	0.000298049	0.00	0.000163931
17.17	0.000270185	9.35	-0.097988121
43.17	0.000119580	59.88	-0.913106707
80.17	0.000032065	89.24	-2.229341315
123.17	0.000023546	92.10	-2.538119387
175.17	0.000022684	92.39	-2.575447246
442.17	0.000022355	92.50	-2.590031454
534.17	0.000018888	93.66	-2.758704721
630.17	0.000009432	96.84	-3.453176698
718.17	0.000011548	96.13	-3.250731977
1223.17	0.000013130	95.59	-3.122338636
1452.17	0.000005254	98.24	-4.038280266

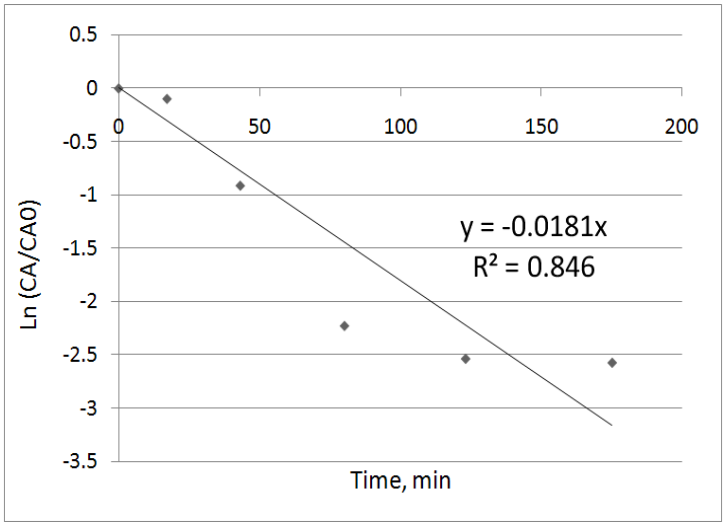

Figure E.1: First-order rate constant calculations for the hydrogenation reaction at 413 K.

t, respectively. K is the first-order rate constant obtained from the slope of the plot $Ln(C_A/C_{A0})$ vs. reaction time, t. Figure E.1 shows the rate constant calculations obtained from the liquid sample analysis. The reaction rate constant was found to be 0.0181 min^{-1}. The reactant initial concentration was 0.0002980 $mol.ml^{-1}$.

Therefore we have:

$$k\,C_{A0} = (0.0181\ min^{-1})(0.0002980\ mol\ min^{-1}) = 5.39 \times 10^{-6}\ \ mol.\,ml^{-1}.\,min^{-1} \quad \text{(E.2)}$$

E.2 Dodecahydro-N-ethylcarbazole dehydrogenation reaction

The following section shows the details of calculations for the dehydrogenation reaction of dodecahydro-N-ethylcarbazole over a 4 wt% Pd/SiO_2 catalyst at 423 K and 101 kPa.

E.2.1 Experiment procedure

1. Loading a 50 ml three-neck glass flask reactor with 10 ml of the hydrogenated product and diluting with 20 ml of decalin.
2. Purging the system with Helium to remove air.
3. Heating the reactor using a heating mantle and controller, and recording the temperature continuously.
4. Monitoring the outlet gas of the reactor continuously with mass spectrometer.
5. Adding 0.07 g of 4 wt% Pd/silica (prepared in the lab, pre-reduced in the quartz U-tube using the muffle furnace) to reactor by the catalyst injection glass tube after temperature reached the set-point.
6. Taking liquid samples.

Table E.4 summarizes the reactant and products concentrations obtained from liquid sample analysis using the Shimadzu GCMS.

Table E.5 summarizes the conversion of the reactant, selectivity to N-ethylcarbazole, as well as the gas phase Hydrogen production.

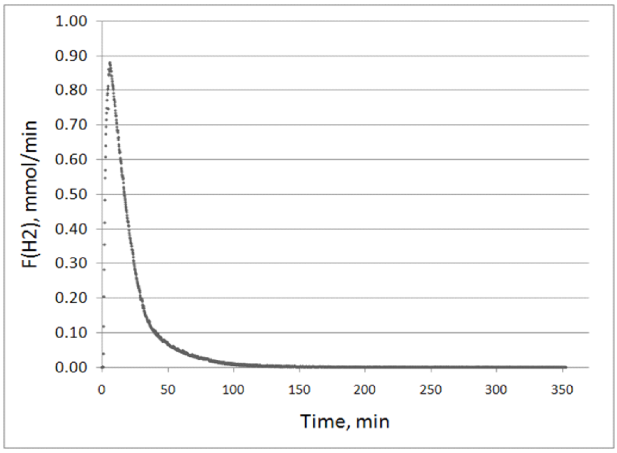

Figure E.2: H_2 profile obtained from the gas phase analysis using MS.

Table E.4: Concentrations of reactants and products in mol/ml.

Sample	Time, min	N-ethylcarbazole	Tetrahydro-	Octahydro-	Dodecahydro-
1	0.00	0.0000	0.0000	0.0000	9.9350×10^{-5}
2	4.67	3.3589	2.2840×10^{-5}	2.6131×10^{-5}	4.7020×10^{-5}
3	9.33	9.5660×10^{-6}	4.6634×10^{-5}	2.5082×10^{-5}	1.8067×10^{-5}
4	14.50	2.9796×10^{-5}	5.0183×10^{-5}	1.4564×10^{-5}	4.8058×10^{-6}
5	22.33	4.1174×10^{-5}	5.2938×10^{-5}	4.5891×10^{-6}	6.4825×10^{-7}
6	29.67	4.7330×10^{-5}	5.0594×10^{-5}	1.4250×10^{-5}	0.0000
7	37.17	5.8841×10^{-5}	4.0119×10^{-5}	3.8946×10^{-5}	0.0000
8	50.50	8.1411×10^{-5}	1.7938×10^{-5}	0.0000	0.0000
9	81.00	9.5924×10^{-5}	3.4258×10^{-6}	0.0000	0.0000
10	119.50	9.9350×10^{-5}	0.0000	0.0000	0.0000

Figure E.3 shows the obtained rate constant for the dehydrogenation reaction of dodecahydro-N-ethylcarbazole assuming a first-order reaction.

Initial reaction rate for the dehydrogenation reaction as well as the reaction TOF were calculated using the initial reactant concentration and the obtained first-

Table E.5: Dehydrogenation reaction data analysis.

Time, min	Conversion, %	N-ethylcarbazole selectivity, %	H_2 production, mmol	Ln(C_A/C_{A0})
0	0	0	0	0
4.67	52.67	6.42	4.9133	-0.7481
9.33	81.81	11.77	8.8229	-1.7045
14.5	95.16	31.52	12.2592	-3.0288
22.33	99.35	41.72	14.0393	-5.0321
29.67	100	47.64	14.6763	
37.17	100	59.23	15.4290	
50.5	100	81.94	16.8066	
81	100	96.55	17.6774	
119.5	100	100	17.8829	

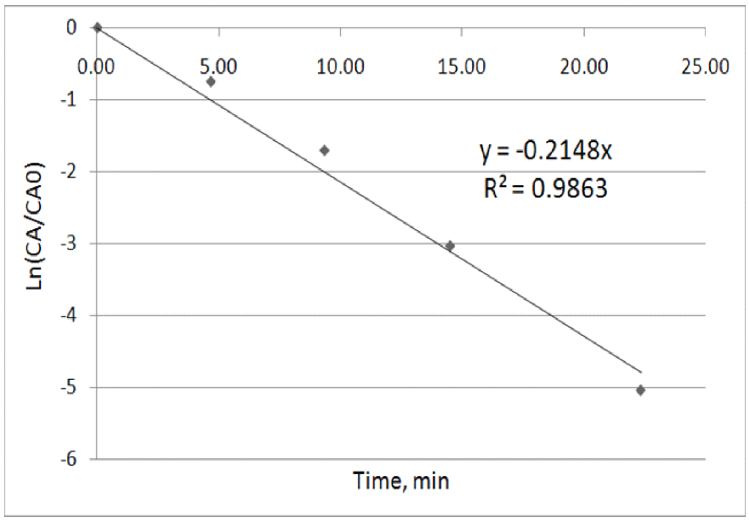

Figure E.3: First-order reaction rate constant calculated using the reactant concentration.

order rate constant as follows:

$$\begin{aligned} Initial\ rate &= (k, min^{-1})(C_{A0}, mol/ml)/(Catalyst, g)(1000, ml/L) \\ &= (0.2148, min^{-1})(9.9350 \times 10^{-5}, mol/ml)/(0.07g)(1000, ml/L) \\ &= 0.3049\ \ mol.L^{-1}.min^{-1}.g_{cat}^{-1}(M.min^{-1}.g_{cat}^{-1}) \end{aligned} \tag{E.3}$$

$$TOF = (0.0921, L.min^{-1}.g_{cat}^{-1})/(0.04, wt\%\ Pd\ loading)(106.4, g.mol^{-1}) \\ /(0.11,\ Pd\ dispersion)(9.9350 \times 10^{-5}, mol/ml)(1000, ml/L) \\ = 221.16\ \ min^{-1} \tag{E.4}$$

E.3 Rate constant sample calculation reported in Table 4.3

Sample calculation for obtaining the rate constant reported in L.min^{-1}.g$_{cat}$$^{-1}$ from the rate constant reported in min^{-1} is as follows:
For a heterogeneous catalytic system, 1st-order reaction rate is defined as,

$$-r = k\, C\, C_{cat}^{-1} \tag{E.5}$$

where r in this equation is the reaction rate (mol.min^{-1}.g$_{cat}$$^{-1}$), k is the rate constant (min^{-1}), C is the reactant concentration (mol/L), and C_{cat} is the catalyst concentration (g$_{cat}$/L). Reaction rate in equation E.5 can also be written as,

$$-r = k'\, C \tag{E.6}$$

where k' is the rate constant (L.min^{-1}.g$_{cat}$$^{-1}$) and C is the reactant concentration (mol/L).
For the dehydrogenation reaction over the 0.5 wt % Pd/SiO_2, we have the following data:

1. catalyst amount = 0.38 g
2. reaction volume = 0.03 L
3. k = 0.0457 min^{-1}

Therefore we have,

C_{cat} = (0.38 g)/(0.03 L) = 12.6667 g/L

$k' = (0.0457\ min^{-1})/(12.6667\ g/L)$

$= 0.0036\ L.min^{-1}.g_{cat}{}^{-1}$

Appendix F

Internal diffusion

F.1 Effective diffusivity

Because of the tortuosity and interconnecting paths of pore bodies in the catalyst with varying cross-sectional areas, diffusion can not be described within each and every one of the pathways individually. Consequently, an effective diffusion coefficient, D_e, is defined to describe the average diffusion as follow [149]:

$$D_e = \frac{D_{AB}\ \phi_P\ \sigma_C}{\tilde{\tau}} \tag{F.1}$$

Where D_{AB} is bulk or Knudsen diffusivity, $\tilde{\tau}$ is tortuosity, ϕ_P is pellet porosity, and σ_C is constriction factor. D_{AB} for liquid phase can be obtained from the Stokes-Einstein equation [150]:

$$D_{AB} = \frac{k_B\ T}{6\pi\mu R_0} \tag{F.2}$$

where k_B is the Boltzmann constant, μ is the solvent viscosity, R_0 is the solute radius and T is the temperature in K.

F.2 Thiele modulus, effectiveness factor and Weisz-Prater criterion

The dimensionless Thiele modulus value is a measure of the ratio of a surface reaction rate to a rate of diffusion through the catalyst. For a zero order reaction,

Thiele modulus is obtained as follow [149]:

$$\phi = R\sqrt{\frac{k_0}{D_e C_A}} \tag{F.3}$$

where k_0 is the zero order reaction rate constant, D_e is effective diffusivity and C_A is concentration of the reactant or product. The magnitude of internal effectiveness factor (ranging from 0 to 1) indicates the relative importance of diffusion and reaction limitations and is defined as:

$$\eta = \frac{3}{\phi^2}(\phi\ coth\phi\ - 1) \tag{F.4}$$

The term $\eta\phi^2$ is the Weisz-Prater parameter (C_{WP}) which shows the ratio of the actual reaction rate to a diffusion rate.

Calculated results for internal diffusion of THCZ and H_2 in mesitylene for THCZ dehydrogenation on Pd/silica at 140 °C and 1 atm are summarized in Table F.1.

Table F.1: THCZ, H_2 internal diffusion in mesitylene on Pd/silica at T=140 °C, P=1 atm

Name	**symbol**	**unit**	**value for THCZ**	**value for H_2**
Boltzmann Constant	k_B	$J.K^{-1}$	1.38E-23	1.38E-23
Temperature	T	K	413	413
Solvent viscosity	μ	kg/(m.sec)	7.77E-4	7.77E-4
Solute radius	R_0	m	5E-10	5E-11
Tortuosity	$\tilde{\tau}$	dimensionless	3.0	3.0
Constriction factor	σ_C	dimensionless	0.8	0.8
Porosity	ϕ_P	dimensionless	0.4	0.4
Diffusivity	D_{AB}	m^2/sec	7.78E-10	7.78E-09
Effective diffusivity	D_e	m^2/sec	8.30E-11	8.30E-10
Catalyst radius	R	m	1.14E-04	1.14E-04
Reaction rate	k_0	$mM/min.g_{cat}$	17	17
Concentration	C_A	mol/lit	0.2	0.26
Thiele modulus	ϕ	dimensionless	0.47	0.13
Effectiveness factor	η	dimensionless	0.99	1

The obtained effectiveness factor for both THCZ and H_2 shows that the reaction is not diffusion-limited within the catalyst.

Appendix G

Reaction modeling

G.1 Standard error of the parameter estimation

The parameter estimation and the standard error calculations have been done using the method described by Englezos et al. [151]. The covariance matrix of distribution, denoted as Cov(k*), was calculated to measure the reliability of the estimated k parameters as follows:

$$COV(k^*) = \sigma_\varepsilon^2 [A^*]^{-1} \tag{G.1}$$

The matrix A* in this equation is calculated at k*. σ_ε^2 is the variance and is calculated using the following equation:

$$\sigma_\varepsilon^2 = \frac{S(k^*)}{degree\ of\ freedom} = \frac{S(k^*)}{Nm - P} \tag{G.2}$$

in which degree of freedom is defined as the number of measurements minus the number of unknown parameters. The standard error associated with the estimated parameter is denoted as σ_{K_i} and is calculated using the diagonal elements of the A* matrix, defined as:

$$\sigma_{K_i} = \sigma_\varepsilon \sqrt{\{[A^*]^{-1}\}_{ii}} \tag{G.3}$$

This method have been used for calculating the standard errors of the estimated rate constants as parameters, shown in the following section.

G.2 Codes

The following codes were used to Model the hydrogenation reactions of N-ethylcarbazole at 423 K using MATLAB software.

==========

G.2.1 Main body

```
FARNAZ SOTOODEH, JULY 2009
clear all;
clc
% Order of reactions:
n1=1;
n2=1;
n3=1;
n4=1;
n5=1;
n6=1;
n7=1;
y60= 2.98027E-1;
h=1e-10;
global n1 n2 n3 n4 n5 n6 n7
DATA=[
0          0          0          0          0          0          2.98E-1
2.58       8.18E-4  1.72E-3  2.22E-4  1.50E-5   4.60E-4  2.77E-1
7.58       2.57E-3  2.05E-2  2.12E-3  1.06E-4   4.86E-3  1.68E-1
26.58       2.13E-3    5.25E-2  3.20E-3  5.00E-4   5.59E-2   9.52E-2
34.58       12.00E-5   7.11E-2  3.79E-3  9.73E-4   7.51E-2   8.00E-2
53.58       6.40E-5    6.20E-2  4.15E-3  1.44E-3  1.06E-1    5.00E-2
114.58     9.50E-5    4.00E-2  17.21E-4  1.57E-3  2.47E-1   7.61E-4
```

```
275.58     4.00E-6    0.90E-3  4.44E-4   1.00E-3  2.69E-1   3.43E-4
416.58     3.00E-6    0.70E-3  3.10E-4   5.00E-4  2.79E-1   2.71E-4];
T =DATA(:,1)';
CAX=DATA(:,2)';
CBX=DATA(:,3)';
CCX=DATA(:,4)';
CDX=DATA(:,5)';
CEX=DATA(:,6)';
CFX=DATA(:,7)';
t=T;
options=optimset('display', 'iter','LargeScale', 'off','MaxIter', 10000, 'MaxFu-
nEvals', 10000);
lb=[0 0 0 0 0 0 0 ]; ub=[10 10 10 10 10 10 10 ];
% inital guess for parameters
k0=[0.1 0.1 0.1 0.1 0.1 0.1 0.1];
[k,S]=fminsearchbnd(@OBJECTIVE150Cmech8, k0,lb,ub,
options,T,CAX,CBX,CCX,CDX,CEX,CFX);
x0 = [ 0  0  0  0  0  0];
tspan=0:1:500;
[t,yk1r]=ode45('ODE150Cmech8',tspan,x0,[],[k(1)+h k(2) k(3) k(4) k(5) k(6) k(7)]);
[t,yk2r]=ode45('ODE150Cmech8',tspan,x0,[],[k(1) k(2)+h k(3) k(4) k(5) k(6) k(7)]);
[t,yk3r]=ode45('ODE150Cmech8',tspan,x0,[],[k(1) k(2) k(3)+h k(4) k(5) k(6) k(7)]);
[t,yk4r]=ode45('ODE150Cmech8',tspan,x0,[],[k(1) k(2) k(3) k(4)+h k(5) k(6) k(7)]);
[t,yk5r]=ode45('ODE150Cmech8',tspan,x0,[],[k(1) k(2) k(3) k(4) k(5)+h k(6) k(7)]);
[t,yk6r]=ode45('ODE150Cmech8',tspan,x0,[],[k(1) k(2) k(3) k(4) k(5) k(6)+h k(7)]);
[t,yk7r]=ode45('ODE150Cmech8',tspan,x0,[],[k(1) k(2) k(3) k(4) k(5) k(6) k(7)+h]);
[t,yk1l]=ode45('ODE150Cmech8',tspan,x0,[],[k(1)-h k(2) k(3) k(4) k(5) k(6) k(7)]);
[t,yk2l]=ode45('ODE150Cmech8',tspan,x0,[],[k(1) k(2)-h k(3) k(4) k(5) k(6) k(7)]);
[t,yk3l]=ode45('ODE150Cmech8',tspan,x0,[],[k(1) k(2) k(3)-h k(4) k(5) k(6) k(7)]);
[t,yk4l]=ode45('ODE150Cmech8',tspan,x0,[],[k(1) k(2) k(3) k(4)-h k(5) k(6) k(7)]);
[t,yk5l]=ode45('ODE150Cmech8',tspan,x0,[],[k(1) k(2) k(3) k(4) k(5)-h k(6) k(7)]);
[t,yk6l]=ode45('ODE150Cmech8',tspan,x0,[],[k(1) k(2) k(3) k(4) k(5) k(6)-h k(7)]);
[t,yk7l]=ode45('ODE150Cmech8',tspan,x0,[],[k(1) k(2) k(3) k(4) k(5) k(6) k(7)-
```

```
h]);
df1dk1=(yk1r(:,1)-yk1l(:,1))/2/h; df1dk2=(yk2r(:,1)-yk2l(:,1))/2/h;
df1dk3=(yk3r(:,1)-yk3l(:,1))/2/h; df1dk4=(yk4r(:,1)-yk4l(:,1))/2/h;
df1dk5=(yk5r(:,1)-yk5l(:,1))/2/h; df1dk6=(yk6r(:,1)-yk6l(:,1))/2/h;
df1dk7=(yk7r(:,1)-yk7l(:,1))/2/h; df2dk1=(yk1r(:,2)-yk1l(:,2))/2/h;
df2dk2=(yk2r(:,2)-yk2l(:,2))/2/h; df2dk3=(yk3r(:,2)-yk3l(:,2))/2/h;
df2dk4=(yk4r(:,2)-yk4l(:,2))/2/h; df2dk5=(yk5r(:,2)-yk5l(:,2))/2/h;
df2dk6=(yk6r(:,2)-yk6l(:,2))/2/h; df2dk7=(yk7r(:,2)-yk7l(:,2))/2/h;
df3dk1=(yk1r(:,3)-yk1l(:,3))/2/h; df3dk2=(yk2r(:,3)-yk2l(:,3))/2/h;
df3dk3=(yk3r(:,3)-yk3l(:,3))/2/h; df3dk4=(yk4r(:,3)-yk4l(:,3))/2/h;
df3dk5=(yk5r(:,3)-yk5l(:,3))/2/h; df3dk6=(yk6r(:,3)-yk6l(:,3))/2/h;
df3dk7=(yk7r(:,3)-yk7l(:,3))/2/h; df4dk1=(yk1r(:,4)-yk1l(:,4))/2/h;
df4dk2=(yk2r(:,4)-yk2l(:,4))/2/h; df4dk3=(yk3r(:,4)-yk3l(:,4))/2/h;
df4dk4=(yk4r(:,4)-yk4l(:,4))/2/h; df4dk5=(yk5r(:,4)-yk5l(:,4))/2/h;
df4dk6=(yk6r(:,4)-yk6l(:,4))/2/h; df4dk7=(yk7r(:,4)-yk7l(:,4))/2/h;
df5dk1=(yk1r(:,5)-yk1l(:,5))/2/h; df5dk2=(yk2r(:,5)-yk2l(:,5))/2/h;
df5dk3=(yk3r(:,5)-yk3l(:,5))/2/h; df5dk4=(yk4r(:,5)-yk4l(:,5))/2/h;
df5dk5=(yk5r(:,5)-yk5l(:,5))/2/h; df5dk6=(yk6r(:,5)-yk6l(:,5))/2/h;
df5dk7=(yk7r(:,5)-yk7l(:,5))/2/h;
Jac1=
[df1dk1 df1dk2 df1dk3 df1dk4 df1dk5 df1dk6 df1dk7
df2dk1 df2dk2 df2dk3 df2dk4 df2dk5 df2dk6 df2dk7
df3dk1 df3dk2 df3dk3 df3dk4 df3dk5 df3dk6 df3dk7
df4dk1 df4dk2 df4dk3 df4dk4 df4dk5 df4dk6 df4dk7
df5dk1 df5dk2 df5dk3 df5dk4 df5dk5 df5dk6 df5dk7];
[t,YM]=ode45('ODE150Cmech8',tspan,x0,[],[k(1) k(2) k(3) k(4) k(5)
k(6) k(7)]);
CA =real(abs(YM(:,1)))'; CB =real(abs(YM(:,2)))';
CC=real(abs(YM(:,3)))'; CD =real(abs(YM(:,4)))';
CE=real(abs(YM(:,5)))'; CF=y60-CA-CB-CC-CD-CE;
DF=5*9-7;
Astar=Jac1'*Jac1; Astarinv=inv(Astar);
std-error=SE*sqrt(diag(Astarinv)) alpha=0.05;
```

```
tval=tinv(1-alpha/2,DF);
k1CI-left=k(1)-tval*std-error(1) k1CI-right=k(1)+tval*std-error(1)
k2CI-left=k(2)-tval*std-error(2) k2CI-right=k(2)+tval*std-error(2)
k3CI-left=k(3)-tval*std-error(3) k3CI-right=k(3)+tval*std-error(3)
k4CI-left=k(4)-tval*std-error(4) k4CI-right=k(4)+tval*std-error(4)
k5CI-left=k(5)-tval*std-error(5) k5CI-right=k(5)+tval*std-error(5)
k6CI-left=k(6)-tval*std-error(6) k6CI-right=k(6)+tval*std-error(6)
k7CI-left=k(7)-tval*std-error(7) k7CI-right=k(7)+tval*std-error(7)
fprintf('k1 Confidence interval=%.2f =< k1 <= %.2f \ n', k1CI-left, k1CI-right);
fprintf('k2 Confidence interval= %.2f =< k2 <= %.2f\ n', k2CI-left, k2CI-right);
fprintf('k3 Confidence interval= %.2f =< k3 <= %.2f\ n', k3CI-left, k3CI-right);
fprintf('k4 Confidence interval= %.2f =< k4 <= %.2f\ n', k4CI-left, k4CI-right);
fprintf('k5 Confidence interval= %.2f =< k5 <= %.2f\ n', k5CI-left, k5CI-right);
fprintf('k6 Confidence interval= %.2f =< k6 <= %.2f\ n', k6CI-left, k6CI-right);
fprintf('k7 Confidence interval= %.2f =< k7 <= %.2f\ n', k7CI-left, k7CI-right);
subplot(2,3,2),plot(T,CAX,'o',tspan,CA) title('tetra')
ylabel('Concentration, M')
subplot(2,3,3), plot(T,CBX,'o',tspan,CB) title('octa')
subplot(2,3,4), plot(T,CCX,'o',tspan,CC) title('hexa')
subplot(2,3,5), plot(T,CDX,'o',tspan,CD) title('deca')
xlabel('Time, min') ylabel('Concentration, M')
subplot(2,3,6), plot(T,CEX,'o',tspan,CE) title('dodeca')
xlabel('Time, min')
subplot(2,3,1), plot(T,CFX,'o',tspan,CF) title('ECZ')
xlabel('Time, min')
================================================================
```

G.2.2 Objective function

```
function OBJ=OBJECTIVE150Cmech8(x, T,CAX,CBX,CCX,CDX,CEX,CFX)
x0 = [ 2.98027E-1  0  0  0  0  0 ]; [T,Y]=ode45('ODE150Cmech8',T,x0,[],abs(x));
CA =real(abs(Y(:,1)));
CB =real(abs(Y(:,2)));
```

CC =real(abs(Y(:,3)));
CD =real(abs(Y(:,4)));
CE =real(abs(Y(:,5)));
CF =real(abs(Y(:,6)));
CA=CA(2:length(CA)); CB=CB(2:length(CB)); CC=CC(2:length(CC));
CD=CD(2:length(CD)); CE=CE(2:length(CE)); CF=CF(2:length(CF));
CAX=CAX(2:length(CAX));
CBX=CBX(2:length(CBX));
CCX=CCX(2:length(CCX));
CDX=CDX(2:length(CDX));
CEX=CEX(2:length(CEX));
CFX=CFX(2:length(CFX));
OBJ=sum(25 ∗(CA-CAX′).^{2} + 800∗(CB-CBX′).^{2} + 100∗(CC-CCX′).^{2} + 5000∗(CD-CDX′).^{2} + 20000∗(CE-CEX′).^{2} + 5∗(CF-CFX′).^{2});
==========

G.2.3 Ordinary differential equations

function dy = ODE150Cmech8(t,y,flag,p)
global n1 n2 n3 n4 n5 n6 n7
dy=zeros(6,1);
k1=p(1); k2=p(2); k3=p(3); k4=p(4); k5=p(5); k6=p(6); k7=p(7);
dy(1)=-k1*y(1)^{n1}-k2*y(1)^{n2};
dy(2)=k1*y(1)^{n1}-k3*y(2)^{n3};
dy(3)=k2*y(1)^{n2}-k5*y(3)^{n5}-k6*y(3)^{n6}+k4*y(4)^{n4};
dy(4)=k3*y(2)^{n3}-k4*y(4)^{n4};
dy(5)=k5*y(3)^{n5}-k7*y(5)^{n7};
dy(6)=k6*y(3)^{n6}+k7*y(5)^{n7};
==========

Appendix H

Additional publications

This appendix explains the following manuscript:
L. Zhao, F. Sotoodeh and K.J. Smith, Increased surface area of unsupported Mo_2C catalyst by alkali-treatment, Catalysis Communications 11 (2010) 391 - 395.

Preparation of the alkali-treated Mo_2C for 12 h, catalyst characterizations including XRD, BET surface area and pore size distributions measurements of the 6 h and 12 h alkali-treated Mo_2C, as well as dehydrogenation reactions of THCZ over a 5 wt % Pd/SiO_2 were done by Farnaz Sotoodeh.

H.1 Introduction

Molybdenum carbide is known to have catalytic properties similar to those of noble metals. Consequently, there is a significant interest in Mo_2C as a catalyst for a wide range of reactions, including hydrogenation [152, 153], dehydrogenation [154–157], synthesis gas conversion [158, 159], hydrocarbon isomerization [160], watergas-shift [161] and hydrogen production from methanol and ethanol [162]. Several methods have been developed for the synthesis of Mo_2C, including the most often used temperature-programmed reduction (TPR) of oxide precursors using CH_4 or CH_4/H_2 mixtures [75]. Other approaches have also been reported such as TPR using butane [163], carbothermal hydrogen reduction [164], the pyrolysis of metal precursors [165], solution reactions [166], and photochemically promoted

formation of carbide from metallic molybdenum and graphite [167]. The goal of almost all these synthesis methods is to enhance the catalyst surface area and hence increase the activity of Mo_2C catalysts. However, some of the known preparation methods are subject to limitations associated with cost and convenience. Furthermore, the surface area of the Mo_2C produced by temperature- programmed reduction of oxide precursors is greatly influenced by preparation conditions. The temperature ramp rate, the flow rate and composition of the reducing gas (CH_4, C_2H_6, H_2), and the precursor, all impact the product surface area and consequently, reported surface areas of unsupported Mo_2C vary widely [75, 152–163, 168–170]. An alternative, simple method of producing high surface area Mo_2C would be of significant benefit.

Alkali-treatment is a well known post-treatment technique used in zeolite synthesis, which introduces mesopore and macropore structure to the zeolite pore system [171, 172]. The alkali-treated zeolites show higher catalytic activity and increased surface area compared to un-treated zeolites. Although this technique has been used to prepare high surface area zeolites, it has not been applied to Mo_2C catalysts. In the present study, we report a simple post-treatment of Mo_2C using a hot alkali solution that enhances the Mo_2C surface area while retaining the structural integrity of the Mo_2C. The obtained high surface area Mo_2C has been used as a catalyst for the dehydrogenation of 1,2,3,4-tetrahydrocarbazole (THCZ) and the hydrogenation of CO. THCZ is a candidate heteroaromatic compound for hydrogen storage. Hydrogen is released through catalytic dehydrogenation at low temperature (< 423 K), using platinum group metal catalysts (Pd, Pt, Rh and Ru) [53, 54, 106]. Because of the cost of the platinum group metals, metal carbides are possible alternatives for this reaction. Metal carbides have also been shown to be active in several CO hydrogenation reactions aimed at producing higher hydrocarbons [168] and alcohols [159] and consequently we have tested the prepared Mo_2C for syngas conversion as well.

H.2 Experimental

H.2.1 Catalyst preparation

Unsupported Mo_2C was synthesized by temperature-programmed reduction of an oxide precursor. Approximately 3 g of MoO_3 (MoO_3, +99.5 %, SigmaAldrich) was placed in a quartz tubular reactor and heated at a rate of 5 K/min from room temperature to 573 K, followed by heating at a rate of 1 K/min from 573 K to 948 K in 100 ml(STP)/min of CH_4/H_2 (1:4 vol). The final temperature was held for 2 h in the same CH_4/H_2 flow. The sample was then rapidly cooled to room temperature in a 80 ml(STP)/min flow of H_2. The sample was passivated by exposure to a mixture of 1 % O_2 in He at a flow rate of 133 ml(STP)/min for 4 h before being removed from the reactor. Approximately 3 g of the passivated Mo_2C was placed in 90 ml of a 5 M NaOH solution and stirred for 2, 6 and 12 h at 363 K. The mixture was subsequently cooled in an ice bath. The liquid and solid were separated by centrifuging at 12,000 rpm for 20 min at 288 K. The solid was washed with deionized water until the washings showed a neutral pH. The catalyst was then dried at room temperature and activated in H_2 (510 ml(STP)/min) at 573 K for 2 h before being used for reaction. The catalysts are designated AT-2, AT-6 and AT-12 to identify the duration of the alkali-treatment in each case.

H.2.2 Characterization

The passivated catalysts were characterized by powder X-ray diffraction (XRD), scanning electron microscopy (SEM), energy dispersive X-ray analysis (EDX), N_2-adsorption/desorption at 77 K and thermogravimetric analysis. Prior to N_2 adsorption, the samples were degassed at 423 K in 30 mol % N_2/He (15 ml(STP)/min) for 2 h to remove moisture. All other analyses were carried out on the passivated samples without further treatment. The XRD analysis was performed using a Siemens D500 Cu K_α X-ray source of wavelength (λ) 1.54 $\mathring{A}$. The scan rate was 2° per min for a range of 580° to confirm the structure of Mo_2C, and 0.5° per min for the range of 3242° to estimate the crystallite size (d_c) of the Mo_2C using the Scherrer equation, $d_c = K\lambda/\beta\cos\theta$, where the constant K was considered 0.9, λ is the wavelength of radiation, β is the peak width in radians and θ is the angle of diffraction.

N_2- adsorption/desorption isotherms were recorded at 77 K using a Micromeritics ASAP 2020 analyzer. The total surface area was calculated according to the BET isotherm, and the micropore volume, the mesopore volume, and external surface area were evaluated by the t-plot method. The pore size was reported as the average pore diameter. SEM/EDX analysis was performed using a Hitachi S-3000 N electron microscope operated with a 150 kV electron beam acceleration voltage. Thermogravimetric analysis of the catalysts was done using a TGA-50 thermogravimetric analyzer (Shimadzu, Japan). About 5 to 10 mg of the catalyst was loaded into an alumina crucible and heated to 1000 K at a rate of 5 K/min in an air atmosphere (flow rate = 15 ml(STP)/min). The weight change were quantified and differential TGA (DTG) was obtained.

H.2.3 Catalyst activity

Dehydrogenation of 1,2,3,4-tetrahydrocarbazole (THCZ) was performed at 423 K using a solution of 2.0 g THCZ dissolved in 30 ml mesitylene. The solution was loaded into a 50 ml glass flask reactor. The 1.0 g alkali-treated Mo_2C was added to the solution after activation in hydrogen. The reactor was sealed, stirred, purged in a flow of He (100 ml(STP)/min) and heated to 423 K. The He was used as a carrier gas for continuous removal of the produced hydrogen and the exit gas composition was continuously monitored using a quadrupole mass spectrometer. Catalyst activity was determined by the production of H_2 and confirmed by periodic liquid analysis using a gas chromatograph (Shimadzu GC-14A) with a flame ionization detector and an ATTM-5 25 M $\times$ 0.53 mm capillary column. Product identities were also confirmed by a Shimadzu QP-2010S GC/MS using a Restek RTX5 30 M $\times$ 0.25 mm capillary column. The absence of internal and external mass transfer effects on the reaction was confirmed experimentally and by theoretical analysis [107].

The activity of the Mo_2C catalysts for synthesis gas conversion was also measured using a fixed-bed micro reactor (o.d. = 9.53 mm and i.d. = 6.35 mm, copper lined stainless steel tube). The catalyst was loaded into the reactor and fixed on a packed bed of quartz wool and quartz beads. The catalyst bed depth was 5 to 7 cm to ensure plug-flow in the reactor. Synthesis gas (H_2:CO = 1) was reacted at

573 K, a pressure of 8.3 MPa and a GHSV = 3960 h^{-1}. Details of experimental procedure have been discussed elsewhere [173]. Conversion and selectivity data were confirmed to be within ± 10 % of the reported results by repeating the experiments. Internal and external heat and mass transfer rates at the conditions of the experiments were found to be negligible according to the calculations based on the Mears and Weisz−Prater criteria.

H.3 Results and discussion

H.3.1 Mo_2C properties

The properties of the Mo_2C and the alkali-treated Mo_2C, reported in Table H.1, show that several changes occurred to the Mo_2C after alkali-treatment. Compared to the un-treated Mo_2C, the alkali-treated Mo_2C showed a significant increase in surface area, an increase in the micropore area and a decrease in the average pore size of the Mo_2C. The BET surface area of the alkali-treated Mo_2C increased from 29 m^2/g to 40 to 47 m^2/g, an increase of about 50 %. The N_2 adsorption and desorption isotherms of the Mo_2C and the alkali-treated Mo_2C (Figure H.1) showed increased hysteresis effects with increased time of the alkali-treatment.

Figure H.2 presents the pore size distribution of the Mo_2C and the alkali-treated Mo_2C. Clearly, the alkali-treatment increased the fraction of pores < 3 nm in size and decreased the average pore size (d_p) of the Mo_2C treated with NaOH for 2 and 6 h. After 12 h, Figure H.2 shows that a significant increase in pores of size 20 - 30 nm had also occurred. The data of Table H.1 shows that as the alkali-treatment time increased, the micropore area also increased. These results suggest that the alkali-treatment initially removed material from the Mo_2C to generate new pores of < 3 nm in diameter, resulting in a decrease in the average pore size. With increased treatment time (12 h) the removal of material from larger pores also occurred. These observations are quite different to changes observed in zeolites treated with alkali. Typically with zeolites, the microporosity decreases and the meso- and macroporosity increases, leading to an increase in the average pore size of the alkali-treated zeolite compared to the un-treated zeolite [171, 172].

Figure H.3 shows the XRD patterns of the Mo_2C and the alkali-treated Mo_2C.

Table H.1: Properties of the unsupported Mo_2C catalysts.

Property	Mo_2C	Alkali-treated Mo_2C[a]		
		2 h AT-2	6 h AT-6	12 h AT-12
N_2 adsorption−desorption				
S_{BET} (m^2/g)	29.4 ± 1.1[b]	44.5	47.3 ± 3.1[b]	40.0
$S_{t-micro}$ (m^2/g)	0.06 ± 0.05	0.05	4.8 ± 2.5	10.4
S_{t-ext} (m^2/g)	29.9 ± 1.9	44.4	42.5 ± 0.6	29.6
V_p (cm^3/g)	0.031 ± 0.005	0.043	0.036 ± 0.001	0.030
d_p (nm)	4.19 ± 0.5	3.82	3.01 ± 0.12	2.98
XRD analysis				
d_c (1 0 1) (nm)	13.6	13.0	13.1	13.9
d_c (1 0 0) (nm)	15.2	14.5	15.2	14.6
a (Å)	3.005	3.005	3.009	3.012
c (Å)	4.742	4.782	4.764	4.746

[a] Mo_2C treated in 5 M NaOH for the time period shown.
[b] Standard deviation from three repeat measurements.

The eight peaks at 2θ equal to 34.48, 37.96, 39.52, 52.28, 61.76, 69.56, 74.80, and 75.72 can be indexed to hexagonal Mo_2C (1 0 0), (0 0 2), (1 0 1), (1 0 2), (1 1 0), (1 0 3), (1 1 2), and (2 0 1). There were no differences between the peaks before and after alkali-treatment, indicating that the crystal structure of the Mo_2C was not changed by the alkali-treatment. The Mo_2C crystallite size was calculated from the Scherrer equation and the results, summarized in Table H.1, suggest that no significant change in crystallite size occurred after alkali-treatment of the Mo_2C either. The lattice parameters of the catalysts were also calculated using the Bragg equation and the results are listed in Table H.1. According to the JCPDS card No. 11-0680, the lattice parameters of Mo_2C are a = 3.006 Å and c = 4.733 Å and the results obtained in the present work (Table H.1) are in good agreement with these values. Hence we conclude that the crystal structure of the Mo_2C was not affected by alkali-treatment. Also, the SEM micrographs of Figure H.4 show that the Mo_2C and the alkali-treated Mo_2C had very similar macro-morphology. The materials consisted of platelet-like grains, < 5 μm in size, and the alkali-treatment had no discernable effect on this Mo_2C morphology.

Figure H.5 shows the differential TGA curves of the Mo_2C and the 2 h alkali-treated Mo_2C. Both samples had very similar characteristics, with two main peaks

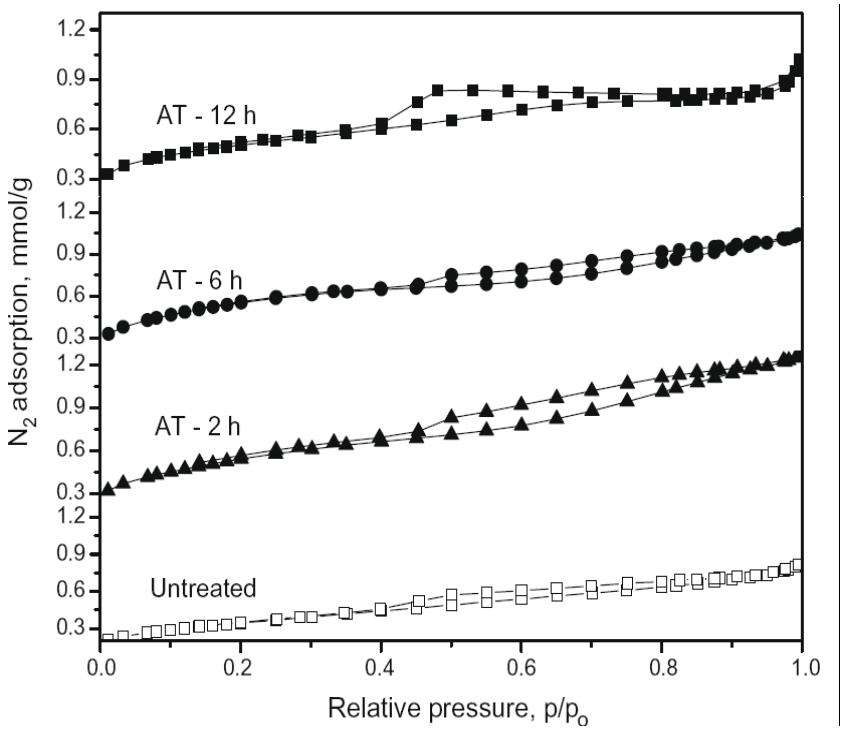

Figure H.1: N_2 adsorptiondesorption isotherms measured at 77 K for Mo_2C and alkali-treated Mo_2C catalysts.

generated as the Mo_2C was oxidized to MoO_2 and then MoO_3. The total weight gain in both cases was 95 % of the expected gain for pure Mo_2C conversion to MoO_3, confirming that the bulk of the material was phase pure Mo_2C. These results indicate that the new pores of < 3 nm diameter generated by alkali-treatment were a consequence of Mo_2C dissolution, rather than simply due to the selective removal of excess carbon or other impurity from the pores of the catalyst.

H.3.2 THCZ dehydrogenation

Since THCZ is a solid powder at ambient conditions with high boiling point (598 K) and melting point (391 K), the dehydrogenation reaction was carried out in the liquid phase by dissolving the THCZ in mesitylene. Over supported Pd catalysts, the reaction was zero-order in substrate (THCZ) concentration, and the catalysts

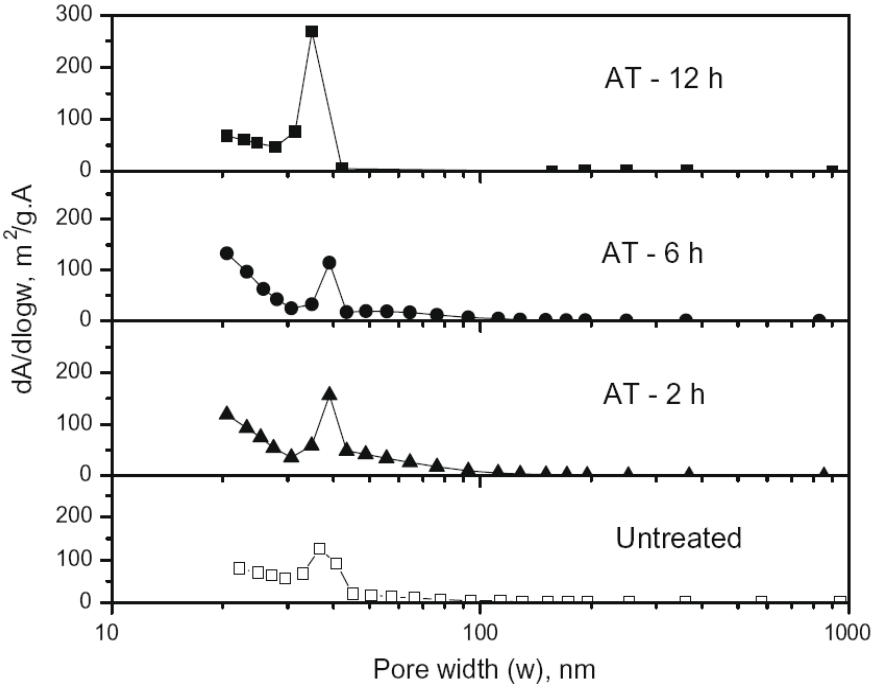

Figure H.2: Pore size distribution of Mo_2C and alkali-treated Mo_2C catalysts.

showed 100 % selectivity to the desired carbazole product. However, it was shown from experiment that product inhibition slowed the rate of reaction and 81 % conversion was obtained after about 27 h at 101 kPa and 413 K. The initial rate of THCZ dehydrogenation at these conditions was 10 $mM.g_{cat}{}^{-1}.min^{-1}$ [53]. The dehydrogenation activity of Mo_2C and the 2 h alkali-treated Mo_2C was determined at 423 K. The data for the two catalysts presented in Table H.2, show an initial THCZ dehydrogenation rate of 0.014 and 0.048 $mM.g_{cat}{}^{-1}.min^{-1}$, respectively. The alkali-treated Mo_2C had about 3$\times$ the initial activity of the un-treated Mo_2C for THCZ conversion. The H_2 produced in the first 30 min of reaction was similarly higher on the alkali-treated catalyst. The activity (on a mass basis) of both Mo_2C catalysts was approximately two orders of magnitude lower than that reported for supported Pd catalysts used for the dehydrogenation reaction.

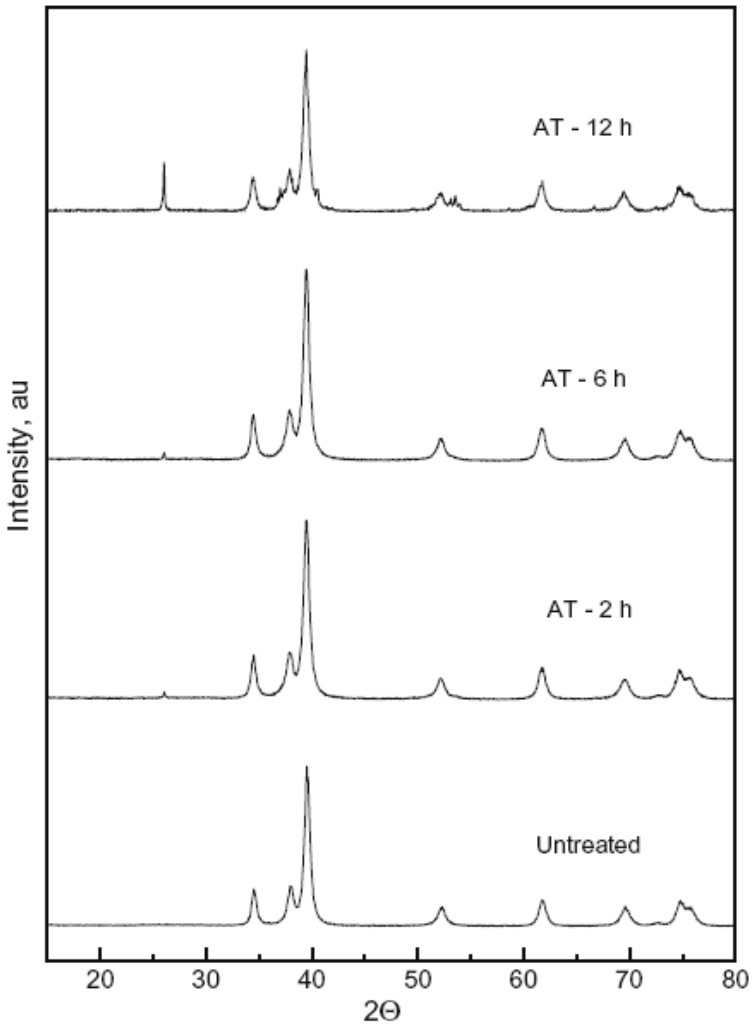

Figure H.3: X-ray diffractograms of Mo_2C and alkali-treated Mo_2C catalysts.

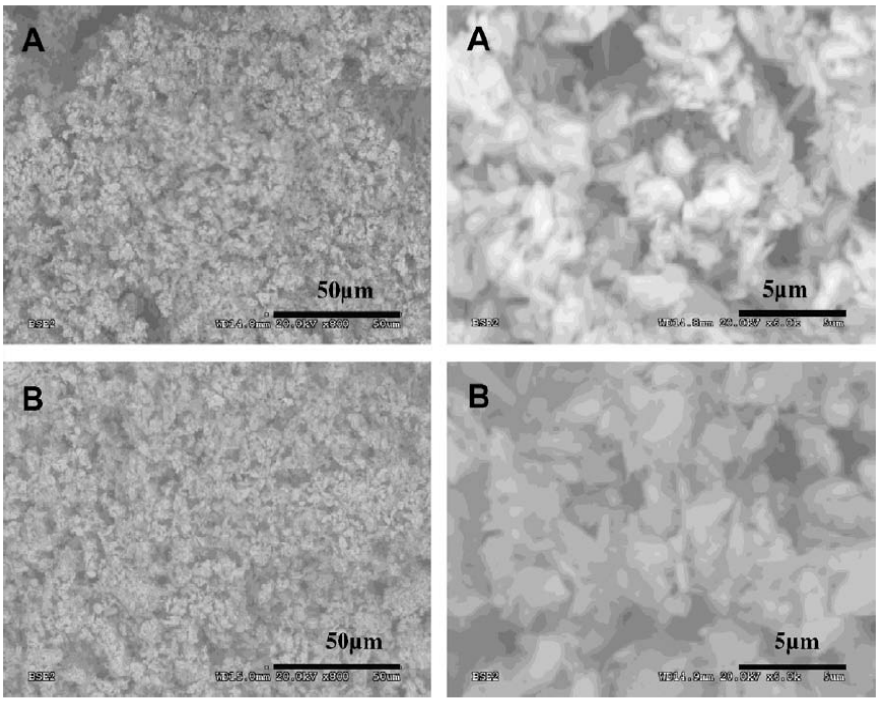

Figure H.4: SEM micrographs of (A) Mo_2C and (B) 2 h alkali-treated Mo_2C.

Table H.2: THCZ dehydrogenation activity measured in a batch reactor at 101 kPa and 423 K over unsupported Mo_2C catalysts.

Catalyst	Reaction temperature (K)	Initial rate ($mM.g_{cat}{}^{-1}.min^{-1}$)[a]	H_2 produced/g_{cat} ($mmol/g_{cat}$)[a]
Mo_2C	423	0.014	0.056
AT-2 Mo_2C	423	0.048	0.184

[a] After 30 min reaction.

H.3.3 CO hydrogenation reaction

Several Mo compounds have also been investigated for synthesis gas conversion. MoS_2, Mo_2O_3 and Mo_2C show high selectivity towards liquid oxygenates, especially ethanol, when doped with alkali earth metals. In addition, the Mo_2C has high CO_2 yield rather than water, a consequence of high watergas-shift activity

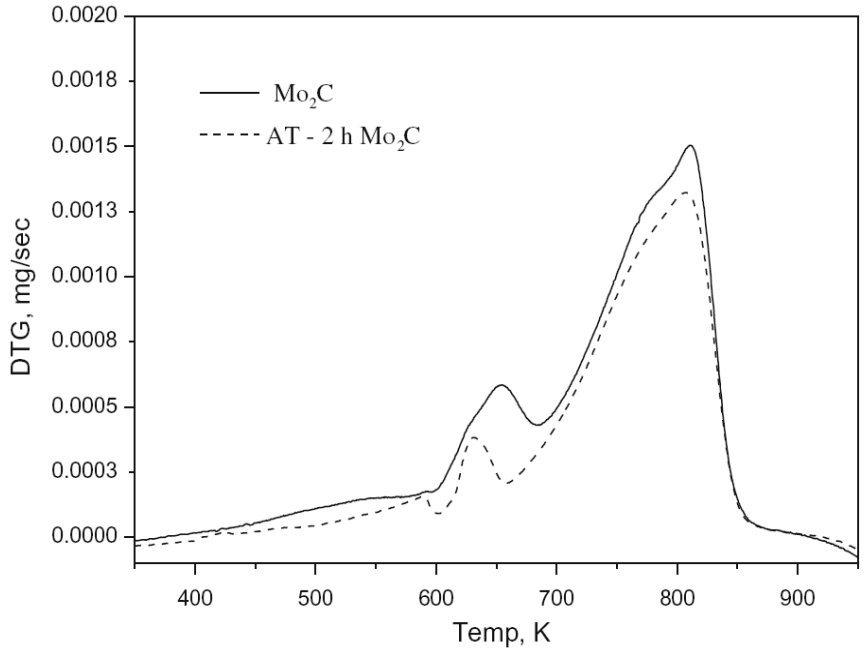

Figure H.5: Temperature-programmed oxidation of Mo_2C and 2 h alkali-treated Mo_2C catalysts.

[161]. For example, the rate of CO consumption over Mo_2C with low surface area (approximately 5 m^2/g) at 573 K and 8.0 MPa with a H_2:CO ratio 1:1, was approximately 0.4 $mmol.g_{cat}{}^{-1}.min^{-1}$ based on a reported CO conversion of 58 % at a GHSV of 2000 h^{-1} [159]. In the present work, Mo_2C and the 2 h alkali-treated Mo_2C were tested for synthesis gas conversion at 573 K and 8.0 MPa with a H_2:CO ratio 1:1 and a GHSV of 3960 h^{-1}. The initial catalyst activities (after a 2 h stabilization period) are reported in Table H.3. The data show that alkali-treated Mo_2C increased the CO consumption rate by about 10 % compared to the un-treated Mo_2C. The data show higher CO consumption rates than that reported by Xiang et al. [159] on both the Mo_2C and the alkali-treated Mo_2C. High CH_4 and CO_2 selectivities were also obtained on the two catalysts of the present study.

Typically, Mo_2C catalysts are promoted with alkali metal to reduce selectivity

Table H.3: Syngas conversion on Mo_2C and alkali-treated Mo_2C. Reaction conditions: pressure = 8.2 MPa, temperature = 573 K, CO:H_2 = 1 and GHSV = 3960 h^{-1}.

Catalyst	Initial CO consumption rate (mmol.$g_{cat}{}^{-1}$.min^{-1})[a]	Initial product selectivity[a] C_2 + alcohols and HCs C atom%	CH_4	CO_2
Mo_2C	2.06	25.4	26.0	48.6
AT-2 Mo_2C	2.24	27.5	20.9	51.7

[a]Measured 2 h after the start of the experiment.

to CH_4 so the high selectivity obtained in the present work was not unexpected. The alkali-treated catalysts had been thoroughly washed prior to use and EDX confirmed that the Mo_2C was Na-free. The product distribution also showed enhanced watergas-shift activity on the alkali-treated sample compared to the untreated Mo_2C. Figure H.6 shows the change in CO consumption rate and the product selectivity obtained over a period of approximately 10 h. The product selectivities remained relatively constant during the experiments, whereas the alkalitreated catalyst showed some deactivation, possibly because of carbon deposition. A loss in activity in the first 2 h of reaction may also explain why the differences in the CO consumption rates between the un-treated and alkali-treated Mo_2C were not as great as observed for the THCZ dehydrogenation reaction.

H.4 Conclusion

The surface area of an unsupported Mo_2C catalyst was increased by a simple alkali-treatment of the Mo_2C that had been prepared by temperature-programmed reaction of a MoO_3 precursor. The alkali- treatment increased the catalyst surface area by 50 %, primarily through the creation of new pores of size < 3 nm. The alkali-treatment did not change the Mo_2C morphology nor the catalyst composition. The alkali-treated Mo_2C showed enhanced activity for the dehydrogenation of THCZ and for CO hydrogenation, compared to the un-treated Mo_2C.

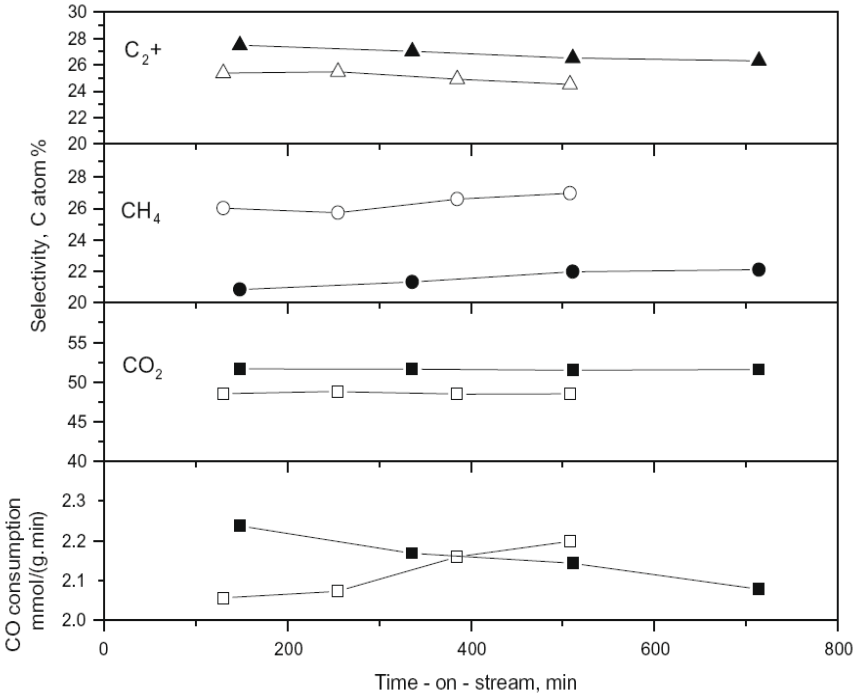

Figure H.6: CO consumption rate and product selectivities obtained over the un-treated Mo_2C (open symbols) and the 2 h alkali-treated Mo_2C (solid symbols) measured at 8.2 MPa, 573 K, CO:H_2 = 1 and GHSV = 3960 h^{-1}.